UNIVERSITÀ
DEGLI STUDI
FIRENZE

PhD in
Civil And Environmental Engineering

CYCLE XXXIII

COORDINATOR Prof. Borri Claudio

Innovative Technologies In Non-Invasive Urodynamics Diagnostic

Academic Discipline (SSD) ICAR/01

Doctoral Candidate
Dr. Lotti Lorenzo

Supervisor
Prof. Paris Enio

Supervisor
Prof. Serni Sergio

Coordinator
Prof. Borri Claudio

Years 2018/2020

ACKNOWLEDGEMENTS

At first, heartfelt thanks to my supervisors, Professors Enio Paris and Sergio Serni, for the time they have devoted to my thesis, for their patience, their suggestions and their corrections. I would also like to thank Prof. Giulio Nicita, who started this project in 2012 together with Prof. Paris, and who followed my work until 2018.

Thanks to the PhD coordinators who have followed one another over these years: Prof. Fabio Castelli, Prof. Claudio Borri and the upcoming Prof. Luca Solari.

Many thanks to the PhD secretariats Margherita Mellini and Giuditta Tirinnanzi for the perfect organization of PhD events.

Thanks to the technicians of the Hydraulic Laboratory of DICEA, Muzio Mascherini and Mauro Gioli, and to the technicians of the Urology Clinic of DMSC, Dr. Martina Milanesi and Dr. Pietro Spatafora, for their invaluable assistance in all these years.

A special thanks to my PhD fellows, who shared with me experiences and travels of the Doctorate.

Finally, thanks to my friends, always close to me; the biggest thanks to my dad, my mom and Alessandro, giving me the strength to keep going on.

ABSTRACT

Nowadays, clinical investigations to understand the functionality of the lower urinary tract (LUT) are based on invasive techniques (e.g. use of catheters) for measuring intra-bladder pressure and flowmetry through urethra. These techniques can lead to significant discomfort and possible complications to patients; moreover, they represent for the health agencies an economic burden in terms of costs associated with supplies, and above all they require a great deal of personnel's time; finally, current techniques are inadequate for urodynamic analysis in pediatric subjects.

This interdisciplinary project intends to verify the possibility to develop an Innovative Instrumentation for non-invasive Urodynamics, that is in which no part of the machine comes in contact with the human body, and moreover it is characterized by the same diagnostic reliability of the techniques in use today. This Innovative Instrumentation can bring many benefits: for the patient, who is relieved of the discomfort related to the traditional methodology, and who takes less time to perform it (15 minutes instead of 60); for the structure that uses this Innovative Instrumentation, which can reduce operating costs both in terms of materials and in terms of personnel.

The basic concept arises from considering the LUT similar to a hydraulic system consisting of a pressure feed tank (bladder) and an outlet elastic duct (urethra) whose physical behavior is governed by the laws of fluid mechanics. Starting from the knowledge of the physical quantities of the urinary jet measurable outside of the urethra it is possible to model the LUT internal urodynamic characteristics.

A physical model of the LUT has been specifically designed and assembled in the Hydraulic Laboratory of the Department of Civil and Environmental Engineering (DICEA) of the University of Florence: basically, it consists of a pressure feed tank connected to a latex elastic collapsible output tube, that has a similar behavior to the urethra. The model has been tested with experiments to evaluate jet external characteristics under many different conditions (i.e. presence or absence of obstructions, type of obstructions, presence of absence of catheter, different types of instrumentations, etc.).

Furthermore, a numerical model of the flow in elastic tube has been developed to simulate the Laboratory experiments and to represent the complex phenomena that occur in the LUT in physiological and pathological conditions. Once the numerical model has been calibrated, the detrusor pressure can be estimated from the values of flow rate and exit velocity obtained by non-invasive measurements, that is measurements taken with no contact with the human body.

In parallel, a prototype of the Innovative Instrumentation has been developed. It has been built in the Hydraulic Laboratory of the DICEA and it has been taken to the Urology Clinic at the Department of Experimental and Clinical Medicine (DMSC) of Careggi Hospital, Florence, to

perform a clinical testing campaign on healthy male volunteers to test and calibrate the diagnostic reliability of the new equipment.

Finally, it is proposed a “Coupled Urodynamic Diagram” that can be used to estimate the detrusorial pressure and that allows to trace the functional status of the patient using only non-invasive data.

List of Figures

Figure 1.1: urinary system 25
Figure 1.2: female (a) and male (b) LUT 26
Figure 1.3: intravesical pressure as a function of the urine volume inside the bladder 27
Figure 1.4: male urethra 28
Figure 1.5: female urethra 29
Figure 1.6: urine flow in a normal (left) and enlarged (right) prostate (https://www.cancer.gov/types/prostate/understanding-prostate-changes) 30
Figure 1.7: diagramatic representation of urethral stricture (Chapple et al, 2020) 31
Figure 1.8: UROBENCHMARK 2000-3 uroflowmeter 32
Figure 1.9: example of a P/F Study recording 33
Figure 1.10: urethral Resistance Relation (URR) 34
Figure 1.11: PURR examples 34
Figure 1.12: Abrams-Griffiths nomogramm 37
Figure 1.13: determination example of URA factor 38
Figure 1.14: Schäfer's diagram: example of compressive obstruction (red line A) or constrictive obstruction (red line B) 39
Figure 1.15: Schäfer's diagram "simplified": patients are considered not obstructed in the green zone and uncertain in the yellow zone 39
Figure 1.16: ICS Previsional Method 40
Figure 2.1: similarity between the LUT and a hydraulic system 44
Figure 2.2: the Laboratory physical model 45
Figure 2.3: Model details: (a) close-up of the Model and of the cylindrical tank; (b) the Tube 46
Figure 2.4: the Tube compared to a one euro coin 47
Figure 2.5: lower foam block with the Tube placed on it 47
Figure 2.6: overall scheme of the Model 48
Figure 2.7: pressure transducer placed on the bottom of the tank 49
Figure 2.8: National Instruments NI-9203 current input module (a); NI-cDAQ-9174 USB chassis (b) 50
Figure 2.9: water tank levels: the black dots (transducer's data), the blue line (polyline estimation) and the red line (spline estimation) almost overlap; the area in the purple box is enlarged in Figure 2.10 51
Figure 2.10: part of the water tank data in the purple box of Figure 2.9 52
Figure 2.11: flow rate Q evaluated from the level data H_0 shown in Figure 2.9 53
Figure 2.12: scheme of the Model with position of the Tube entrance (H_c section) 54
Figure 2.13: modified Model to replicate the system emptying tests without the Tube 55
Figure 2.14: energy losses due to the various pipe components between the tank and the Tube. 56

Figure 2.15: the purple line represents the estimated total head at Tube entrance $H_{c,estimated}$ as a function of the measured total head $H_{c,measured}$; σ is the standard deviation and σ* the relative standard deviation between the two values 57

Figure 2.16: Celmi srl load cell ECX-100 60

Figure 2.17: procedure to draw an orthogonal surface (red line); the blue lines are the jet exit parabolas with the exit angles θ_e indicated in the blue boxes 60

Figure 2.18: orthogonal surfaces for a jet exit distance (a) h_{lc}=10 cm, (b) h_{lc}=20 cm, (c) h_{lc}=50 cm and various jet exit velocity u_e as shown in legends 62

Figure 2.19: example of the impact of a jet on a load cell knowing the distance h_{lc} and the flow rate Q 63

Figure 2.20: disposition of the three load cells and the connected flat plates; the red line represents the u_e=2 m/s line in Figure 2.18b 64

Figure 2.21: position of the load cells with respect to the Tube's exit; the red line represents the u_e=2 m/s line in Figure 2.18b 65

Figure 2.22: results of test 871 (a) and 873 (b) on estimating u_e with load cells: the green line is the estimated data with the load cells, the red line represents the moving average of estimated data, the black line is the real velocity 66

Figure 2.23: Eltra optical encoder (left), mounted on a plexiglas panel with a reel on the axes (right) 67

Figure 2.24: example of jet exit velocity estimation with the optical encoder 67

Figure 2.25: parabolic trajectory of a jet outside a tube 69

Figure 2.26: the jet outside the Tube has a parabolic trajectory 69

Figure 2.27: example of an image acquisition during a test: the red box is the jet area 70

Figure 2.28: highlight of the jet stream (black dots) and interpolation as a parabola (red line): the relative standard deviation is 1.9%. 70

Figure 2.29: results of the tests for jet exit velocity estimation with image processing varying the jet exit angle 71

Figure 2.30: section of the Tube to evaluate thickness and external diameter 72

Figure 2.31: (a) the Tube on a flat support; (b) claw used to close the Tube downstream 74

Figure 2.32: pictures of the Tube taken on the vertical (a) and the horizontal (b) plane 74

Figure 2.33: correlation between water level inside the tank H and the Tube's average external diameter D 75

Figure 2.34: variation of the elasticity modulus E of the Tube with respect of the static water level inside the tank H 76

Figure 2.35: comparison between the jet exit momentum measured in the tests with the Tube subjected to different loads (represented with the colored lines) and Griffiths' data from clinical trials (black dots) 77

Figure 2.36: comparison between tests results of different external pressures on the Tube plotted on Schäfer's diagram 78

Figure 3.1: Final "Physiological flow condition" tests (Physiological-tests): the dashed lines represents the decreasing of the water level inside the tank over time during emptying 82

Figure 3.2: Flow rate Q in "Physiological flow condition" tests (Physiological-tests) as a function of the water level inside the tank H_0: dashed lines are the single tests, bold purple line is the tests' average 83

Figure 3.3: Schäfer's diagram with the results of the Physiological-tests: the bold purple line is the tests' average 84

Figure 3.4: the black dotted line is average correlation between jet exit velocity u_e and total head at the Tube's entrance H_c (between 0.2 and 0.8 m, black dashed vertical lines) in Physiological-tests; the purple, blue, green and red lines are the 1st, 2nd, 3rd and 4th degree polynomial interpolation, respectively 85

Figure 3.5: correlation between real Hc and estimated Hc data with 1st, 2nd, 3rd and 4th polynomial interpolation curve; in the box of the same color, the relative deviation standard for each curve 86

Figure 3.6: metal cylinders used as obstructions in Pathological-tests with internal diameters D_{ob} 88

Figure 3.7: lengths L_{ob} of the metal cylinders 88

Figure 3.8: positions X_{ob} of the metal cylinders 88

Figure 3.9: Pathological-tests results on Schäfer's diagram with internal diameter D_{ob}=4 mm: each line is the average of at least 4 repetitions. The black line is the test without obstruction 90

Figure 3.10: Pathological-tests results on Schäfer's diagram with internal diameter D_{ob}=3 mm: each line is the average of at least 4 repetitions. The black line is the test without obstruction 91

Figure 3.11: Pathological-tests results on Schäfer's diagram with internal diameter D_{ob}=2 mm: each line is the average of at least 4 repetitions. The black line is the test without obstruction 92

Figure 3.12: double-way catheter used in Diagnostic-tests compared to a one euro coin 94

Figure 3.13: the catheter was placed inside the Tube and, through the connectors and the valve, goes inside the tank 95

Figure 3.14: Q and Q_{cat} trend as a function of the total head at the Tube's entrance H_c 96

Figure 3.15: percentage of the relative flow rate reduction ΔQ* as a function of the total head at the Tube's entrance H_c 96

Figure 3.16: comparison between Diagnostic-tests (black line) and clinical data from literature (red marks) 98

Figure 3.17: MDWC type 1 (upper), used to measure the piezometric head inside the Tube & MDWC type 2 (lower), used to measure the total head inside the Tube 100

Figure 3.18: measurements sections of piezometric and total head inside the Tube 101

Figure 3.19: Biotrans pressure transducer 101

Figure 3.20: FV-tests results: piezometric head h in the Tube's sections; same color represents the same total head at the Tube's entrance H_c 102

Figure 3.21: FV-tests results: total head H in the Tube's sections; same color represents the same total head at the Tube's entrance H_c 103

Figure 3.22: the purple line represents the total head at Tube entrance H_c as a function of the measured total head with MDWC type 2: the relative standard deviation σ* between the two values is about 1% (σ=6.6 mm the standard deviation) 104

Figure 3.23: water velocity u in the Tube's sections; same color represents the same total head at the Tube's entrance H_c 105

Figure 3.24: cross-sectional area ratio $\boldsymbol{\alpha}$ in the Tube's sections; same color represents the same total head at the Tube's entrance H_c 106

Figure 4.1: behavior of the section of an elastic tube when varying the transmural pressure (Carpenter & Pedley, 2003) 108

Figure 4.2: (a) isotropic external pressure; (b) our case study: the pressure is oriented only in the vertical direction 109

Figure 4.3: experimental measures of area ratio $\boldsymbol{\alpha}$ (blue dots) and an example of the literature TL 4.5 (black line) 110

Figure 4.4: experimental data classified by H_c values (see legend); the lines, colored same as the markers, represent the interpolation of the data with the TL (equation 4.7) 111

Figure 4.5: level in the supply tank, referred to the horizontal axis of the Tube, during the emptying phase 112

Figure 4.6: time variation of first derivative of H_0 113

Figure 4.7: study domain: the regions from section 1 to 6 and from section 20 to 21 are excluded from the numerical simulation 115

Figure 4.8: speed index S from experimental data as a function of the area ratio $\boldsymbol{\alpha}$ 116

Figure 4.9: comparison between Laboratory test (red dots) and numerical upstream simulation (blue line) with a total head at the Tube's entrance H_c=0.6 m: (a) cross-sectional area ratio $\boldsymbol{\alpha}$, (b) total head H and (c) piezometric head h, along the Tube 120

Figure 4.10: comparison between Laboratory test (red dots) and numerical upstream simulation (blue line) with a total head at the Tube's entrance H_c=1.2 m: (a) cross-sectional area ratio $\boldsymbol{\alpha}$, (b) total head H and (c) piezometric head h, along the Tube 122

Figure 4.11: comparison between Laboratory tests and numerical simulation: (a) cross-sectional area ratio $\boldsymbol{\alpha}$; (b) total head H; (c) piezometric head h 124

Figure 4.12: total head reduction ratio ΔH_c^* between section c (the Tube's entrance) and section 7 (a), total head increase ratio ΔH_e^* between section e (the Tube's exit) and section 19 (b), cross-sectional area ratio increase ratio $\Delta\boldsymbol{\alpha c}*$ between section c and section 7 (c), as a function of H_c estimated using Diagnostic-tests data: the blue line is the Laboratory data while the red dashed line is the mean value (a,b) or the 2nd order polynomial fitting (c) 126

Figure 4.13: results of the numerical model applied to Physiological-tests: (a) cross-sectional area ratio $\boldsymbol{\alpha}$, (b) total head H, (c) piezometric head h. Solid lines represent the numerical simulation, while dots are the Laboratory tests data; each color represents the situation at a fixed total head at the Tube's entrance H_c, as shown in the legend. 128

Figure 4.14: results of the numerical simulation applied to Pathological-tests with an obstruction 5 mm long, having 4 mm internal diameter and placed in the center: (a) cross-sectional area ratio $\boldsymbol{\alpha}$, (b) total head H, (c) piezometric head h. Solid lines represent the numerical simulation, while dots are the Laboratory tests data; each color represents the situation at a fixed total head at the Tube's entrance H_c, as shown in the legend. The black line with the triangles represents the obstruction 132

Figure 4.15: results of the numerical simulation applied to Pathological-tests with an obstruction 20 mm long, having 3 mm internal diameter and placed upstream: (a) cross-sectional area ratio $\boldsymbol{\alpha}$, (b) total head H, (c) piezometric head h. Solid lines represent the numerical simulation, while dots are the Laboratory tests data; each color represents the situation at a fixed total head at the beginning of the Tube H_c, as shown in the legend. The black line with the triangles represents the obstruction 134

Figure 4.16: results of the numerical simulation applied to Pathological-tests with an obstruction 50 mm long, having 2 mm internal diameter and placed in the center: (a) cross-sectional area ratio α, (b) total head H, (c) piezometric head h. Solid lines represent the numerical simulation, while dots are the Laboratory tests data; each color represents the situation at a fixed total head at the beginning of the Tube H_c, as shown in the legend. The black line with the triangles represents the obstruction 136

Figure 4.17: comparison between Physiological-tests and Pathological-tests with the numerical simulation in section 7 (see Figure 4.7): (a) cross-sectional area ratio α; (b) total head H; (c) piezometric head h; the colors represent the obstruction internal diameter D_{ob}, as shown in the legend 138

Figure 5.1: prototype of the Innovative Instrumentation 139

Figure 5.2: diagram of the components of the Innovative Instrumentation 140

Figure 5.3: project of the Innovative Instrumentation, all measures in cm 140

Figure 5.4: Innovative Instrumentation hardware: webcam Logitech c270 (a); digital scale Kern 440 (b) 141

Figure 5.5: overall view of the Innovative Instrumentation 142

Figure 5.6: first screen of the Innovative Instrumentation software: check instrumentation (a), data acquisition (b) 143

Figure 5.7: patient data entering window of the Innovative Instrumentation 143

Figure 5.8: interface of the Innovative Instrumentation during micturition data acquisition 144

Figure 5.9: plot example of flow rate Q: the red line is Q, while the thin green line is Q_{raw}. From left to right, vertical dashed black, magenta, blue and black lines represent the time of the beginning of the micturition, the maximum flow Q_{peak}, the maximum detrusorial pressure P_{det} and the ending of the micturition, respectively 145

Figure 5.10: sample digital camera frame 146

Figure 5.11: parabola trajectory of the frame in Figure 5.10: the blue dots are the real jet and the red line represents the estimated parabola; in the red boxes the relative & standard deviation values are reported 146

Figure 5.12: plot example of exit velocity u_e: the red line is u_e, while the thin blue line represents $u_{e,raw}$. From left to right, vertical dashed black, magenta, blue and black lines represent the time of the beginning of the micturition, the maximum flow Q_{peak}, the maximum detrusorial pressure P_{det} and the ending of the micturition, respectively 147

Figure 5.13: plot of intravesical pressure P_{det} (red line) estimated from jet exit velocity u_e values shown in Figure 5.12. From left to right, vertical dashed black, magenta, blue and black lines represent the time of the beginning of the micturition, the maximum flow Q_{peak}, the maximum detrusorial pressure P_{det} and the ending of the micturition, respectively 148

Figure 5.14: evaluation of lag time TL between acquisition of jet velocity and flow rate: the blue line is the flow rate Q, the grey line is the jet exit velocity u_e, and the green line is again u_e shifted by +1.8 s 149

Figure 5.15: clinical report example 150

Figure 5.16: clinical trials on the Innovative Instrumentation; each star represents a different test 159

Figure 5.17: reproducibility test on the Innovative Instrumentation; each color represents a test of the same healthy male 160

Figure 6.1: new version of Schäfer's diagram: lab data (dots) and clinical data (stars); the black and red lines divide the chart in three areas (healthy subjects, uncertain or lightly obstructed, and obstructed) 163

Figure 6.2: Coupled Urodynamic Diagram: above, the new version of Schäfer's diagram; below, "Pathological flow condition" tests (colored dots) with trend dashed lines (blue for healthy, green for lightly obstructed and red for obstructed) 164

Figure 6.3: Coupled Urodynamic Diagram: the cyan star represents one of the healthy clinical trials: the detrusorial pressure (cyan cross) can be estimated following the relation in the second diagram according to the state of the patient (healthy, lightly obstructed or obstructed) 165

Figure 6.4: total head at the Tube entrance H_c (corresponding to detrusorial pressure P_{det}) as a function of kinetic head at the Tube exit K_e: comparison between Lab tests (dots) and numerical model (crosses) 166

List of Tables

Table 1.1: methods to quantify urodynamic functionality 36

Table 2.1: main geometric data of the Model 48

Table 2.2: calibrated values of roughness and concentrated head loss coefficients of the valve and the metal connector of the Model 57

Table 2.3: values of Tube's thickness 73

Table 2.4: values of Tube's external diameter 73

Table 3.1: summary of Pathological-tests; D0L00X0 represents the Physiological-test 89

Table 3.2: clinical measurements compared with the results of the Diagnostic-tests 97

Table 4.1: the average values of ∂H/∂x and the correspondent H_c 114

Table 4.2: parameters and constants used in the numerical model 118

Table 5.1: summary of clinical tests on healthy males (a) 153

List of Acronyms

Acronym	*Meaning*
BPH	benign prostatic hyperplasia
BOO	bladder outlet obstruction
Diagnostic-tests	tests on the Model with a catheter inside the Tube
FV-tests	flow variables measurements tests on the Model
ICS	International Continence Society
LUT	lower urinary tract
Innovative Instrumentation	prototype of our Innovative Instrumentation for non-invasive Urodynamics
MDWC	"modified" double-way catheter
Model	laboratory physical model of the LUT
P/F Study	Pressure/Flow Study
Pathological-tests	tests on the Model with obstructions inside the Tube
PDE system	partial derivative equations system
PURR	passive urethral resistance relation
Physiological-tests	system emptying tests on the Model
TL	Tube Law
Tube	latex elastic collapsible tube used in the Laboratory experiments on the Model
URR	urethral resistance relation

List of Symbols

Symbol	*Meaning*	*Unit*
α	Tube's cross-sectional area ratio	[-]
α_{ob}	obstruction internal area ratio	[-]
β	flat plate angle of the load cells to the horizontal	[°]
β_1, β_2	literature Tube law parameters	[-]
γ	water specific weight	[N/m^3]
ΔH_{cc}	concentrated head loss at the entrance of the Model's metal connector	[m]
ΔH_{cv}	concentrated head loss at the entrance of the Model's valve	[m]
ΔH_{dc}	distributed head loss inside the Model's metal connector	[m]
ΔH_{dv}	distributed head loss inside the Model's valve	[m]
ΔQ^*	percentage of relative flow rate reduction between Q and Q_{cat}	[%]
ε	Tube's roughness	[-]
ε_c	Model's metal connector roughness	[m]
ε_d	relative deformation in Hooke's formula	[m]
ε_{ob}	obstruction roughness	[m]
ε_v	Model's valve roughness	[m]
θ_e	jet exit angle to the horizontal	[rad]
λ	Tube's friction factor	[-]
λ_c	Model's metal connector friction factor	[-]
λ_v	Model's valve friction factor	[-]
μ	water dynamic viscosity	[Pa·s]
ν	water kinematic viscosity	[m^2/s]
ν_P	latex Poisson coefficient	[-]
ρ	water density	[kg/m^3]
ρ_u	average urine density	[kg/m^3]
σ	standard deviation	[m]
σ^*	percentage of standard deviation	[%]
σ_H	tension in Hooke's formula	[Pa]
ω	angular velocity of the optical encoder reel	[rad/s]
Ω	Tube's cross-sectional area	[m^2]
Ω_c	internal area of the Model's metal connector	[m^2]
Ω_{ob}	internal area of the obstruction	[m^2]
Ω_t	internal area of the Model's tank	[m^2]
Ω_u	Tube's "undisturbed" internal cross-sectional area (section 2.3.5.1)	[m^2]

Ω_v	internal area of the Model's valve	[m^2]
a	1st parameter of jet exit parabolic trajectory	[-]
A/G Number	Abrams/Griffiths Number	[-]
b	2nd parameter of jet exit parabolic trajectory	[-]
BOOI	Bladder Outlet Obstruction Index	[-]
BCI	Bladder Contraction Index	[-]
c	3rd parameter of jet exit parabolic trajectory	[-]
c_w	wave speed of small area perturbations inside the Tube	[m/s]
D_c	internal diameter of the Model's metal connector	[m^2]
D_{cat}	catheter external diameter	[m]
D_{ext}	Tube's "undisturbed" external diameter (section 2.3.5.1)	[m]
D_{ob}	obstruction internal diameter	[m]
D_u	Tube's "undisturbed" internal diameter (section 2.3.5.1)	[m]
D_v	internal diameter of the Model's valve	[m^2]
E	Tube's elasticity	[Pa]
g	gravity acceleration	[m/s^2]
h	piezometric head inside the Tube	[m]
h_{lc}	distance of the load cells from the Tube's exit	[m]
H	total head inside the Tube	[m]
H_0	level of the water inside the Model's tank	[m]
$H_{0,max}$	maximum level of the water inside the Model's tank	[m]
$H_{0,min}$	minimum level of the water inside the Model's tank	[m]
H_c	total head at the Tube's entrance	[m]
$H_{c,estimated}$	total head at the Tube's entrance estimated from literature hydraulic formulas	[m]
$H_{c,measured}$	total head at the Tube's entrance measured in experimental tests	[m]
J	Tube's flow resistance per unit length	[-]
K	Tube's effective stiffness	[N/m]
K_c	concentrated head loss coefficient at the entrance of the Model's metal connector	[-]
K_e	kinetic head at the Tube's exit	[m]
$K_{e[Qpeak]}$	kinetic head at the Tube's exit recorded at the same time of the maximum flow rate Q_{peak}	[m]
K_v	concentrated head loss coefficient at the entrance of the Model's valve	[-]
L	Tube's length	[m]
L_c	Model's metal connector length	[m]
L_{ob}	obstruction length	[m]
L_v	Model's valve length	[m]

M	momentum recorded by the load cells	[N]
M_e	jet exit momentum	[N]
m_1, m_2	Tube law parameters	[-]
OCO	Obstruction Coefficient	[-]
p_{cat}	catheter perimeter	[m]
p_u	Tube's "undisturbed" perimeter (section 2.3.5.1)	[m]
P	pressure inside the Tube	[Pa]
P_{abd}	abdominal pressure	[cm H_2O]
P_{det}	detrusorial pressure	[cm H_2O]
$P_{det[Qpeak]}$	detrusorial pressure recorded at the same time of maximum flow rate Q_{peak}	[cm H_2O]
P_{ext}	external pressure on the Tube	[Pa]
P_{muo}	minimal urethral opening pressure	[cm H_2O]
P_{tm}	transmural pressure inside the Tube (i.e. P-P_{ext})	[Pa]
P_{ves}	intravesical pressure	[cm H_2O]
Q	flow rate	[m^3/s]
Q_{cat}	flow rate in Tube with catheter	[m^3/s]
$Q_{cat,peak}$	maximum flow rate in Tube with catheter	[m^3/s]
Q_{mean}	average flow rate	[ml/s]
Q_{peak}	maximum flow rate	[ml/s]
$Q_{peak,mod}$	maximum flow rate reduced by ΔQ*	[ml/s]
Q_{raw}	flow rate elaborated from W data	[ml/s]
R	radius of the optical encoder reel	[m]
Re	Reynolds number inside theTube	[-]
Re_c	Reynolds number inside the Model's metal connector	[-]
R_h	hydraulic radius	[m]
Re_v	Reynolds number inside the Model's valve	[-]
R_u	Tube's "undisturbed" radius (section 2.3.5.1)	[m]
S	speed index	[-]
s_u	Tube's "undisturbed" thickness (section 2.3.5.1)	[m]
T_{tot}	total voiding time	[s]
u	average velocity inside the Tube	[m/s]
u_c	average velocity inside the Model's metal connector	[m/s]
u_e	jet exit average velocity	[m/s]
$u_{e,estimated}$	jet exit average velocity estimated with image acquisition and processing system	[m/s]
$u_{e,measured}$	jet exit average velocity measured in "simplified" Model	[m/s]
$u_{e[Qpeak]}$	average velocity of the urine stream recorded at the same time of the maximum flow rate Q_{peak}	[m/s]

$u_{e,raw}$	jet exit average velocity of the urine stream recorded on the Innovative Instrumentation	[m/s]
u_{ob}	average velocity inside the obstruction	[m/s]
u_p	peripheral velocity of the optical encoder reel	[m/s]
u_v	average velocity inside the Model's valve	[m/s]
URA	Urethral Resistance Factor	[-]
V_{tot}	total volume voided	[ml]
W	moving average of W_{raw} data	[kg]
W_{raw}	weight recorded by digital scale on the Innovative Instrumentation	[kg]
X_{ob}	obstruction position	[-]

CONTENTS

Acknowledgements 3
Abstract 5
List of Figures 7
List of Tables 13
List of Acronyms 15
List of Symbols 17
Contents 21
1 State of the art 25
1.1 Lower urinary tract anatomy 25
1.1.1 Vessel 26
1.1.2 Urethra 27
1.2 Urethral obstructions 29
1.2.1 Urethral strictures 30
1.3 Urodynamics today: main clinical investigations 31
1.3.1 Uroflowmetry 31
1.3.2 Pressure/Flow Study 32
1.4 Quantification of urodynamic functionality 35
1.4.1 Abrams-Griffiths nomogram & A/G Number 36
1.4.2 Urethral Resistance Factor (URA) 37
1.4.3 Schäfer's diagram 38
1.4.4 ICS previsional method 40
1.5 Urodynamic functionality parameters 41
1.6 Current non-invasive techniques in Urodynamics 41
2 The development of an innovative methodology in Urodynamics 43
2.1 Formulation of the hypothesis 43
2.2 The Laboratory physical model 46
2.2.1 Experimental setup and procedures 49
2.2.2 Water level inside the tank H_0 51
2.2.3 Flow rate Q 52
2.2.4 Total head at the Tube entrance H_c 53
2.3 Preliminary Laboratory tests 59
2.3.1 Measure of jet exit velocity u_e 59
2.3.2 Dynamic impact of the exit jet on load cells 59
2.3.2.1 Numerical scheme & instrumentation 59
2.3.2.2 Orthogonal surface 60
2.3.2.1 Results 64
2.3.3 Exit velocity estimation with an optical encoder 66

2.3.4 Exit velocity through image analysis 68
2.3.4.1 Numerical scheme 68
2.3.4.2 Image acquisition and processing system 70
2.3.4.3 Analysis of the results 71
2.3.5 Physical properties of the Tube 72
2.3.5.1 Evaluation of "undisturbed" Tube thickness s_u and internal diameter D_u 72
2.3.5.2 Evaluation of Tube's elasticity E 73
2.3.5.3 Comparison with urethra's physical properties 76
2.3.6 External pressure on the Tube 77
2.4 The Innovative Instrumentation 79
3 Extensive Laboratory tests 81
3.1 "Physiological flow condition" tests 81
3.1.1 Results 82
3.1.2 Correlation between u_e and P_{det} 84
3.2 "Pathological flow condition" tests 86
3.2.1 Types of obstructions 87
3.2.2 Results 90
3.3 Tests with catheter 93
3.4 "Diagnostic flow condition" tests 93
3.4.1 The catheter 94
3.4.2 Results 95
3.5 Flow variables measurements inside the Tube 99
3.5.1 The "modified" double-way catheters MDWC type 1 & type 2 99
3.5.2 Results 101
4 Numerical model and simulation 107
4.1 One-dimensional governing equations 107
4.1.1 Mass and momentum conservation 107
4.1.2 Tube Law equation 108
4.2 Model implementation 111
4.2.1 Quasi-steady flow hypothesis 112
4.2.2 The simulated physical system 115
4.3 Results 118
4.3.1 "Diagnostic flow condition" simulations 119
4.3.2 "Physiological flow condition" simulations 124
4.3.3 "Pathological flow condition" simulations 129
5 Innovative Instrumentation for non-invasive Urodynamics 139
5.1 Design and construction 139
5.2 Hardware & Software 141
5.3 Mathematical schemes 144

5.3.1 Flow rate Q 144
5.3.2 Jet exit velocity u_e 145
5.3.3 Detrusorial pressure P_{det} 147
5.3.4 “Lag time” evaluation 148
5.4 Clinical report 149
5.5 Clinical trials: preliminary results 151
6 Results and Discussion 161
Conclusions 167
Bibliography 171

1 State of the art

1.1 Lower urinary tract anatomy

The urinary system handles the production and elimination of urine; it is composed of two kidneys, two ureters, a bladder and a urethra (Figure 1.1). Urine is an amber-colored solution produced by the filtering activity of the kidneys, organs dedicated to maintaining constant volume, osmotic concentration and pH of the blood, and to balancing the concentrations of the solutes that circulate within the blood.

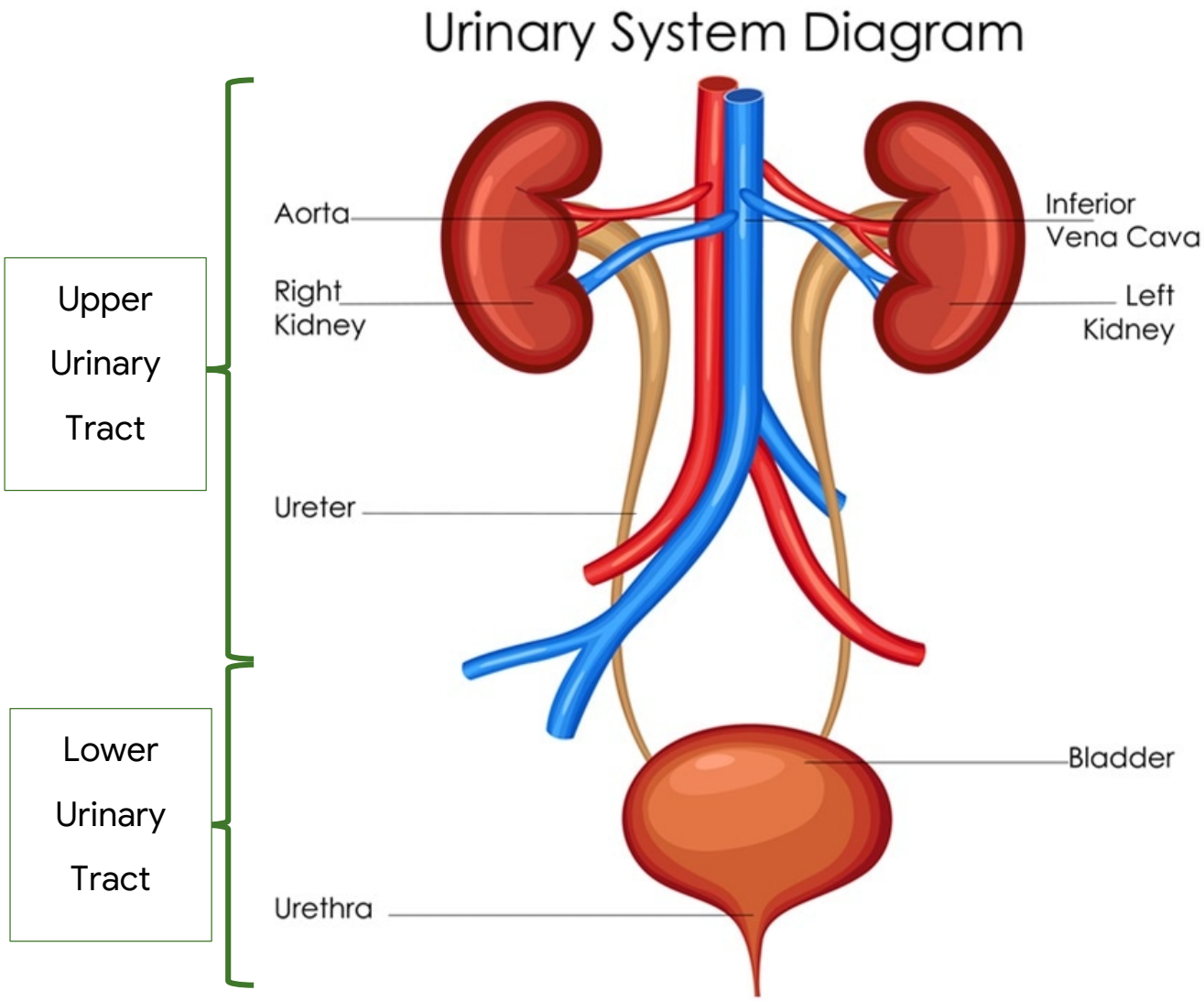

Figure 1.1: urinary system

The ureters are symmetrical conduits that connect the kidneys with the urinary bladder; through them the urine produced by the kidneys is conveyed with an almost continuous flow into the bladder, where it is deposited as a tank.

The ***lower urinary tract (LUT)*** is made up of bladder and urethra: in Figure 1.2 the female (a) and the male (b) LUT are represented.

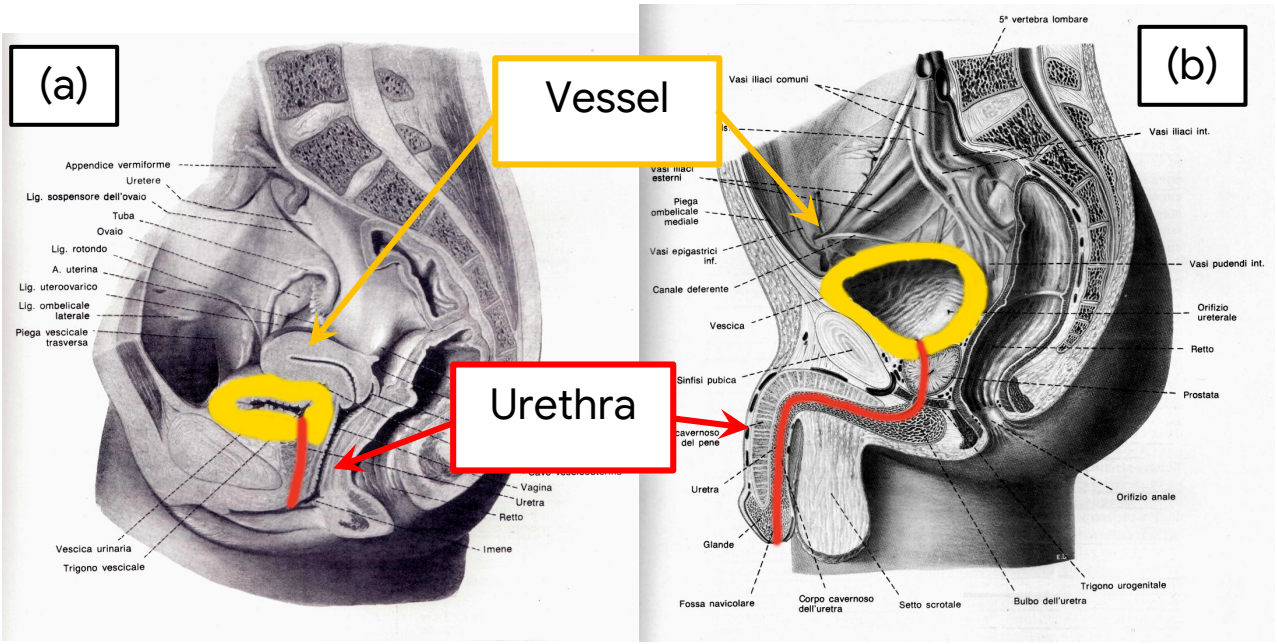

Figure 1.2: female (a) and male (b) LUT

1.1.1 VESSEL

The urinary bladder represents the tank of the urine that comes from the ureters. Once a certain amount is reached (the average physiological capacity is 250-350 cm^3), the urine is expelled from the body through the urethra with the act of micturition. The bladder has very extendable walls, so much that under certain pathological conditions it can contain over 2000 cm^3.

Its shape and dimensions vary greatly according to its filling level: if empty it is flattened and the cavity is a crack; if full, it has an ovoid shape with an average major axis of 10-12 cm. At the base of the bladder there are three orifices that delimit a triangle with the two ureteral meatus at the ends of the base and the internal urethral meatus at the vertex facing downwards.

The wall thickness of the bladder can vary from 1.5 cm to 0.4 cm, depending on how much it is filled. This wall mainly consists of a muscle layer; this muscle is particularly developed, it forms the *detrusor muscle of the bladder*, whose contraction determines micturition. Around the internal urethral meatus, this muscle layer has a spiral arrangement: it thickens and becomes involved in the formation of the sphincter muscle of the bladder.

The urine collected in the bladder is expelled at more or less long intervals through the urethra; the intravesical pressure during the filling and at the time of the expulsion of the urine is linked both to the amount of urine inside the bladder and to the degree of contraction of the detrusor muscle.

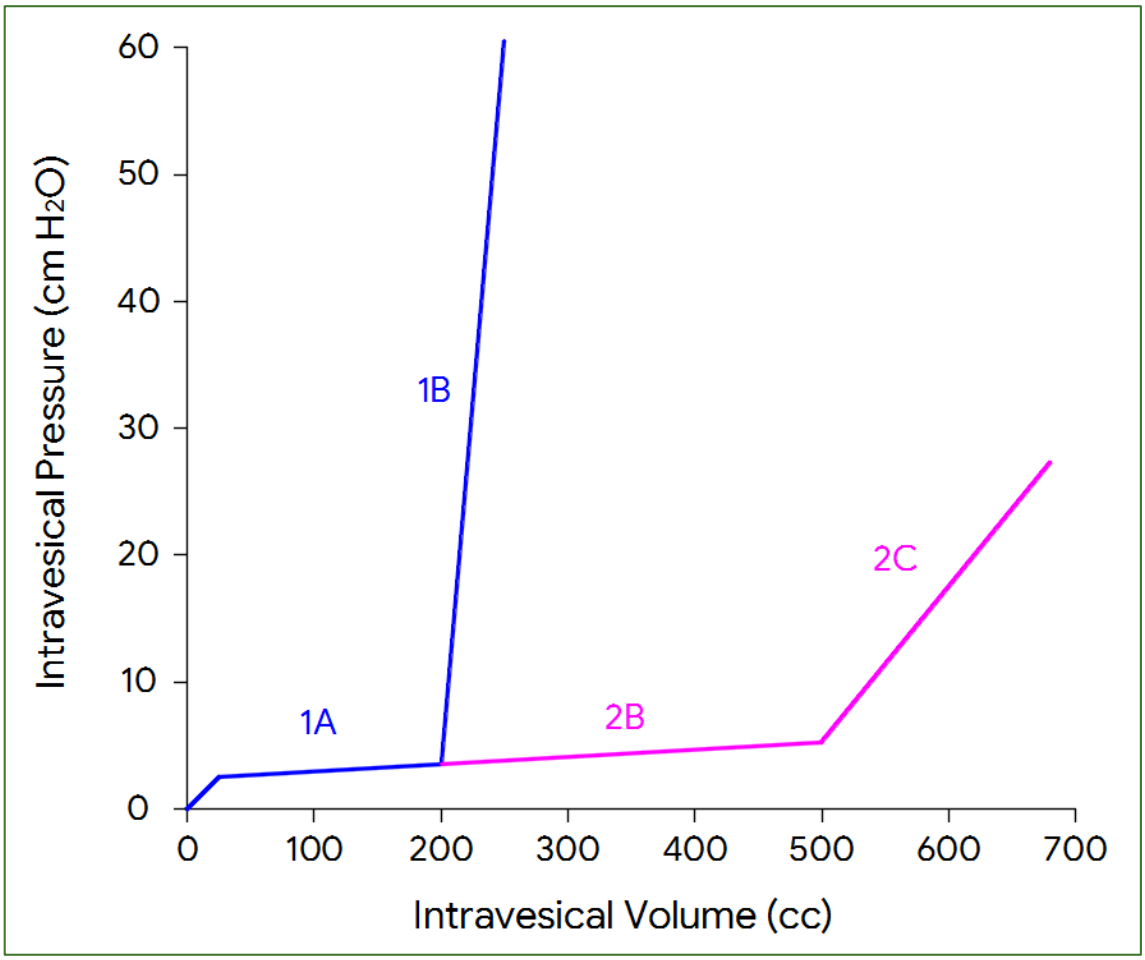

Figure 1.3: intravesical pressure as a function of the urine volume inside the bladder

Figure 1.3 shows the intravesical pressure, expressed in cm H_2O, as a function of the urine volume inside the bladder, expressed in cc. During the filling of the bladder, the tone of the detrusor muscle adapts to the volume increase (1A), keeping the pressure at very low levels, usually below 10 cm H_2O. In a normally innervated bladder, segment 1A is interrupted by the activation of the urination reflex, characterized by a sharp increase in intravesical pressure (1B).

If the reflex is absent, segment 1A continues to rise slowly: the bladder collects a lot of liquid with only a small rise of the pressure (2B); this slow increase in pressure has a rapid surge when the bladder volume reaches a significant size (2C).

1.1.2 URETHRA

The male urethra (Figure 1.4) is a duct on average 20 cm long in adults; it originates in the bladder and ends at the far end of the penis (*external urethral meatus*).

According to a systematic criterion which takes into consideration the relationships with the other organs, the male urethra can be divided into a prostatic urethra, about 4 cm long, corresponding to the initial tract through the prostate followed by the membranous urethra, about 2 cm long, when the duct crosses urogenital diaphragm surrounded by the distal urethral sphincter.

The anterior urethral tract, 14 cm long, is wrapped by the spongious body of penis and it is called penile urethra.

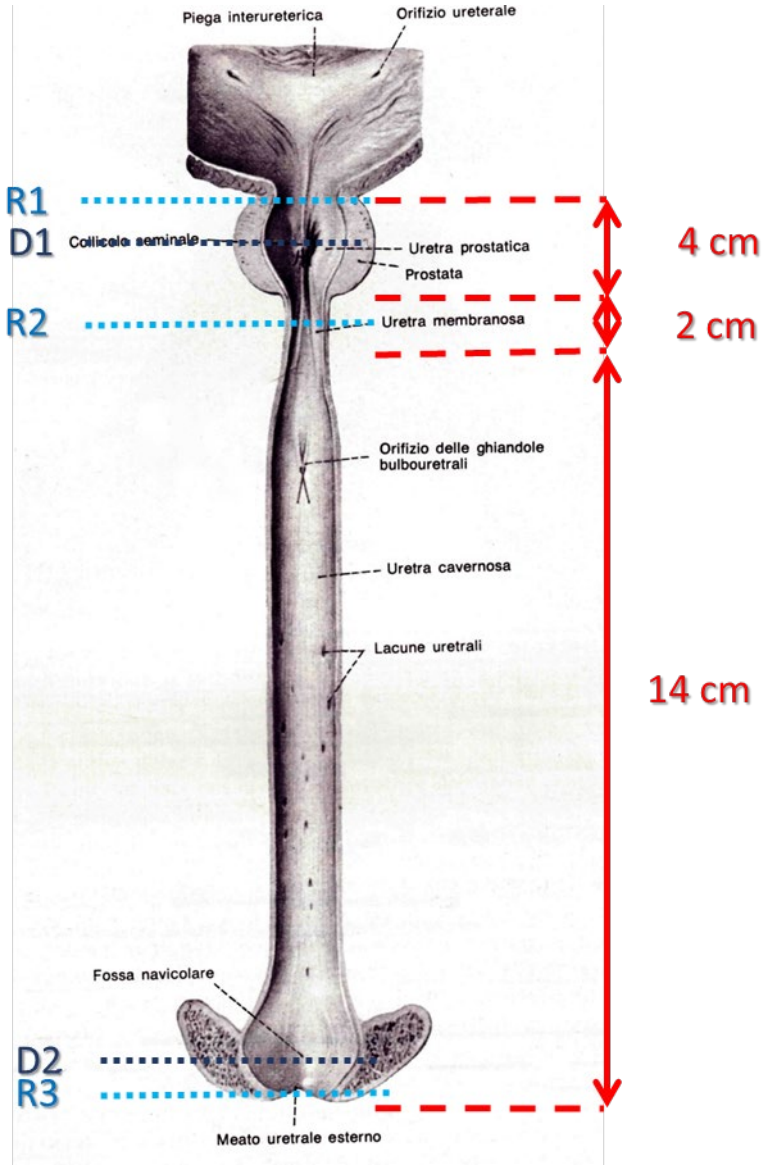

Figure 1.4: male urethra

The urethra is a collapsible elastic tube: elastic because its area adapts to the changes in internal pressure; collapsible because its lumen at rest is virtual and appears as a crack while it becomes cylindrical during micturition. It has three narrowings: at the internal urethral meatus (R1), at the exit of the prostatic urethra (R2) and at the external urethral meatus (R3); and two enlargements: at the prostate (D1) and at the navicular fossa, that's immediately proximal to the external urethral meatus (D2). The smallest diameter is at the external urethral meatus.

The female urethra (Figure 1.5) is about 5 cm long, it begins in the urinary bladder and opens into the vestibule of the vagina. It has a variable size, being wider in the intermediate section where it reaches a diameter of about 8 mm; however, it is easily expandable. While the internal urethral meatus is constantly circular, the external meatus has a very varied conformation, but usually it

appears as a longitudinal crack; it represents the narrowest and least dilatable portion of the urethra.

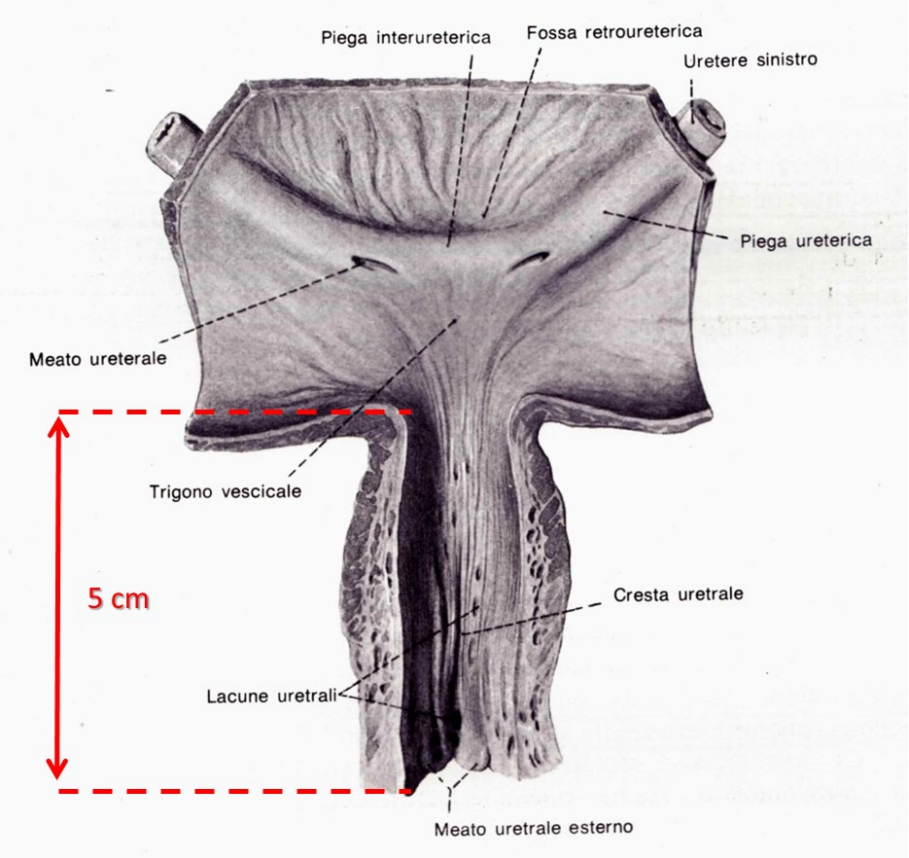

Figure 1.5: female urethra

1.2 URETHRAL OBSTRUCTIONS

Urethral obstructions can be divided in two types: compressive obstructions and constrictive obstructions.

Compressive obstructions are due to an external compression on the urethra. An example is the compression of prostate. The gland, following a biological overdevelopment (benign prostatic hyperplasia BPH, Figure 1.6), compress the urethra causing urinary dysfunction.

The main effects are:

- very low flow;
- very prolonged voiding times (beyond one minute);
- presence of a significant post voiding residual.

Constrictive obstructions are due to a stiffening and a narrowing of the urethral wall which therefore acts as an obstacle to the free flow of urine. The loss of elasticity of the urethra and the stiffening of the internal surface are commonly associated with urethral strictures.

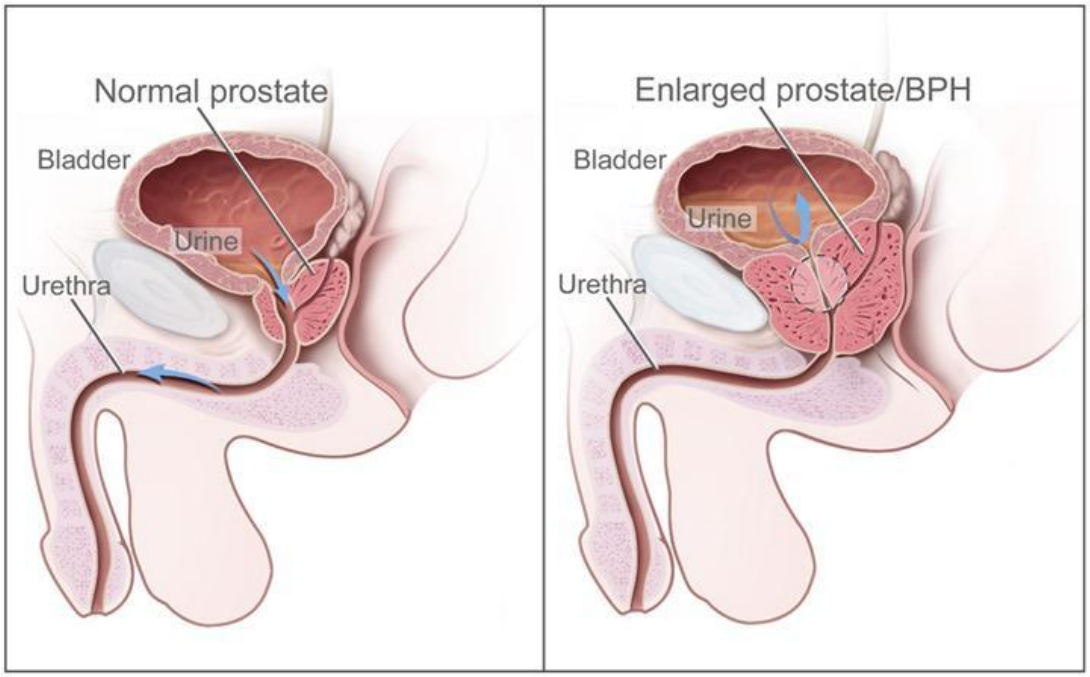

Figure 1.6: urine flow in a normal (left) and enlarged (right) prostate (https://www.cancer.gov/types/prostate/understanding-prostate-changes)

1.2.1 URETHRAL STRICTURES

A urethral stricture (hereafter, stricture) is a narrowing of the lumen of the urethra caused by a scar that develops in the urethral wall from a lesion. Strictures can be classified (Palminteri et al, 2013) by their:

- site: penile, bulbar, panurethral, penile plus and posterior, from the outlet to the bladder;
- etiology: there are several causes of strictures, possible causes include infections of the LUT (e.g., urethritis), but also catheterization or non-inflammatory tissue alterations, such as spongiofibrosis;
- length: strictures can be divided in short strictures or long strictures (Figure 1.7), the length is very related to the cause;
- patient age: stricture is an age-related disease, in fact, it is definitely rare in children and increases linearly up to 55 years; after this age the incidence increases significantly (Santucci et al, 2007).

During the early stages of urethral stricture, the subject may experience pain when urinating and an inability to completely empty the bladder. It is not uncommon for the bladder to tend to relax significantly due to this inability to complete urination. Urethral stricture can cause urination problems and sometimes even the complete inability to urinate; the latter occurrence is called acute urine retention and is a medical emergency. Obstructive emptying symptoms are the most common.

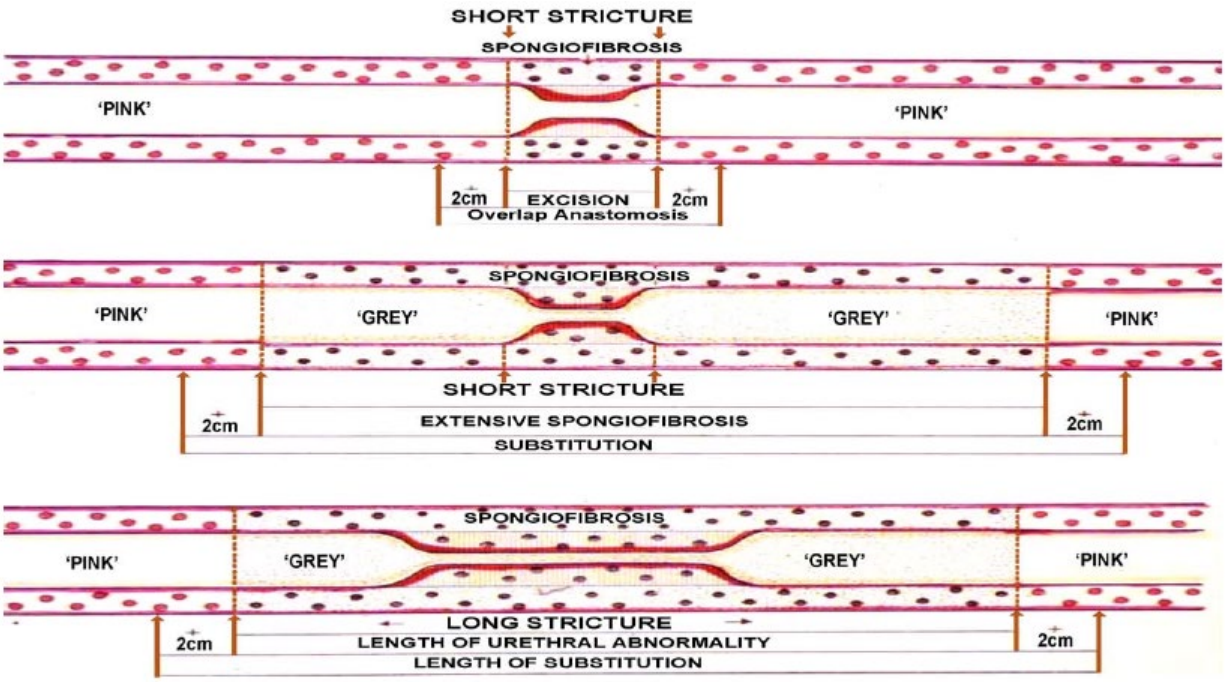

Figure 1.7: diagramatic representation of urethral stricture (Chapple et al, 2020)

1.3 URODYNAMICS TODAY: MAIN CLINICAL INVESTIGATIONS

Functional study of the LUT is carried out by analyzing primarily the activity of the detrusor muscle to evaluate the filling and the emptying of the bladder, to monitor vesicourethral dysfunction or to verify the effectiveness of a therapeutic treatment. The urodynamic evaluation includes general and specific anamnesis, physical examination and standard urological examination.

The preliminary investigation currently used is the Uroflowmetry, eventually with ultrasound evaluation of postvoid residual. In case of Uroflowmetry abnormalities, a urodynamic examination can be suggested to detect the physiopathology of voiding disorder. When there is the suspect of obstructed void the Pressure/Flow Study is the indicated urodynamic examination (Schäfer, 1990, Abrams, 2006).

1.3.1 UROFLOWMETRY

Uroflowmetry is not invasive, it is cheap and does not require special preparations: it simply measures urine flow over time [ml/s] and the total volume voided [ml].

Micturition should occur when the patient feels the physiological urination stimulus. The recommended total volume voided to obtain reliable data is between 200 and 400 ml. A normal flow has a harmonic curve, without sudden changes in amplitude.

An example of instrumentation used in Uroflowmetry is the UROBENCHMARK 2000-3 Uroflowmeter (Figure 1.8).

Figure 1.8: UROBENCHMARK 2000-3 uroflowmeter

1.3.2 Pressure/Flow Study

The main tool to evaluate the urodynamic function is the Pressure/Flow Study (P/F Study). This exam is highly invasive. During the cystometry a bladder double-way catheter is used to gradually fill the bladder recording simultaneously the endoluminal pressure through a pressure transducer connected to one of the two channels. To record endoabdominal pressure an endorectal sensor is used. The detrusor emptying pressure during the micturition is calculated subtracting the abdominal pressure to the vesical pressure. Usually the P/F Study is performed after having filled the bladder with a saline solution. The P/F study analyzes the bladder emptying phase recording at the same time urinary flow, vesical and abdominal pressures. (Schäfer et al, 2002, Di Benedetto et al, 2005, Sekido, 2012).

The urethral catheter used in the P/F Study usually has a diameter of 6 Ch, that is 2 mm.

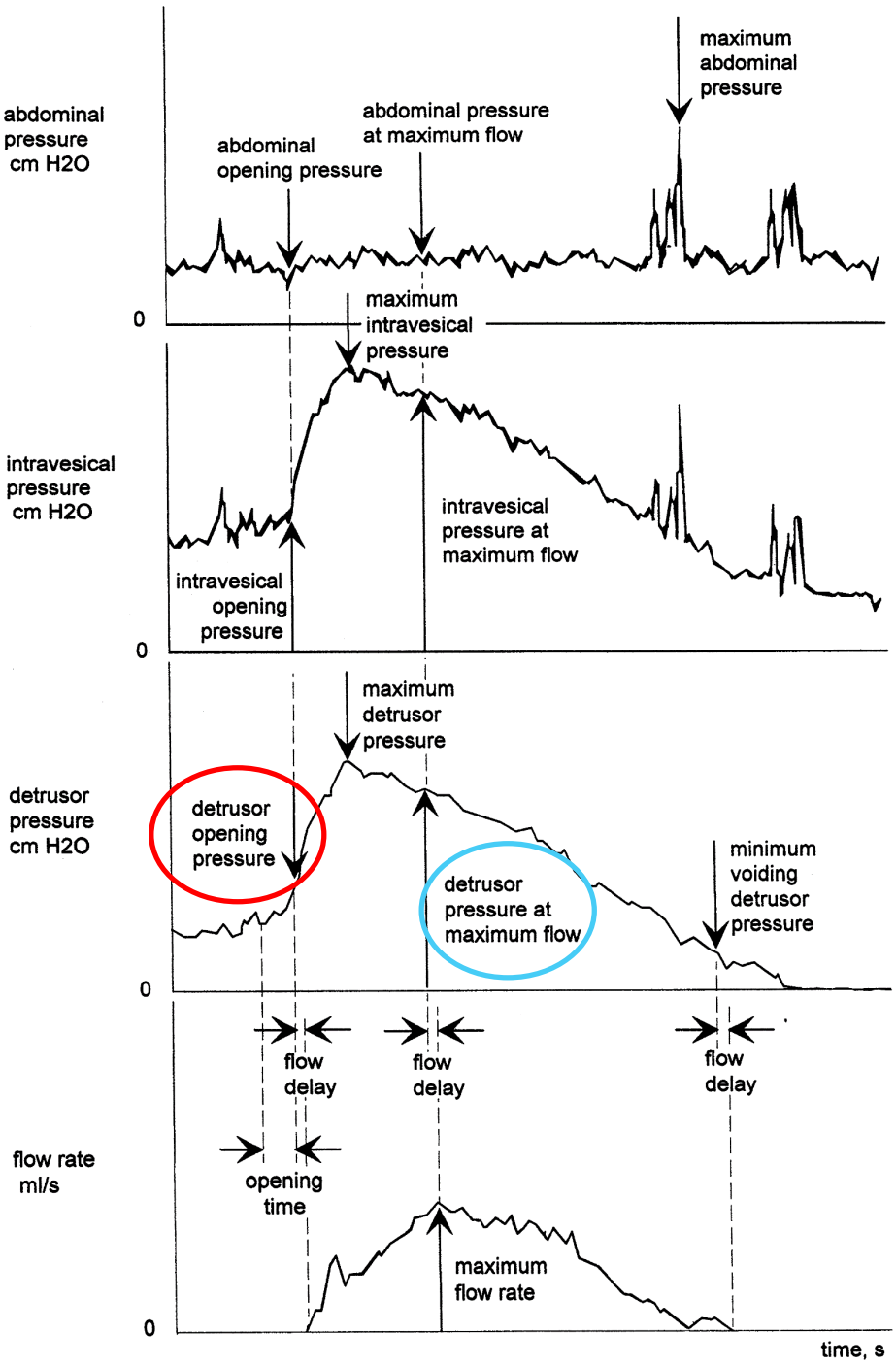

Figure 1.9: example of a P/F Study recording

Figure 1.9 shows an example of the recording of a P/F Study; from top to bottom, as a function of time, we have:

- abdominal pressure P_{abd} [cm H_2O], recorded through the rectal probe;
- intravesical pressure P_{ves} [cm H_2O], recorded through the pressure transducer on the tip of the catheter;
- detrusor pressure P_{det} [cm H_2O], given by the difference between intravesical and abdominal pressure;
- the flow Q [ml/s].

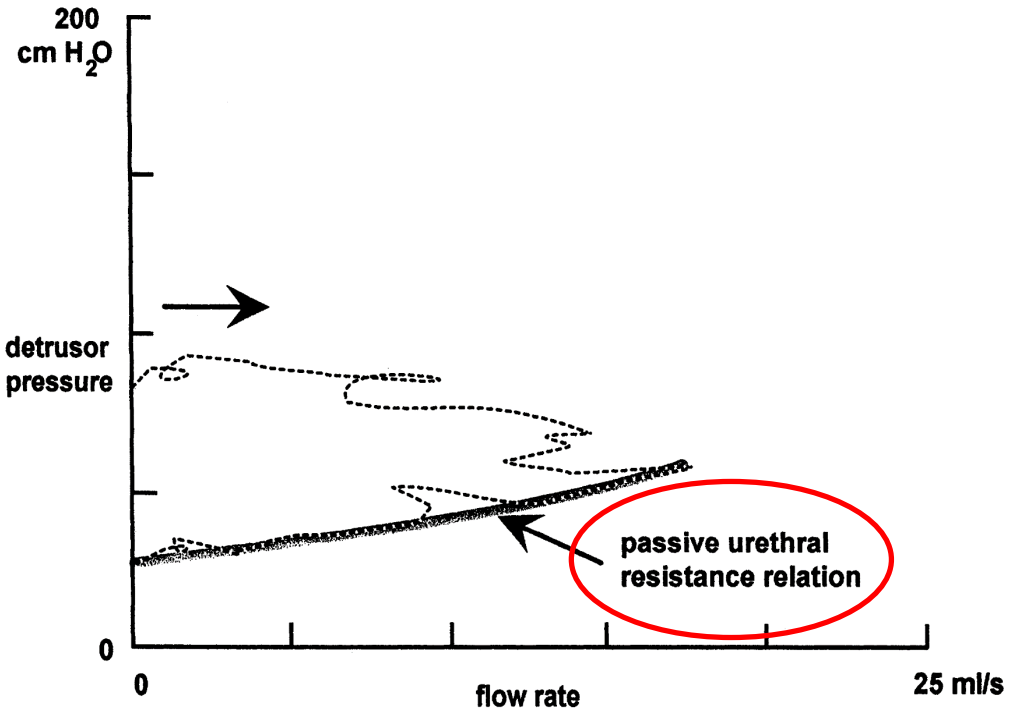

Figure 1.10: urethral Resistance Relation (URR)

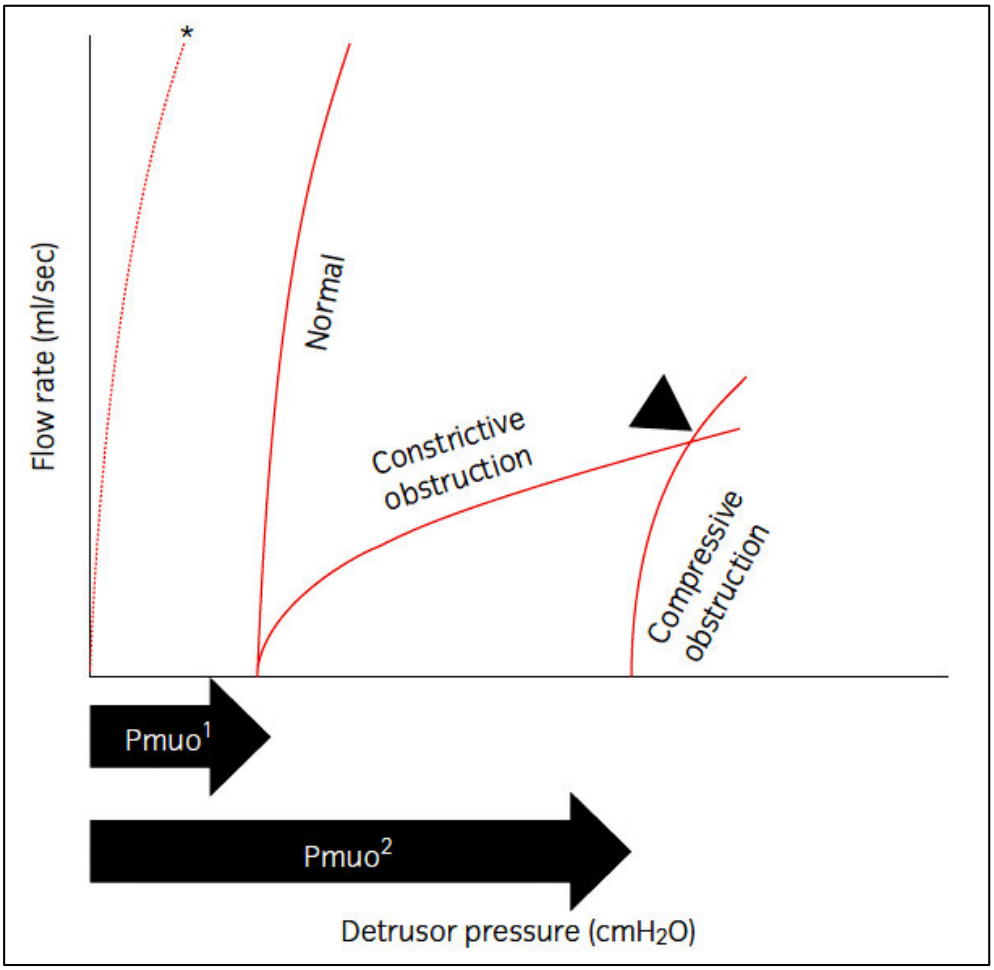

Figure 1.11: PURR examples

In addition, two important parameters for the definition of urinary function are:

- the minimum detrusor opening pressure (P_{muo} [cm H_2O], red circled in Figure 1.9), which represents the minimum detrusor pressure that must be established inside the bladder, so that the urethra "opens" and micturition begins;
- the detrusor pressure at the maximum flow ($P_{det[Qpeak]}$ [cm H_2O], blue circled in Figure 1.9), which represents the detrusor pressure recorded at the same time of the maximum flow.

The *Urethral Resistance Relation* (URR, Figure 1.10) is the relationship between pressure and flow during micturition, thus associating the pressure required to provide a certain flow through the urethra.

Ideally, the urethra is completely relaxed during bladder emptying; therefore, the urethral resistance is at its minimum and the detrusor pressure has its minimum values for each flow value. However, this circumstance happens only in the final part of the flow, usually after the maximum flow. During this phase, the URR is characterized only by the intrinsic mechanics and morphological properties of the urethra and is called *Passive Urethral Resistance Relation* (PURR) (Figure 1.10, red circled).

The shape of the PURR curve gives indications on the functionality of the LUT: in Figure 1.11, the curve "*" represents the PURR in a rigid tube while the "Normal" curve represents the PURR of a healthy person, in which P_{muo} is also crucial.

If we have a bladder obstruction, whatever the cause (urethral hyperactivity or abnormal structure), this implies that the urethral resistance to flow is abnormally high:

- if the section of the urethra is reduced (e.g. urethral stricture), the curve flattens on the abscissas ("Constrictive obstruction");
- if P_{muo} increases from P_{muo}^1 to P_{muo}^2 (e.g. in patients with BPH), the curve shifts to the right on higher pressures ("compressive obstruction").

1.4 Quantification of urodynamic functionality

Several methods have been developed to quantify P/F diagrams using one or more numerical parameters (Table 1.1). These parameters are based on various aspects such as the position, the slope or the curvature of the URR; most of them were developed primarily to diagnose the possibility of urinary obstruction in adult males.

The properties of the flow of urine in the urethra have also been quantified in various ways. Gleason & Lattimer, 1962, and Arbuckle & Paquin, 1963, determined the urethral resistance by assuming laminar flow and calculating its losses. Since fully developed urinary flow was considered turbulent, other researchers have suggested a formula where resistance is equal to the ratio of intravesical pressure to square of urinary flow (Bryndorf & Sandøe, 1960, Smith, 1968, Claridge & Shuttleworth, 1964) or 7/4 of the flow (Holm, 1964).

Method	Target	Number of P/Q points	Supposed PURR shape	Parameters number
Abrams-Griffiths Nomogram	Diagnosis	1	n/a	n/a
URA	Resistance	1	Curve	1
Schäfer LPURR	Resistance	1*	Linear	1
A/G Number	Resistance	1	Linear	1
Spångberg Nomogram	Diagnosis	1	n/a	n/a
CHESS	Resistance	Many	Curve	2
OBI	Resistance	Many	Linear	1
Spångberg et al.	Resistance	Many	Linear or curve	3
DAMPF	Resistance	2	Linear	1

Table 1.1: methods to quantify urodynamic functionality

1.4.1 Abrams-Griffiths nomogram & A/G Number

The first research in which the urethra was considered as an elastic tube was that of Scott et al, 1966, but it's the model presented by Griffiths, 1969, 1971, that changes the scientific approach to the LUT, also because the introduction of the idea of urethral opening pressure. Griffiths developed the URR concept, popularizing the method of plotting pressure and flow rate parameters point by point in a Cartesian axis system (Figure 1.10). An important consequence of this model is that the elastic properties of the urethra can be obtained from the P/F graph.

Abrams & Griffiths, 1979, developed the nomogram represented in Figure 1.12: there is the flow rate (ml/s) on the x-axis, the detrusor pressure (cm H_2O) on the y-axis, and it is divided into three zones (obstructed, equivocal, and unobstructed). Only one point of the URR is shown on this graph, the maximum flow Q_{peak} and the corresponding detrusor pressure $P_{det[Qpeak]}$: in this way, the patient is classified according to the area of the graph where the point is located.

Based on the Abrams-Griffiths Nomogram, Abrams & Lim, 1995, introduced the Abrams/Griffiths Number (A/G Number) to quantify urethral resistance. The A/G Number [-] is expressed by the following relationship:

$$A/\ \ \text{Number} = P_{det[Qpeak]} - 2 \cdot Q_{max} \qquad 1.1$$

where Q_{peak} is the maximum flow and $P_{det[Qpeak]}$ is the detrusor pressure recorder at the same time.

The patients are classified as follows:

- if A/G Number>40, the patient is obstructed;
- if A/G Number<15, the patient is not obstructed;

otherwise, the study is uncertain.

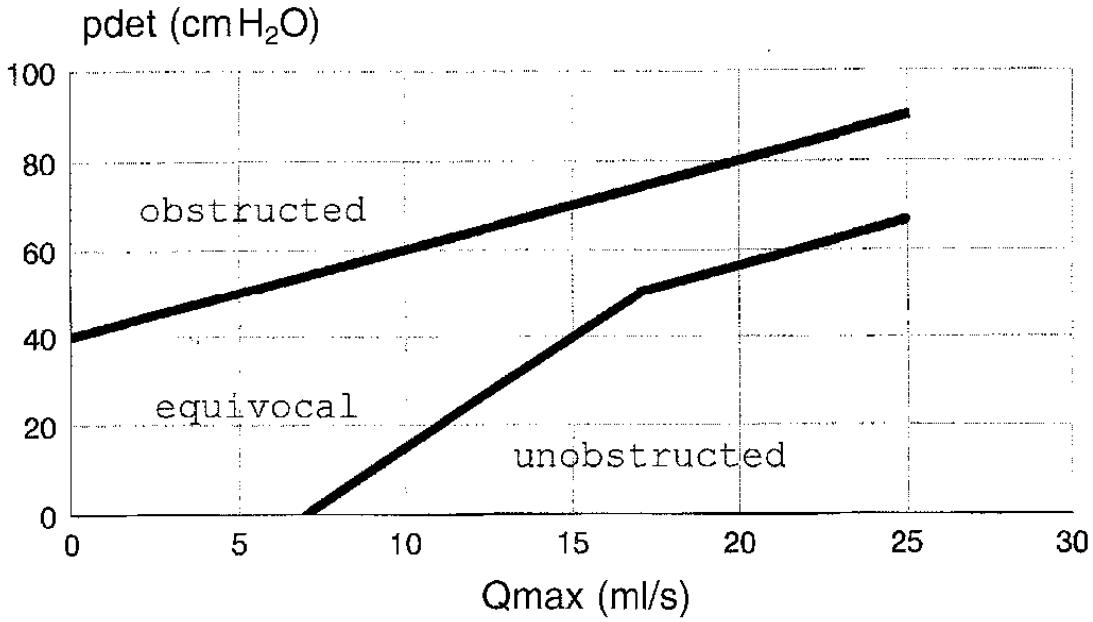

Figure 1.12: Abrams-Griffiths nomogramm

1.4.2 URETHRAL RESISTANCE FACTOR (URA)

Urethral resistance is usually quantified using the Urethral Resistance Factor (URA) which is empirically based on the P/F diagrams obtained from a large amount of micturitions from adult patients. The value of the P/F curve that intercepts the axis of the P (therefore at zero F) defines the URA value, which therefore represents the minimum opening pressure P_{muo}; the unit of measurement is the same as the pressure, cm H_2O. The URA [-] is defined by the following relationship:

$$\mathrm{URA} = \left[(1 + 4 \cdot d \cdot Q^2 \cdot P_{det})^{1/2} - 1\right] / (2 \cdot d \cdot Q^2) \qquad 1.2$$

where $d=3.8 \cdot 10^{-4}$ m and, usually, $P_{det}=P_{det[Qpeak]}$ and $Q=Q_{peak}$. In Figure 1.13, we can see an example of URA determination: the star, that has $P_{det[Qpeak]}=100$ cm H_2O and $Q_{peak}=5$ ml/s, is located on the curve of URA=60 cm H_2O, which is therefore the urethral resistance value of the patient at the moment.

Patients with URA>29 are classified as obstructed and those with URA<21 as unobstructed; others as uncertain.

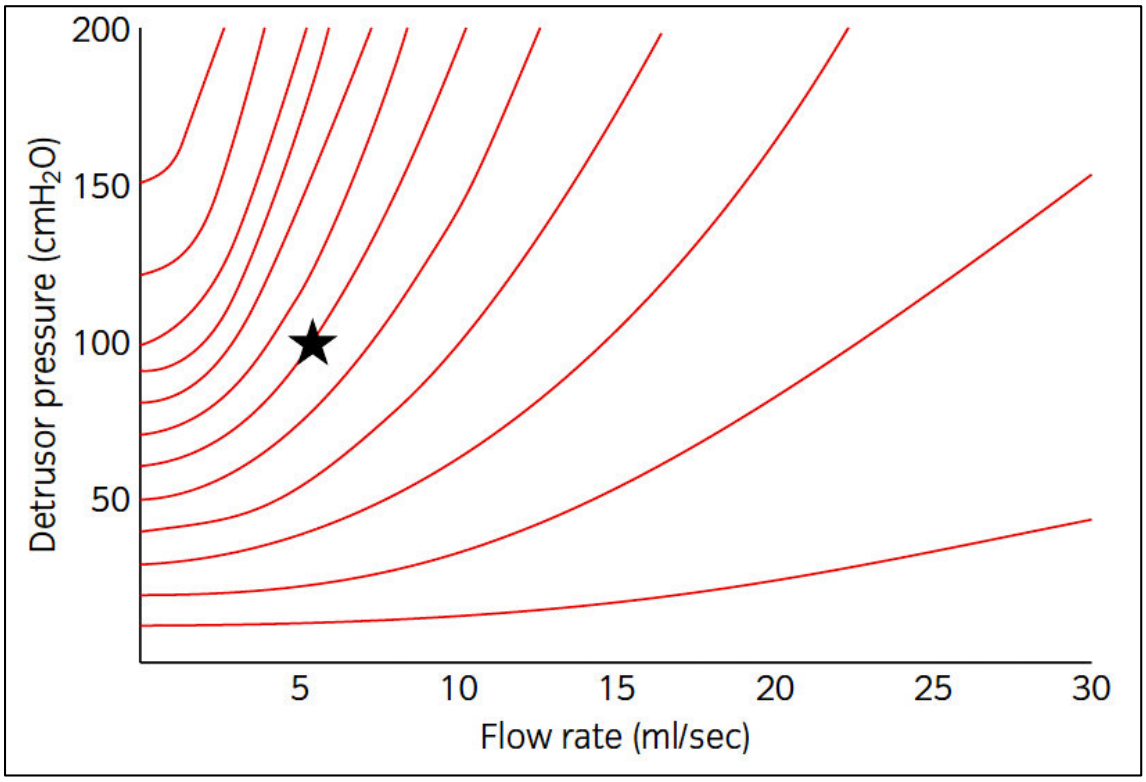

Figure 1.13: determination example of URA factor

1.4.3 SCHÄFER'S DIAGRAM

Subsequently Schäfer, 1983, using the urethral opening pressure described in the Griffiths model, simplified it by assuming the dilation of the urethra equal to a fixed area by obtaining it directly from the P/F graph. In addition, he only considered the part of the plot where the urethra is most released and therefore most open, i.e. the portion of low detrusor pressure, starting at the value (Q_{peak},$P_{det[Qpeak]}$): the PURR (Figure 1.10).

Schäfer then proposed a further evolution of the PURR, the PURR Line (LPURR), in which the P/F ratio is assumed to be constant: LPURR is obtained by joining (Q_{peak},$P_{det[Qpeak]}$) and (0,P_{muo}). This simplification has been very successful, and the diagram (Figure 1.14) derived from the LPURR for diagnosis and classification in areas of different levels of the obstruction has had great diffusion. It is divided into 7 areas (black lines), characterized by roman numbers from 0 to IV, corresponding to different outflow conditions, called Schäfer obstruction grade. Patients with obstruction grade 0 or I are defined as unobstructed, those with grade III or greater as obstructed, and those with grade II as uncertain. The diagram also highlights the detrusor contractile force, divided into 6 zones (blue lines): VW (very weak), W- and W+(weak), N- and N+ (normal), ST (strong).

In this diagram, it is plotted only the point (Q_{peak},$P_{det[Qpeak]}$): if this point is inside the green highlighted zone, the patient is considered not obstructed, while if the point is inside the yellow zone, the patient is considered uncertain.

Furthermore, by drawing the LPURR, it is possible to discriminate the type of obstruction: compressive (red line A) or constrictive (red line B).

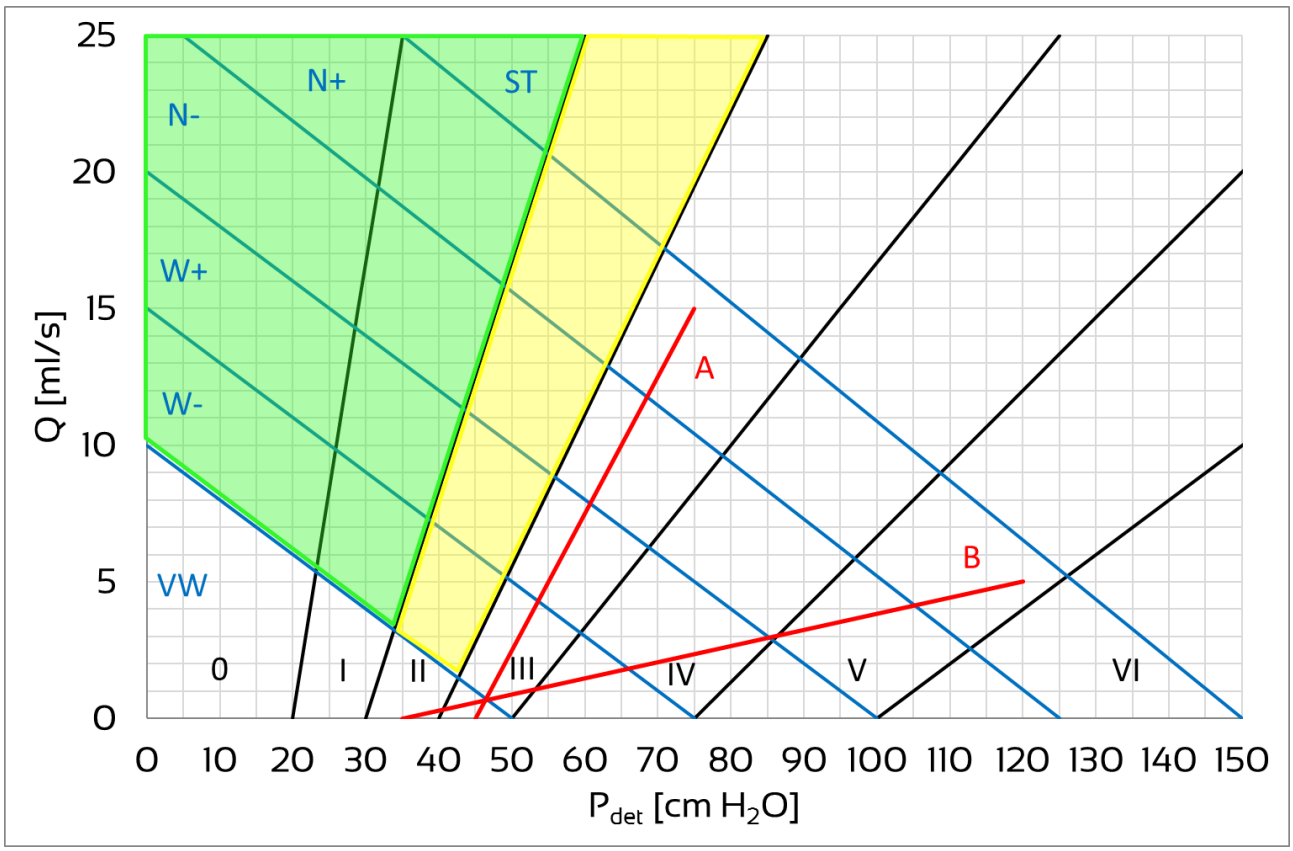

Figure 1.14: Schäfer's diagram: example of compressive obstruction (red line A) or constrictive obstruction (red line B)

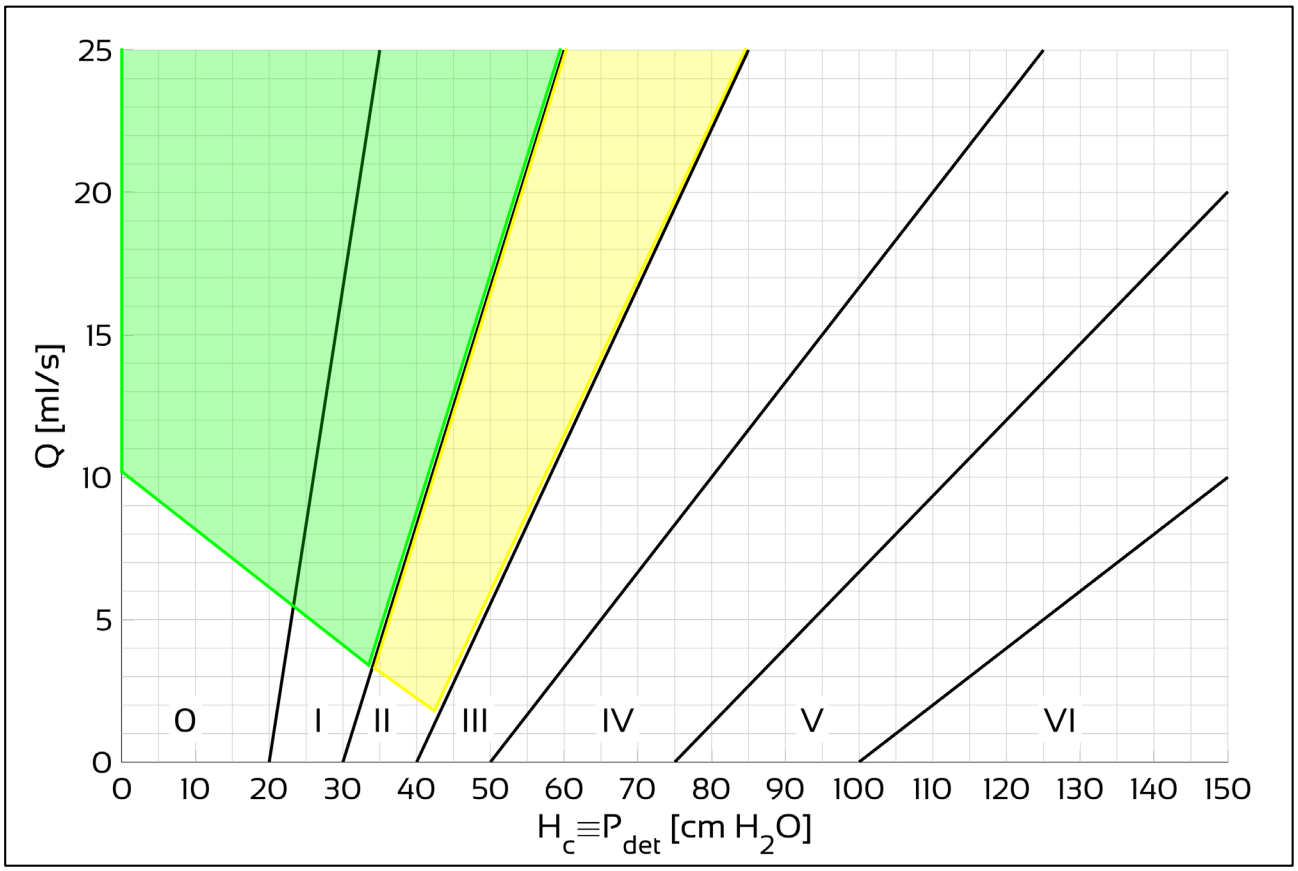

Figure 1.15: Schäfer's diagram "simplified": patients are considered not obstructed in the green zone and uncertain in the yellow zone

In the following sections, when possible it will be used a "simplified" version of the Schäfer's diagram (Figure 1.15): it shows only the obstruction grade (from 0 to VI in roman numbers) and the highlighted green and yellow zones, corresponding to patient not obstructed and uncertain, respectively.

1.4.4 ICS PREVISIONAL METHOD

In 1997 the International Continence Society (ICS) introduced the Previsional Method of Analysis (Griffiths et al, 1997, Abrams et al, 2002) attempting to identify:

- a simple and reproducible method with a high degree of validity in the diagnosis of obstructions;
- a sensitive and reproducible method with a high degree of validity in the measurement of urethral resistance and in changes in this resistance.

The ICS Previsional Method should be used in addition to any other method chosen, in order to be able to compare the results obtained in different research centers. This Method derives from a modification of the A/G Number, and it classifies the values of $P_{det[Qpeak]}$ and Q_{peak} as follows (Figure 1.16):

if $P_{det[Qpeak]}-2\cdot Q_{peak} > 40$, the P/F Study is obstructed;

if $P_{det[Qpeak]}-2\cdot Q_{peak} < 20$, the P/F Study is not obstructed;

otherwise, the Study is uncertain.

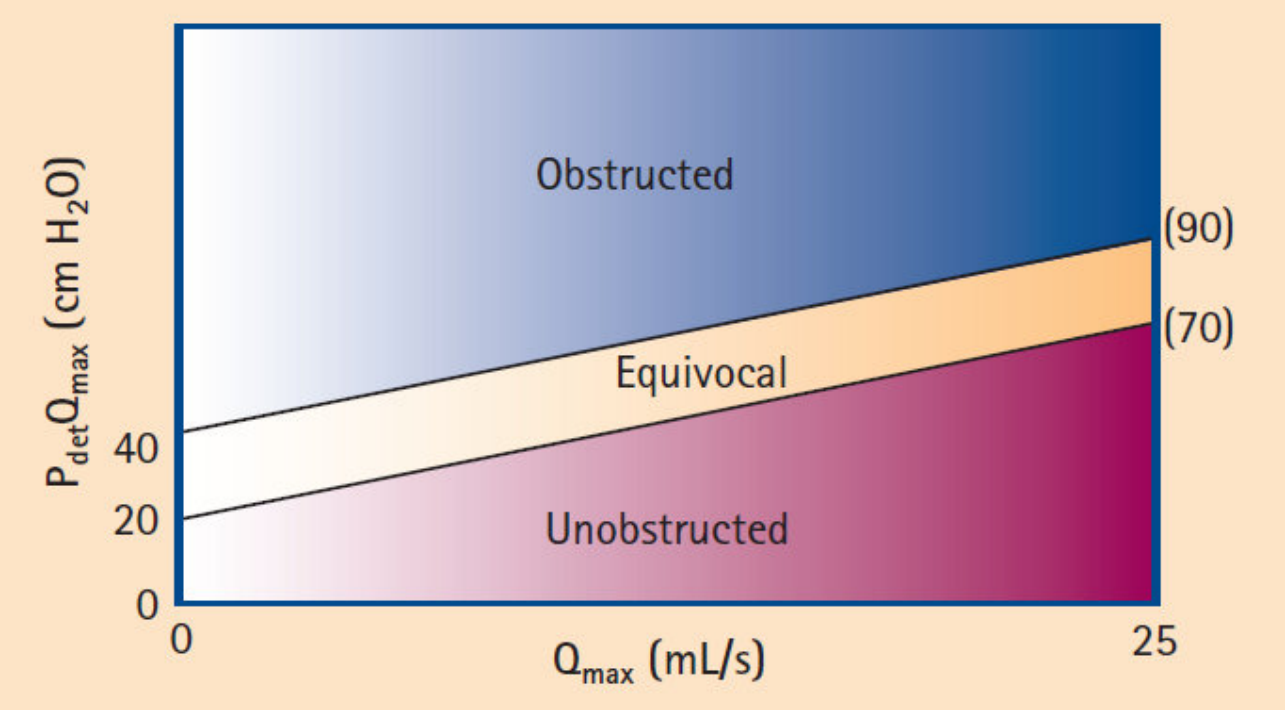

Figure 1.16: ICS Previsional Method

1.5 Urodynamic functionality parameters

The main parameters used to assess the functionality of the LUT are:

- BOOI [-], bladder outlet obstruction index. Derived from the A/G number, it is expressed by the following relationship:

$$BOOI = P_{det[Qpeak]} - 2 \cdot Q_{peak} \quad (1.3)$$

  The patient is considered not obstructed if BOOI < 20, obstructed otherwise;
- BCI [-], bladder contraction index. It is expressed by:

$$BCI = P_{det[Qpeak]} + 5 \cdot Q_{peak} \quad (1.4)$$

  If BCI > 150, the bladder contraction is “strong”;
  if BCI < 100, the bladder contraction is “weak”;
  bladder contraction “normal” otherwise;
- OCO [-], obstruction coefficient, expressed by:

$$OCO = \frac{P_{det[Qpeak]}}{40 + 2 \cdot Q_{peak}} \quad (1.5)$$

  If OCO > 1, the patient is considered not obstructed.

1.6 Current non-invasive techniques in Urodynamics

To date, various techniques have been analyzed to assess the functionality of the LUT and to measuring the detrusorial pressure in a non-invasive way.

Despite the fact that flow-rate measurements can be used to pre-select patients for further testing, thus limiting the number of invasive studies necessary in a given population of patients, it has often been proposed to diagnose obstruction on the basis of non-invasive free flow-rate measurements: this is fundamentally impossible (Van Mastrigt & Pel, 1999).

Though several show promise when used in combination, the diagnostic accuracy of these methods remains less than ideal. There are large variations in sensitivity and specificity of these measures, and clinical application is often challenging from a practical standpoint (Blake & Abrams, 2004, Belal & Abrams, 2005, Elterman et al, 2013).

Some methodologies are imprecise and can only be used on men (e.g., penile interruption technique, Griffiths et al, 2005), while others are expensive (e.g., Doppler measurements, Nose et al, 2004).

To date, invasive P/F Studies remain the gold standard for measuring the detrusorial pressure and for diagnosing BOO.

2 The development of an innovative methodology in Urodynamics

The functional study of the LUT urethra is carried out by analyzing mainly the activity of the detrusor muscle to evaluate the bladder filling and emptying phases, to monitor the progression of a urinary dysfunction induced by a pathology, or to verify the effectiveness of a therapeutic treatment. The main investigations that are currently used include Uroflowmetry (section 1.3.1) with possible ultrasound evaluation of the post-urination residue and, mainly, the P/F Study. As it has been seen in section 1.3.2, this study is highly invasive; it is carried out through a catheter positioned in the bladder through the urethra and an endorectal sensor that allow to record the pressures inside the bladder and in the rectum (abdominal pressure) during the urination act. It is clear that these techniques cause serious inconvenience to the patient, constitute an economic burden for the healthcare structure in terms of costs due to consumables, and above all require time for the medical and nursing staff (every invasive urodynamic investigation requires a doctor and a nurse); moreover, the presence of a catheter inside the urethral and bladder lumen determines a non-physiological condition that certainly affects the interpretation of the results (Groutz et al., 2000, Baseman et al., 2002). The only non-invasive investigation is Uroflowmetry, which measures only the volume of urine emitted over time. This data is however partial and not sufficient, in case of suspected dysfunction, to assess whether or not there are pathologies. Therefore, today, there isn't any non-invasive tool that allows the evaluation of the function of the LUT (Nitti, 2005, Parsons et al., 2011, Elterman et al., 2013).

The general objective of the present project is the development of a device that allows the evaluation of the functionality of the LUT in a very non-invasive way. This equipment, implemented as medical equipment to be used in the urology departments, will allow the progressive replacement of current invasive technologies for cystomanometric examination and P/F Study with non-invasive technologies, thus reducing discomfort for patients and eliminating any complications due to the positioning of the bladder catheter and the rectal probe necessary for a correct execution of the investigations. Furthermore, the operating costs (in terms of materials and human resources) for healthcare facilities are considerably reduced. Thanks to the reduced costs and non-invasiveness, the proposed equipment is suitable for large-scale prevention actions through the possibility of carrying out mass screening.

2.1 Formulation of the hypothesis

Unlike blood flow in arteries and veins (Pedley, 1980), urine flow in LUT has been poorly studied. In this work, the basic concept arises from considering the LUT similar to a hydraulic system consisting of a pressure feed tank (bladder) and an outlet elastic duct (urethra) whose physical behavior is governed by the laws of fluid mechanics (Figure 2.1). Starting from the knowledge of

the physical quantities of the urinary jet measurable outside of the urethra it is possible to model the LUT internal urodynamic characteristics.

In this way, it can be described almost completely in mechanical terms, as Griffiths did in his 1980 study, on which most subsequent modelings are based. However, it must be remembered that the LUT is not purely mechanical but is under neuromuscular control, both conscious and unconscious; and then the structure of the urethra-bladder system and its relationship with adjacent organs make its behavior rather complicated. Currently, Schäfer diagrams (section 1.4.3), essentially derived on an empirical basis, are generally used to assess the functionality of the LUT. Unfortunately, there are very few non-invasive measures on the mechanical behavior of the LUT; some are inaccurate and can only be used on men (e.g. the "penile interruption technique", Griffiths CJ et al, 2005), while others, such as Doppler measurements, are expensive (Nose et al., 2005). In fact, to date, the P/F Study is the diagnostic standard.

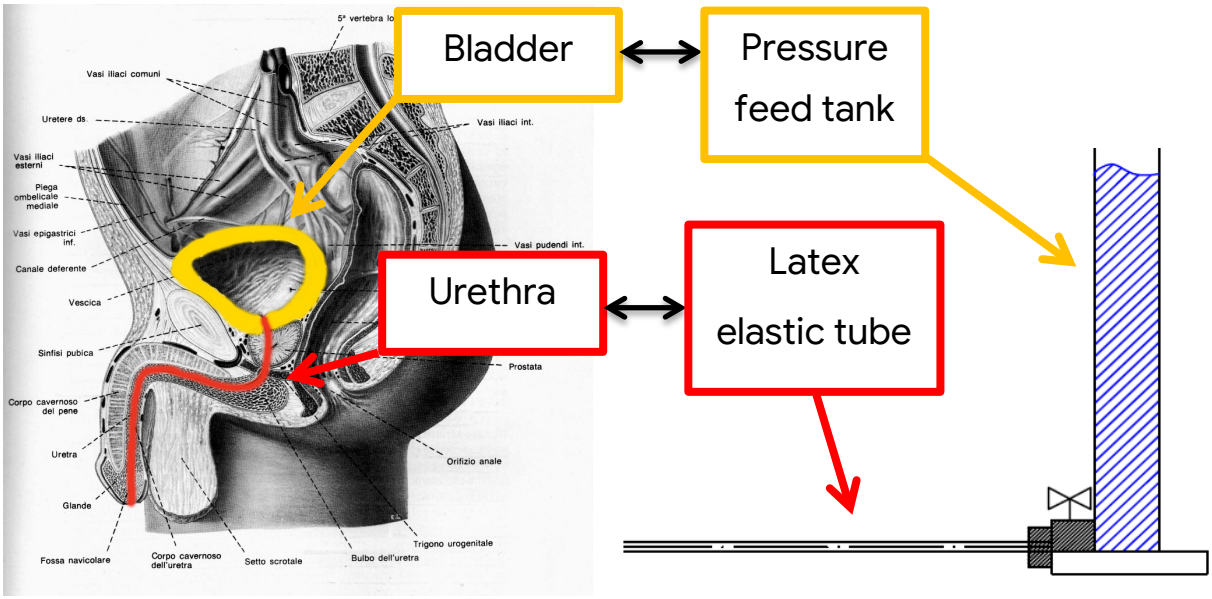

Figure 2.1: similarity between the LUT and a hydraulic system

The aim of this work is therefore twofold: first, to define a new method for non-invasive Urodynamics diagnostic, second, to reformulate the current Schäfer diagram in terms of variables not affected by the current invasive methods.

To this end, an extensive experimental activity has been carried out in the Fluvial and Lagoon Hydraulics and Biofluidodynamics Laboratory of the Department of Civil and Environmental Engineering of the University of Florence, which can be divided in two main phases:

- ***preliminary tests*** to identify the most suitable method for non-invasive analysis (section 2.3);
- ***extensive tests*** to investigate the characteristics of the innovative method (section 3).

The Laboratory physical model (hereafter, ***Model***) which has been used through all the experimental activity is described in the following section.

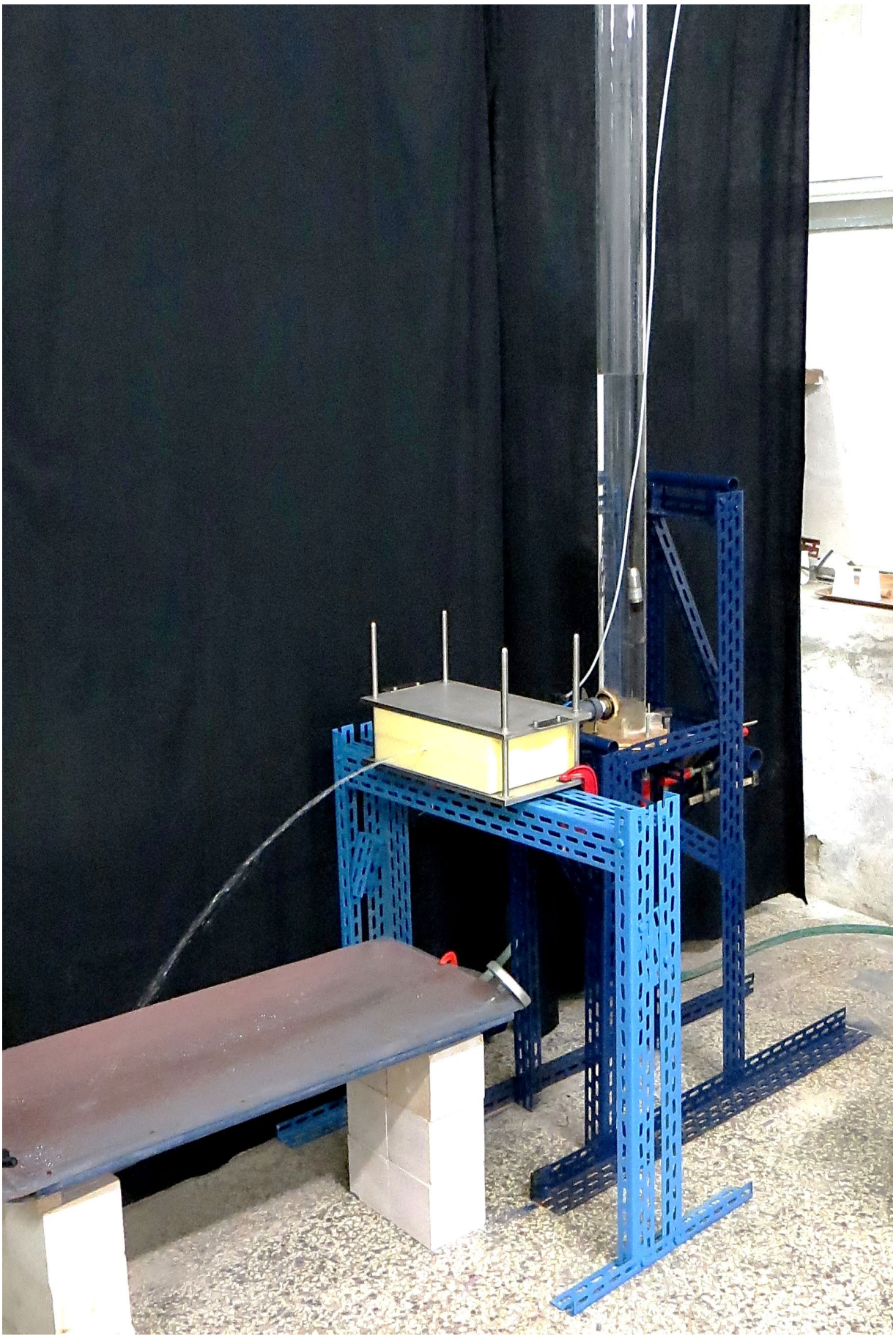

Figure 2.2: the Laboratory physical model

2.2 THE LABORATORY PHYSICAL MODEL

A Model of the LUT has been specifically designed and assembled in the Fluvial and Lagoon Hydraulics and Biofluidodynamics Laboratory of the Department of Civil and Environmental Engineering of the University of Florence (Figure 2.2): basically, it consists of a pressure feed tank connected to a latex elastic collapsible output tube (hereafter, ***Tube***), that it is assumed to have a similar behavior to the urethra. The Model has been tested with experiments to evaluate jet external characteristics under many different conditions (i.e. presence or absence of obstructions, type of obstructions, presence of absence of catheter, different types of instrumentations, etc.).

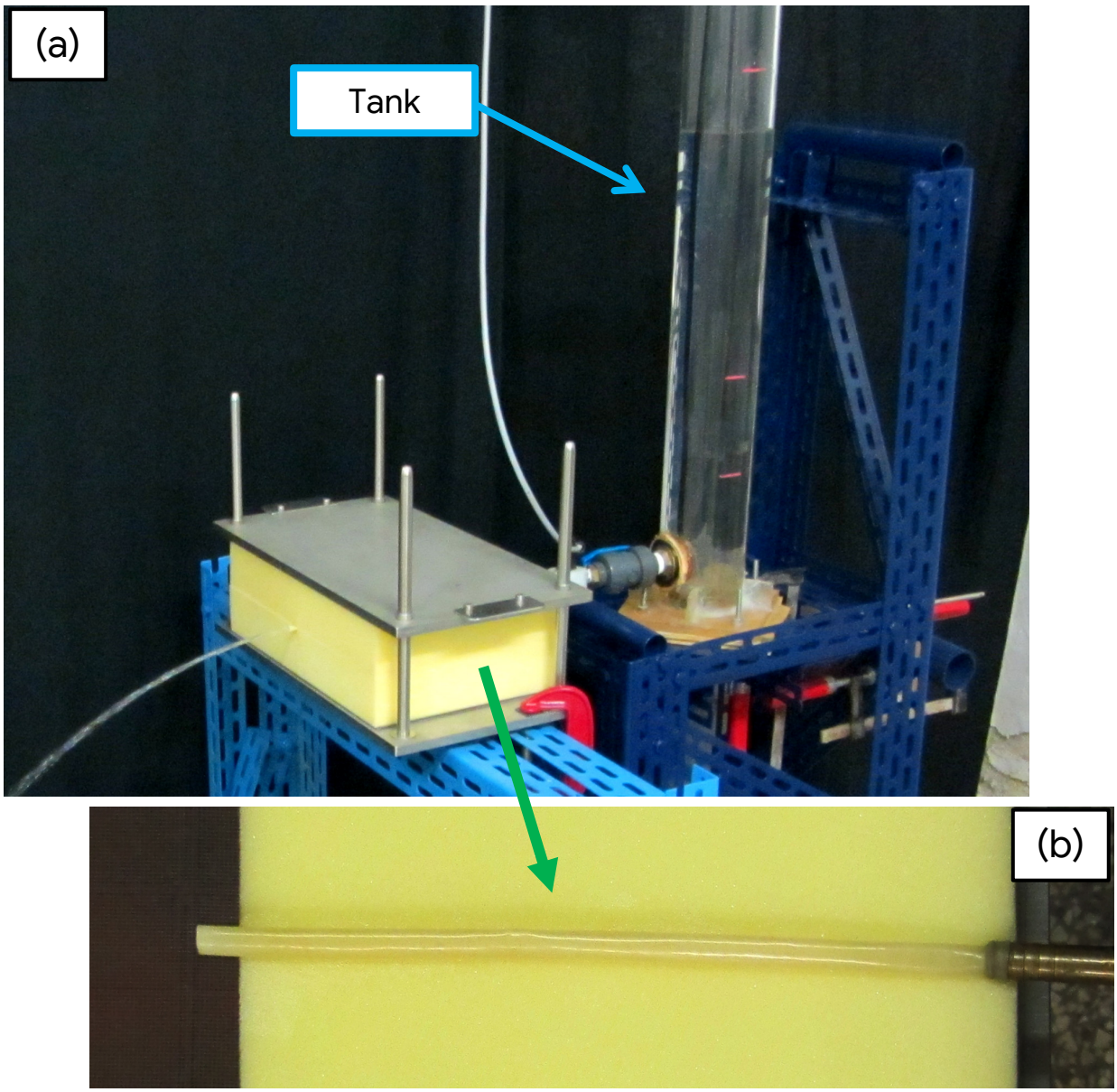

Figure 2.3: Model details: (a) close-up of the Model and of the cylindrical tank; (b) the Tube

The Model consists of a 2 m high cylindrical plexiglas supply tank which provides the upstream hydraulic head (Figure 2.3a) with a drain hole on the bottom connected to a Tube which is supposed to simulate the urethra (Figure 2.3b). The Tube is a Penrose drainage 20 cm long, 0.3 mm

in thickness that nominally has a 6 mm internal diameter at rest (Figure 2.4). The Tube maintains both a constant length and a constant cross-sectional area at its upstream end thanks to the connection to a rigid tube.

Figure 2.4: the Tube compared to a one euro coin

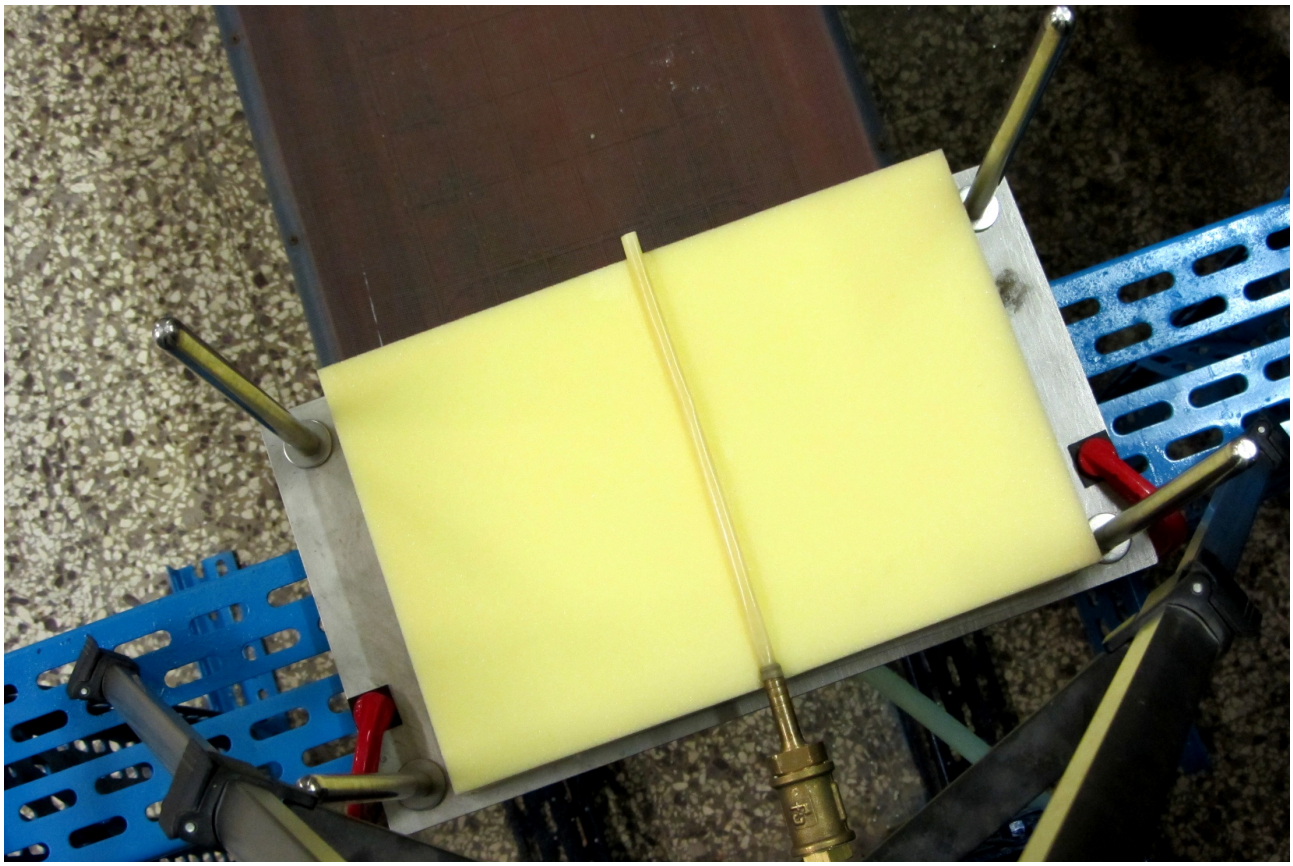

Figure 2.5: lower foam block with the Tube placed on it

The elastic compression on the urethra due to the internal organs was simulated by positioning the Tube between two foam rubber blocks of size 30x20x5 cm^3 (Figure 2.5) with a 58.8 N (6 kg) load placed on the upper side, in order to have a uniform pressure on the tube equal to 981 Pa. The Tube is linked to a metal connector, which in turn is linked to the tank by a valve, in order to close the system. The downstream last centimeter of the Tube is placed outside the foam

in order to reproduce the navicular fossa, an enlargement of the urethra immediately proximal to the external urethral meatus (D2 in Figure 1.4): the navicular fossa is a part of the urethra that is not subject to compression but always remains open; it was therefore considered appropriate to leave it outside the foam compression, so as to be as similar as possible to the real situation.

parameter	*meaning*	*value*
Ω_c	internal area of the metal connector	$4.0715 \cdot 10^{-5}$ m^2
$\Omega_{c,ext}$	external area of the metal connector	$6.3617 \cdot 10^{-5}$ m^2
Ω_t	internal area of the tank	$4.84 \cdot 10^{-3}$ m^2
Ω_v	internal area of the valve	$1.767 \cdot 10^{-4}$ m^2
D_c	internal diameter of the metal connector	$7.2 \cdot 10^{-3}$ m
$D_{c,ext}$	external diameter of the metal connector	$9 \cdot 10^{-3}$ m
D_v	internal diameter of the valve	$1.5 \cdot 10^{-2}$ m
L_c	internal length of the metal connector	$6 \cdot 10^{-2}$ m
L_T	length of the Tube	0.2 m
L_v	internal length of the valve	$8 \cdot 10^{-2}$ m

Table 2.1: main geometric data of the Model

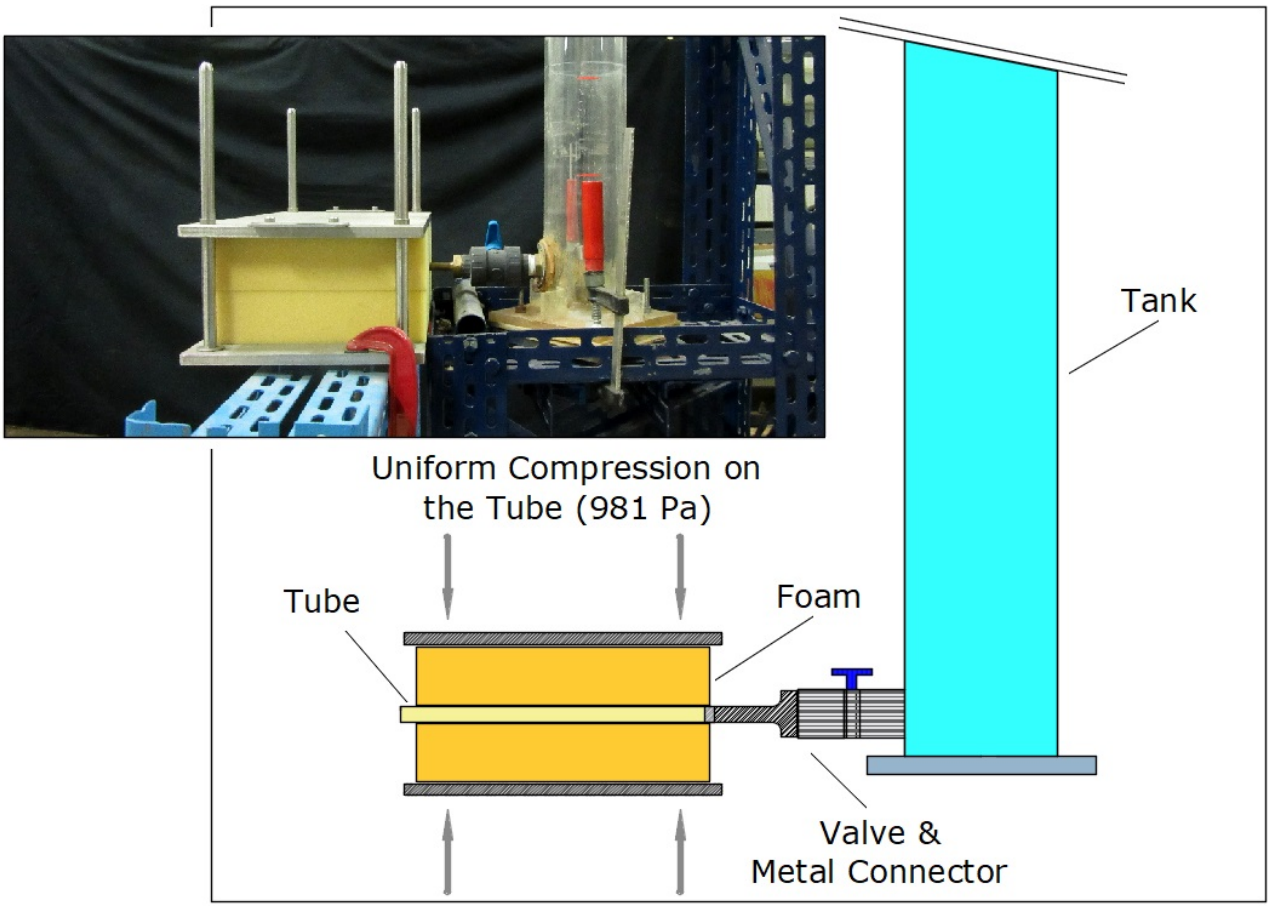

Figure 2.6: overall scheme of the Model

In Figure 2.6 a scheme of the Model is presented, while in Table 2.1 the main geometric data of the Model are shown.

Despite the simplified structure, the Model is able to preserve some main characteristics of the LUT; in particular, it simulates correctly the main physical processes within the lower urinary tract: the resistance to motion of the walls of the urethra, their deformability varying intramural pressure, localized and distributed obstructions.

2.2.1 Experimental setup and procedures

All tests of all types were carried out according to the following scheme:

- fill the tank with the valve closed at least until $H_{0,max}$,
- turn on the data acquisition instrumentation,
- open the valve and wait for the tank to empty at least until $H_{0,min}$.

The main physical parameters considered in all tests are: the static head inside the tank H_0, the flow rate passing through the system Q, the total head at the Tube entrance H_c and the jet exit velocity u_e. All these parameters change in time during the emptying phase.

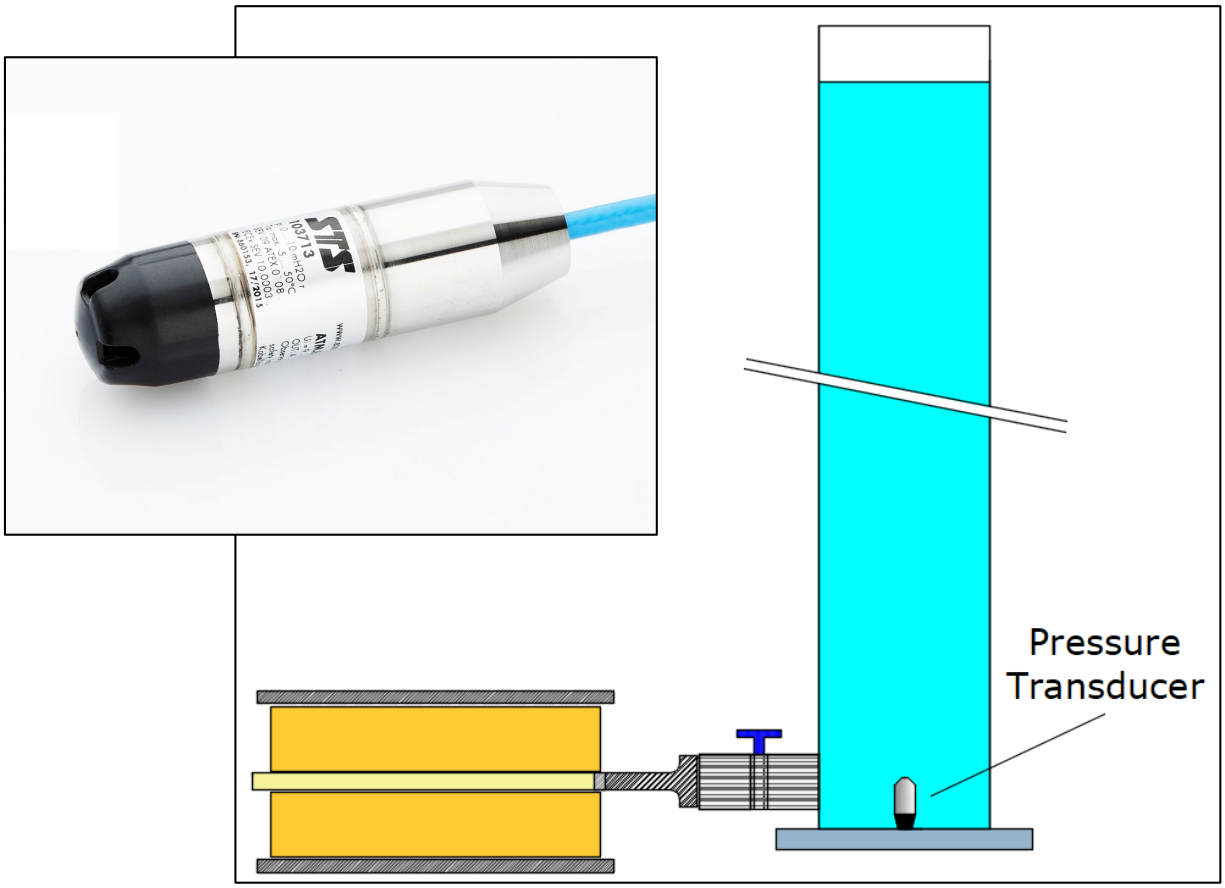

Figure 2.7: pressure transducer placed on the bottom of the tank

The electronic instrumentation consists mainly of a ATM-1ST/N pressure transducer, produced by STS Italia, positioned on the bottom of the tank to monitor H_0 (Figure 2.7). It is a

"current to pressure" transducer that converts a pressure input (in this case, 0-250 cm H_2O) to a proportional linear analog signal output (4-20 mA); the maximum error is the 0.1 % of the full-scale (0.25 cm H_2O in this case).

Figure 2.8: National Instruments NI-9203 current input module (a); NI-cDAQ-9174 USB chassis (b)

The pressure transducer is connected to a dedicated data acquisition hardware and software, that saves the converted data on an text file that can be used in subsequent processing. In particular, it has been used a NI-9203 16-bit analog current input module produced by National Instruments (Figure 2.8a), connected to NI-cDAQ-9174, a 4-slot USB chassis (Figure 2.8b). The acquisition frequency was set to 12.5 Hz, that is a sampling period of Δt=0.08 s.

The acquisition software used is LabVIEW (Laboratory Virtual Instrument Engineering Workbench): it is a visual programming language, developed and produced by National Instruments, that was aimed at enabling all forms of system to be developed, while the subsequent processing has been done with MATLAB, a high-performance language for technical computing: it integrates computation, visualization, and programming in an easy-to-use environment where problems and solutions are expressed in familiar mathematical notation.

All the experimental runs have been carried out according the following procedures:

- the fluid used is water at ambient temperature (T=20÷25 °C, ρ=1000 kg/m^3), incompressible fluid, with dynamic viscosity $\mu=10^{-3}$ Pa·s and kinematic viscosity $v=10^{-6}$ m^2/s;
- flow is turbulent;
- maximum level inside the tank $H_{0,max}$=1.6 m;
- minimum level inside the tank $H_{0,min}$=0.2 m;

The emptying of the tank is designed in order to have output flow characteristics, i.e. flow and pressure, in a range of values similar to those occurring during micturition. In healthy people, the detrusorial pressure range is between 0-60 cm H_2O, while it can increase up to 150 cm H_2O in people with obstructions; the maximum level $H_{0,max}$=1.6 m was chosen to take into account the energy losses between the tank and the beginning of the Tube, as explained further on in section 2.2.4.

2.2.2 WATER LEVEL INSIDE THE TANK H_0

As mentioned before, the level in the tank during emptying was monitored by means of a pressure transducer placed on the bottom of the tank, from level $H_{0,max}$ to level $H_{0,min}$.

To reduce the noise on the digital signal, two approximations were tested, a second-degree polynomial and a b-spline. In Figure 2.9 an example of the emptying process is reported: the black dots represents the transducer's data ($H_{0,raw}$), while the blue line and the red line are the polynomial estimation ($H_{0,poly}$) and the b-spline estimation ($H_{0,spline}$) of the $H_{0,raw}$ data, respectively. Because the three data almost overlap, Figure 2.10 shows the part of the graph in the purple box of Figure 2.9.

Both approximations proved to be acceptable, as the relative standard deviation between real and estimated value is under 0.1 %, so the polynomial was chosen for simplicity of use. Hereafter, ***$H_{0,poly}$ will be denoted as H_0***.

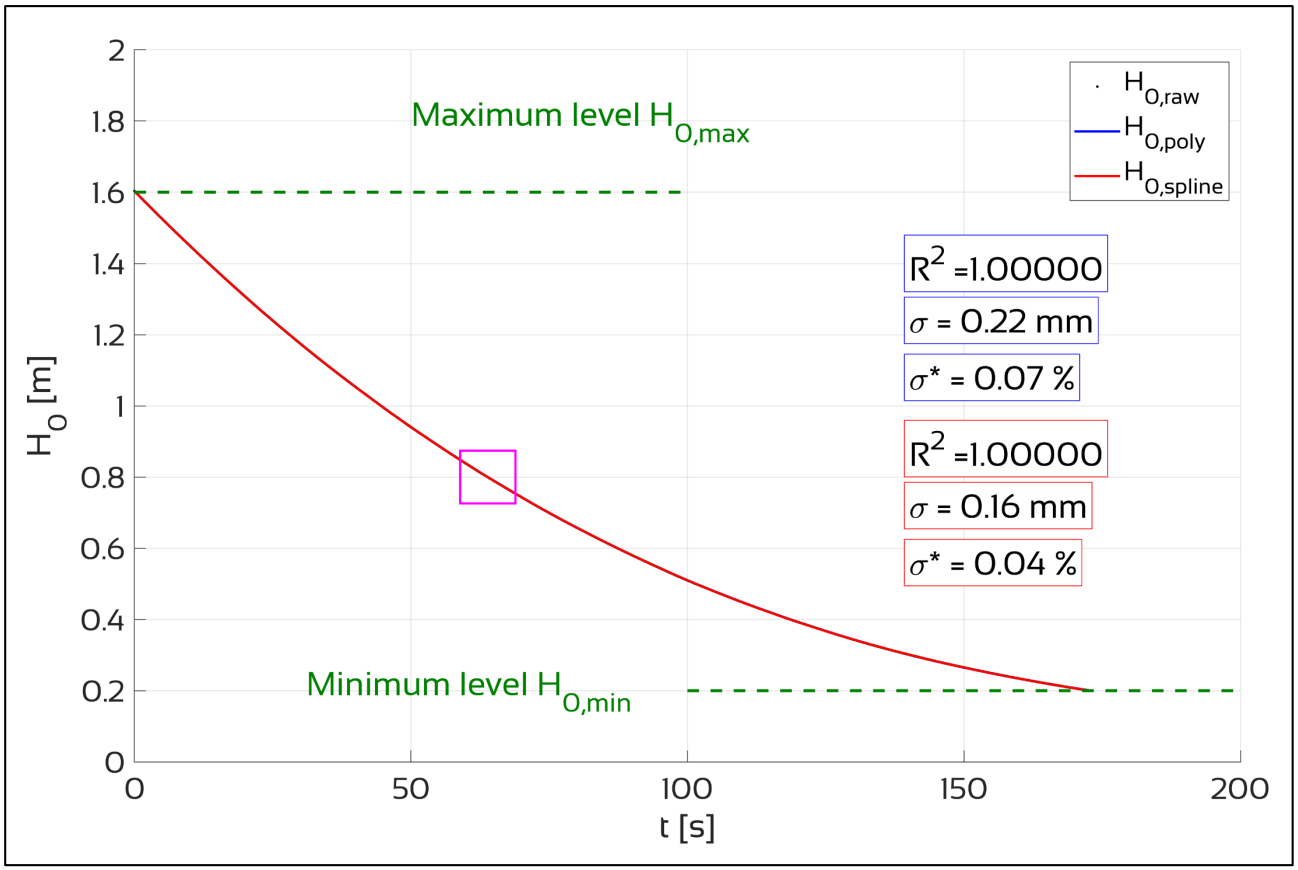

Figure 2.9: water tank levels: the black dots (transducer's data), the blue line (polyline estimation) and the red line (spline estimation) almost overlap; the area in the purple box is enlarged in Figure 2.10

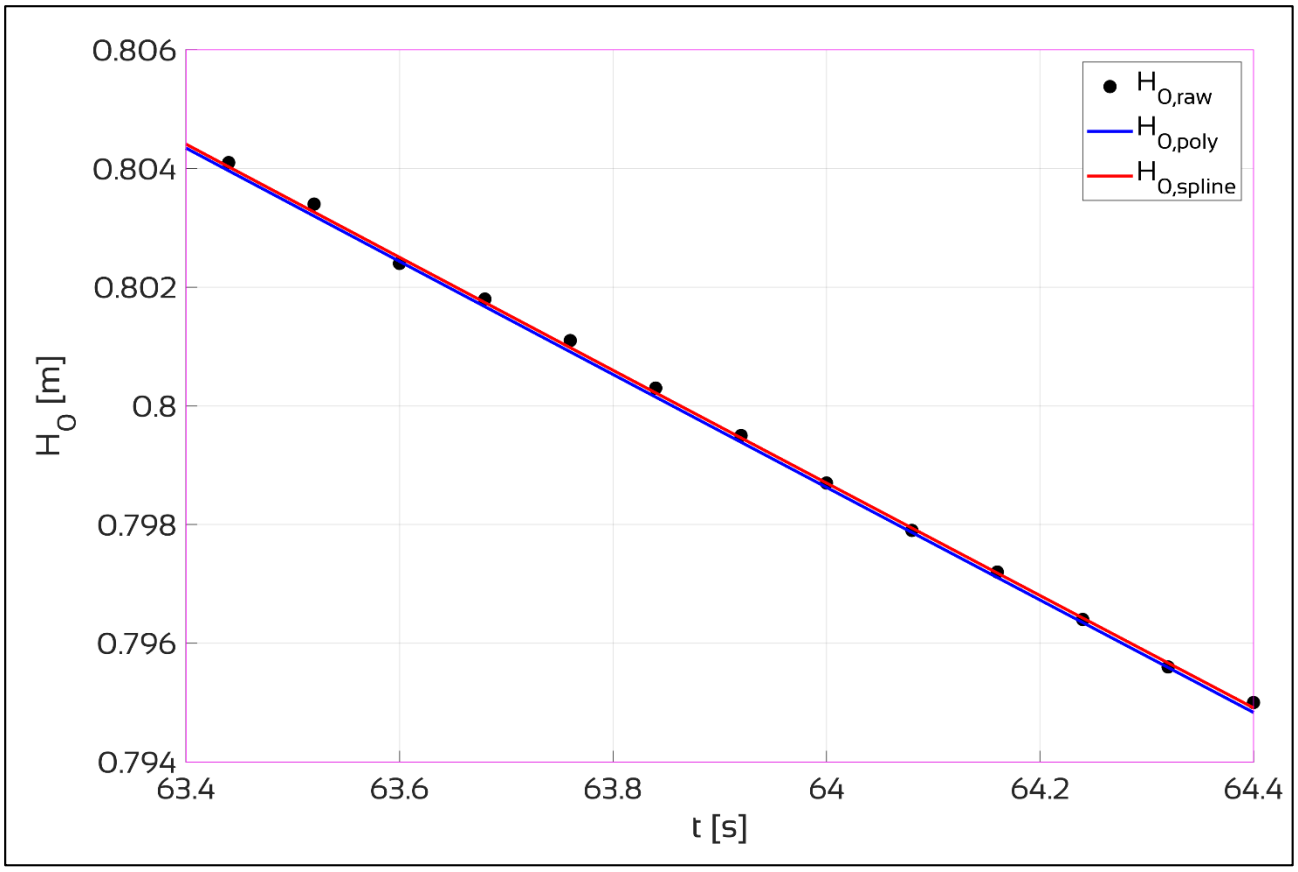

Figure 2.10: part of the water tank data in the purple box of Figure 2.9

2.2.3 FLOW RATE Q

Flow rate Q was evaluated (Figure 2.11) by applying the principle of mass conservation to the tank by measuring the volume change within the time step in the tank; so, at i^{th} instant the flow is:

$$Q_i = \frac{(H_{0,i} - H_{0,i+1}) \cdot \Omega_t}{\Delta t} \qquad 2.1$$

assuming steady flow between two consecutive recordings; $H_{0,i}$ and $H_{0,i+1}$ are the H_0 values in two successive instants, Δt=0.08 s is the interval between acquisitions and Ω_t=4.8·10^{-3} m^2 is the internal area of the tank.

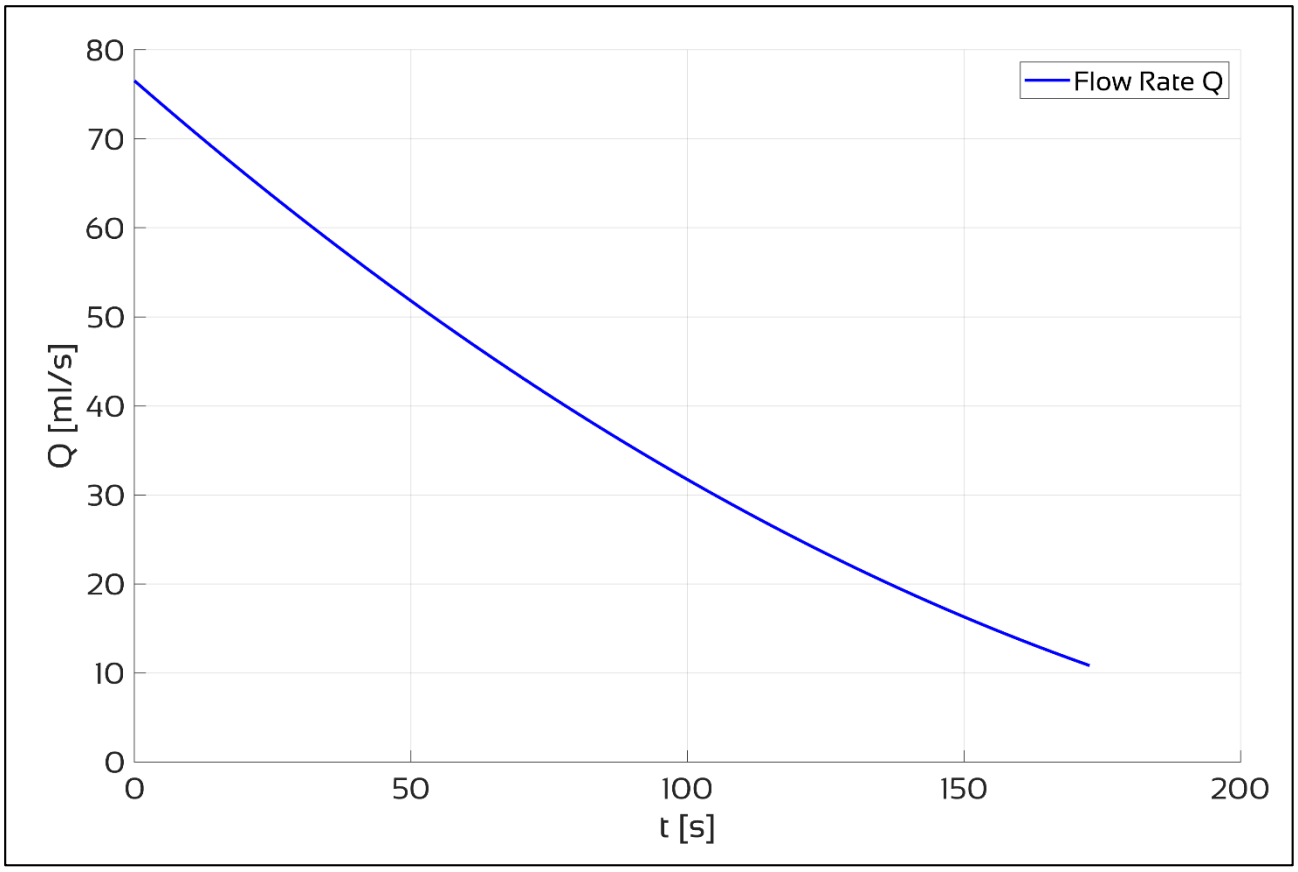

Figure 2.11: flow rate Q evaluated from the level data H_0 shown in Figure 2.9

2.2.4 TOTAL HEAD AT THE TUBE ENTRANCE H_c

In women and men the urethra is connected directly to the bladder (Figure 2.1), so in our system the total head at the Tube entrance H_c was taken as representative of the detrusorial pressure (Figure 2.12).

The Model attempts to reproduce the complex functioning of the human urethra-bladder system as realistically as possible. The clinical quantities measured refer to the pressure in the bladder, which is to be considered as a static pressure tank where the total head and the piezometric head coincide. In the Model, the Tube is not connected directly to the tank but through "special" fittings that introduce pressure drops not present in the LUT. The reference to the total load H_c intends to assume a quantity that should be the most correlated to the total head in the supply tank subtracting the unavoidable artificially introduced losses.

H_c has been calculated considering the total energy losses upstream of the Tube, due to the various pipe components. In order to calibrate the resistance coefficients of the pipe upstream of the Tube, specific measurements have been taken from the system by replicating the tank emptying experiments without the Tube (Figure 2.13). In this case, the total head in the exit section equals the kinetic energy of the flow, or:

$$H_{c,measured} = \frac{u_c^2}{2g} = \frac{Q^2}{\Omega_c^2 \cdot 2g} \qquad 2.2$$

where u_c and Ω_c=4.07·10^{-5} m^2 are respectively the velocity and the area in the terminal section of the metal connector and g is the gravity acceleration; the velocity u_c was measured through an image acquisition and processing system, as explained later in section 2.3.4.

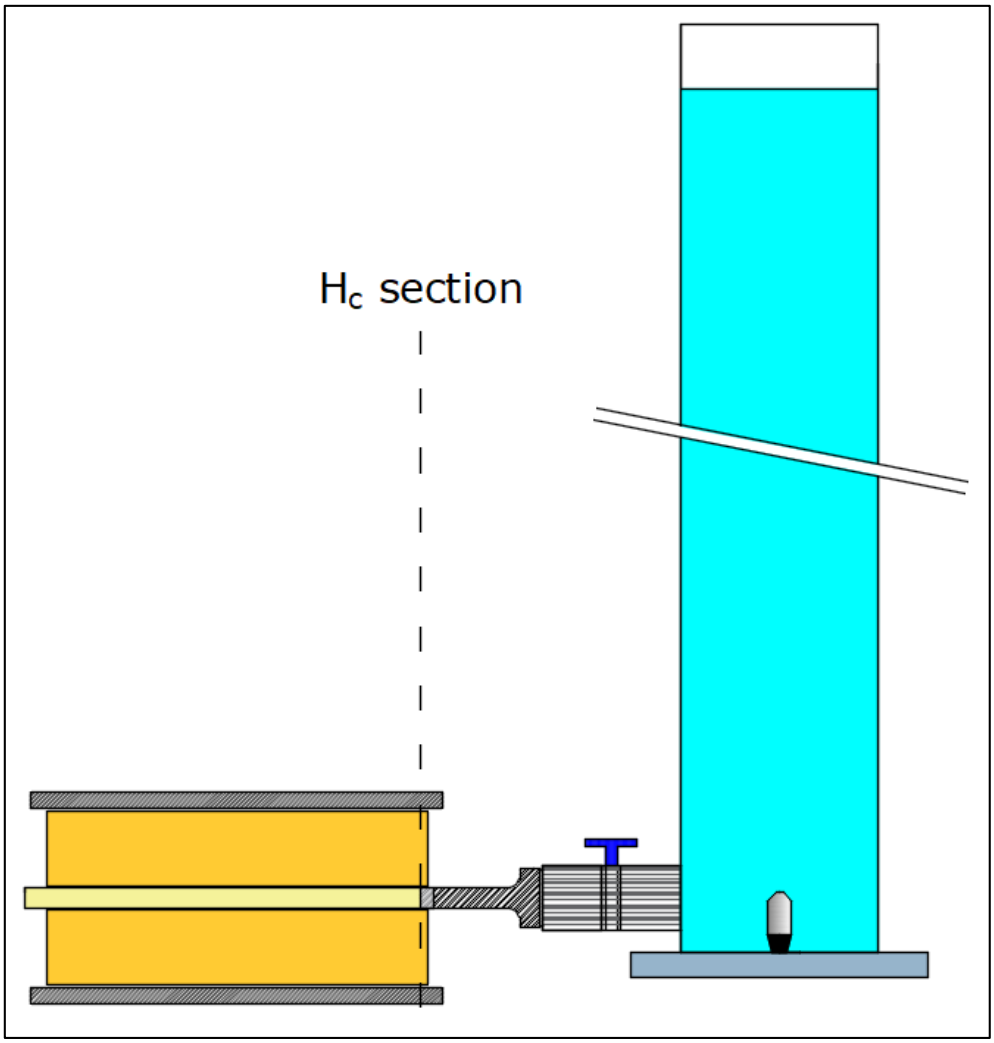

Figure 2.12: scheme of the Model with position of the Tube entrance (H_c section)

The values of $H_{c,measured}$ have been compared with $H_{c,estimated}$ values obtained by subtracting the energy losses inside the various pipe components between the tank and the Tube (Figure 2.14):

$$H_{c,estimated} = H_0 - \Delta H_{cv} - \Delta H_{dv} - \Delta H_{cc} - \Delta H_{dc} \qquad 2.3$$

where ΔH_{dv} and ΔH_{dc} are the distributed head losses inside the valve and the metal connector, respectively, and ΔH_{cv} and ΔH_{cc} the concentrated head losses at the entrance of the valve and of the metal connector, respectively.

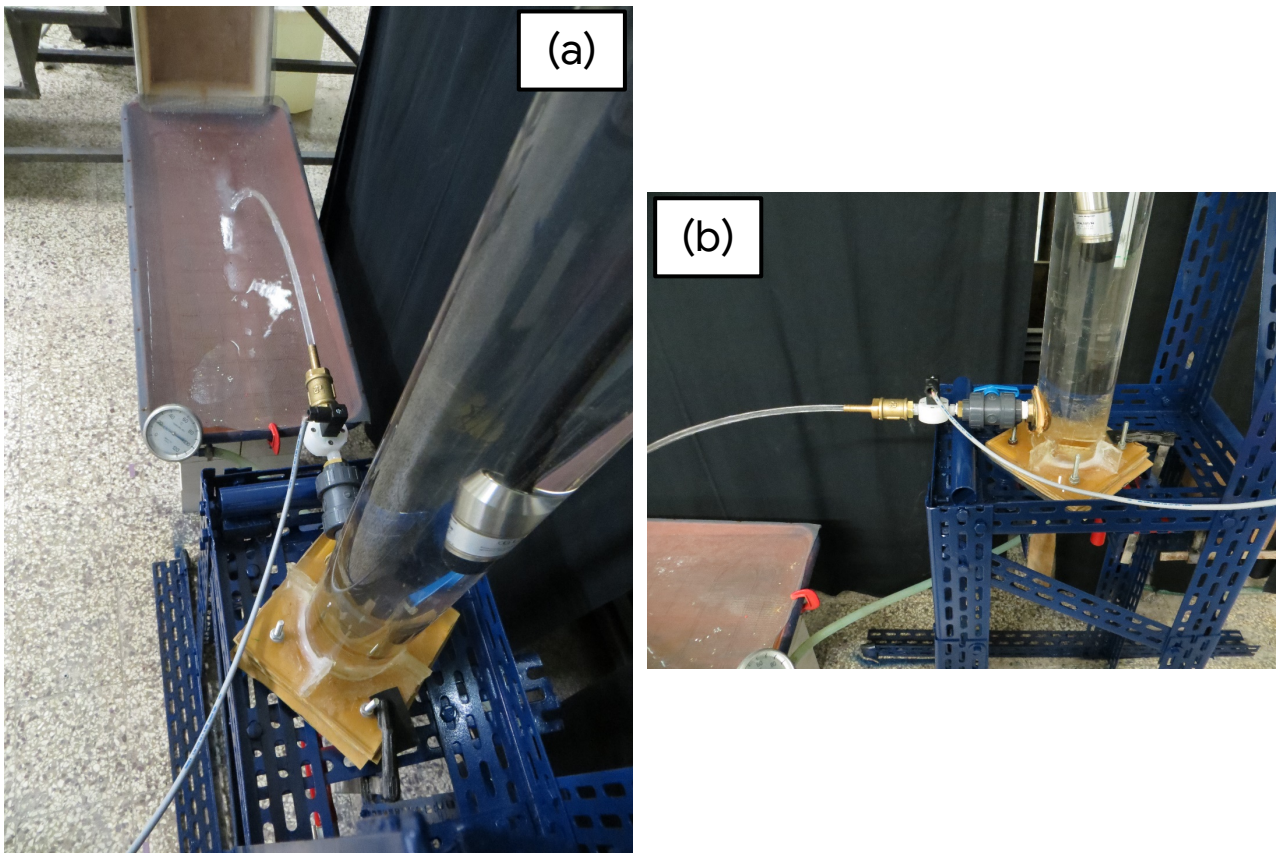

Figure 2.13: modified Model to replicate the system emptying tests without the Tube

Using the classical resistance formulas for rigid circular pipes, $H_{c,estimated}$ can be written as:

$$H_{c,estimated} = H_0 - K_v \frac{{u_v}^2}{2g} - \frac{\lambda_v}{D_v}\frac{{u_v}^2}{2g} L_v - K_r \frac{{u_c}^2}{2g} - \frac{\lambda_c}{D_c}\frac{{u_c}^2}{2g} L_c \quad 2.4$$

where λ_v, λ_c are the friction factors, D_v, D_c the diameters, L_v, L_c the duct lengths, u_v, u_c the mean velocities inside and K_v, K_c the concentrated loss head coefficient at the entrance of the valve and of the metal connector, respectively.

Given the fact that the diameters can be written as:

$$D_v = \frac{2 \cdot {\Omega_v}^{0.5}}{\pi^{0.5}} \quad 2.5$$

$$D_c = \frac{2 \cdot {\Omega_c}^{0.5}}{\pi^{0.5}} \quad 2.6$$

where Ω_v, Ω_c are the internal areas of the valve and of the metal connector, respectively, and the fact that the velocities inside the valve and the metal connector can be written, respectively:

$$u_v = \frac{Q}{\Omega_v} \quad 2.7$$

$$u_c = \frac{Q}{\Omega_c} \quad 2.8$$

the equation 2.4 becomes:

$$H_{c,estimated} = H_0 - \frac{K_v}{2g}\frac{Q^2}{\Omega_v{}^2} - \frac{\lambda_v \pi^{0.5}}{4g}\frac{Q^2}{\Omega_v{}^{2.5}}L_v - \frac{K_c}{2g}\frac{Q^2}{\Omega_c{}^2} - \frac{\lambda_c \pi^{0.5}}{4g}\frac{Q^2}{\Omega_c{}^{2.5}}L_c \quad 2.9$$

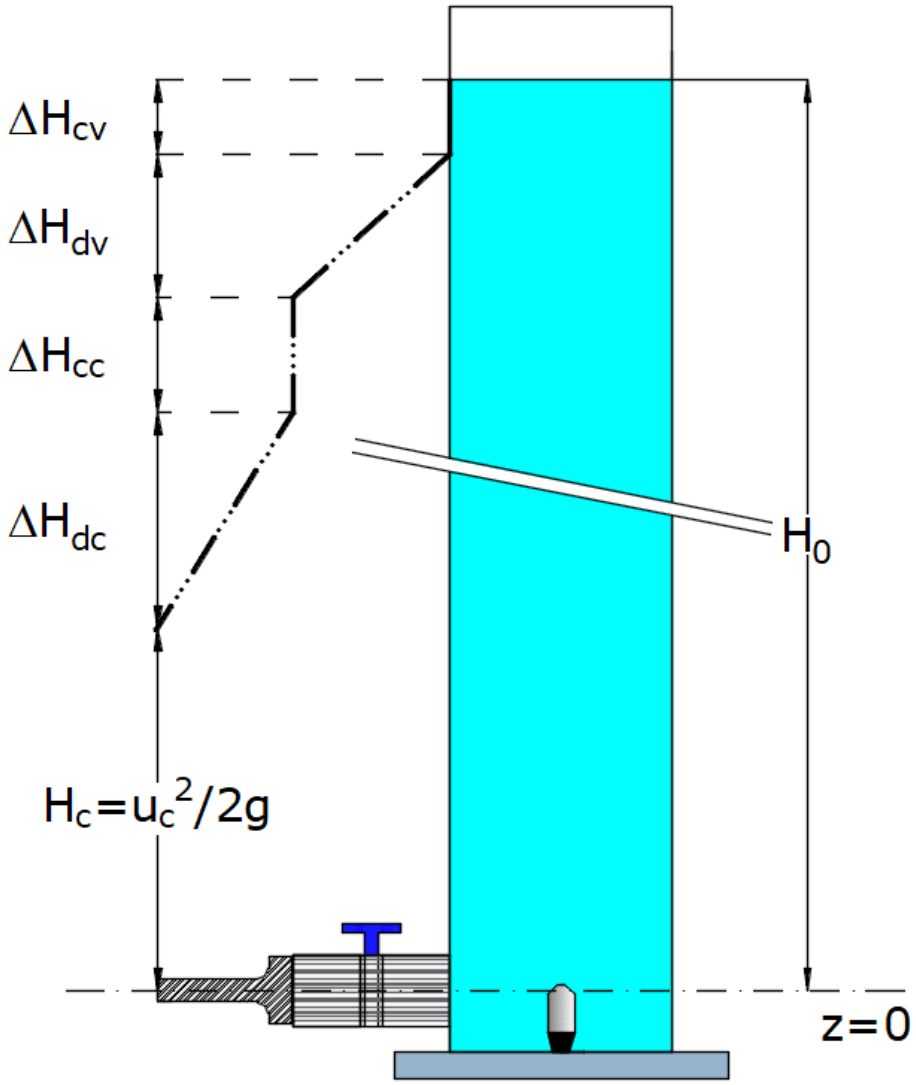

Figure 2.14: energy losses due to the various pipe components between the tank and the Tube

The friction factors are assumed for turbulent flow as described by (Colebrook, 1939):

$$\frac{1}{\sqrt{\lambda_v}} = -2\log\left(\frac{2.51}{Re_v\sqrt{\lambda_v}} + \frac{\varepsilon_v}{D_v}\right) \quad 2.10$$

$$\frac{1}{\sqrt{\lambda_c}} = -2\log\left(\frac{2.51}{Re_c\sqrt{\lambda_c}} + \frac{\varepsilon_c}{D_c}\right) \quad 2.11$$

where Re_v, Re_c are the Reynolds number and ε_v, ε_c the roughness of the valve and of the metal connector, respectively.

ε_v, ε_c K_v and K_c values were calibrated with our experiments, the chosen values are shown in Table 2.2; the geometric data are reported in Table 2.1.

parameter	*meaning*	*value*
ε_c	metal connector roughness	0.02 mm
ε_v	valve roughness	0.01 mm
K_c	concentrated loss head coefficient at the entrance of the metal connector	0.1
K_v	concentrated loss head coefficient at the entrance of the valve	0.3

Table 2.2: calibrated values of roughness and concentrated head loss coefficients of the valve and the metal connector of the Model

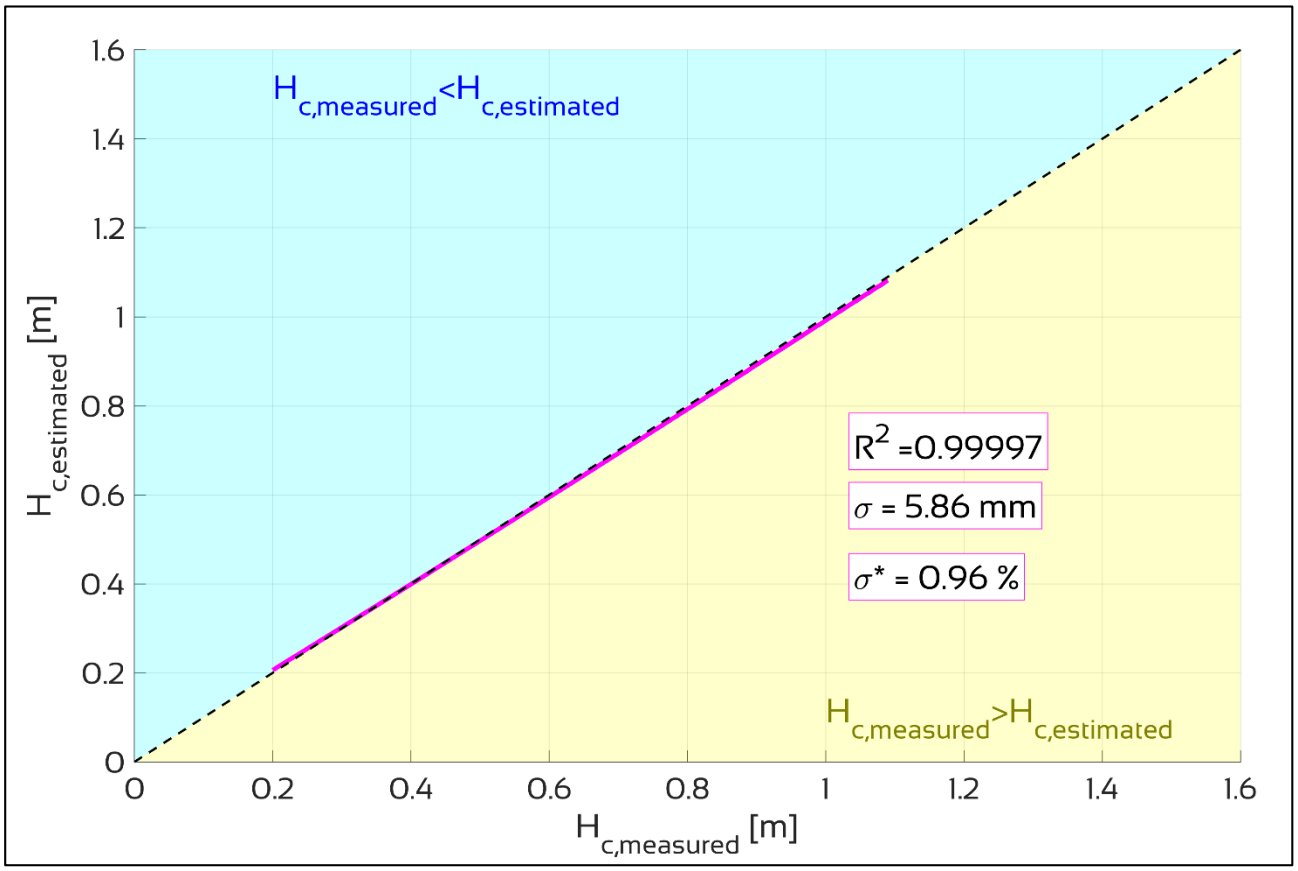

Figure 2.15: the purple line represents the estimated total head at Tube entrance $H_{c,estimated}$ as a function of the measured total head $H_{c,measured}$; σ is the standard deviation and σ* the relative standard deviation between the two values

In Figure 2.15 the purple line shows the correlation between the measured ($H_{c,measured}$) and the estimated data ($H_{c,estimated}$). The yellow part represents the area of the graph where

$H_{c,measured}>H_{c,estimated}$, the blue part represents the area where $H_{c,measured}<H_{c,estimated}$, while the perfect agreement between the two data is the dashed black line.

It can be seen that there is a very good accordance between the measured data and the corresponding estimated data, with the purple line almost over the dashed black line; the relative standard deviation is less than 1 % (5.9 mm the standard deviation). Hereafter, ***$H_{c,estimated}$ will be denoted as H_c.***

2.3 PRELIMINARY LABORATORY TESTS

The preliminary Laboratory tests concerned three main aspects of the Model:

- defining a simple and effective way to evaluate the jet exit velocity from the Tube (from section 2.3.1 to section 2.3.4);
- evaluating physical properties of the Tube (section 2.3.5);
- determining the appropriate external pressure on the foam and consequently over the Tube (section 2.3.6).

2.3.1 MEASURE OF JET EXIT VELOCITY U_E

Together with the flow rate, the measure of jet exit velocity is a fundamental parameter for estimating the intravesical pressure. The analyzed methods were three:

- measurement of the ***dynamic impact of the jet*** using load cells (section 2.3.2);
- measurement of the angular speed impressed on a reel by the jet through an ***optical encoder*** (section 2.3.3);
- estimation of the jet velocity by detecting the jet parabola through ***image acquisition and processing system*** (section 2.3.4).

The selection criterion was based on simplicity of use, reproducibility of the results and accuracy of the estimate. Let's now see the three systems in detail.

2.3.2 DYNAMIC IMPACT OF THE EXIT JET ON LOAD CELLS

2.3.2.1 NUMERICAL SCHEME & INSTRUMENTATION

The operating principle of this measuring system is based on the detection of the dynamic impact of a jet on a flat plate, which can be written as:

$$M = \rho \cdot Q \cdot u \qquad 2.12$$

where M is the momentum, ρ=1000 kg/m^3 the water density and u the jet velocity. Being known M and Q, it's possible to evaluate u by reversing equation 2.12.

The instrumentation used for momentum measurement consists of three load cells ECX-100 (Celmi srl, Figure 2.16), each connected to a flat plate. The flat plate was arranged to always be orthogonal to the liquid jet, in order to measure the total momentum and not a component of it, following a procedure explained in the following section.

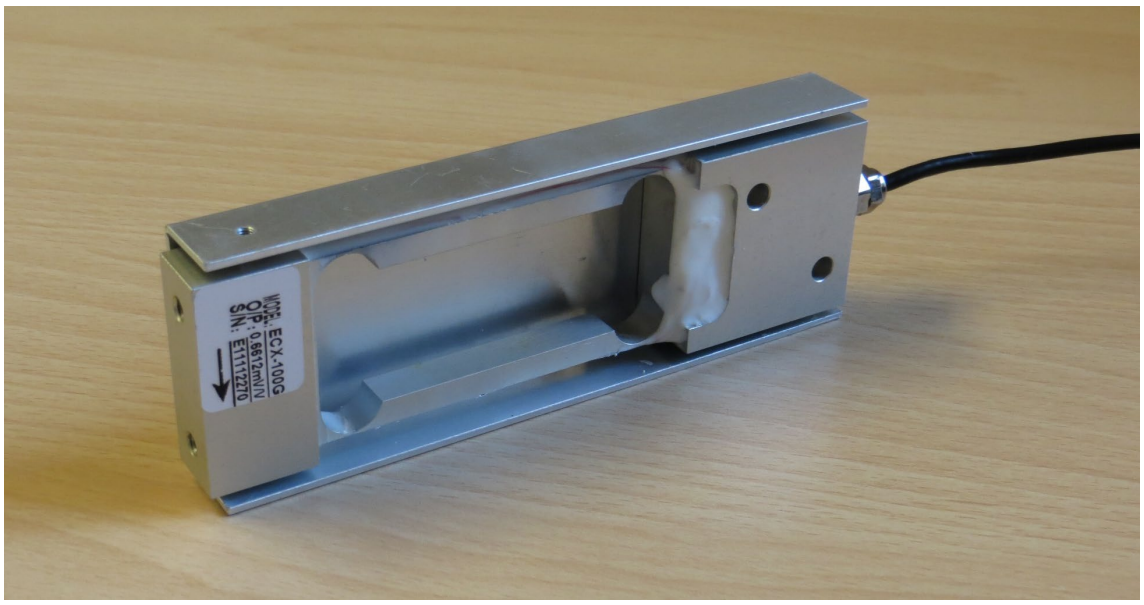

Figure 2.16: Celmi srl load cell ECX-100

2.3.2.2 ORTHOGONAL SURFACE

For each parabola of the exit jet, the orthogonal surface up to the intersection with the subsequent parabola was considered, starting from an exit angle θ_e=90° up to θ_e=0°; the example in Figure 2.17 shows the surface (red line) that is h_{lc}=10 cm distance from the exit jet with steps between the exit angles θ_e of 20° (exit jets in blue lines).

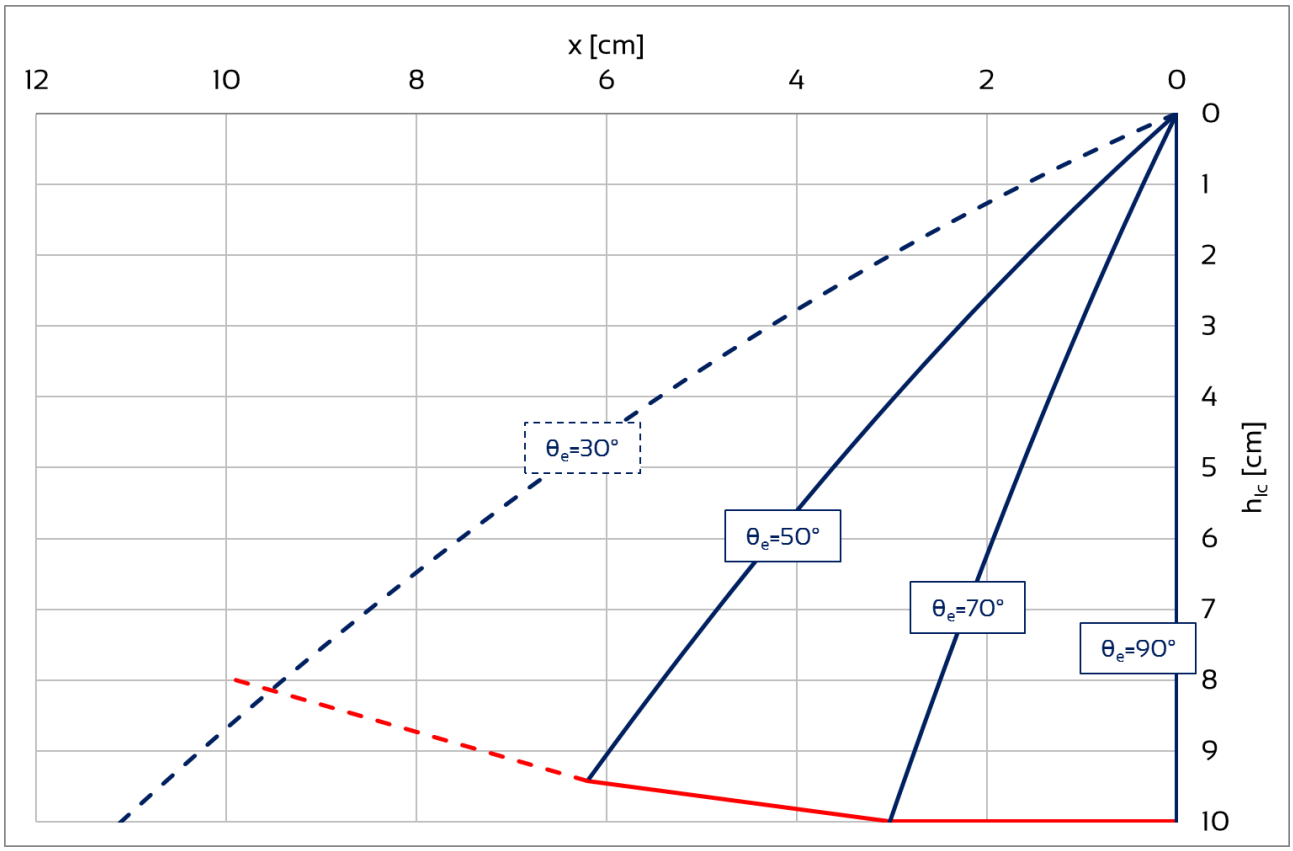

Figure 2.17: procedure to draw an orthogonal surface (red line); the blue lines are the jet exit parabolas with the exit angles θ_e indicated in the blue boxes

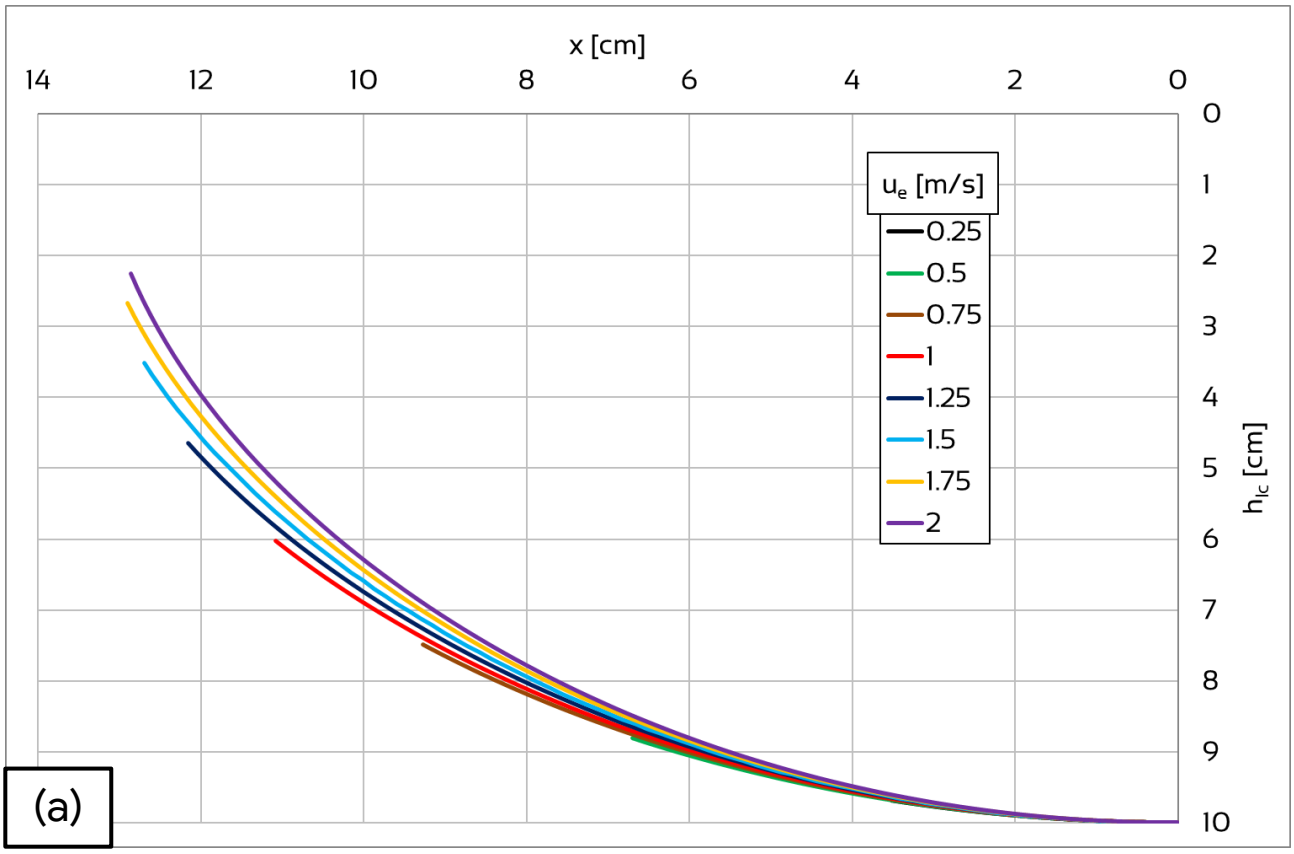
x [cm]
14
12
10
8
6
4
2
0
0
1
2
3
4
5
6
7
8
9
10
h_{lc} [cm]
u_e [m/s]
0.25
0.5
0.75
1
1.25
1.5
1.75
2
(a)

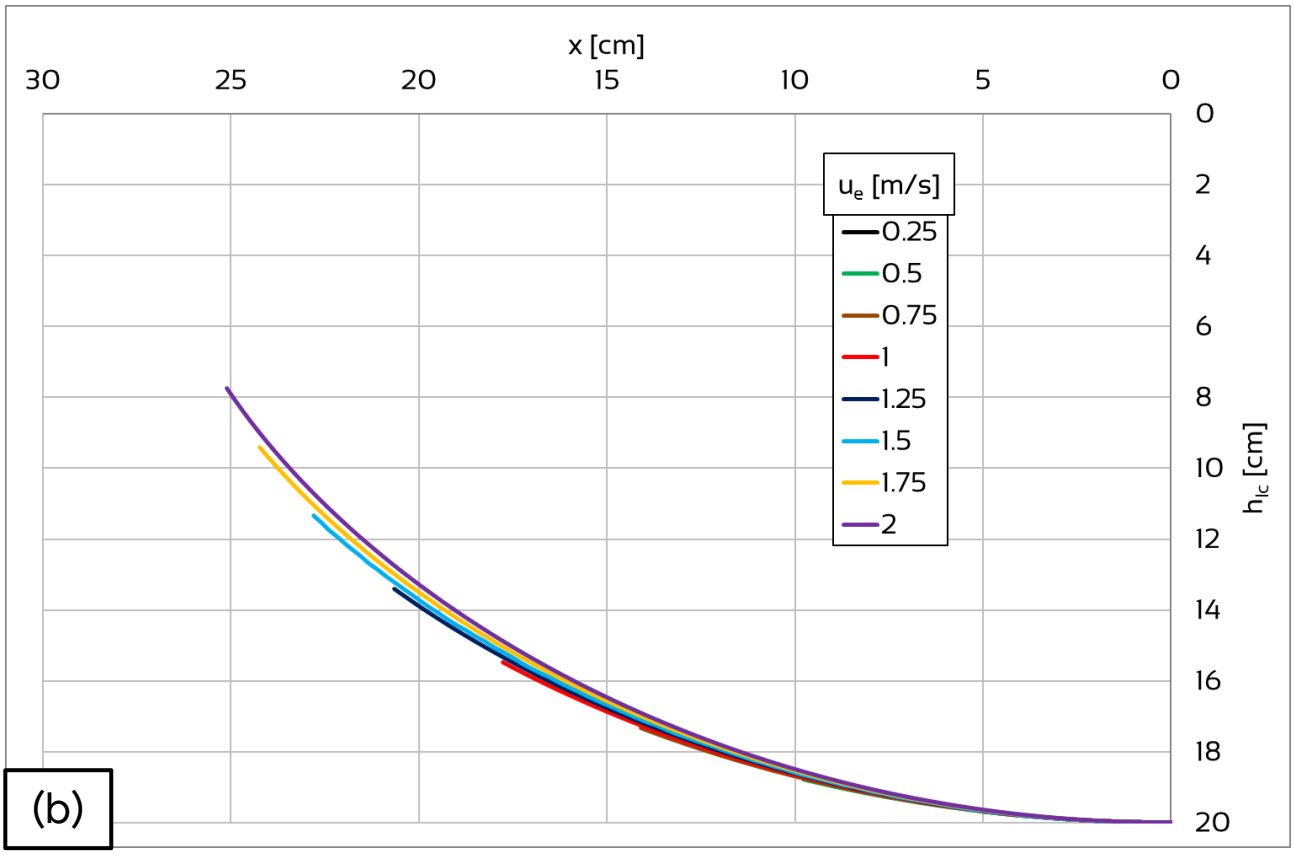
x [cm]
30
25
20
15
10
5
0
0
2
4
6
8
10
12
14
16
18
20
h_{lc} [cm]
u_e [m/s]
0.25
0.5
0.75
1
1.25
1.5
1.75
2
(b)

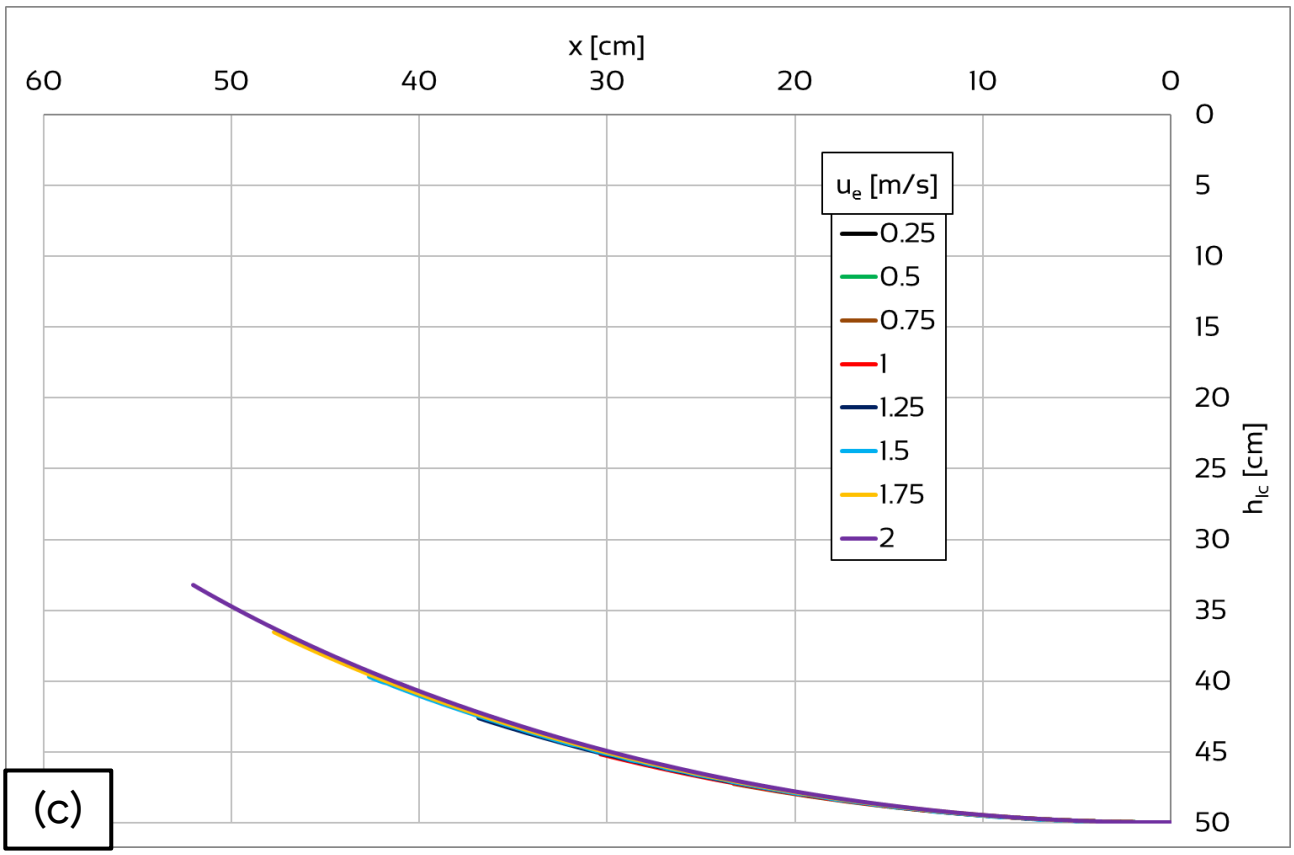

Figure 2.18: orthogonal surfaces for a jet exit distance (a) h_{lc}=10 cm, (b) h_{lc}=20 cm, (c) h_{lc}=50 cm and various jet exit velocity u_e as shown in legends

By reducing the step between the angles to 1°, and repeating the procedure for various jet exit velocities u_e (from 0.25 m/s to 2 m/s with a 0.25 m/s step), it has been found the surfaces shown in Figure 2.18a. It is possible to notice that the surfaces are very near to each other, independently from the exit velocity. Replicating the procedure with greater exit jet distance, the surfaces almost overlap, as shown in Figure 2.18b for an exit distance h_{lc}=20 cm and in Figure 2.18c for h_{lc}=50 cm.

The load cells measure the momentum M of the jet impact. Following the scheme in Figure 2.19, with three load cells disposed as in one of the configurations seen above, the jet velocity at the moment of the impact on the flat plate can be expressed by reversing equation 2.12:

$$u = \frac{M}{\rho \cdot Q} \qquad 2.13$$

Being know the angle β of the flat plate with respect to the horizontal, it's possible to calculate the component u_x and u_y of velocity u by:

$$u_x = u \cdot \sin(\beta) \qquad 2.14$$

$$u_y = u \cdot \cos(\beta) \qquad 2.15$$

and then, assuming constant distance h in every impact point on the flat plate and knowing that the horizontal component u_x is constant, going back to u_e exit velocity by equation 2.18:

$$u_{ex} = u_x \quad 2.16$$

$$u_{ey} = u_y - \sqrt{2gh_{lc}} \quad 2.17$$

$$u_e = \sqrt{{u_{ex}}^2 + {u_{ey}}^2} \quad 2.18$$

where g is the acceleration gravity.

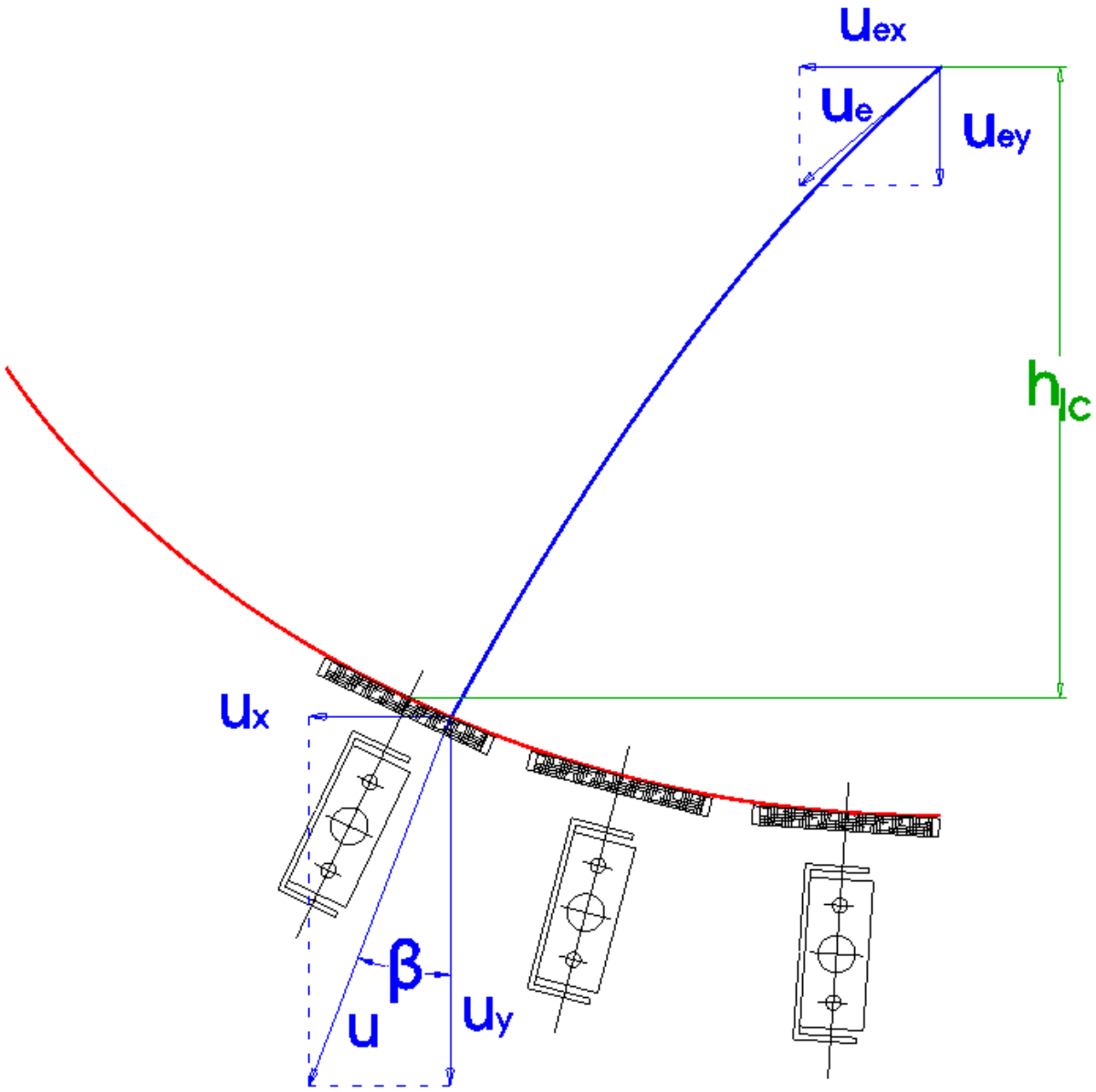

Figure 2.19: example of the impact of a jet on a load cell knowing the distance h_{lc} and the flow rate Q

The chosen distance between jet exit point and the load cells was h_{lc}=20 cm, so that the component of the gravity force $\sqrt{2gh_{lc}}$ in the measured jet momentum was not too great compared to the total momentum u_y; consequently, the flat plates linked to the load cells was arranged to reproduce the surface corresponding to jet exit velocity u_e=2 m/s in Figure 2.18b.

The final set-up is shown in Figure 2.20, while in Figure 2.21 it's possible to see the distance of the load cells with respect to the Tube's exit and the flat plate inclination with respect to horizontal; in both figures, the red line represents the u_e=2 m/s line in Figure 2.18b.

2.3.2.1 RESULTS

In Figure 2.22 two of the final results from tests 871 (a) and 873 (b) were presented: it's possible to see the excellent correspondence between the real exit velocity from the Tube (black line) and the exit velocity estimated through the load cells (the red line represents the moving average of the estimated data, the green line).

Note that under 1 m/s the real and estimated velocities begin to deviate from each other; a possible explanation could be that the component of the gravity force $\sqrt{2gh_{lc}}$ is much higher than the component u_{ey} of the exit velocity (about 50 times and more).

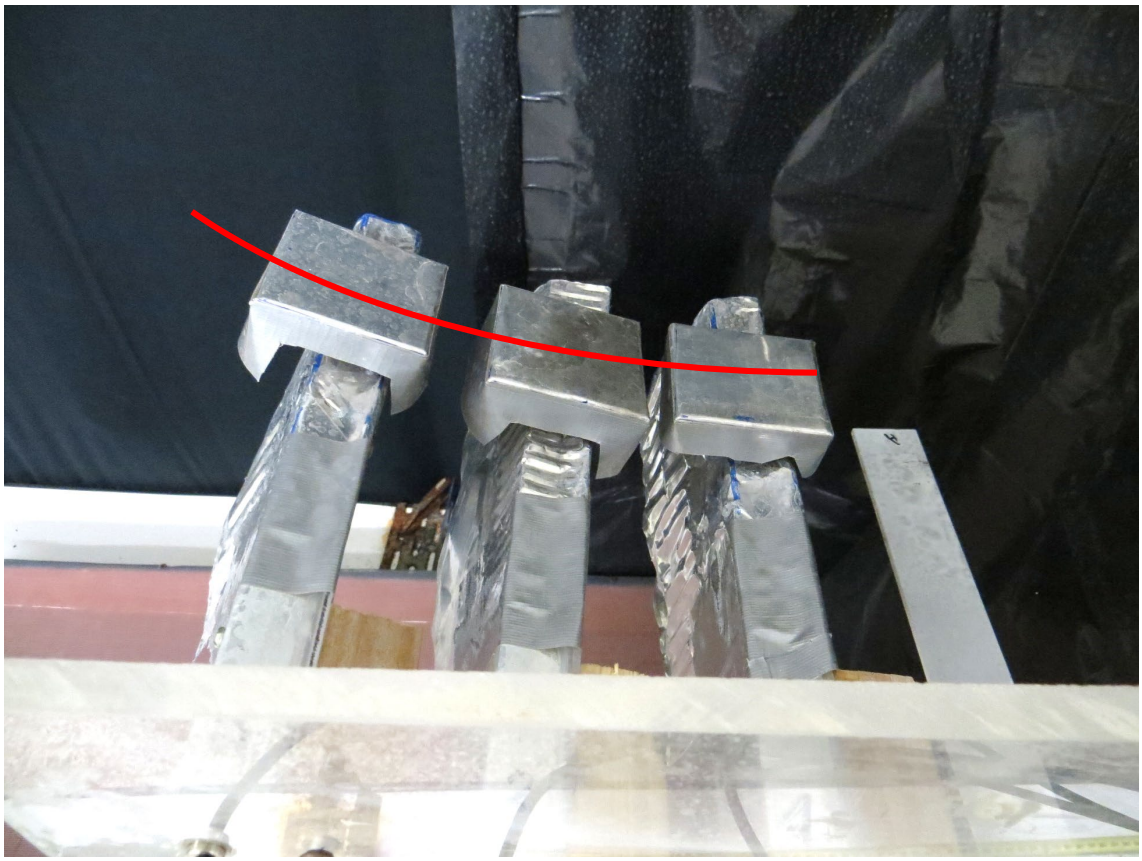

Figure 2.20: disposition of the three load cells and the connected flat plates; the red line represents the u_e=2 m/s line in Figure 2.18b

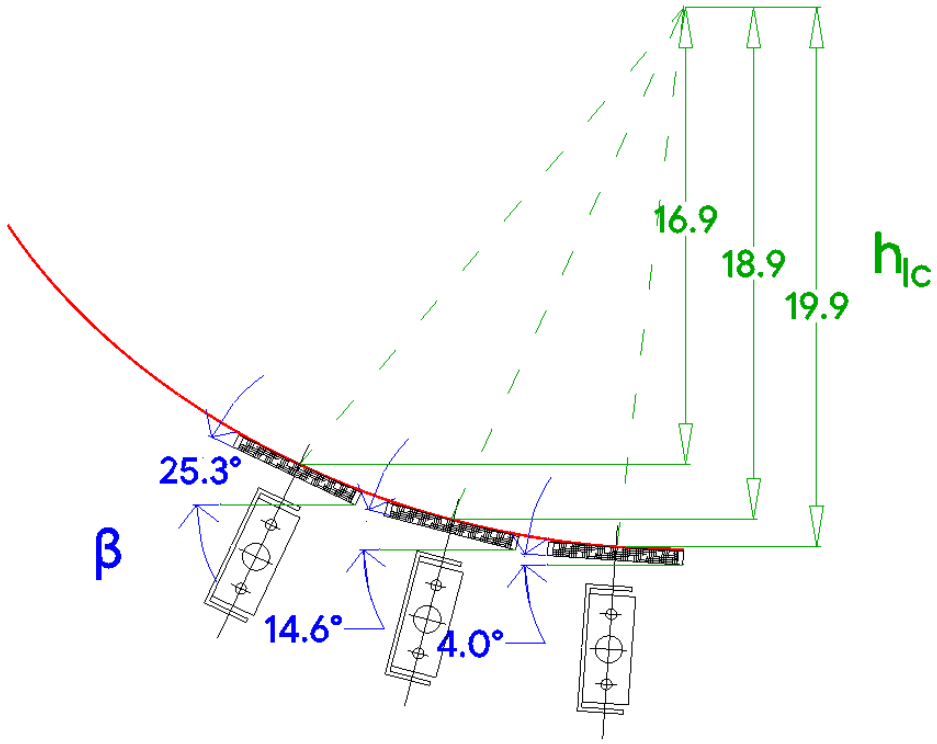

Figure 2.21: position of the load cells with respect to the Tube's exit; the red line represents the u_e=2 m/s line in Figure 2.18b

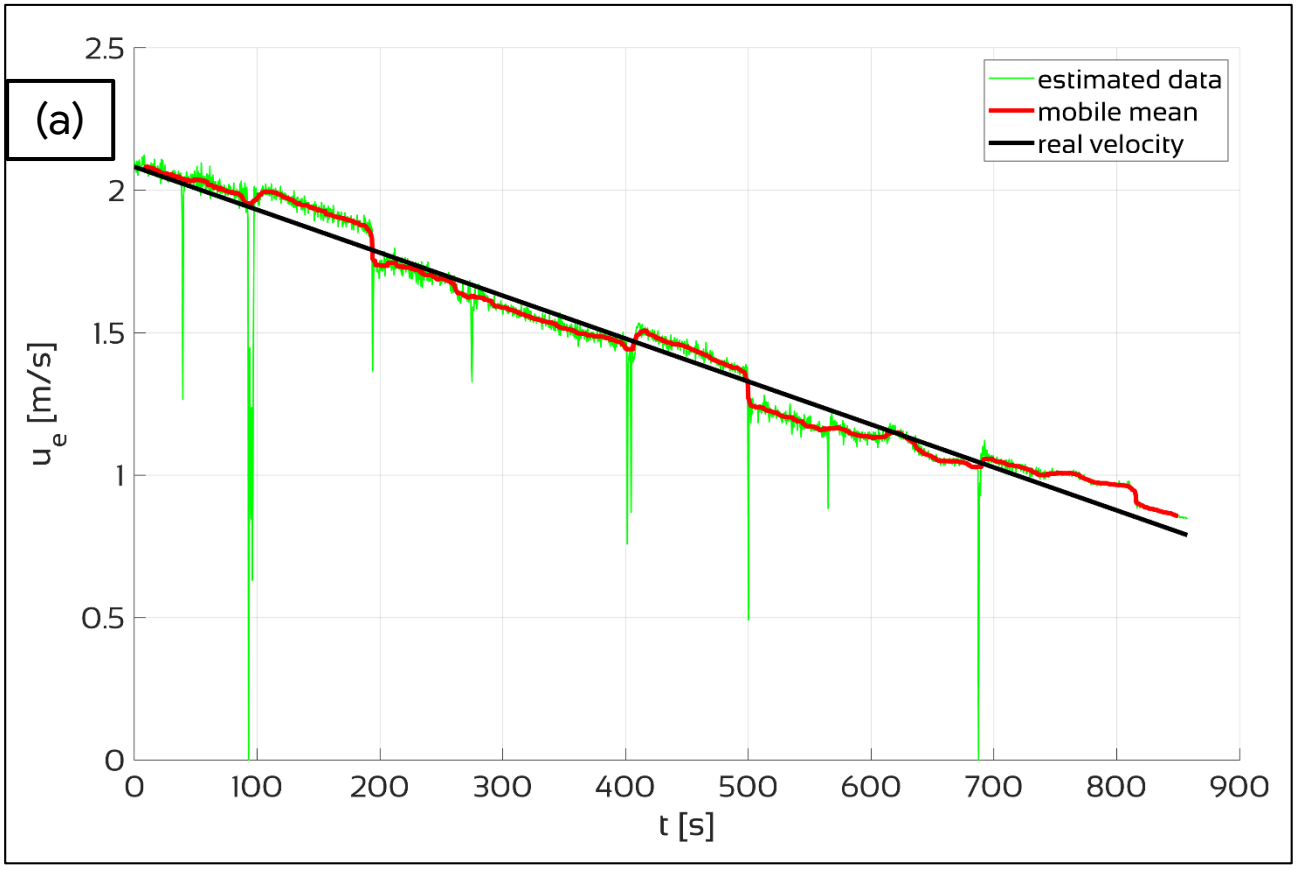

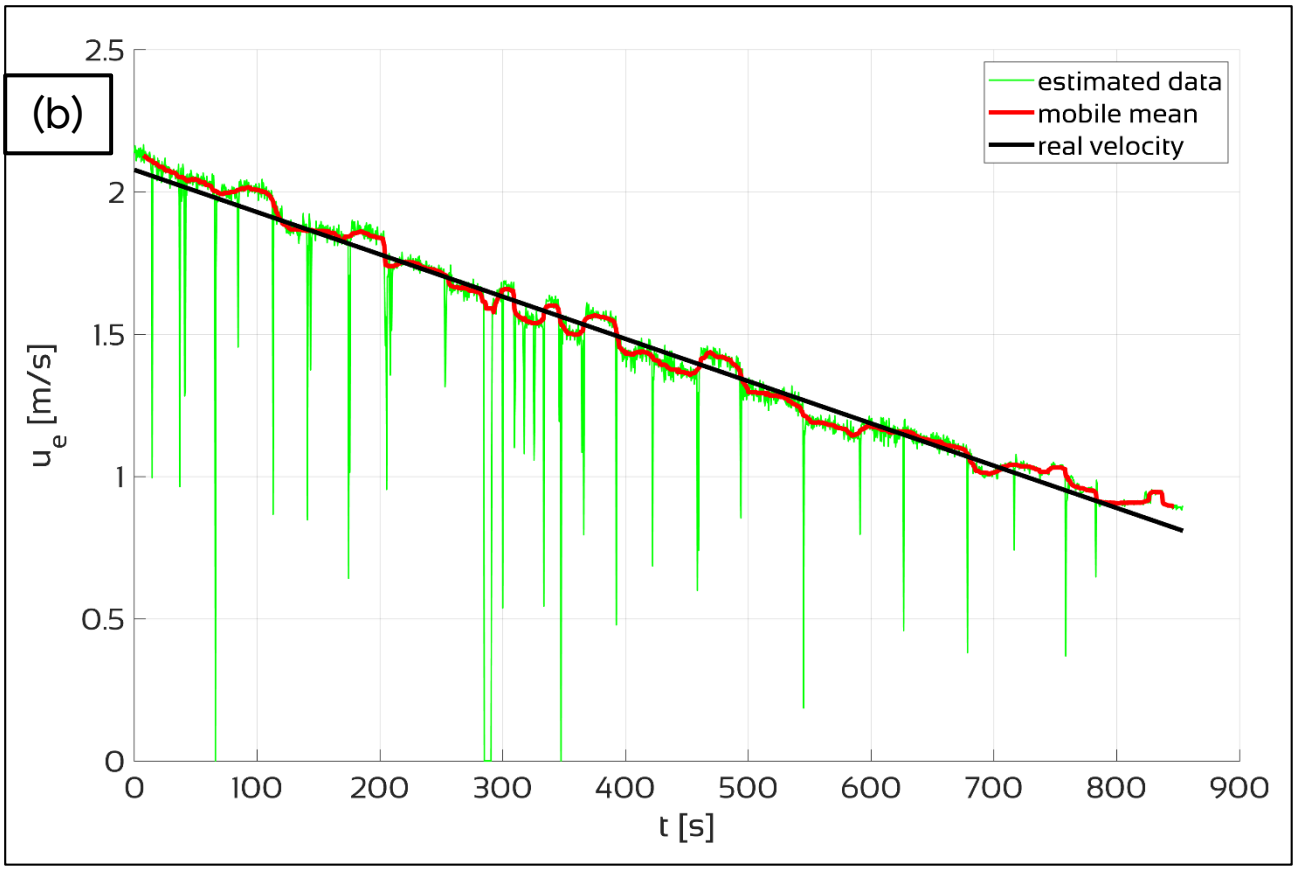

Figure 2.22: results of test 871 (a) and 873 (b) on estimating u_e with load cells: the green line is the estimated data with the load cells, the red line represents the moving average of estimated data, the black line is the real velocity

2.3.3 EXIT VELOCITY ESTIMATION WITH AN OPTICAL ENCODER

Another tested method for measuring the jet exit velocity is by measuring the angular speed impressed by the jet to a reel through an optical encoder, an optical-electronic device used as transducer of angular position and axes speed rotation. In particular, an Eltra EH-EL 63 incremental encoder was used, fixed on a plexiglas panel to protect it from water; the axis of the encoder passed through the panel and a reel was mounted on it (Figure 2.23).

Peripheral velocity u_p of the reel can be written as:

$$u_p = \omega \cdot R \qquad 2.19$$

where R is the reel radius, ω the angular velocity recorded by the optical encoder, with f the rotation frequency. Taking into account the vertical distance h between the Tube exit and the impact on the reel, the jet exit velocity u_e can be written as:

$$u_e = u_p - \sqrt{2 \cdot g \cdot h} \qquad 2.20$$

Unfortunately, the results were not satisfactory. Notwithstanding several deep investigations, the reasons of the unsatisfactory performance could not be identified; in Figure 2.24 it is possible to see an example of output speed from the tube estimated with the encoder

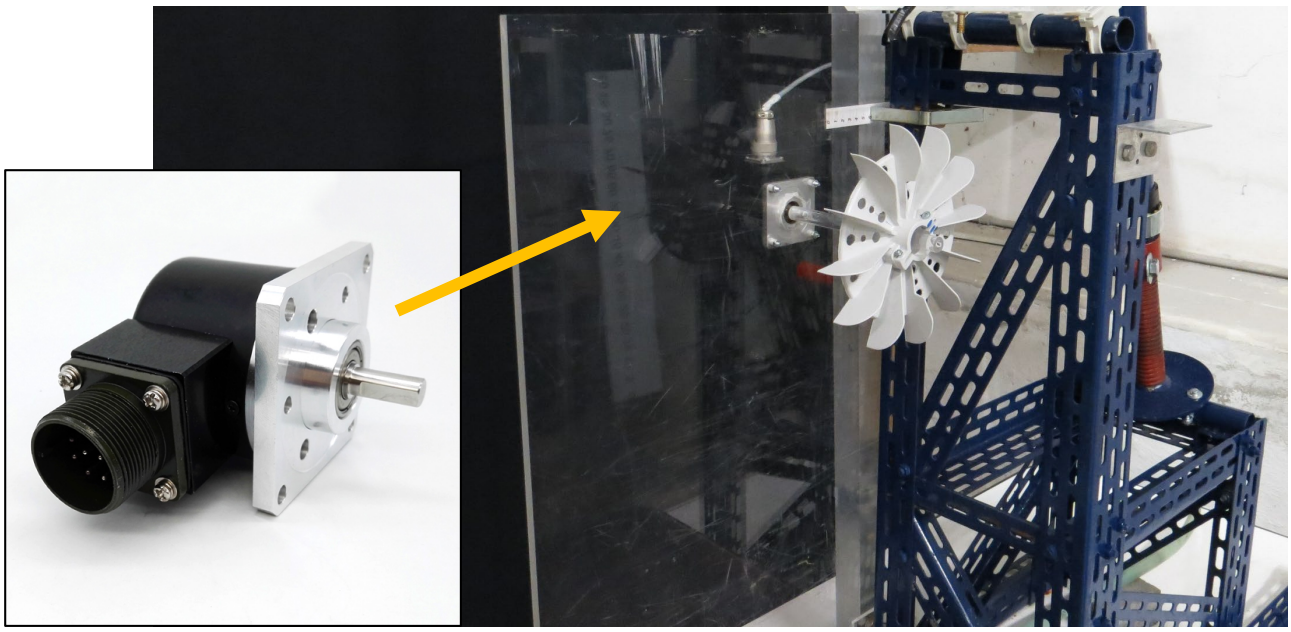

Figure 2.23: Eltra optical encoder (left), mounted on a plexiglas panel with a reel on the axes (right)

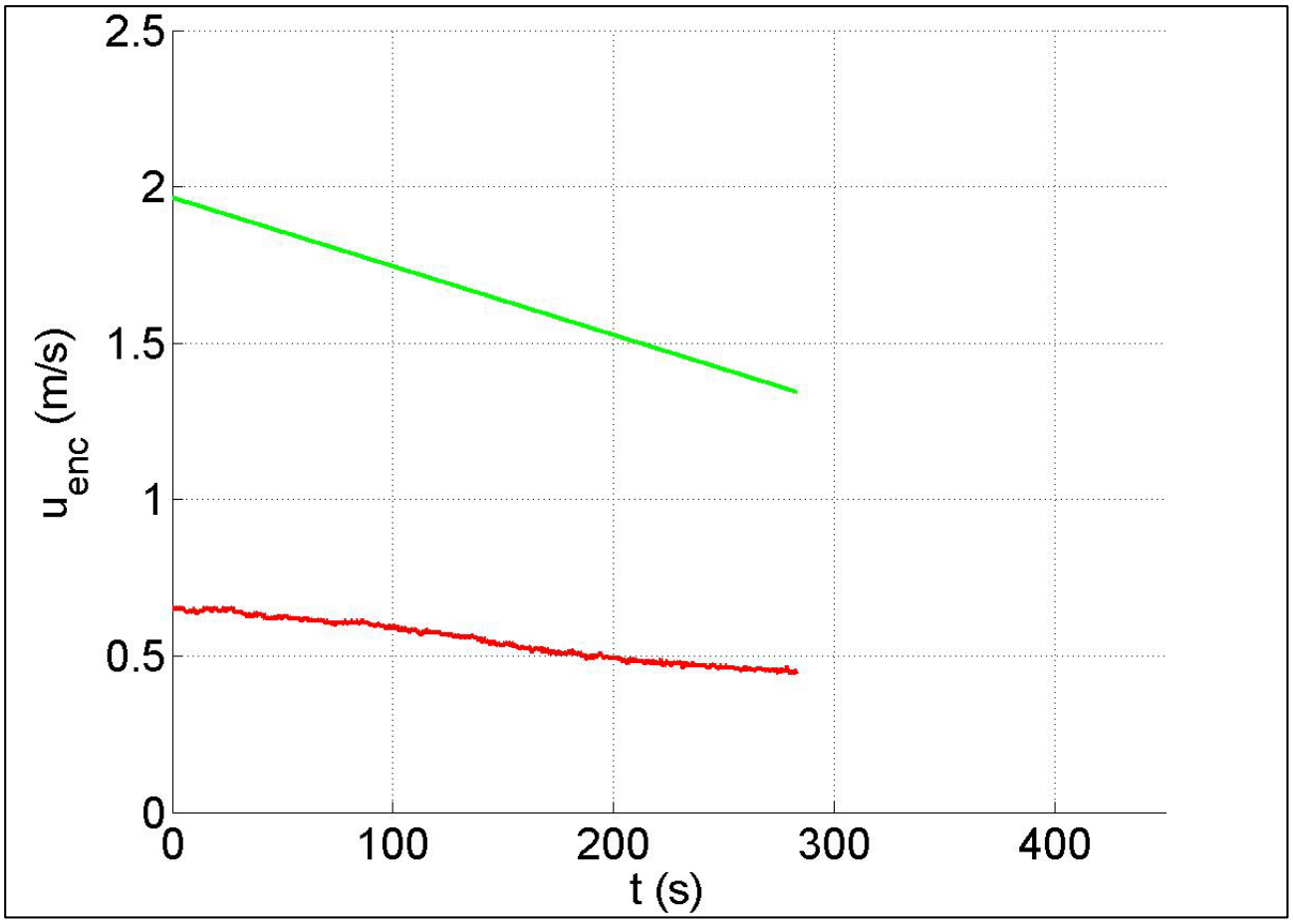

Figure 2.24: example of jet exit velocity estimation with the optical encoder

In addition, there is an American patent of 1981, "Device for measuring the velocity of a urine discharge", a patent of an instrument that measures the velocity of the urine jet with a system similar to the one tested here.

2.3.4 EXIT VELOCITY THROUGH IMAGE ANALYSIS

2.3.4.1 NUMERICAL SCHEME

The third tested estimation system to evaluate jet exit velocity was by detecting the jet parabola through image acquisition, considering the fact that the parabola trajectory of a jet is uniquely associated to its velocity.

The trajectory of a liquid coming out of a tube is parabolic (Figure 2.25), described by the equations:

$$x(t) = u_e \cdot \cos\theta_e \cdot t \quad (2.21)$$

$$y(t) = u_e \cdot \sin\theta_e \cdot t + \frac{1}{2} \cdot g \cdot t^2 \quad (2.22)$$

where u_e is the jet exit velocity, θ_e is the jet outside angle to the horizontal, g the gravity acceleration and t the time. The velocity components are given by:

$$u_x = u_e \cdot \cos\theta_e \quad (2.23)$$

$$u_y = u_e \cdot \sin\theta_e + \sqrt{2 \cdot g \cdot h} \quad (2.24)$$

The trajectory is obtained by eliminating the time variable, i.e. by specifying the parameter t from 2.21:

$$t = \frac{x}{u_e \cdot \cos\theta_e} \quad (2.25)$$

and then, by replacing 2.25 in 2.22, it can be obtained, in the classic parabola form $y=ax^2+bx+c$ (Figure 2.26):

$$y = \frac{g}{2 \cdot {u_e}^2 \cdot \cos^2\theta_e} \cdot x^2 + \tan\theta_e \cdot x \quad (2.26)$$

Knowing the parabola parameters a and b, it is then possible to evaluate the jet exit velocity u_e by:

$$\theta_e = \tan^{-1} b \quad (2.27)$$

$$u_e = \sqrt{\frac{g}{2 \cdot a \cdot \cos^2\theta_e}} \quad (2.28)$$

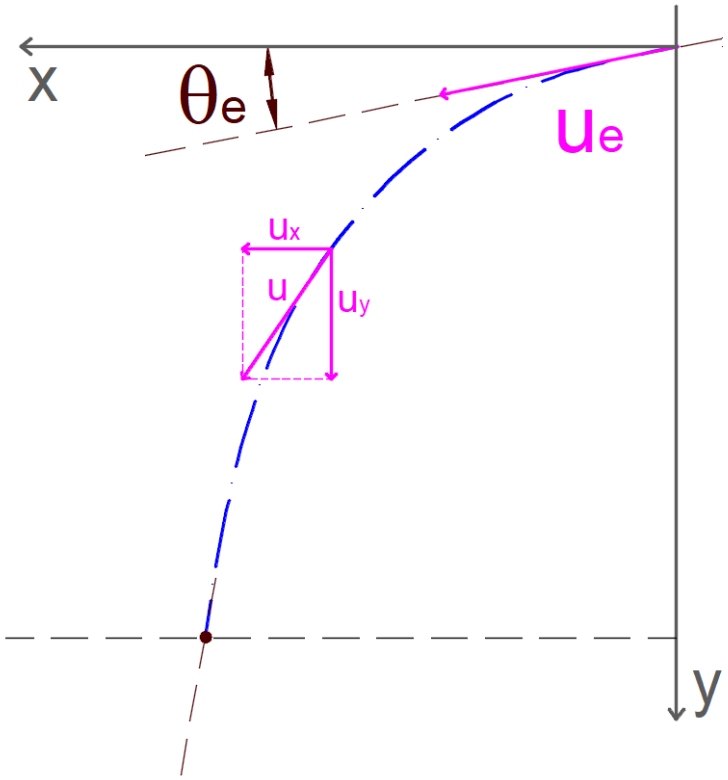

Figure 2.25: parabolic trajectory of a jet outside a tube

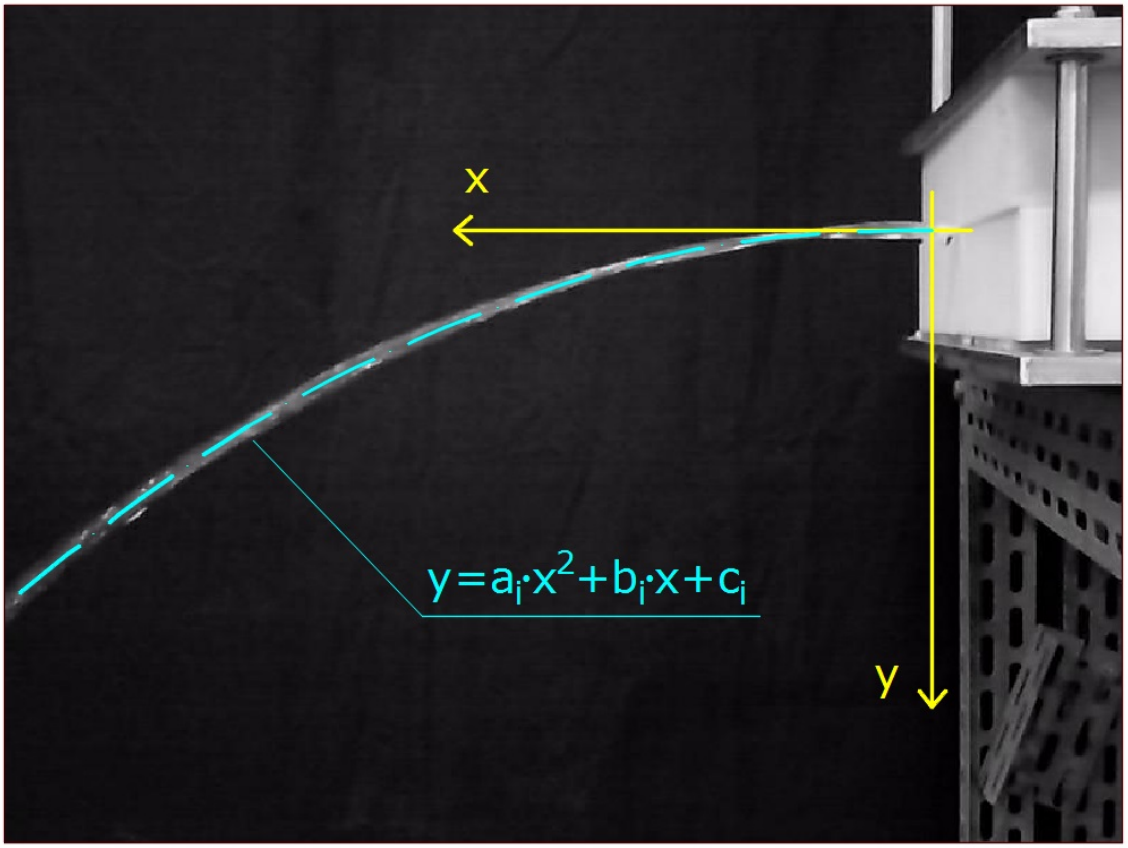

Figure 2.26: the jet outside the Tube has a parabolic trajectory

2.3.4.2 IMAGE ACQUISITION AND PROCESSING SYSTEM

The detection of the parabola of the jet is obtained through an image acquisition system with a digital camera and a subsequent image processing.

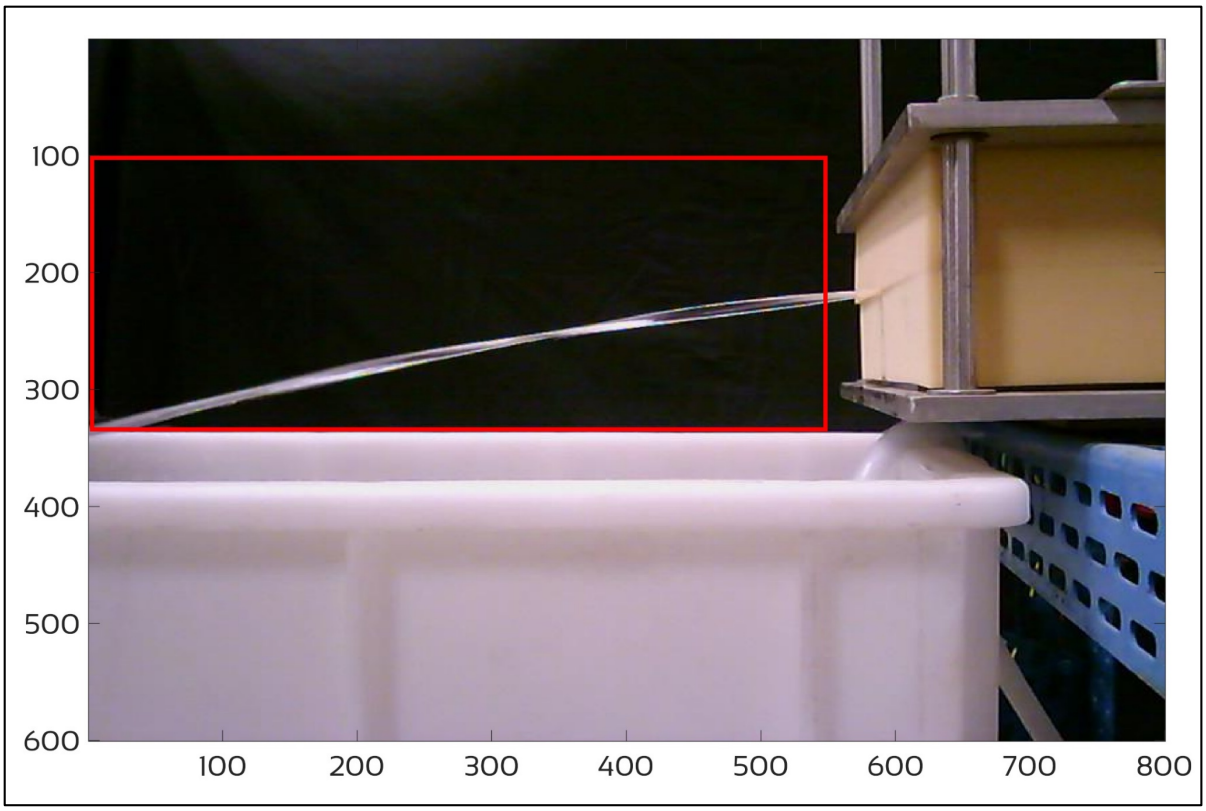

Figure 2.27: example of an image acquisition during a test: the red box is the jet area

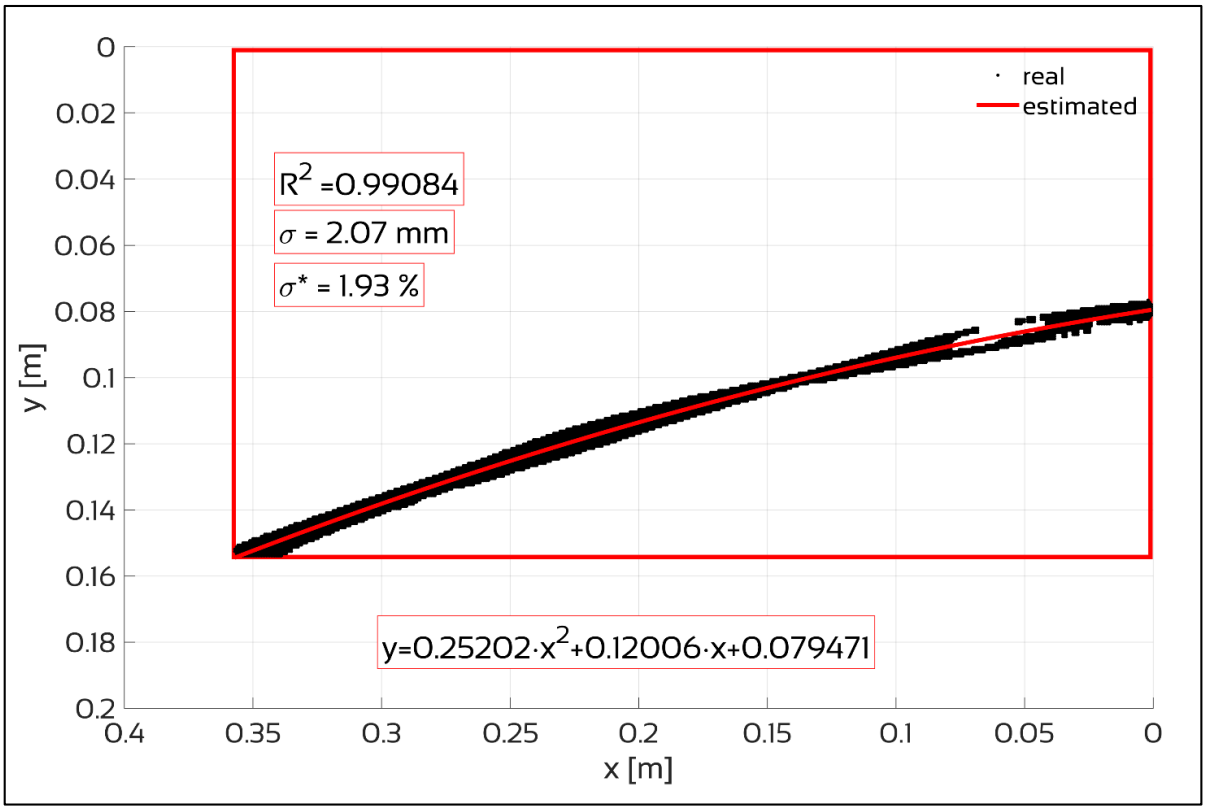

Figure 2.28: highlight of the jet stream (black dots) and interpolation as a parabola (red line): the relative standard deviation is 1.9%.

A black background has been placed behind the jet to highlight it; subsequently, a software specifically written in Matlab isolates the jet area (red box in Figure 2.27), converts the pixel in m with a previously estimated pixel/m conversion factor, and interpolates the points like a parabola (Figure 2.28); in this way the parameters a and b were obtained, and then the angle and the exit velocity from the Tube were estimated.

2.3.4.3 ANALYSIS OF THE RESULTS

Various laboratory tests have been performed on the Model without the Tube, similar to the one used in the tests to estimate H_c (Figure 2.14 in section 2.2.4), to easily calculate the output speed, therefore given by $u_{e,measured}=Q/\Omega_c$, where Ω_c is the internal area of the metal connector. The tests were performed by varying the jet exit angle with respect to the horizontal θ_e and subsequently comparing $u_{e,measured}$ with the velocity estimated by the image processing method $u_{e,estimated}$.

In Figure 2.29 it is shown the correlation between the measured ($u_{e,measured}$) and the estimated data ($u_{e,estimated}$). The yellow part represents the area of the graph where $u_{e,measured}>u_{e,estimated}$, the blue part represents the area where $u_{e,measured}<u_{e,estimated}$, while the perfect agreement between the two data is the dashed black line.

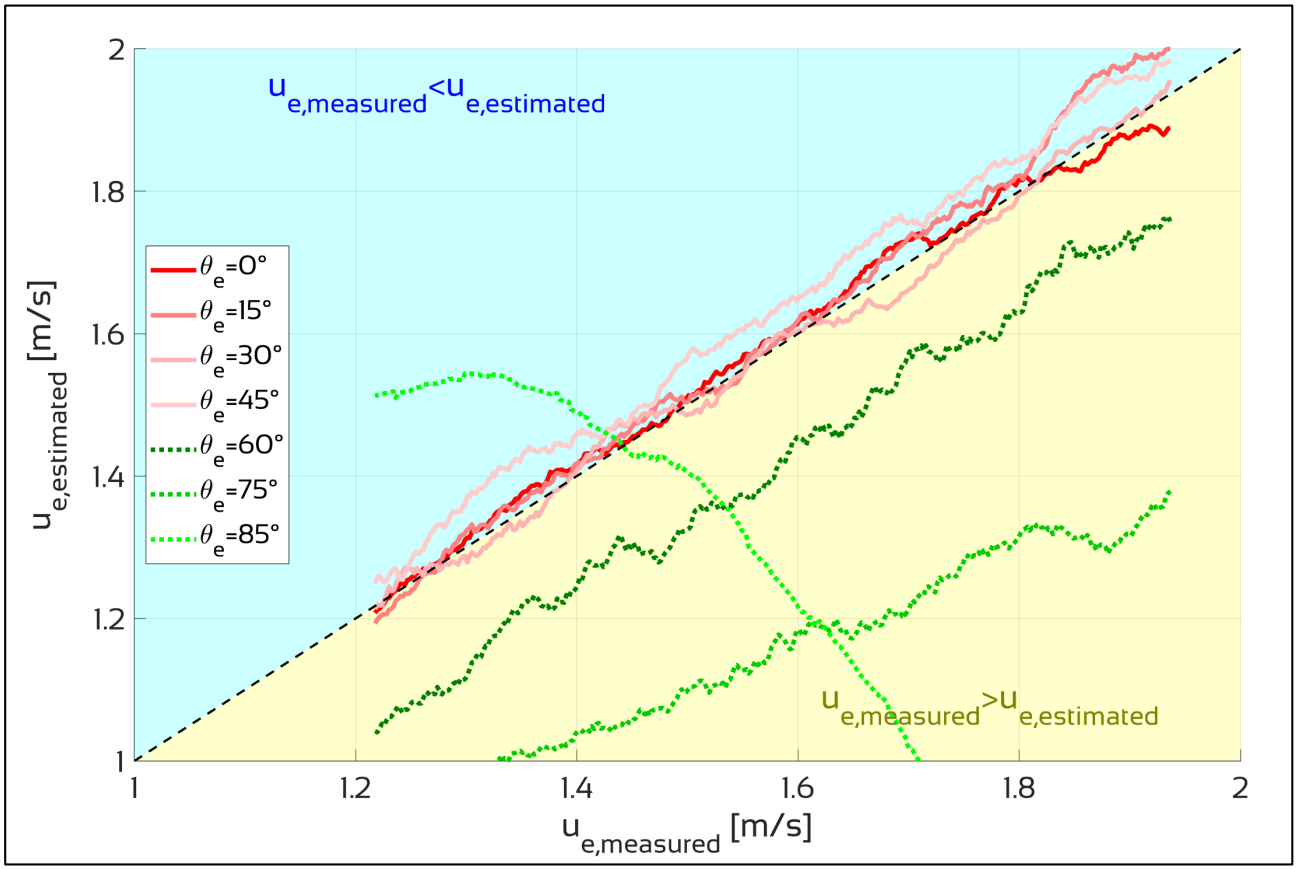

Figure 2.29: results of the tests for jet exit velocity estimation with image processing varying the jet exit angle

It can be seen the excellent accordance between the measured data and the corresponding estimated data for Θ_e lower than 45°, that are represented as solid shades-of-red lines; as the angle increase, the estimation errors are instead particularly evident (dotted shades-of-green lines).

Given the fact that the Tube is placed horizontally, the simplicity of the system and the accuracy of the results, this method has been selected for the measurement of the jet exit velocity in all subsequent Laboratory tests on the Model. Hereafter, ***u_e has been measured by using this method***, unless otherwise stated.

2.3.5 Physical properties of the Tube

The tests described here are aimed to measure the physical characteristics of the Tube, that are its thickness, its internal diameter and its elasticity, by using high-resolution photographic images.

2.3.5.1 Evaluation of "undisturbed" Tube thickness s_u and internal diameter D_u

First, three geometric properties of the Tube were analyzed: the "undisturbed" thickness s_u, internal diameter D_u and external diameter D_{ext}; they are called "undisturbed" because it's when the pressure inside the Tube is the same as the outside pressure $P=P_{ext}$.

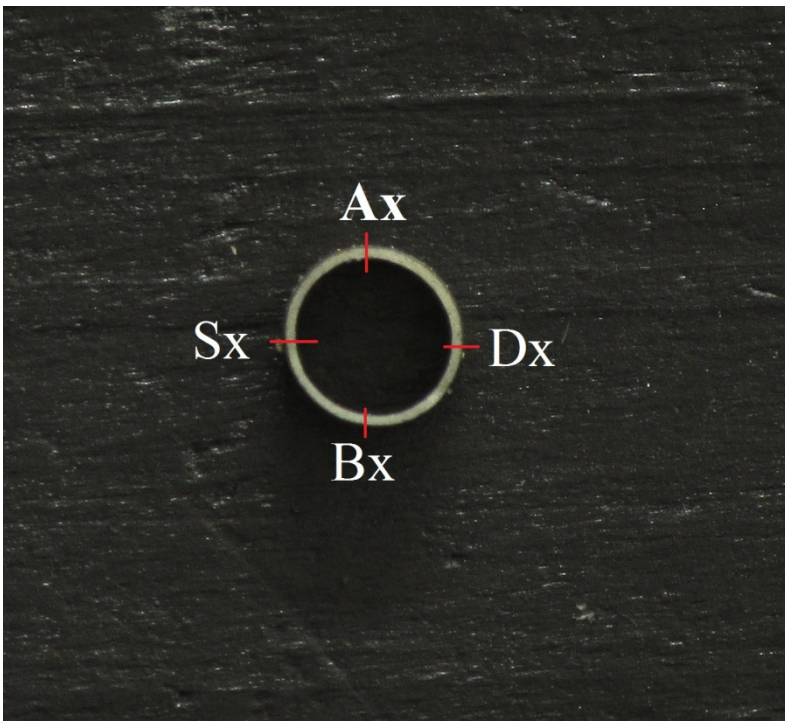

Figure 2.30: section of the Tube to evaluate thickness and external diameter

The Tube was cut in a section orthogonal to the axis of the pipeline, put under a black background, and a high-resolution picture was taken (Figure 2.30). The thickness was assessed in the four sections Ax, Bx, Sx and Dx, indicated in the figure, counting the bright pixels and then dividing these values by a previously estimated pixel/mm conversion factor (Table 2.3 and Table 2.4).

section	[pixel]	[mm]
Ax	14	0.303
Bx	14	0.303
Sx	18	0.389
Dx	15	0.324
average		0.33

Table 2.3: values of Tube's thickness

section	[pixel]	[mm]
Ax-Bx	299	6.46
Sx-Dx	303	6.56
average		6.51

Table 2.4: values of Tube's external diameter

The value of s_u=0.33 mm was obtained averaging the four sections thickness, as the value of the external diameter D_{ext}=6.5 mm averaging the two sections diameters; the internal diameter can be easily determined by:

$$D_u = D_{ext} - 2 \cdot s_u = 5.9 \text{ mm} \qquad 2.29$$

2.3.5.2 Evaluation of Tube's elasticity E

The methodology used for the evaluation of deformation is based on high-resolution photographic data obtained by means of two cameras arranged to acquire horizontal and vertical diameters in various sections of the elastic tube. The knowledge of the diameters on the two orthogonal planes allows us, by referring to the geometric model of the ellipse, to evaluate the variation of the cross-area section inside the Tube.

In these tests, the Tube was positioned on a flat support, divided into sectors and colored black to allow the highlighting of the Tube with respect to the background and to be able to close it at the downstream end (Figure 2.31).

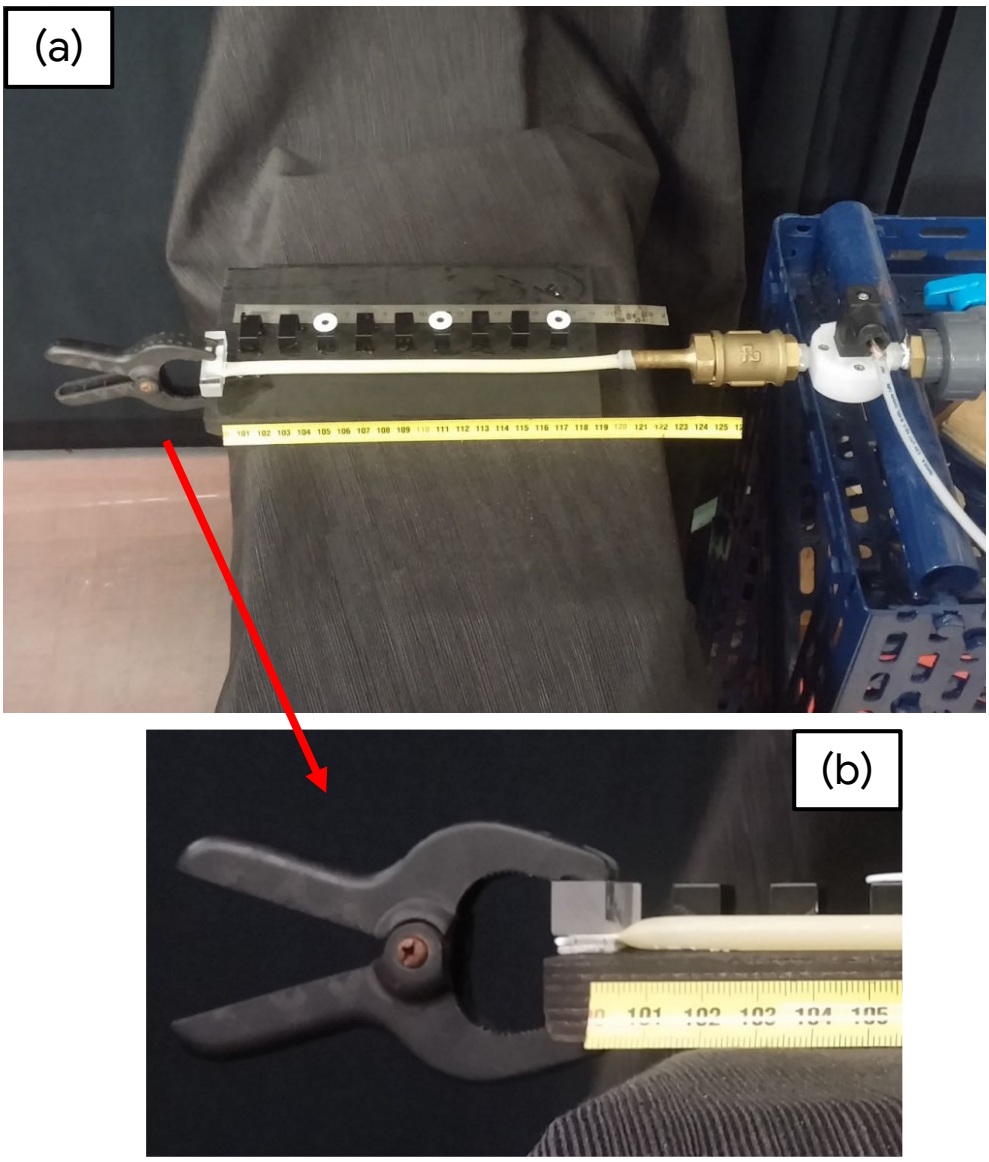

Figure 2.31: (a) the Tube on a flat support; (b) claw used to close the Tube downstream

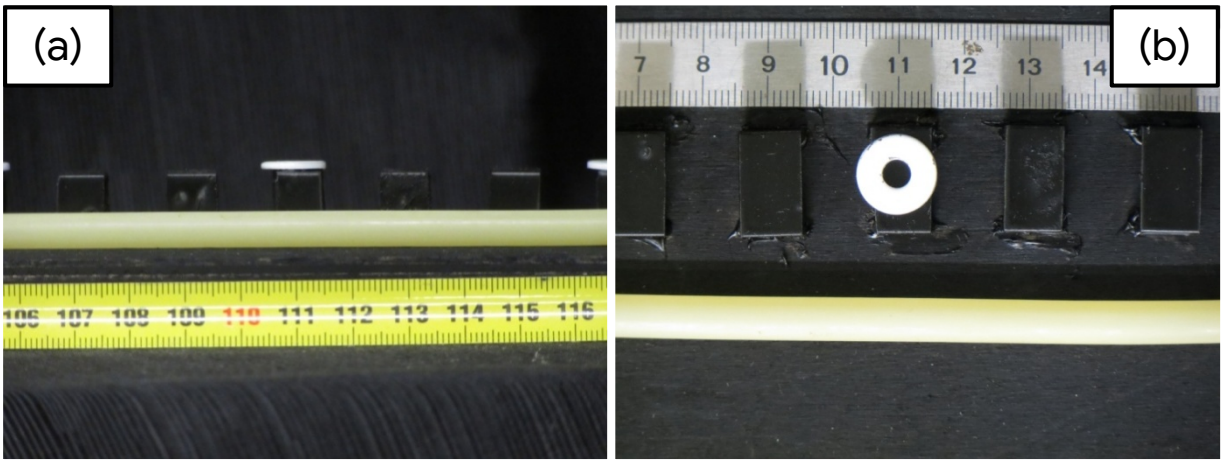

Figure 2.32: pictures of the Tube taken on the vertical (a) and the horizontal (b) plane

The tank was therefore filled up to predetermined levels, in order to establish a static head due to the water load inside the Tube; the level was varied between 0.2 and 1.6 m with 0.2 m steps. For each level, two pictures were taken, one on the horizontal plane and one on the vertical plane (Figure 2.32) in many sections of the Tube. From the images, the pixel lengths of the two external diameters were obtained and subsequently divided by the previously estimated pixel/mm conversion factor. The diameters obtained along the two dimensions were averaged and an almost linear correlation with the total head inside the Tube (equal to the water level inside the tank H) was obtained, as shown in Figure 2.33.

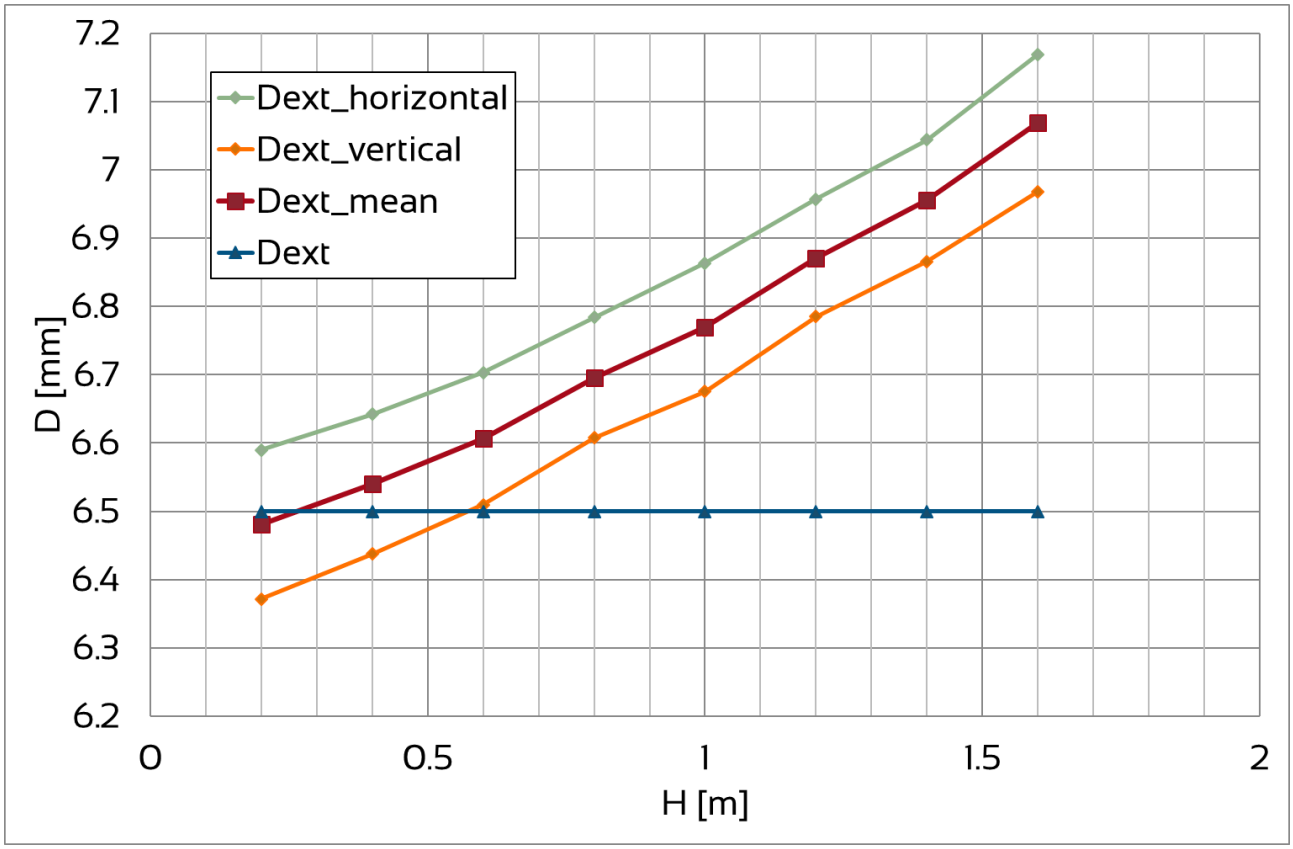

Figure 2.33: correlation between water level inside the tank H and the Tube's average external diameter D

Now, assuming normal and uniform tensions on the internal walls of the Tube and a Tube thickness small with respect to the Tube radius, an estimation of the elasticity of the material (latex) was made using the known Hooke formula:

$$E = \frac{\sigma}{\varepsilon_d} \qquad 2.30$$

where E is the Young elasticity modulus of the Tube, σ is the tension and ε_d the relative deformation, defined by:

$$\sigma = \frac{\Delta P \cdot R_u}{s_u} \qquad 2.31$$

$$\varepsilon_d = \frac{\Delta R}{R_u} \qquad 2.32$$

in which $\Delta P = P - P_u$ is the relative variation of pressure (P_u=0 Pa the pressure for the "undisturbed" Tube), $\Delta R = R - R_u$ the relative variation of radius, and s_u and R_u are the "undisturbed" Tube's thickness and radius, respectively.

Figure 2.34 shows the trend of the elasticity modulus E as a function of the total head inside the tank H (and also inside the Tube): the average value of $E=1.7 \cdot 10^6$ Pa has been assumed.

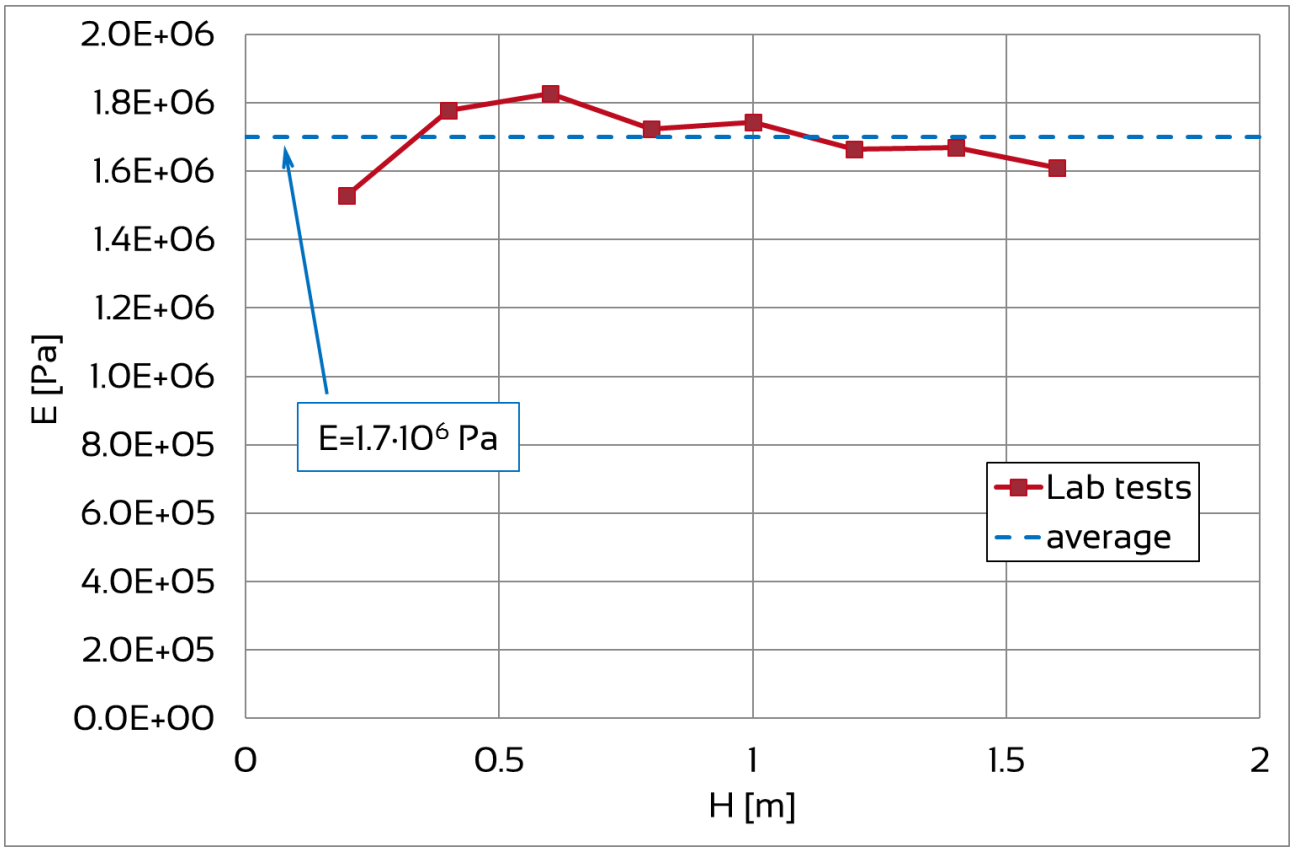

Figure 2.34: variation of the elasticity modulus E of the Tube with respect of the static water level inside the tank H

2.3.5.3 Comparison with urethra's physical properties

The average "undisturbed" internal diameter of the male urethra is about 6 mm, slightly more than the female urethra (about 7 mm); the elasticity is higher, in the order of 10^5 Pa. However, this has been considered irrelevant, since the internal area during the tests has always been lower than the "undisturbed" area, and therefore the expansion elasticity of the Tube played a negligible role compared to the load exerted on the Tube by the external pressure on the foam (explained in the next section).

2.3.6 External pressure on the Tube

The urethra, both male and female, is placed between other various organs (Figure 1.2) which exert an elastic compression on it, variable from point to point (section 1.1.2): in the resting phase, is completely collapsed, while during urination it widens as a function of the pressure in the bladder. The pressure generated by the internal organs is not uniform, on average it is between 10 and 20 cm H_2O (there is a specific invasive test that measures it using a catheter, Brown & Wickham, 1969, Griffiths, 1971).

So, it has been considered to reproduce this compression in the Model by positioning the Tube between two foam blocks of size 30x20x5 cm^3 (Figure 2.5), and placing a weight on the upper one. In this way, the pressure is generated "at rest", that is when no water passes through the Tube. During the emptying of the tank, the Tube expands and the pressure generated by the foam certainly increases (depending on the cross-sectional area), which is exactly what happens in the LUT.

Tests with different weights on the foam were carried out to verify the correct functioning of the system: the tests were made by imposing different values of containment pressure on the Tube, obtained by applying a load F of 58.8, 98.1, 147.1 or 196.1 N (that correspond to 6, 10, 15 or 20 kg, respectively) on the upper surface of the foam, uniformly distributed.

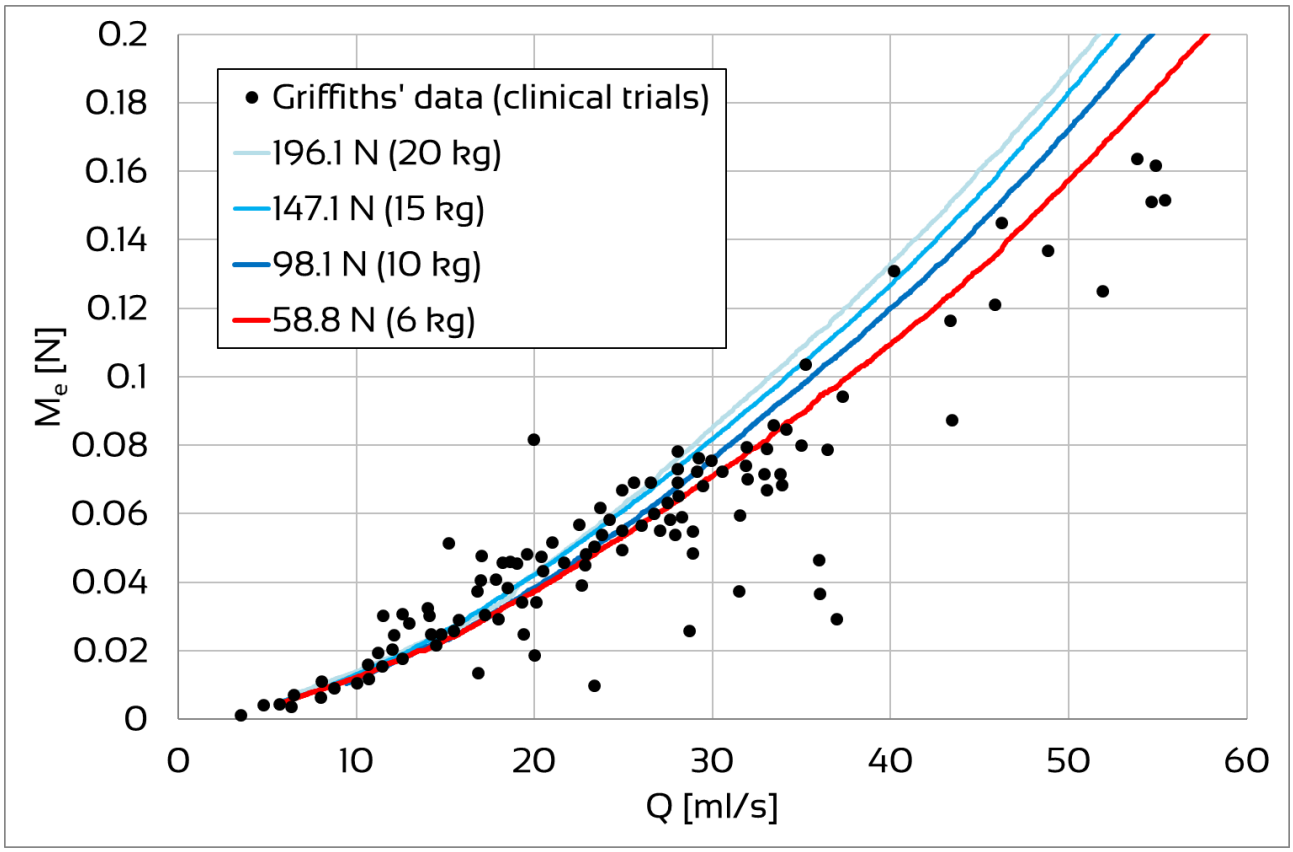

Figure 2.35: comparison between the jet exit momentum measured in the tests with the Tube subjected to different loads (represented with the colored lines) and Griffiths' data from clinical trials (black dots)

Figure 2.35 shows the flow of the exit momentum from the Tube M_e as a function of the flow rate Q for the different loads F:

$$M_e = \rho \cdot Q \cdot u_e \qquad 2.33$$

where ρ is the water density and u_e the jet exit velocity. The four colored lines represent the dots series of the experimental tests during the system emptying with the foam subjected to four different load compression, while the black dots are the clinical data from Griffiths (1980), obtained from measurements of the momentum flow on healthy males at the peak of urinary flow (Q_{peak}) and the corresponding exit velocity ($u_{e[Qpeak]}$):

$$M_e = \rho \cdot Q_{peak} \cdot u_{e[Qpeak]} \qquad 2.34$$

Note the good agreement between the red experimental curve (which corresponds to a load F=58.8 N, or 6 kg) and the clinical data taken from Griffiths (1980).

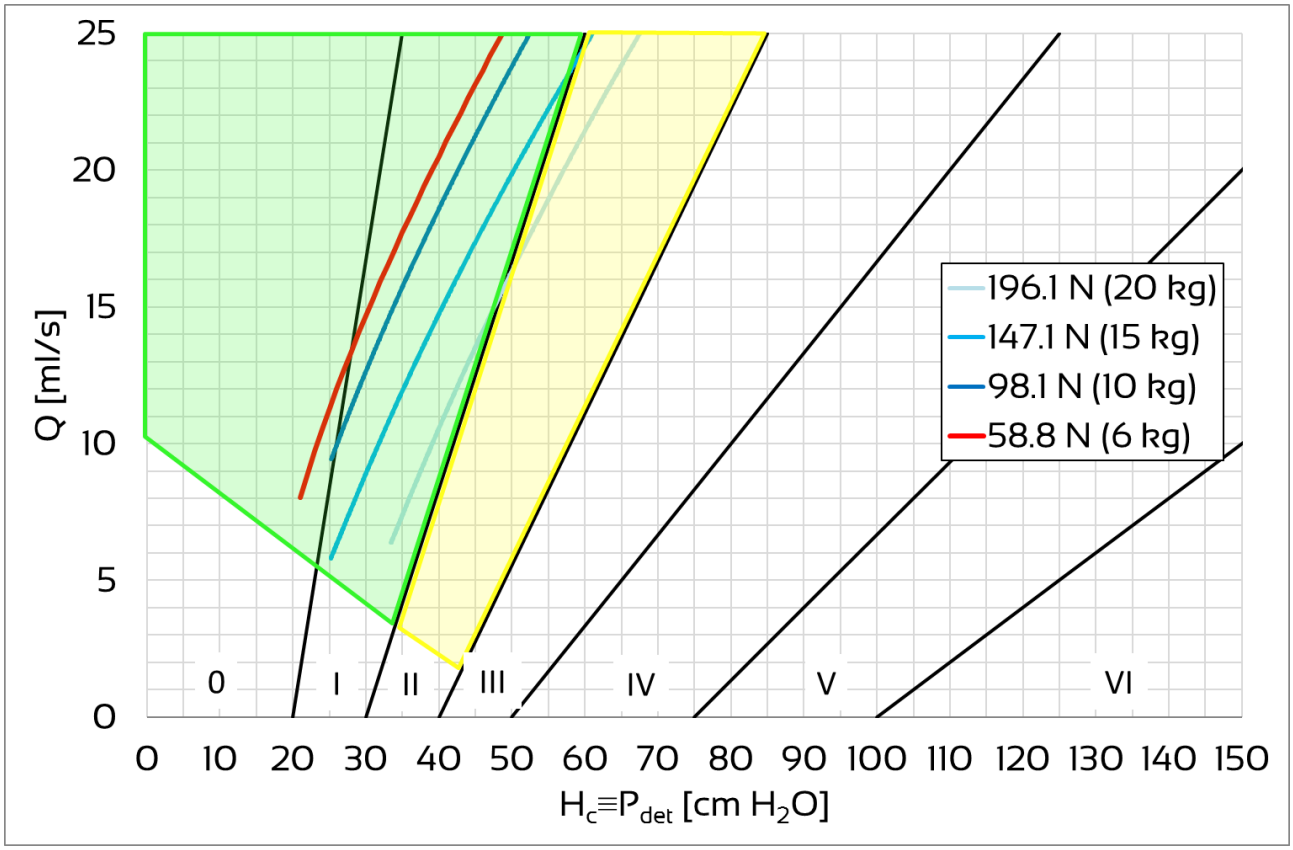

Figure 2.36: comparison between tests results of different external pressures on the Tube plotted on Schäfer's diagram

The results in Figure 2.36 show the flow rate Q as a function of the detrusorial pressure in the bladder P_{det} (that here correspond to the total head at the Tube's entrance H_c) on the Schäfer's diagram (section 1.4.3); the color scheme of the lines is the same as in the previous figure. Tests

have shown that as the load F, and therefore the containment pressure, increases, the pressure required P_{ves} increases, in order to have the same flow; in other words, with the same P_{ves}, the flow rate Q decreases with increasing F. From the comparison with the Schäfer lines, it can be seen how the experimental curves remain within the area of the diagram that represents the flow in healthy subjects (the green area).

From the results of the tests, an applied load F=6 kg corresponding to a containment pressure of 10 cm H_2O (i.e. 981 Pa) seems to be optimal to represent the real pressure induced on the urethra by the interaction with the muscle tissues and adjacent organs.

2.4 The Innovative Instrumentation

The main goal of this project is therefore the feasibility study of a new equipment (hereafter, ***Innovative Instrumentation***) that allows the evaluation of the functionality of the LUT in a totally non-invasive way, that is in which no part of the machine comes in contact with the human body. This Innovative Instrumentation, implemented in the urology departments and in private and public structures, could allow the progressive replacement of current invasive technologies for cystomanometric examination and P/F Study with non-invasive technologies, thus reducing discomfort for patients and eliminating any complications due to the urethral catheter necessary for a correct execution of the investigations. Furthermore, the operating costs (in terms of materials and human resources) of healthcare facilities are considerably reduced, which for each urological reality annually exceed the costs of the instruments themselves. Thanks to the reduced costs and the non-invasiveness, the proposed Innovative Instrumentation could be used to large-scale prevention actions, also with the possibility of mass screening.

The idea behind it is to build an instrument that functions in a very simple way, like a classic wall urinal for men, also considering the fact that the chosen velocity measurement system does not allow the measurement of the velocity of vertical jets, like those of women (see section 2.3.4). This choice is certainly a limitation of the present project, however it is to be considered the fact that obstruction problems are much more common in men, while in women the most frequent problem is the opposite, that is urinary losses.

This Innovative Instrumentation, which would represent a significant step forward in the prevention and control of citizens' health, could be installed in any public and private structure like a common toilet, and can give a first indication of the functional conditions of the LUT through simple urination.

The description of the Innovative Instrumentation is presented in section 5.

3 EXTENSIVE LABORATORY TESTS

The extensive tests on the Model concern the study of the physical and mechanical characteristics of the innovative methodology and the calibration of the instruments running on the Innovative Instrumentation. The Model is the same as described in section 2.2, as well as:

- the instrumentation and the hypotheses (section 2.2.1);
- the compression on the Tube defined in section 2.3.6;
- the evaluation of the water level inside the tank H_0 (section 2.2.2), of the flow rate Q (section 2.2.3) and of the total head at the Tube entrance H_c (section 2.2.4);
- the estimation of the jet exit velocity u_e through image acquisition and processing system (section 2.3.4).

In particular, the tests have been divided into three main types; each of them is associated with a particular physical condition of the LUT:

- ***"Physiological flow condition" tests (Physiological-tests)***, used to calibrate the Innovative Instrumentation and to correlate the jet exit velocity u_e with the detrusorial pressure P_{det} on healthy people;
- ***"Pathological flow condition" tests (Pathological-tests)***, to correlate the flow output characteristics in people with urethral obstructions;
- ***"Diagnostic flow condition" tests***, characterized by the presence of a catheter inside the Tube. These tests are subdivided in: ***Diagnostic-tests***, to evaluate the effects of the catheter on urethral flow; ***FV-tests***, to measure flow variables inside the Tube.

Now let's see in detail the three types and the results obtained, along with the additional instruments used in each test type.

3.1 "PHYSIOLOGICAL FLOW CONDITION" TESTS

Physiological-tests are a sort of summary of the previous experiences to set and calibrate the model: they consist in recording the various physical parameters of the jet at the Tube's exit while emptying the tank, considering the following hypothesis:

- the fluid used is water at ambient temperature (T=20÷25 °C, ρ=1000 kg/m^3), incompressible fluid, with dynamic viscosity μ=10^{-3} Pa·s and kinematic viscosity v=10^{-6} m^2/s;
- acquisition frequency of the instrumentation is 12.5 Hz, that is a sampling period of Δt=0.08 s;
- quasi-steady conditions inside the Tube;
- maximum level inside the tank $H_{0,max}$=1.5 m;
- minimum level inside the tank $H_{0,min}$=0.2 m.

In Physiological-tests, the electronic instrumentation consists of a pressure transducer, positioned on the bottom of the tank, and of a digital camera positioned on an orthogonal plane

to the jet, both connected to a dedicated data acquisition hardware and software. As said before, Physiological -tests were carried out according to the following scheme:

- positioning the Tube between the two foam blocks and compressing the foam with the 6 kg load (Figure 2.3, Figure 2.5 and Figure 2.6);
- fill the tank with the valve closed at least until $H_{0,max}$,
- turn on the data acquisition instrumentation,
- open the valve and wait for the tank to empty at least until $H_{0,min}$.

To minimize the possibility of errors in Tube positioning and the reduction of the foam elastic capacity due to the prolonged compression of the 6 kg load, each test was repeated at least four times using a different set of foam blocks. It is worth to recall that the 6 kg load is aimed to generate an external almost uniform pressure on the Tube wall of P_{ext}=981 Pa or equivalently 10 cm H_2O.

3.1.1 RESULTS

Hundreds of tests have been made to calibrate hardware and software and to tune up the procedures; here only the results of the final six tests are presented.

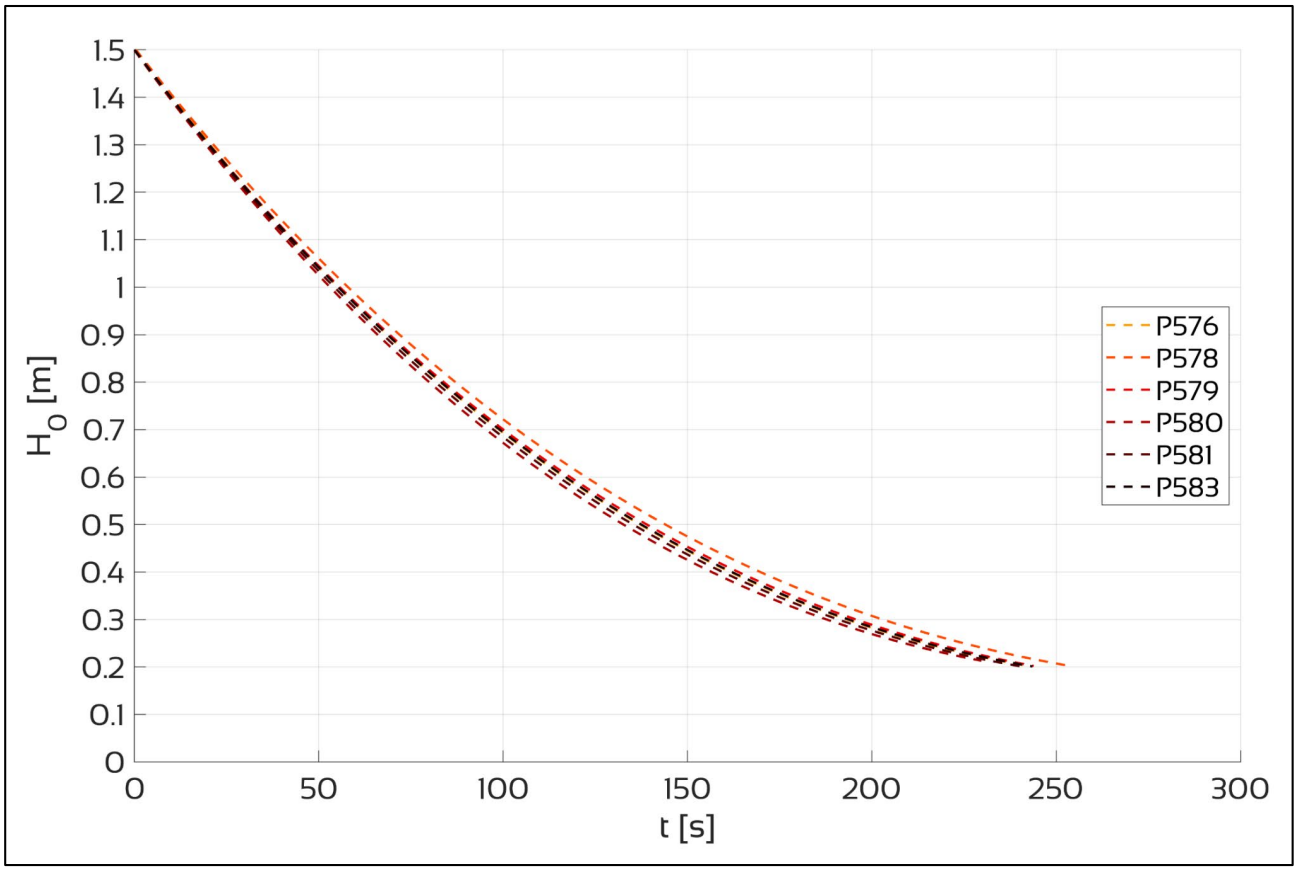

Figure 3.1: Final "Physiological flow condition" tests (Physiological-tests): the dashed lines represents the decreasing of the water level inside the tank over time during emptying

In Figure 3.1 it is shown the decreasing of the water level inside the tank H_0 over time during the emptying: the total time taken varies from 230 to 254 seconds. Figure 3.2 shows the flow rate Q as a function of the water level inside the tank H_0 for the same tests, along with the tests' average (the bold purple line).

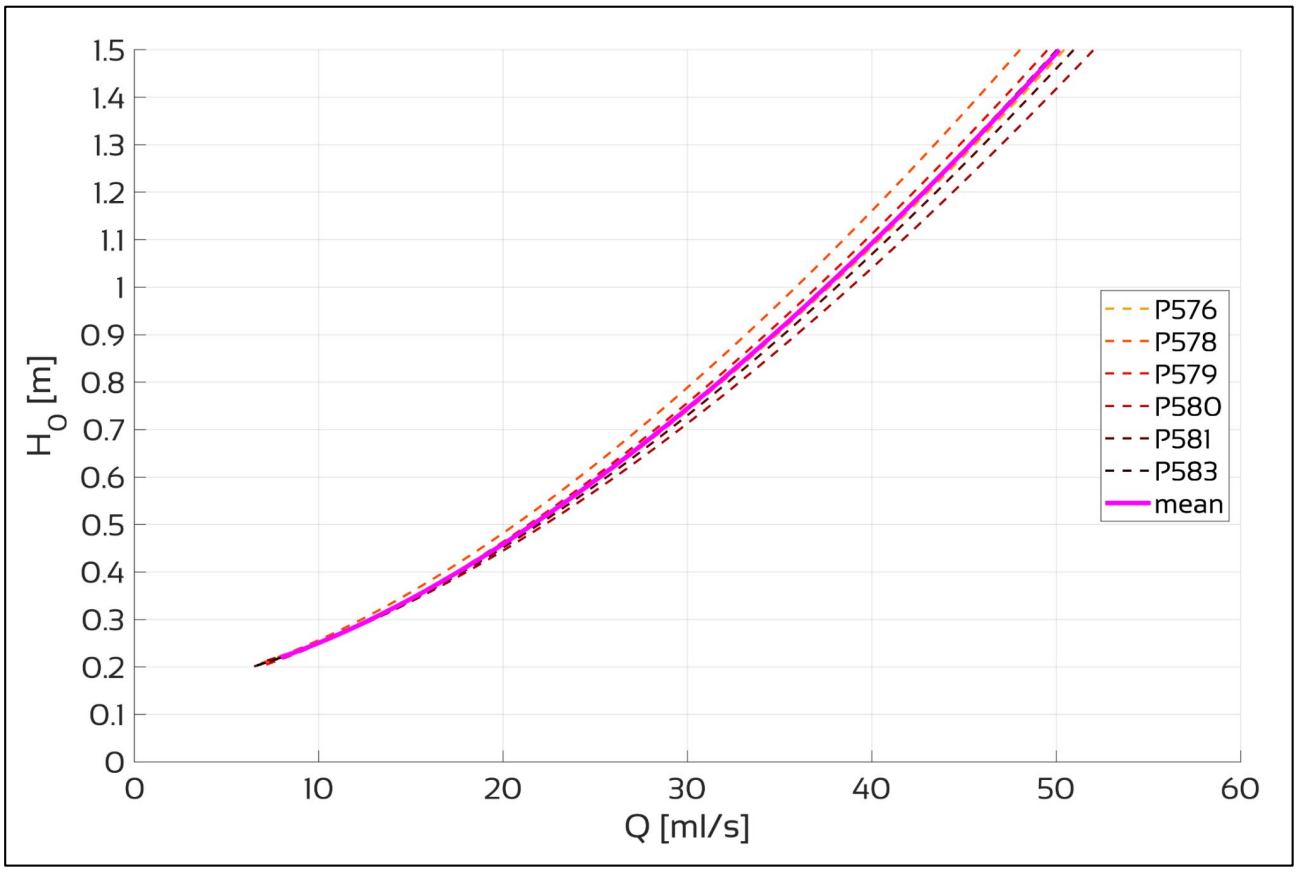

Figure 3.2: Flow rate Q in "Physiological flow condition" tests (Physiological-tests) as a function of the water level inside the tank H_0: dashed lines are the single tests, bold purple line is the tests' average

In Figure 3.3 the results of the Physiological-tests on the Schäfer's diagram are presented: the dashed lines are the single tests, while the bold purple line is the average of all the tests. The latter represents the relationship between flow Q and detrusorial pressure P_{det} (which in our case corresponds to the total head at the Tube's entrance H_c); it is possible to see that it lies inside the green area of the Schäfer's diagram, i.e. the area in which patients are considered not obstructed.

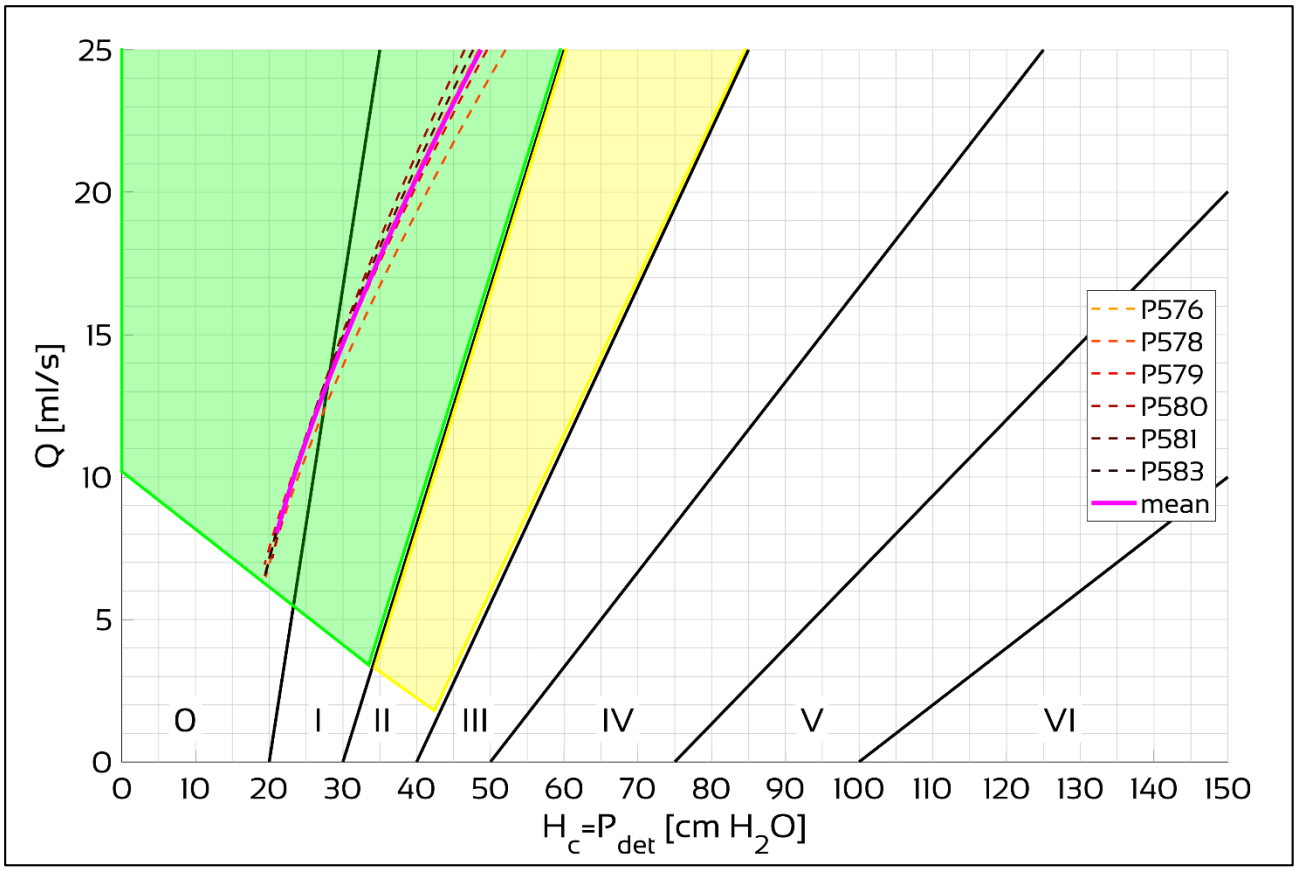

Figure 3.3: Schäfer's diagram with the results of the Physiological-tests: the bold purple line is the tests' average

3.1.2 CORRELATION BETWEEN u_E AND P_{DET}

The Physiological-tests have also been used to correlate the jet exit velocity u_e with the detrusorial pressure P_{det}, that in the present Model corresponds to the total head at the Tube's entrance H_c.

Figure 3.4 shows the average correlation between u_e and H_c in the present tests (dotted black line), along with polynomial interpolations of the 1st, 2nd, 3rd and 4th grade (purple, blue, green and red lines, respectively), with the constraint that if u_e=0, than H_c=0. It was considered only the H_c values between 0.2 and 0.8 m, represented by the vertical black dashed lines, because in healthy people very rarely the pressure inside the bladder is outside this range.

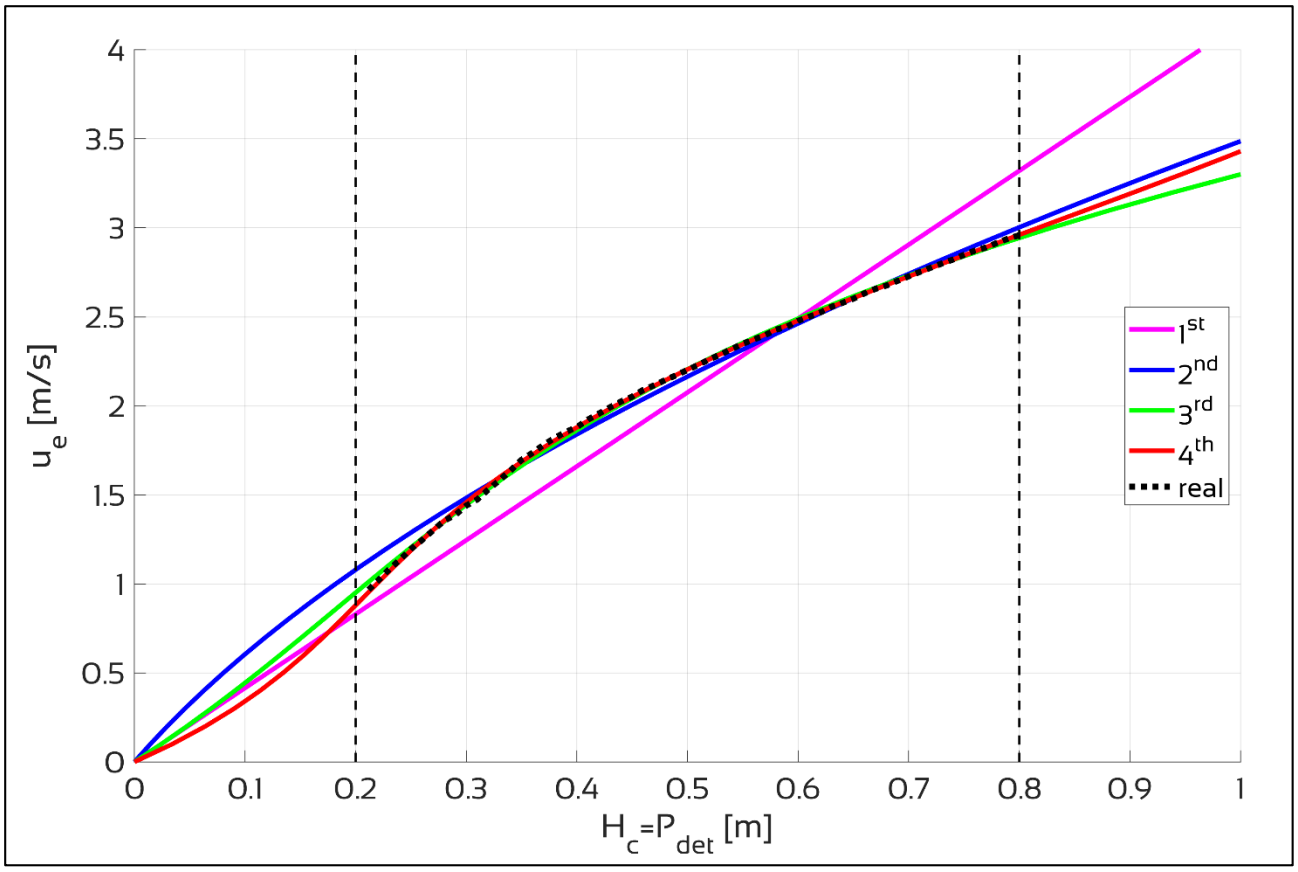

Figure 3.4: the black dotted line is average correlation between jet exit velocity u_e and total head at the Tube's entrance H_c (between 0.2 and 0.8 m, black dashed vertical lines) in Physiological-tests; the purple, blue, green and red lines are the 1st, 2nd, 3rd and 4th degree polynomial interpolation, respectively

In Figure 3.5, the colored lines show the correlation between real H_c and estimated H_c data: the 1st, 2nd, 3rd and 4th grade interpolation curve are represented with a purple, blue, green and red line, respectively. In the box of the same color the relative deviation standard between real H_c and estimated H_c is shown. The yellow part represents the area of the graph where H_c real > H_c estimated, the blue part represents the area where H_c real < H_c estimated, while the perfect agreement between the two data is the dashed black line.

Although the 3rd and the 4th degree interpolations agree better with the tests data, the 2nd degree interpolation seems to be more truthful (Figure 3.4), and also it differs only in the lower part of the graph, for H_c values around 0.2 m (Figure 3.5).

Been said that, the following relation:

$$P_{det} = H_c = 0.0422 \cdot u_e{}^2 + 0.14 \cdot u_e \qquad 3.1$$

has been used in the Innovative Instrumentation to estimate P_{det}.

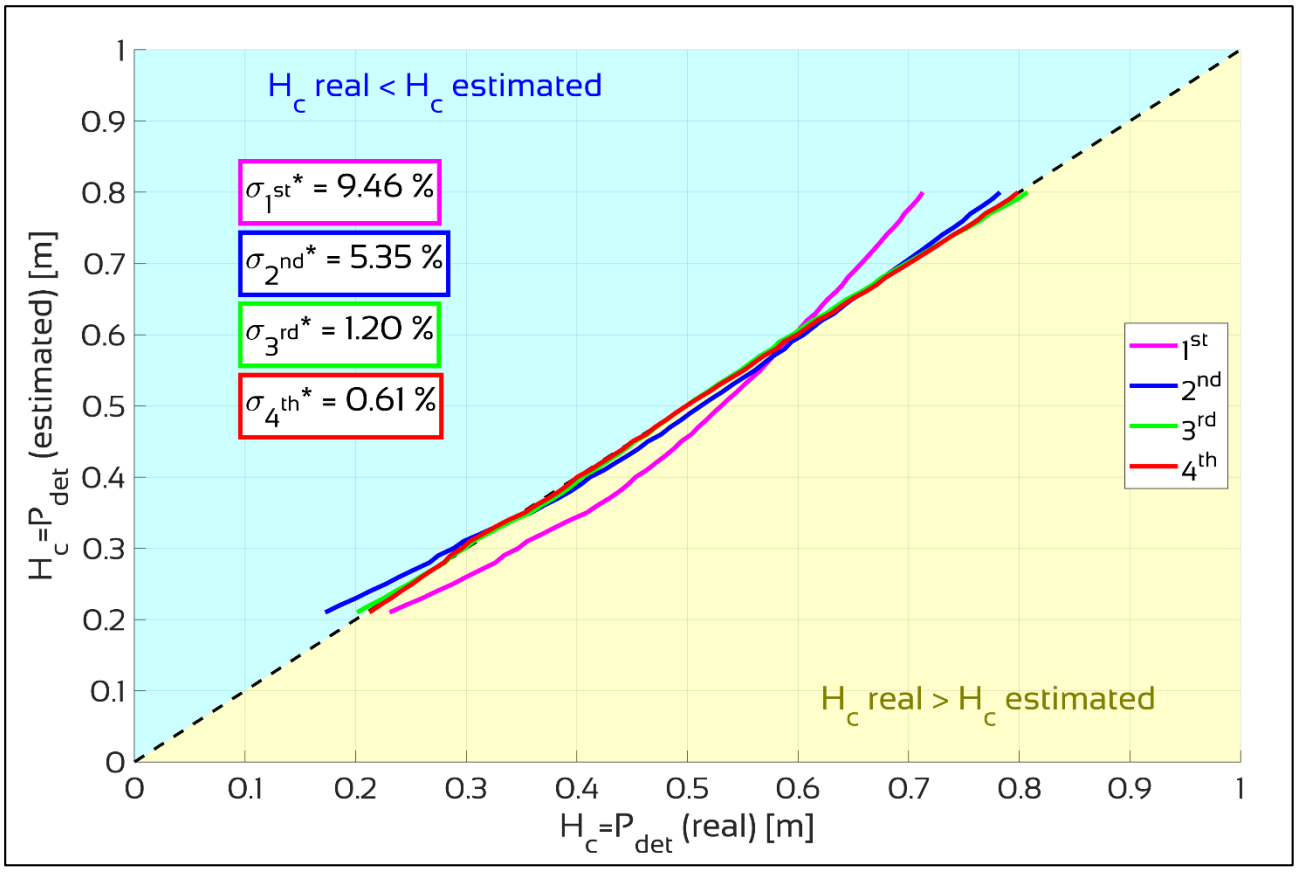

Figure 3.5: correlation between real Hc and estimated Hc data with 1st, 2nd, 3rd and 4th polynomial interpolation curve; in the box of the same color, the relative deviation standard for each curve

3.2 "PATHOLOGICAL FLOW CONDITION" TESTS

Pathological-tests are very similar to Physiological-tests, apart from the fact that an obstruction was inserted inside the Tube. The obstruction represents what is called urethral stricture (section 1.2.1), a stiffening of the urethra (the Tube in the Model) that reduce the flow area during voiding (the emptying of the tank in the Model). As usual, Pathological-tests were carried out according to the following scheme:

- positioning the obstruction inside the Tube (see next paragraph);
- positioning the Tube between the two foam blocks and compressing the foam with the 6 kg load (Figure 2.3, Figure 2.5 and Figure 2.6);
- fill the tank with the valve closed at least until $H_{0,max}$,
- turn on the data acquisition instrumentation,
- open the valve and wait for the tank to empty at least until $H_{0,min}$.

and considering the following hypothesis:

- the fluid used is water at ambient temperature (T=20÷25 °C, ρ=1000 kg/m^3), incompressible fluid, with dynamic viscosity μ=10^{-3} Pa·s and kinematic viscosity v=10^{-6} m^2/s;
- acquisition frequency of the instrumentation is 12.5 Hz, that is a sampling period of Δt=0.08 s;
- quasi-steady conditions inside the Tube;
- maximum level inside the tank $H_{0,max}$=1.6 m;
- minimum level inside the tank $H_{0,min}$=0.2 m.

As in Physiological-tests, each test was repeated at least four times using a different set of foam blocks to minimize the possibility of errors in Tube positioning and the reduction of the foam elastic capacity due to the prolonged compression of the 6 kg load.

It is observed the variations of the physical parameters of the jet at the Tube's exit while emptying the tank. The electronic instrumentation consists of a pressure transducer, positioned on the bottom of the tank, and of a digital camera positioned on an orthogonal plane to the jet, both connected to a dedicated data acquisition hardware and software.

3.2.1 Types of obstructions

The obstructions used are metal cylinders with an external diameter equal to the external diameter of the "undisturbed" Tube D_{ext} and a variable internal diameter, in order to reproduce a rigid section reduction inside the Tube. Obstructions are characterized by three variables to simulate the real and most common urethral strictures (section 1.2.1):

- internal diameter D_{ob}: 4 mm (light obstruction), 3 mm (medium obstruction) and 2 mm (severe obstruction) (Figure 3.6);
- length L_{ob}: 5 mm (short stricture), 20 mm (medium strictures) and 50 mm (long stricture) (Figure 1.7 and Figure 3.7);
- position inside the Tube X_{ob} (Figure 3.8): upstream (U, positioned at 2 cm from the Tube's entrance), center (C, at 10 cm) and downstream (D, at 17 cm), and corresponding to penile, panurethral and bulbar strictures, respectively (see section 1.2.1).

According to Table 3.1, the tests were made with all the possible combination of these parameters, so that, adding the test without obstructions (i.e. Physiological-test), a total of twenty-eight test types were made.

Figure 3.6: metal cylinders used as obstructions in Pathological-tests with internal diameters D_{ob}

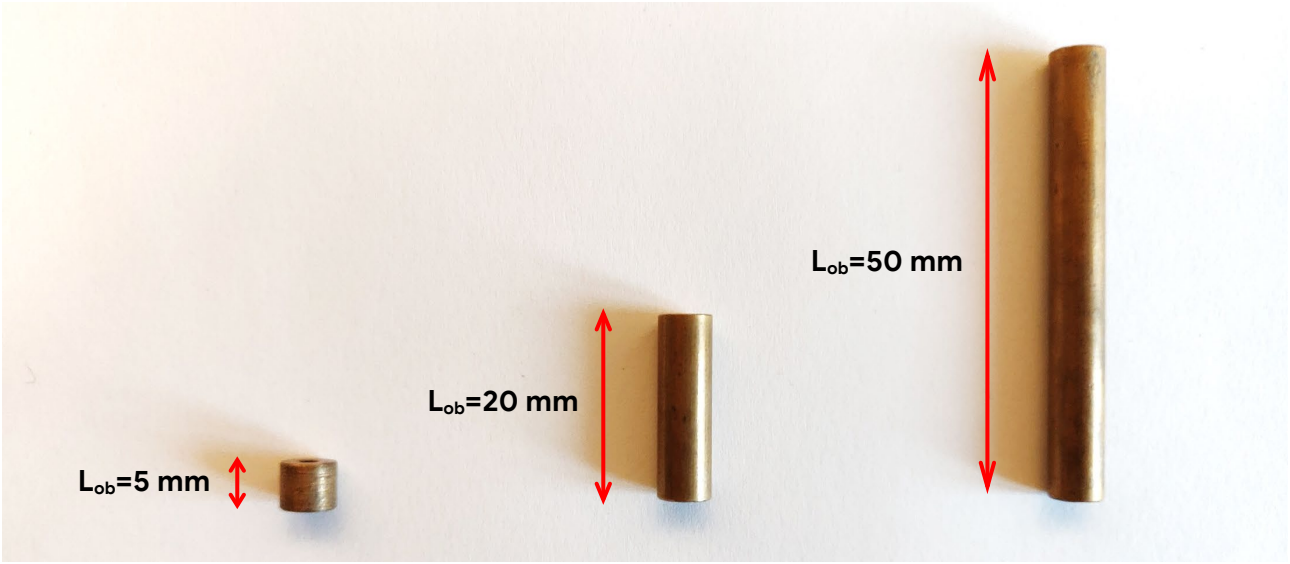

Figure 3.7: lengths L_{ob} of the metal cylinders

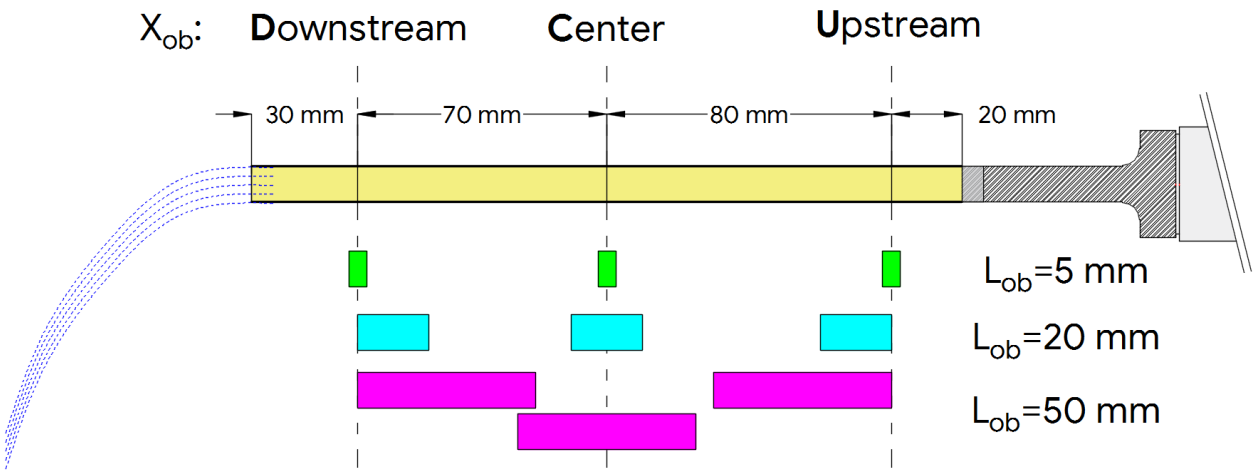

Figure 3.8: positions X_{ob} of the metal cylinders

# test	D_{ob} [mm]	L_{ob} [mm]	X_{ob} [-]
D0L00X0	0	0	0
D4L05XD	4	5	D
D4L05XC	4	5	C
D4L05XU	4	5	U
D4L20XD	4	20	D
D4L20XC	4	20	C
D4L20XU	4	20	U
D4L50XD	4	50	D
D4L50XC	4	50	C
D4L50XU	4	50	U
D3L05XD	3	5	D
D3L05XC	3	5	C
D3L05XU	3	5	U
D3L20XD	3	20	D
D3L20XC	3	20	C
D3L20XU	3	20	U
D3L50XD	3	50	D
D3L50XC	3	50	C
D3L50XU	3	50	U
D2L05XD	2	5	D
D2L05XC	2	5	C
D2L05XU	2	5	U
D2L20XD	2	20	D
D2L20XC	2	20	C
D2L20XU	2	20	U
D2L50XD	2	50	D
D2L50XC	2	50	C
D2L50XU	2	50	U

Table 3.1: summary of Pathological-tests; D0L00X0 represents the Physiological-test

3.2.2 RESULTS

The results of Pathological-tests are presented on Schäfer's diagram in Figure 3.9 (D_{ob}=4 mm), Figure 3.10 (D_{ob}=3 mm) and Figure 3.11 (D_{ob}=2 mm):

- colors represent obstruction's internal diameter D_{ob}: blue, green and red are D_{ob}=4 mm, 3 mm and 2 mm, respectively;
- shades of color represent the position of the obstruction X_{ob}: dark is downstream (D), medium is center (C) and light is upstream (U);
- type of line represents the obstruction's length L_{ob}, which are 5 mm (full line), 20 mm (dashed line) and 50 mm (dotted line);
- the test without obstruction (the SE-test) is the black line.

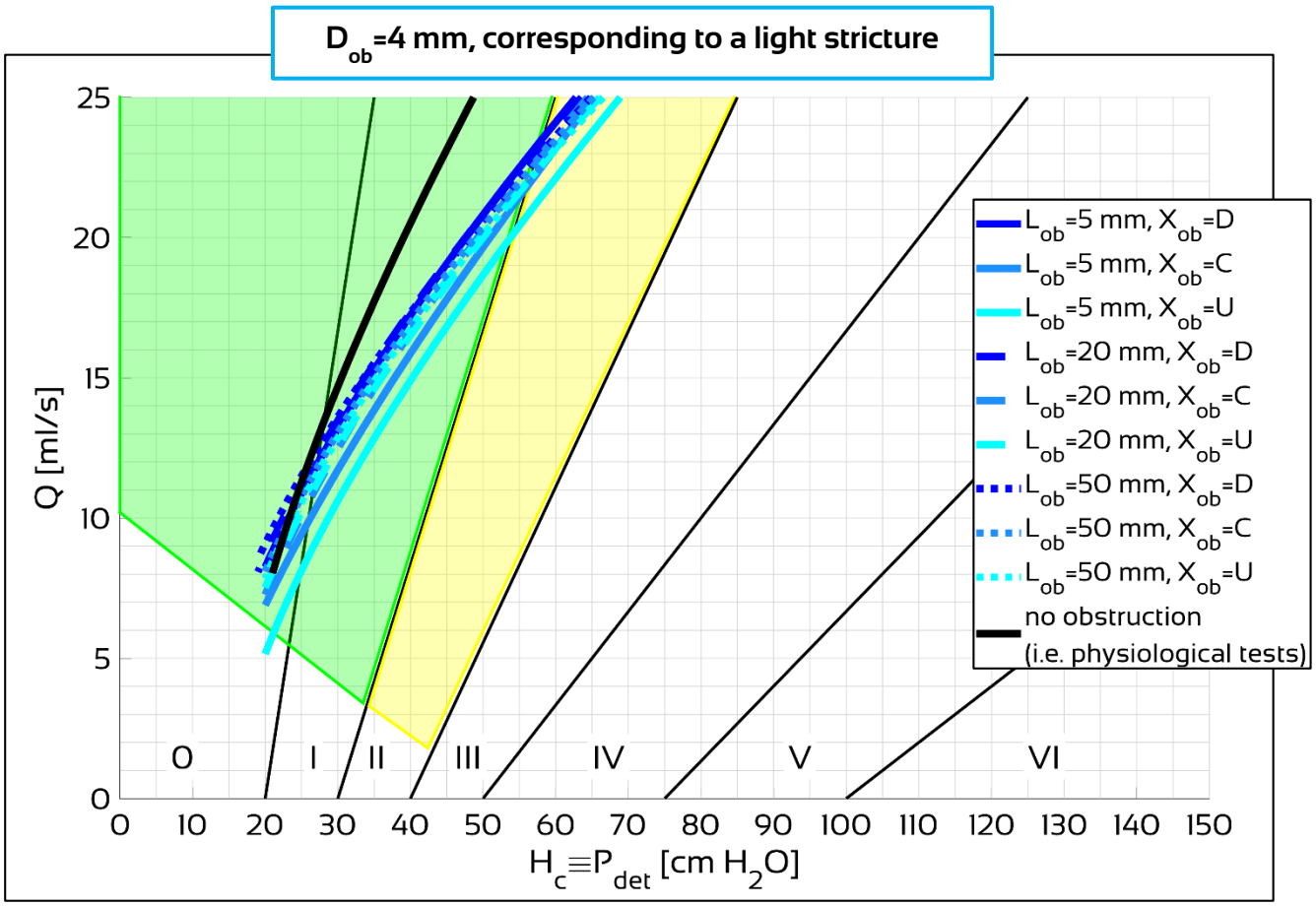

Figure 3.9: Pathological-tests results on Schäfer's diagram with internal diameter D_{ob}=4 mm: each line is the average of at least 4 repetitions. The black line is the test without obstruction

From the analysis of Figure 3.9 (D_{ob}=4 mm), it can be noted that:

- obstructions with D_{ob}=4 mm produce a very light obstacle to flow, with the lines that almost stay in the green zone of the Schäfer's diagram;
- in the case of D_{ob}=4 mm, length and position of the obstruction does not have any influence on flow, given by the fact that lines nearly overlaps.

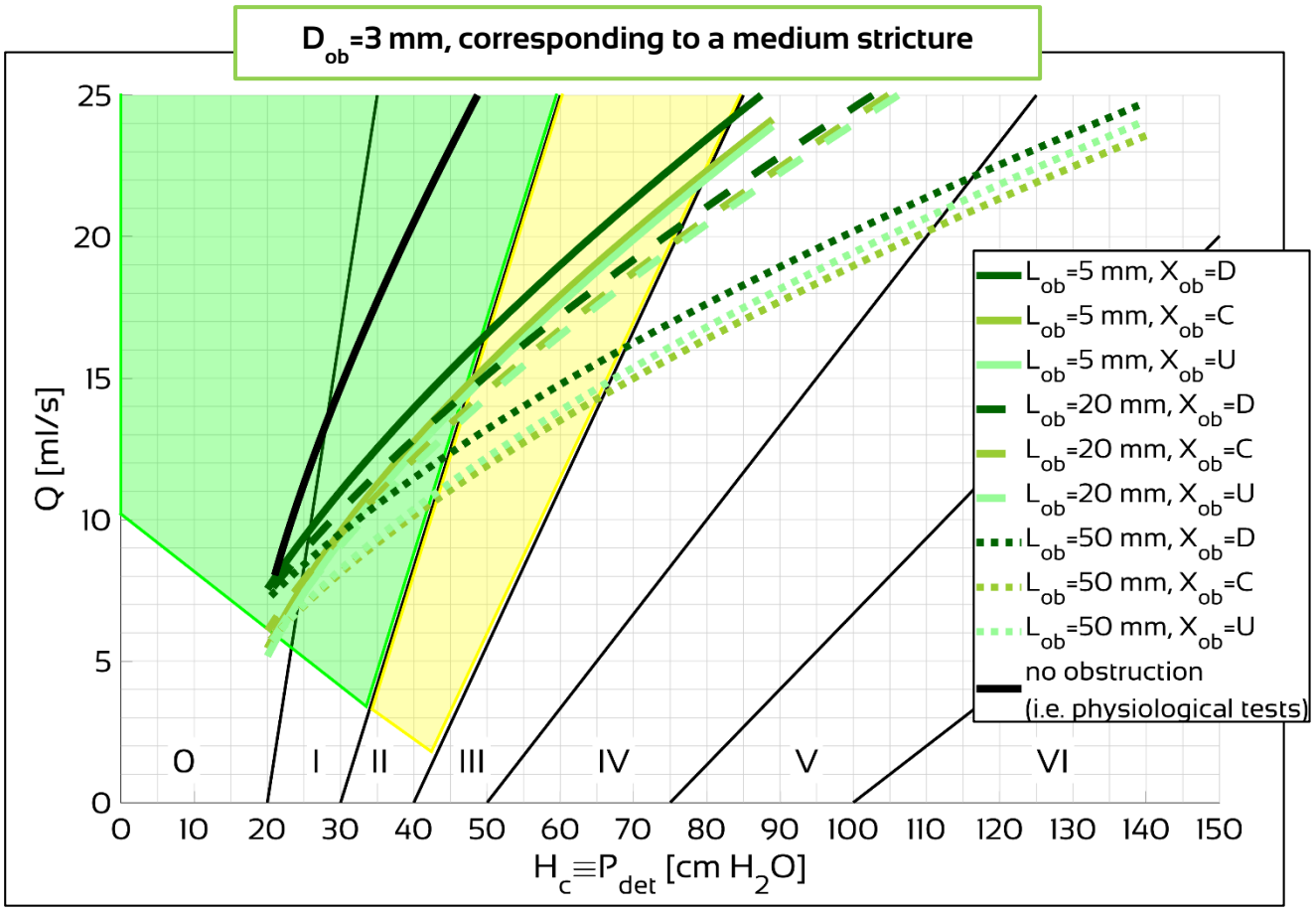

Figure 3.10: Pathological-tests results on Schäfer's diagram with internal diameter D_{ob}=3 mm: each line is the average of at least 4 repetitions. The black line is the test without obstruction

From the analysis of Figure 3.10 (D_{ob}=3 mm), it can be noted that:

- obstructions with D_{ob}=3 mm, that correspond to a medium obstruction, are lying in the correct part of the Schäfer's diagram, i.e. sectors III and IV;
- the higher length L_{ob}=50 mm (dotted lines) significantly reduces the flow inside the Tube, shown by the dotted lines placed in higher sectors of the Schäfer's diagram.

From the analysis of Figure 3.11 (D_{ob}=2 mm), it can be noted that:

- obstructions with D_{ob}=2 mm, that correspond to a severe obstruction, are lying in the correct part of the Schäfer's diagram, i.e. sectors higher than IV;
- the higher length L_{ob}=50 mm (dotted lines) significantly reduces the flow inside the Tube, shown by the dotted lines placed in higher sectors of the Schäfer's diagram.
- Moreover, for every obstruction diameter D_{ob}, the position of the obstruction has a very little influence on the flow (shades of every color are overlapping with each other).

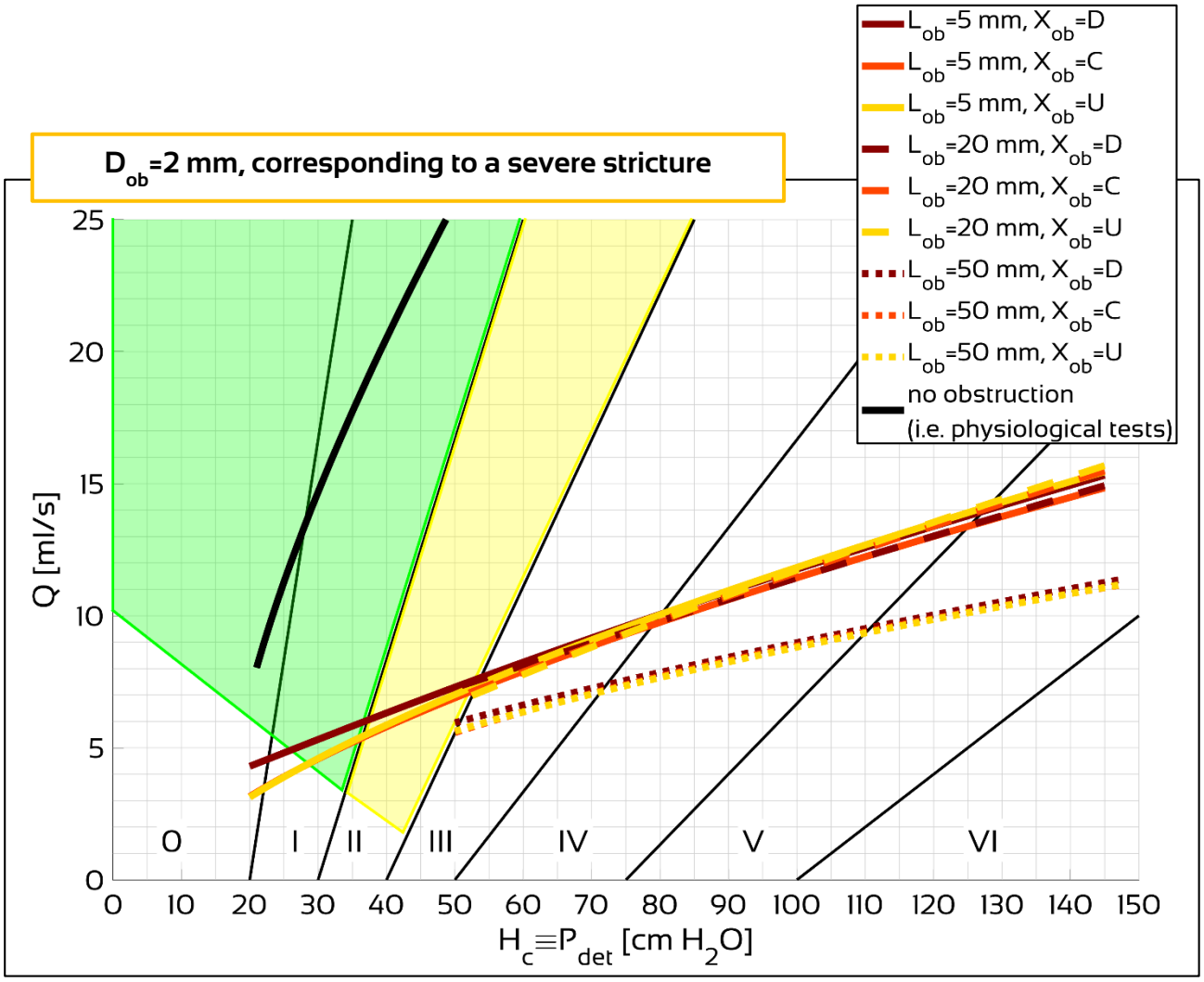

Figure 3.11: Pathological-tests results on Schäfer's diagram with internal diameter D_{ob}=2 mm: each line is the average of at least 4 repetitions. The black line is the test without obstruction

3.3 TESTS WITH CATHETER

As seen in section 1.3.2, the P/F Study, which is the main tool to evaluate the urodynamic function, is a highly invasive exam: it uses a double-way catheter to gradually fill the bladder recording simultaneously the detrusorial pressure through a pressure transducer connected to one of the two channels. Therefore, two types of activities on the Model with the catheter inside the Tube were designed:

- "Diagnostic flow condition" tests (Diagnostic-tests) to analyze the behavior of the system during emptying and compare it to the behavior of the system during emptying without the catheter (that is the Physiological-tests), so to evaluate catheter effects on urethral flow (section 3.4);
- Flow variables measurements inside the Tube tests (FV-tests) to obtain flow characteristics inside the Tube (i.e., pressures, velocity and cross-area sections) through a special pressure measurement system, also used during urodynamic investigations (section 3.5).

In both types the following hypothesis were considered:

- the fluid used is water at ambient temperature (T=20÷25 °C, ρ=1000 kg/m^3), incompressible fluid, with dynamic viscosity μ=10^{-3} Pa·s and kinematic viscosity v=10^{-6} m^2/s;
- acquisition frequency of the instrumentation is 12.5 Hz, that is a sampling period of Δt=0.08 s;
- quasi-steady conditions inside the Tube;
- maximum level inside the tank $H_{0,max}$=1.6 m;
- minimum level inside the tank $H_{0,min}$=0.2 m.

3.4 "DIAGNOSTIC FLOW CONDITION" TESTS

These tests aim at analyzing the hydraulic behavior of the system during emptying of the tank in the presence and in the absence of the catheter; for both set-ups the tests were repeated 10 times.

Every Diagnostic-tests were carried out according to the following scheme:

- positioning the catheter (see next paragraph) inside the Tube;
- positioning the Tube between the two foam blocks and compressing the foam with the 6 kg load (Figure 2.3, Figure 2.5 and Figure 2.6);
- fill the tank with the valve closed at least until $H_{0,max}$,
- turn on the data acquisition instrumentation,
- open the valve and wait for the tank to empty at least until $H_{0,min}$.

3.4.1 THE CATHETER

The double-way catheter used is the same used in P/F Study (Figure 3.12). It is 2 mm (6 Fr) external diameter and the section is split in two separate sub-sections to allow simultaneous pressure measurement (by connecting the catheter to a pressure transducer) and filling the bladder with saline solution. On the external surface there is a graduated scale in centimeters that was useful during the FV-tests to understand in which section of the Tube the measurements are done.

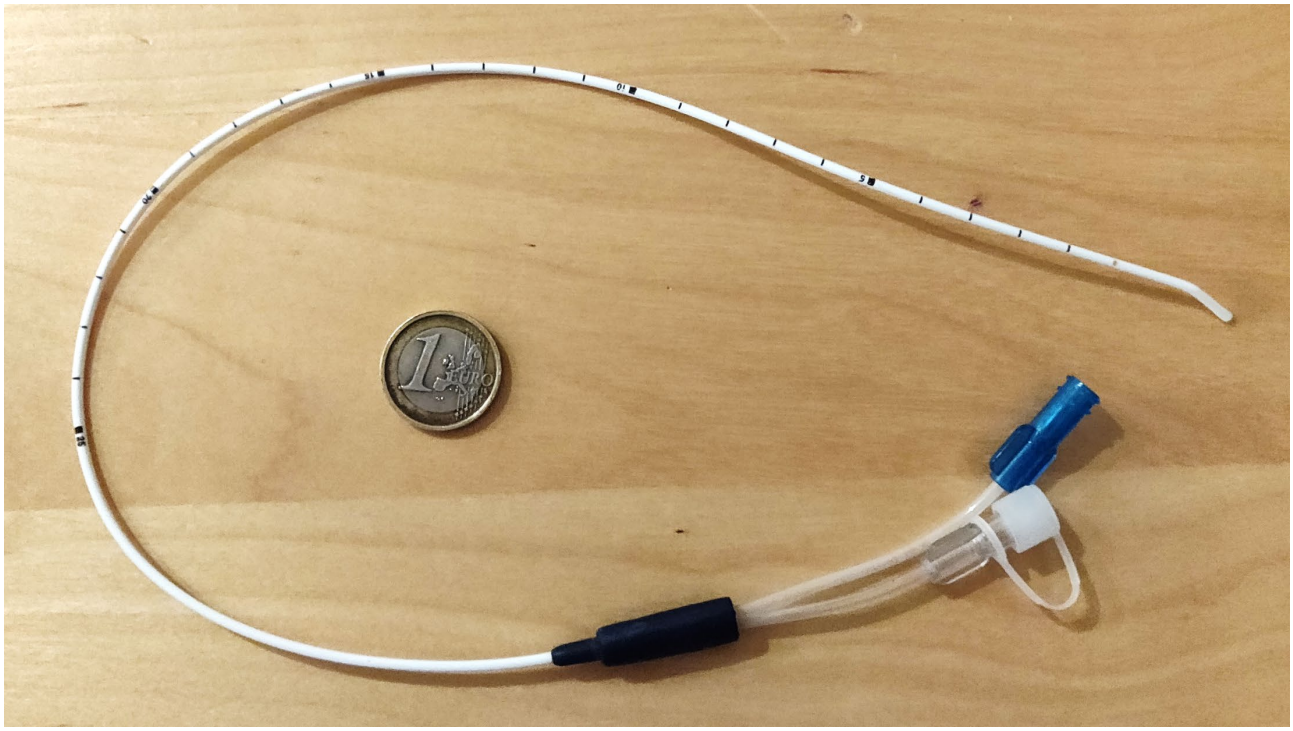

Figure 3.12: double-way catheter used in Diagnostic-tests compared to a one euro coin

The catheter goes inside the Tube and, through the connector and the valve, goes inside the tank: that is for maintaining the same boundary conditions in all tests (Figure 3.13), as it is explained in section 3.5.

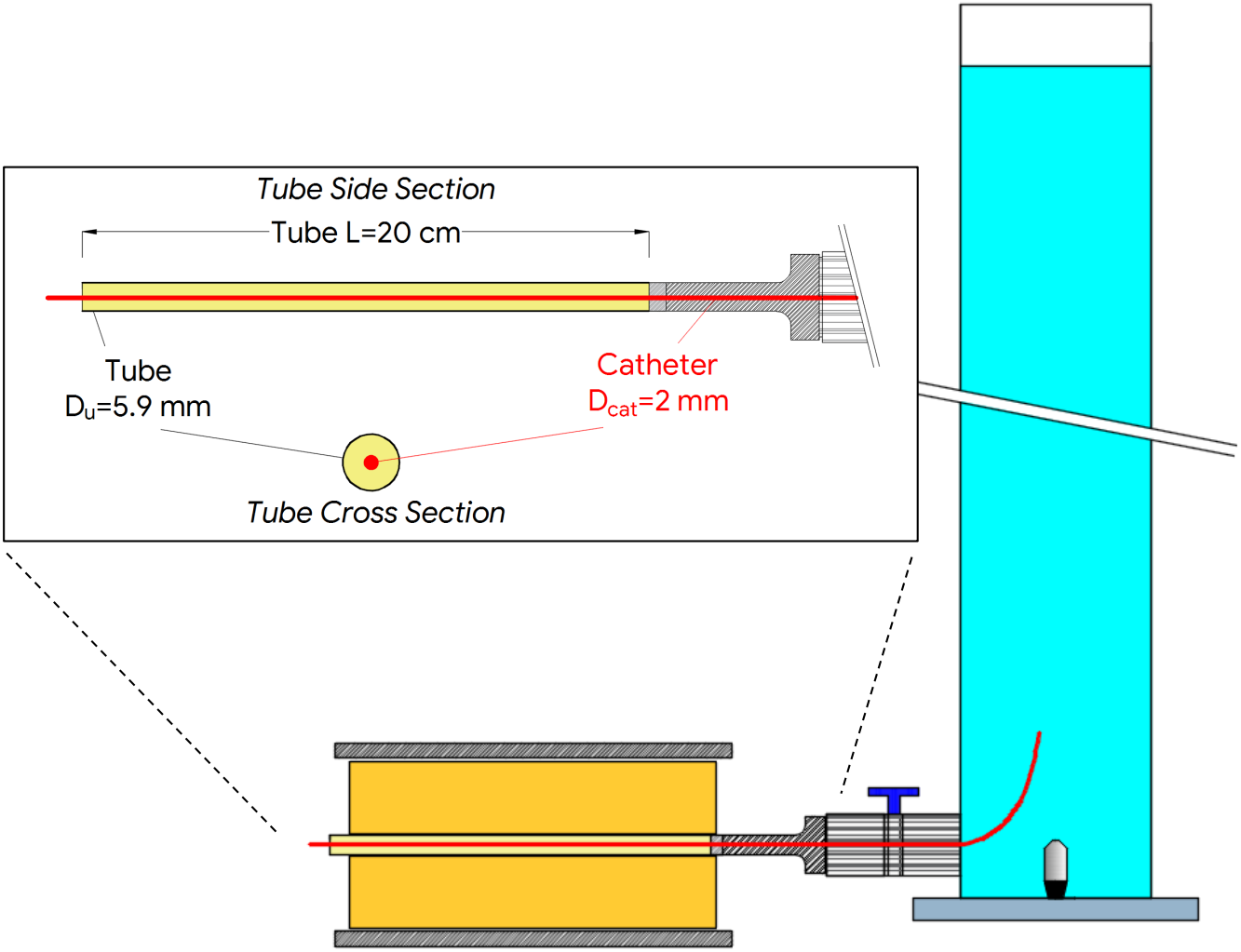

Figure 3.13: the catheter was placed inside the Tube and, through the connectors and the valve, goes inside the tank

3.4.2 RESULTS

Figure 3.14 shows the trend of flow rate Q and Q_{cat} during the emptying of the system as a function of H_c, respectively without the catheter (black line with circles) and with it (black line with crosses); each line is obtained by averaging the acquired data. The dotted lines represent the maximum variation range of the measurements: in the tests without the catheter the variation range in the flow rate is ±1.2 ml/s, while in the tests with the catheter it is ±1.4 ml/s. In any case, the variation is less than 6% when H_c>40 cm H_2O.

Figure 3.14 illustrates that for a given H_c, Q_{cat} is significantly lower than Q; observably, the reduction induced by the catheter grows when flow is increasing.

The entity of the flow reduction ΔQ* is shown in Figure 3.15 in terms of relative percentage:

$$\Delta Q^* = \frac{Q - Q_{cat}}{Q} \cdot 100 \qquad 3.2$$

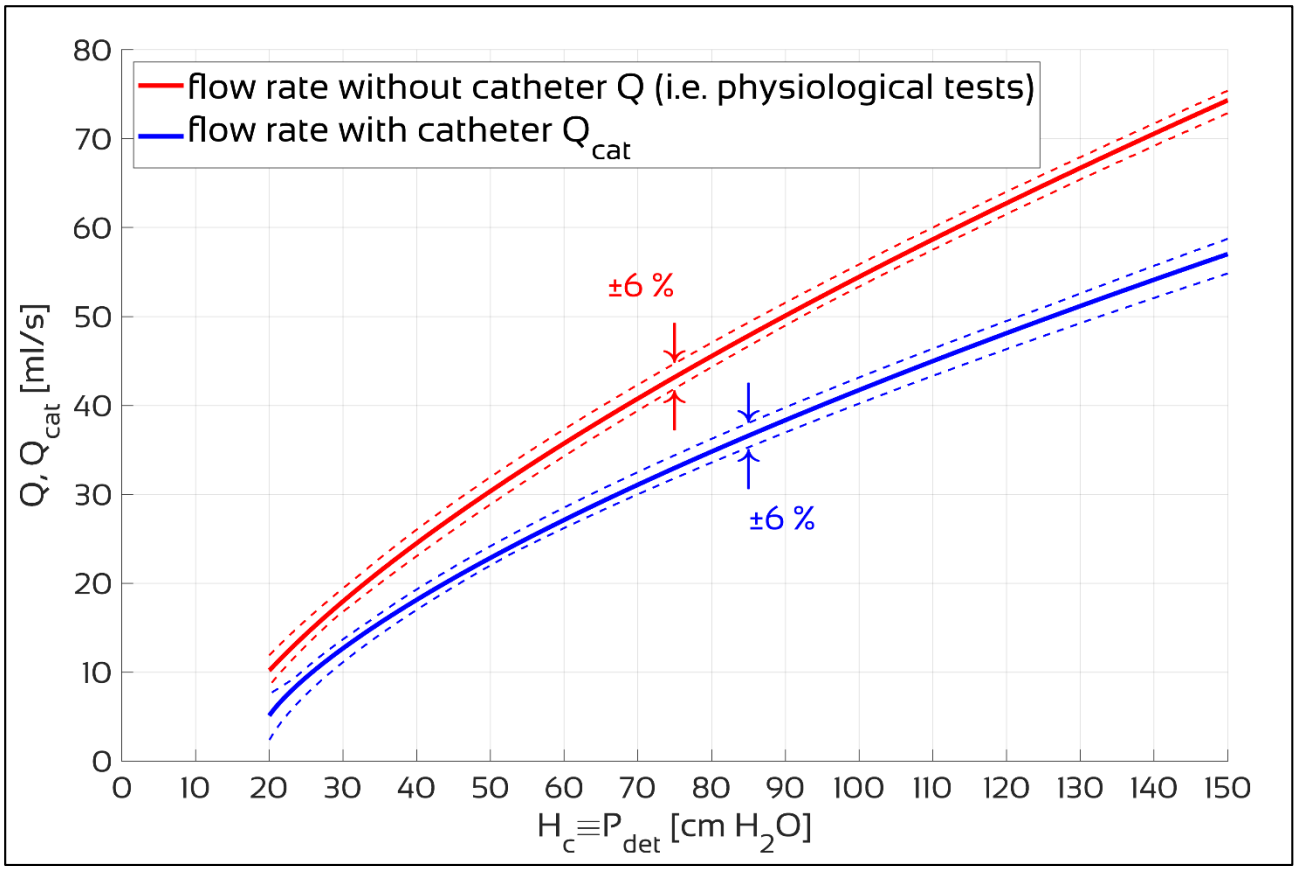

Figure 3.14: Q and Q_{cat} trend as a function of the total head at the Tube's entrance H_c

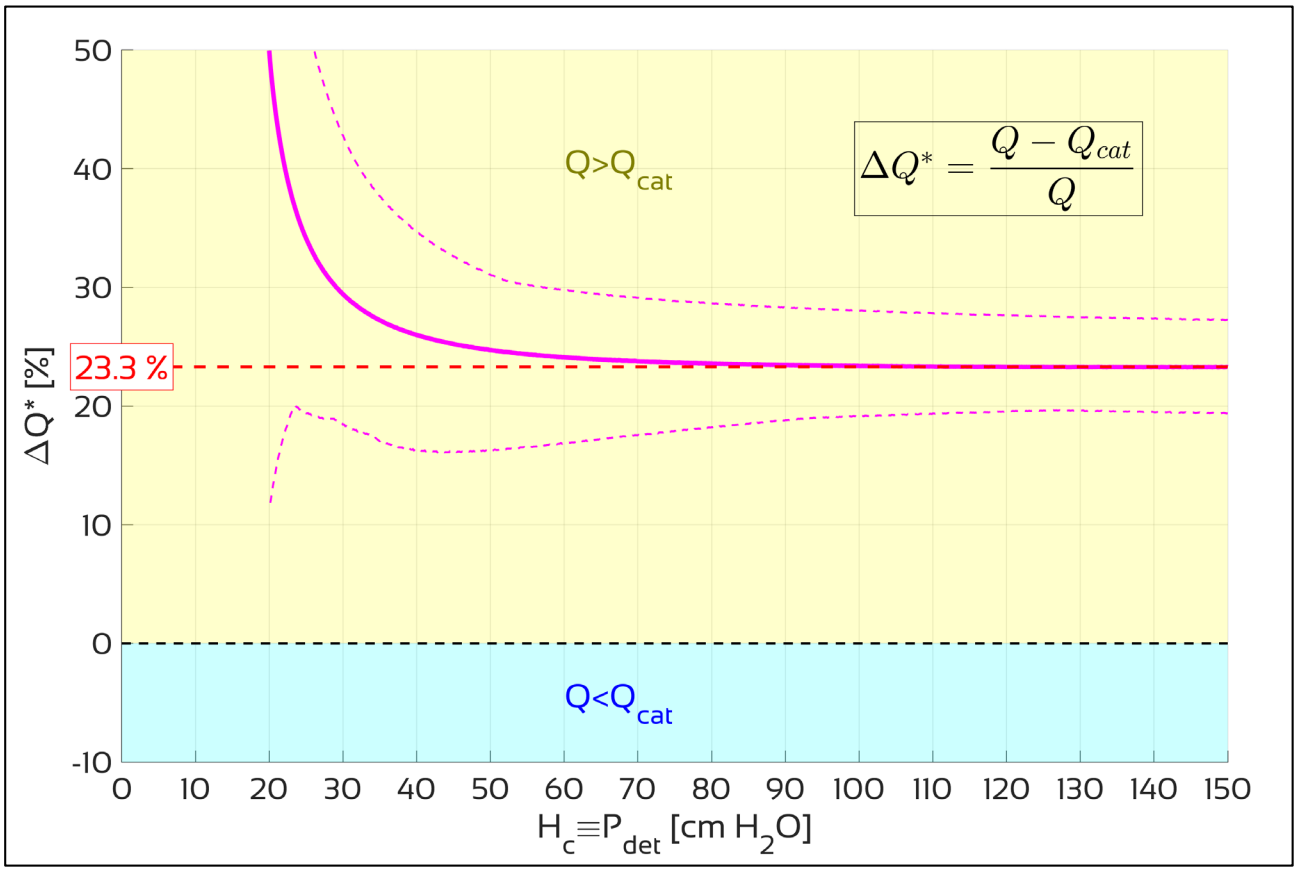

Figure 3.15: percentage of the relative flow rate reduction ΔQ* as a function of the total head at the Tube's entrance H_c

Figure 3.15 shows the effects induced by the urethral catheter on the flow rate: for given total head at the Tube's entrance, the flow rate in the presence of a catheter can be reduced to values around 25% of the flow in the absence of the catheter, and then increase over 50% when H_c falls below 0.2-0.3 m. *The reduction of 23.3 % was chosen to correct the non-invasive Q values recorded with the Innovative Instrumentation to show them in Schäfer diagram*, which is essentially derived on an empirical basis with invasive tests.

Moreover, Diagnostic-tests allow a comparison between experimental results and clinical data obtained from the following sources:

- Richard et al., 2003, clinical measurements on 32 healthy males;
- Baseman et al., 2002, clinical measurements on 20 healthy females;
- DMSC of University of Florence, with data on 8 healthy males recorded in 2015.

In all three groups, a free uroflowmetry and one with a 6 Fr catheter, the same used in the present research, have been compared.

Data source	Q_{peak} *[ml/s]*	$Q_{cat,peak}$ *[ml/s]*	ΔQ^* *(Q_{peak}-Q_{cat_peak})*
Present research (Diagnostic-tests)	19.0 ± 1.3	13.6 ± 1.2	28.6 % (5.4 ml/s)
Richard et al., 2003	19 ± 4	13.5 ± 4.5	28.9 % (5.5 ml/s)
Present research (Diagnostic-tests)	22.6 ± 1.4	16.6 ± 1.2	26.6 % (6.0 ml/s)
Baseman et al., 2002	22.65 ± 9.6	16.25 ± 7.2	28.2 % (6.4 ml/s)
Present research (Diagnostic -tests)	24.1 ± 1.5	17.8 ± 1.2	26.1 % (6.3 ml/s)
DMSC, 2015	24.13 ± 10.1	17.75 ± 8.3	26.4 % (6.4 ml/s)

Table 3.2: clinical measurements compared with the results of the Diagnostic-tests

Table 3.2 summarizes clinical measurements compared with the results of the Diagnostic-tests: Q_{peak} and $Q_{cat,peak}$ are the average of the maximum urinary flow, respectively with and without a catheter, and ΔQ^* is the percentage of the relative reduction between the two measurements (in brackets the absolute difference Q_{peak}-$Q_{cat,peak}$). Regarding clinical measurements, since in uroflowmetry the intravesical pressure is not measured, flow variation was evaluated at the same total of volume drained, a condition which can be assumed representative of the same intravesical pressure. With regard to the experimental data, the closest Q value to real data and the corresponding Q_{cat} value at same H_c were selected.

Figure 3.16 shows both experimental data and clinical data: Q_{cat} is represented as a function of Q. A satisfactory agreement between the results obtained from the Model and the clinical measurements is noted.

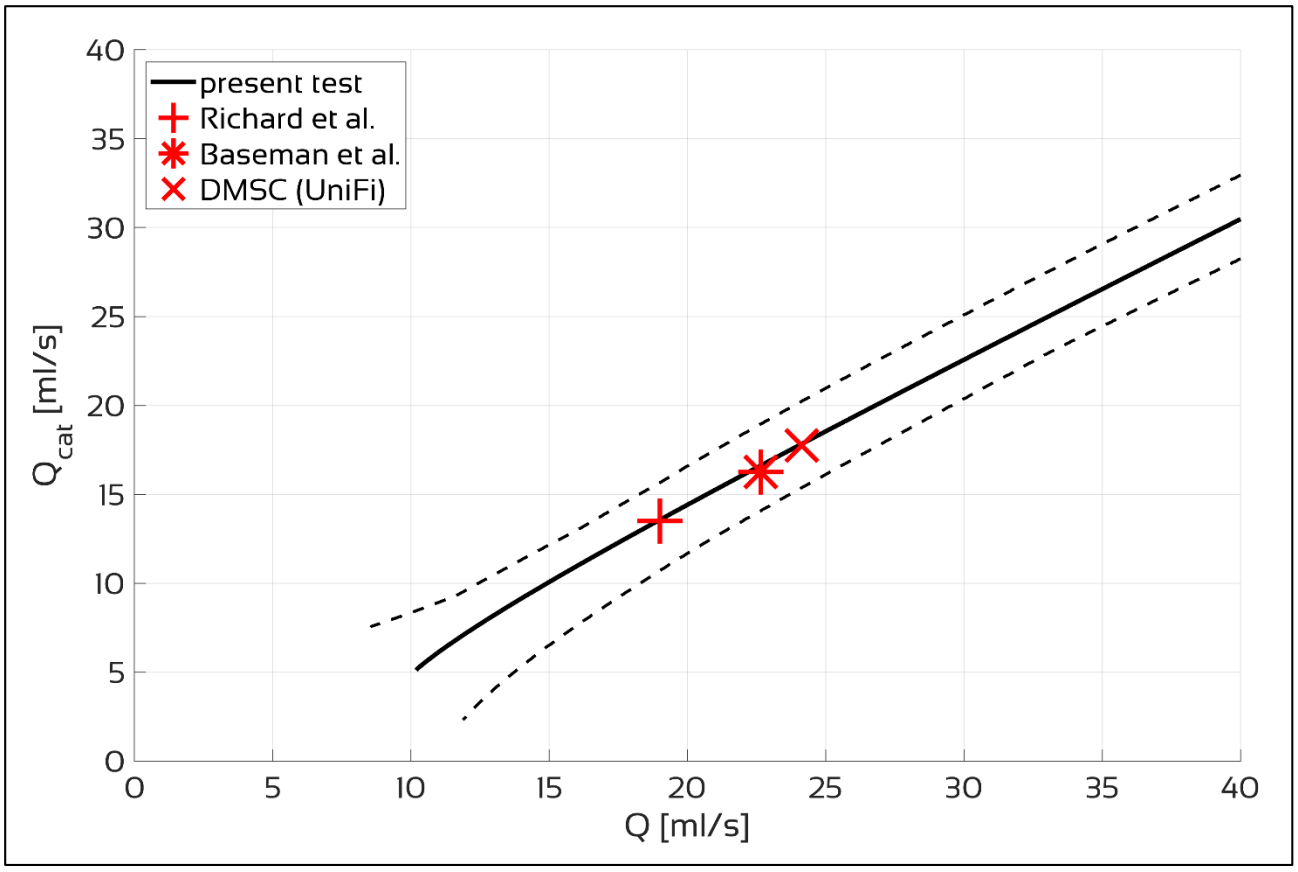

Figure 3.16: comparison between Diagnostic-tests (black line) and clinical data from literature (red marks)

3.5 Flow variables measurements inside the Tube

FV-tests are aimed to obtain pressures, velocity and cross-sectional area inside the Tube during the emptying of the system, along with the other hydrodynamic variables of interest (flow rate Q, total head at the Tube's entrance H_c and jet exit velocity u_e) with the presence the urethral catheter, which is also part of the measurement instrumentation. In particular, the piezometric head h_T and the total head H_T were evaluated in 20 different sections inside the Tube during system emptying with a pressure transducer connected to a catheter especially modified for these tests.

Every FV-tests were carried out according to the following scheme:

- positioning the catheter inside the Tube;
- positioning the Tube between the two foam blocks and compressing the foam with the 6 kg load (Figure 2.3, Figure 2.5 and Figure 2.6);
- fill the tank with the valve closed at least until $H_{0,max}$,
- turn on the data acquisition instrumentation,
- open the valve and wait for the tank to empty at least until $H_{0,min}$.

Each test was repeated at least five times using a different set of foam blocks to minimize the possibility of errors in Tube positioning and the reduction of the foam elastic capacity due to the prolonged compression of the 6 kg load.

3.5.1 The "modified" double-way catheters MDWC type 1 & type 2

In FV-tests two "modified" versions of the standard catheter for the P/F Study, already described in section 3.4.1, were used.

The section of the catheter is split in two separate sub-sections, of which one of them, used in P/F Study to fill the bladder with saline solution, was not used during these tests. The other sub-section allows pressure measurement by filling it with water and connecting it to the pressure transducer: it has a hole on the side in order to work like a piezometer and consequently measure the piezometric head inside the Tube. The position of the side hole inside the Tube determines also the measurement point: the graduated scale in centimeters on the external surface allows the correct placement. The catheter was then connected to another catheter in order to maintain the same boundary conditions in every measurement's positions (Figure 3.17, *MDWC type 1*).

The catheter was then modified to allow total head measurement: it was cut orthogonally, in order to work like a pitot tube, and then connected to another catheter in order to maintain the same boundary conditions in every measurement's positions (Figure 3.17, *MDWC type 2*); the distance between the two sections is 1 cm.

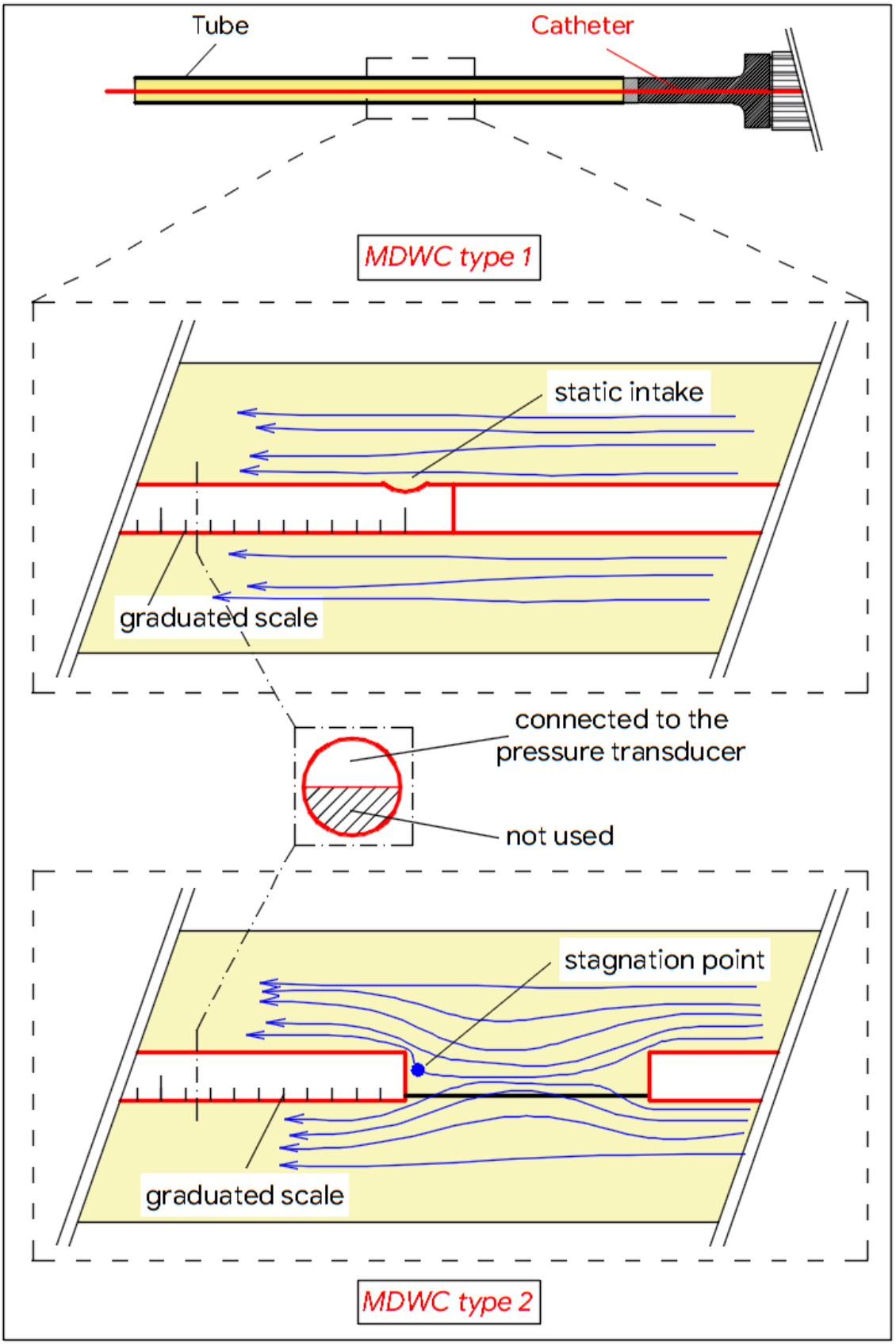

Figure 3.17: MDWC type 1 (upper), used to measure the piezometric head inside the Tube & MDWC type 2 (lower), used to measure the total head inside the Tube

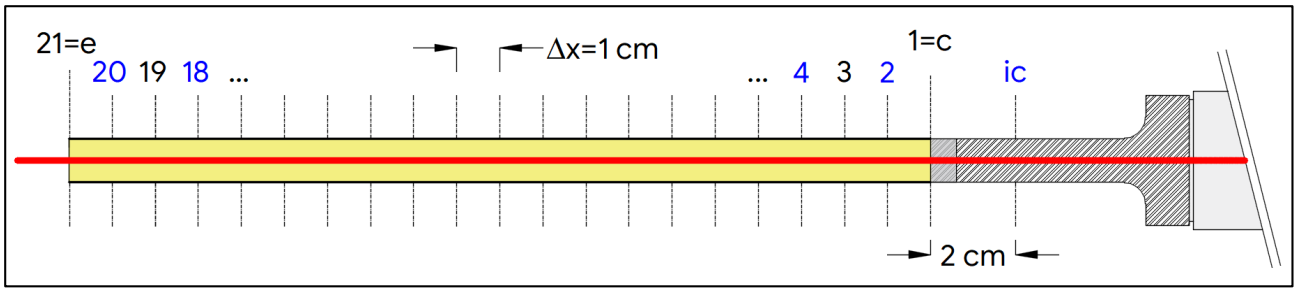

Figure 3.18: measurements sections of piezometric and total head inside the Tube

Measurements was made from the section at the Tube's entrance (section 1, corresponding to the section with c subscript) to the Tube's exit (section 21, corresponding to the section with e subscript) with 1 cm step, adding a section inside the metal connector (section with ic subscript, 2 cm distance from section 1), for a total of 22 sections (Figure 3.18).

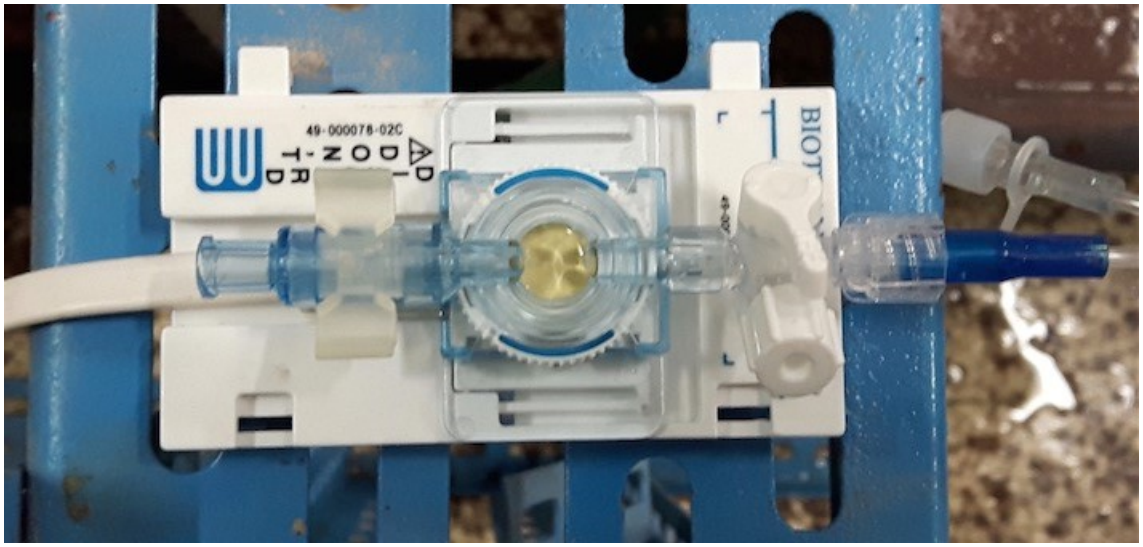

Figure 3.19: Biotrans pressure transducer

The pressure transducer used to measure the pressure inside the Tube is the Biotrans pressure transducer (Figure 3.19, the same utilized in P/F Study), connected to the catheter and of course to the data acquisition system. This transducer can acquire signals between -30 and 300 mm Hg (that is between -41 and 408 cm H_2O).

3.5.2 Results

Every test, in each of the 22 sections and for both MDWC type 1 and 2, was repeated at least five times, thus the total performed tests was more than 220. In each section, the result of the pressure transducer is the average value of the five test repetitions.

The first tests carried out concerned the evaluation of the piezometric head h inside the Tube using MDWC type 1. Figure 3.20 shows the piezometric head in every Tube's sections, considering a total head at the Tube's entrance H_c varying from 1.5 m to 0.3 m with steps of 0.1 m: the circles

are the piezometric head h measured with the pressure transducers, joined with a dotted line. Thus, every line represents a moment in time at a fixed total head at the Tube's entrance H_c; the same color represents the same H_c. It's possible to see that the behavior of the piezometric head h is the same for each H_c: h decrease from upstream to downstream almost monotonically until section 21 (i.e. section with e subscript) where it is zero (at the Tube's exit there is constant atmospheric pressure). Moreover, in each section the piezometric head h decreases linearly as H_c drops.

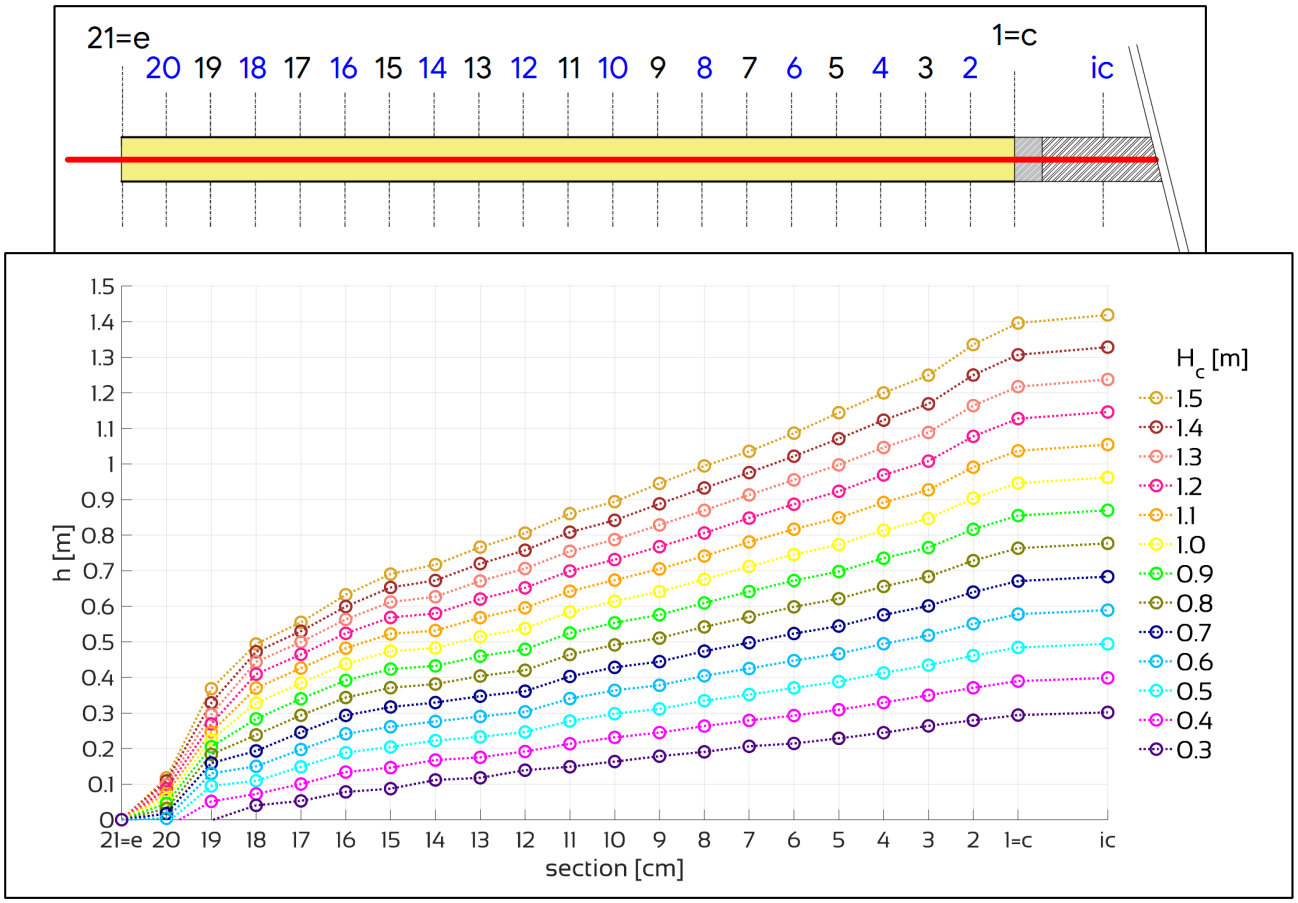

Figure 3.20: FV-tests results: piezometric head h in the Tube's sections; same color represents the same total head at the Tube's entrance H_c

Subsequently, FV-tests with MDWC type 2 was done, to evaluate the total head H inside the Tube. Figure 3.21 shows the total head in every Tube's sections, using the same scheme of the previous Figure 3.20. The trend is like the trend of the piezometric head h: for a given H_c, it decreases from upstream (where of course $H_1 \equiv H_c$) to downstream monotonically until section 21, corresponding to the Tube's exit, so that it can be written as:

$$H_{21} \equiv H_e = \frac{{u_e}^2}{2g} \qquad 3.3$$

where u_e is the jet exit velocity and g is the acceleration gravity.

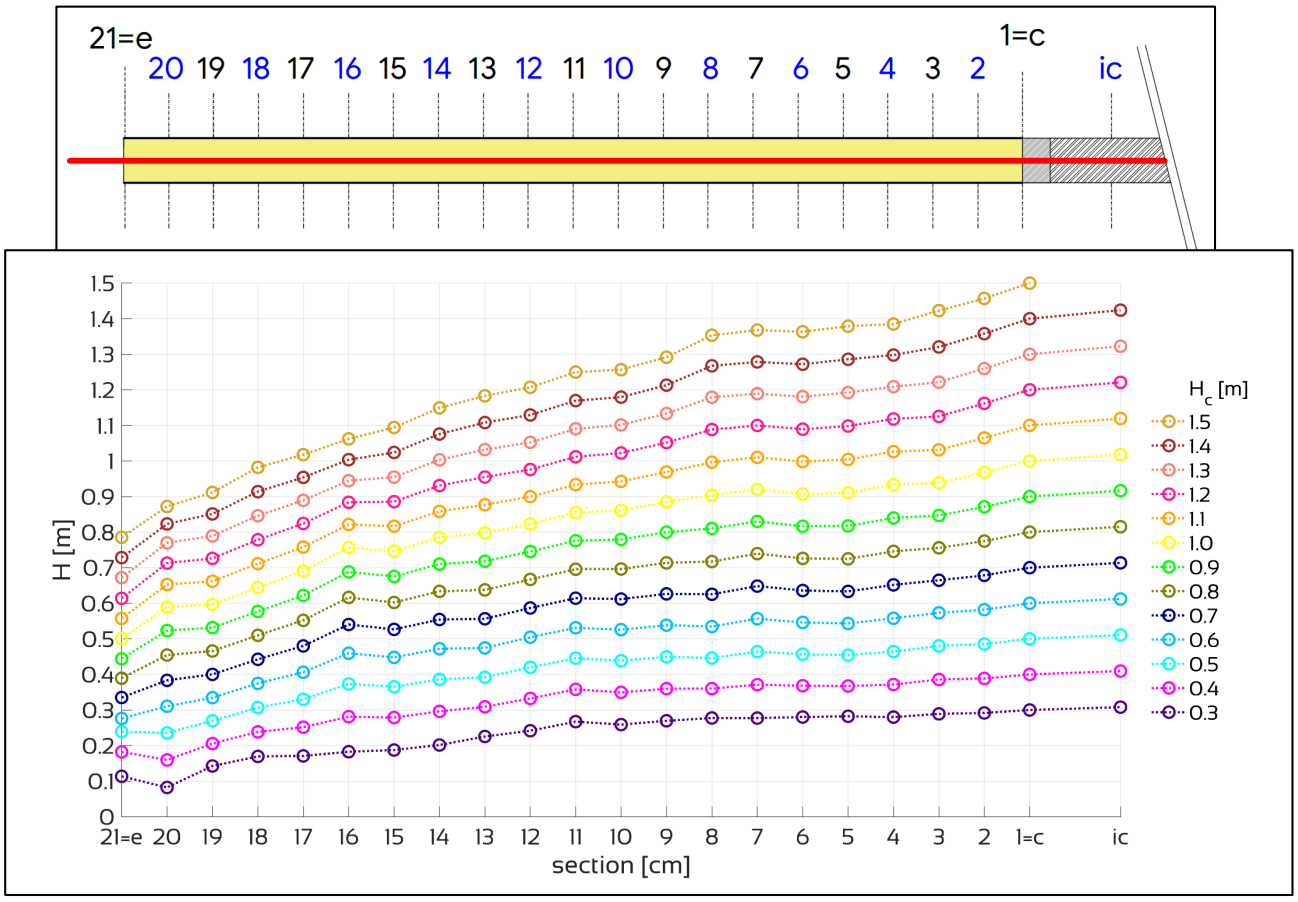

Figure 3.21: FV-tests results: total head H in the Tube's sections; same color represents the same total head at the Tube's entrance H_c

The total head H_1 at section 1 was also used to verify the measurements made with MDWC type 2; in fact, in this section the total head must coincide with the reference head H_c. In Figure 3.22 the purple line shows the correlation between the total head H_c and the measured total head with MDWC tybe 2 $H_{c,MDWC\ type\ 2}$. The yellow part represents the area of the graph where $H_c > H_{c,MDWC\ type\ 2}$, the blue part represents the area where $H_c < H_{c,MDWC\ type\ 2}$, while the perfect agreement between the two data is the dashed black line.

It can be seen that there is a very good accordance between the two values, with the purple line almost over the dashed black line; the relative standard deviation is about 1 % (6.6 mm the standard deviation).

Piezometric head h and total head H can be written:

$$h = z + \frac{P}{\gamma} \tag{3.4}$$

$$H = z + \frac{P}{\gamma} + \frac{u^2}{2g} \tag{3.5}$$

where z is the elevation of the point above a reference plane, P is the pressure inside the Tube, u the velocity, γ the water specific weight and g the acceleration gravity. From 3.4 and 3.5, knowing h and H, and given the fact that z=0 because the Tube is placed on a horizontal plane, it's possible to obtain the velocity of the water in every section of the Tube with:

$$u = \sqrt{(H - h)2g} \qquad 3.6$$

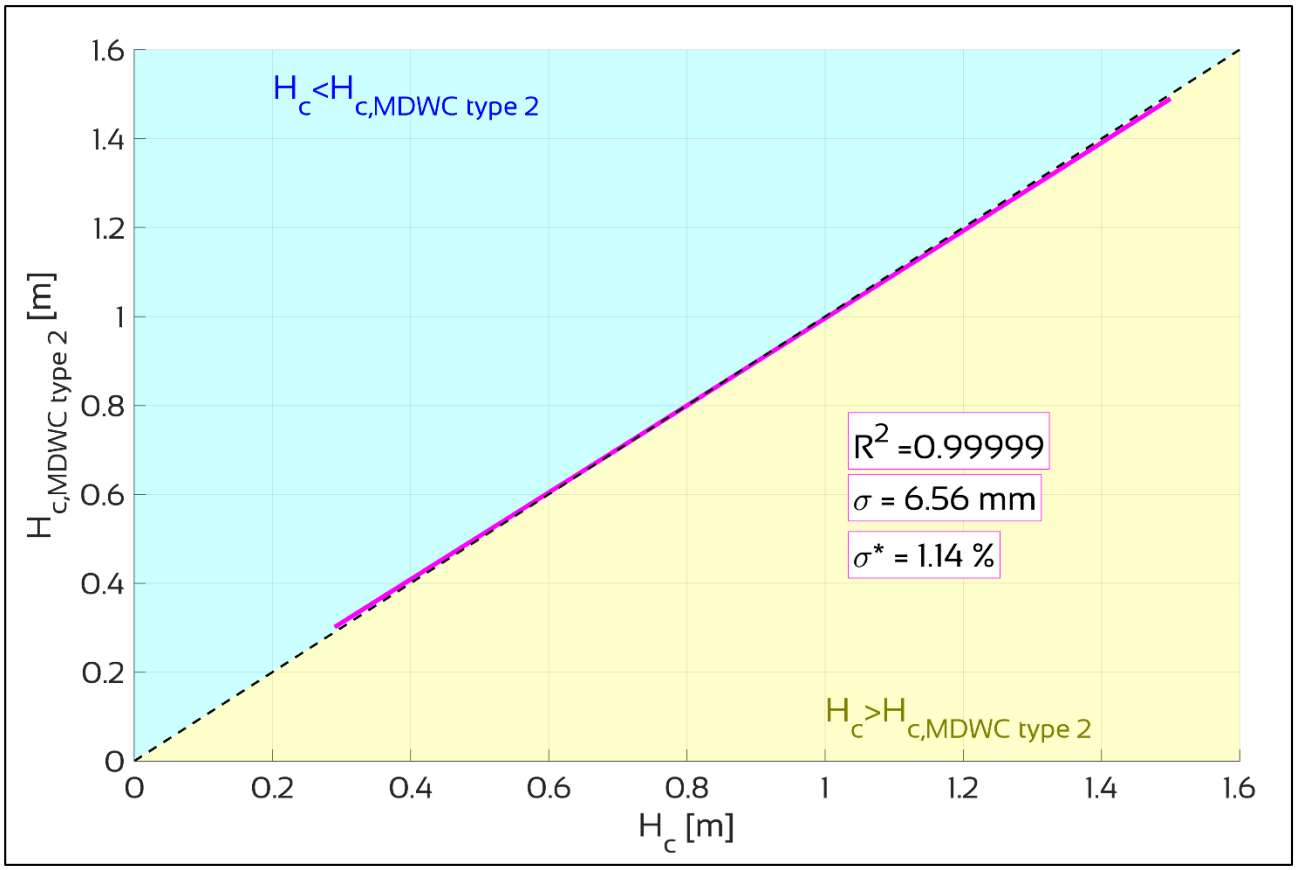

Figure 3.22: the purple line represents the total head at Tube entrance H_c as a function of the measured total head with MDWC type 2: the relative standard deviation σ* between the two values is about 1% (σ=6.6 mm the standard deviation)

The results can be seen in Figure 3.23, using the same scheme of the previous figures: for a given H_c, the velocity of the water gradually increase from upstream, where in section 1 we have $u_1=u_c$, to downstream until reaching u_e in the exit section 21.

It is also possible to analyze the cross-sectional area of the Tube, which can be obtained by dividing the flow rate Q by the water velocity u: Ω=Q/u. In this regard, it can be introduced the area ratio:

$$\alpha = \frac{\Omega}{\Omega_u} \qquad 3.7$$

where Ω_u is the "undisturbed" cross-sectional area of the Tube, as explained in section 2.3.5.1. This dimensionless value of the cross-sectional area will be useful in the next chapter, dedicated to the numerical model.

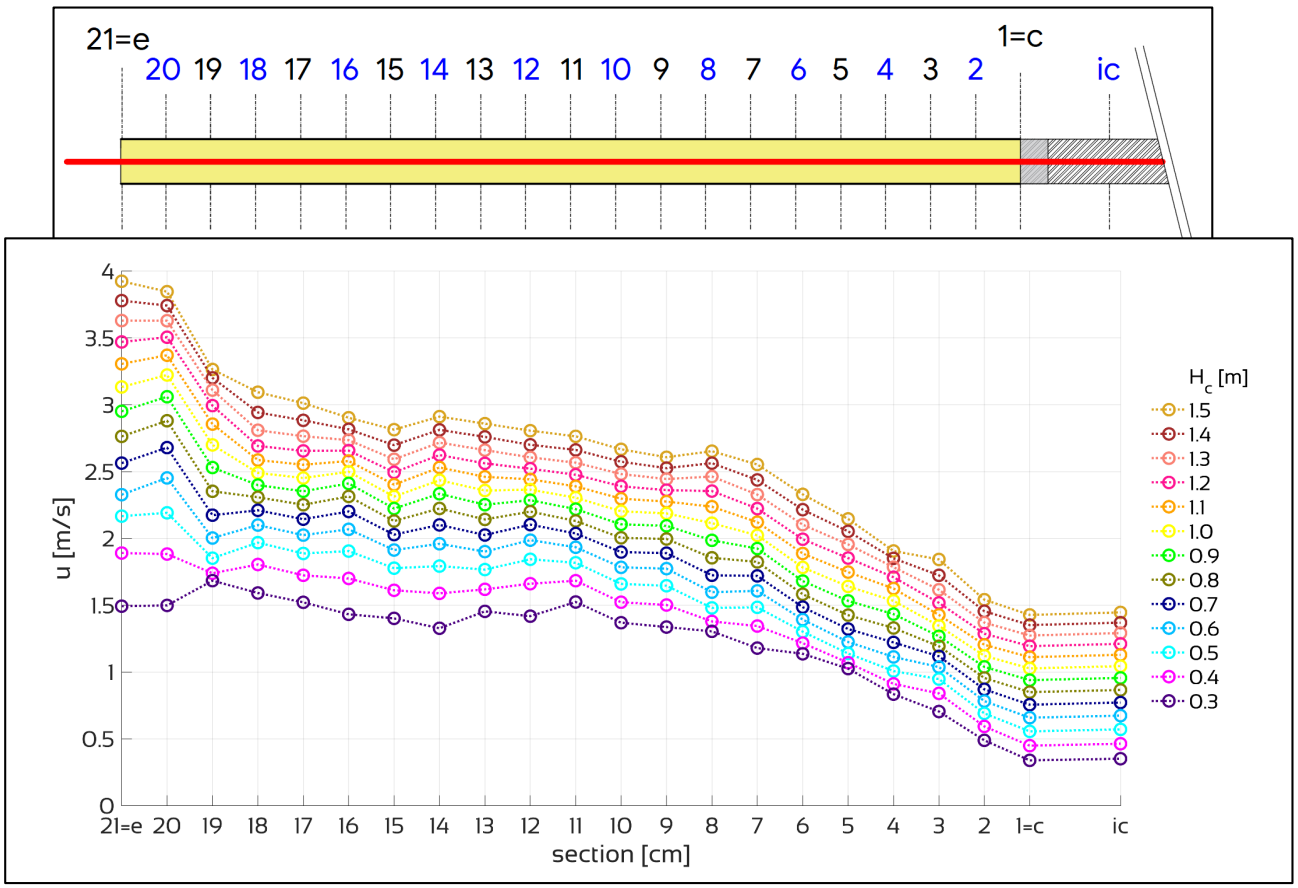

Figure 3.23: water velocity u in the Tube's sections; same color represents the same total head at the Tube's entrance H_c

Figure 3.24 shows the results of the FV-tests regarding the cross-sectional area ratio α: every circle of the same color is the calculated area ratio at same total head at the Tube's entrance H_c (as shown in legend), while the black dashed line represents the "undisturbed" cross-sectional area, that is when $\Omega=\Omega_u$.

It can be seen that in section ic and in section 1, that is the Tube's entrance, the cross-sectional area is fixed by the metal connector, so it is $\alpha_1 = \alpha_c$ (i.e., $\Omega_1=\Omega_c$). Then, from section 1 to section 7 the area abruptly decrease: that is because the Tube is linked to the metal connector, which has a much larger external cross-sectional area then the Tube's internal area (values shown in Table 2.1). Then, from section 7, α slightly decrease till section 21, which corresponds to the Tube's exit ($\alpha_{21} = \alpha_e$, or $\Omega_{21}=\Omega_e$).

To be noted that the collapse of the Tube is higher as the total head at the Tube's entrance H_c decreases.

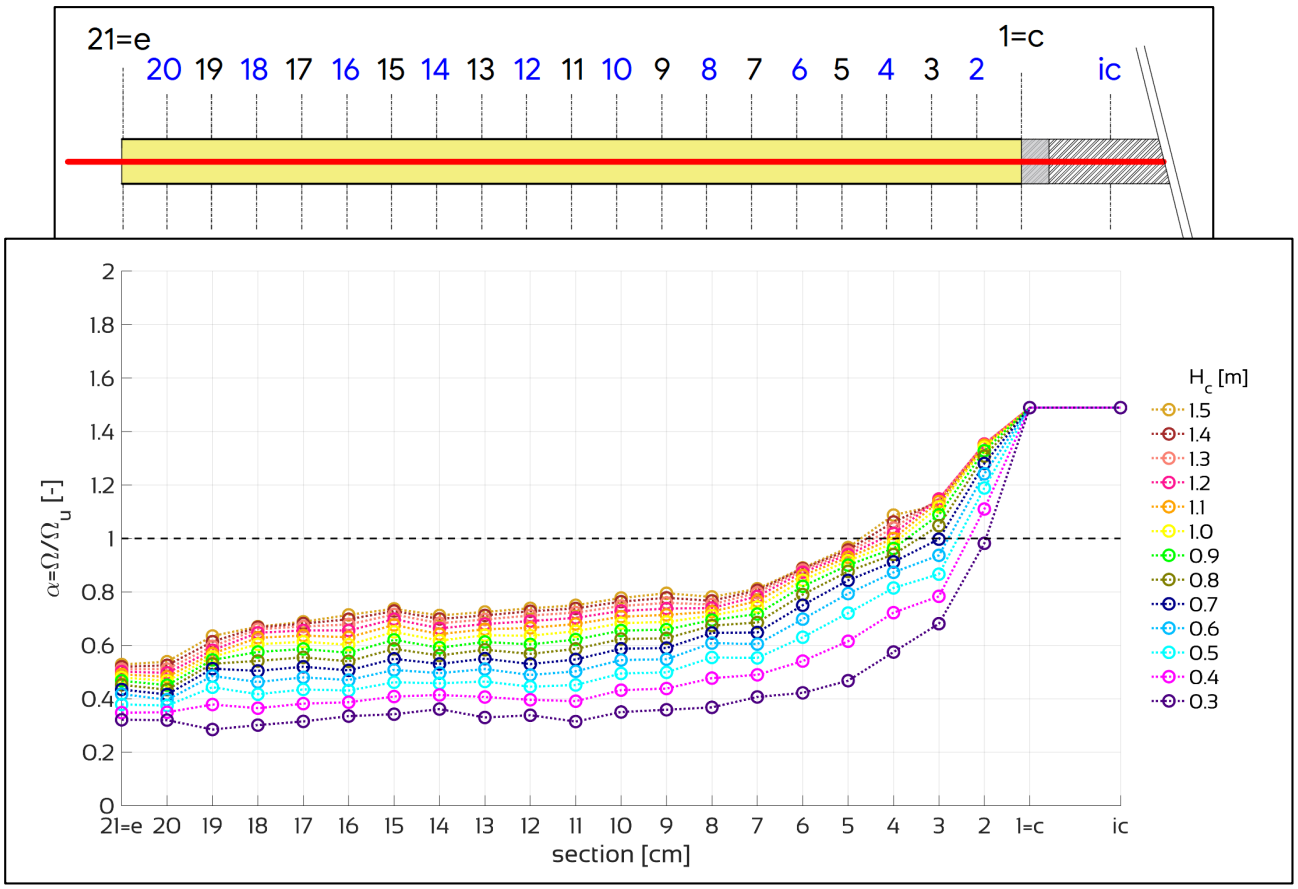

Figure 3.24: cross-sectional area ratio α in the Tube's sections; same color represents the same total head at the Tube's entrance H_c

4 NUMERICAL MODEL AND SIMULATION

The experimental tests have been simulated by using a numerical model based on the equations governing the one-dimensional flow through a collapsible tube. The aims of the numerical simulation are:

- verify the validity of the fluid mechanics equations when applied to the LUT;
- extend the range of the experimental conditions in order to investigate specific problems.

In the following, the structure of the numerical model is described.

4.1 ONE-DIMENSIONAL GOVERNING EQUATIONS

4.1.1 MASS AND MOMENTUM CONSERVATION

The basic equations for one-dimensional flow of an incompressible fluid in elastic collapsible tubes are mass and momentum conservation for the fluid phase:

$$\frac{\partial Q}{\partial x}+\frac{\partial \Omega}{\partial t}=0 \tag{4.1}$$

$$\frac{1}{g}\frac{\partial u}{\partial t}+\frac{u}{g}\frac{\partial u}{\partial x}+\frac{1}{\gamma}\frac{\partial P}{\partial x}=-J \tag{4.2}$$

where u [m/s] is the average velocity of the fluid and P [Pa] is the pressure, Ω [m^2] is the Tube's cross-sectional area, Q [m^3/s] the flow rate, γ [N/m^3] the water specific weight and g [m/s^2] the gravity acceleration.

Complementary equations can be written to quantify energy losses. Denoting by J [-] the total head loss per unit length of the Tube, the Darcy-Weisbach equation provides the following relationship:

$$J=\frac{\lambda}{4R_h}\frac{u^2}{2g} \tag{4.3}$$

with R_h=Ω/p [m] hydraulic radius of the Tube's cross-sectional area and p [m] the wetted perimeter. λ [-] is the friction factor assumed for turbulent flow as described by (Colebrook, 1939):

$$\frac{1}{\sqrt{\lambda}}=-2\log\left(\frac{2.51}{Re\sqrt{\lambda}}+\frac{\varepsilon}{4R_h}\right) \tag{4.4}$$

where Re [-] is the Reynolds number and ε [m] the roughness of the Tube.

4.1.2 TUBE LAW EQUATION

For given values of Q, ε and D_u, there are five unknowns (Ω, P, u, J and λ) and four equations (4.1, 4.2, 4.3 and 4.4). Hence, an additional equation is required, which is known as the Tube Law (hereafter, ***TL***), relating the transmural pressure P_{tm} to the cross-sectional area ratio α of the Tube. The main purpose of the TL is to reproduce the mechanical deformation of the Tube, which may show distinct behavior depending on the values of the internal and external pressure. A currently used TL is the following (Elad et al, 1987):

$$P = K \cdot \left(\alpha^{\beta_1} - \alpha^{-\beta_2}\right) + P_{ext} \qquad 4.5$$

where P_{ext} is the external pressure (that is, the pressure outside the Tube), $\alpha = \Omega/\Omega_u$ is the area ratio, with Ω_u the "undisturbed" cross-sectional area of the Tube (section 2.3.5.1) and the exponents β_1 and β_2 are two real numbers whose usual ranges to describe the behavior of collapsible tubes are $\beta_1 \geq 0$ and $0 < \beta_2 \leq 2$ (Toro & Siviglia, 2013).

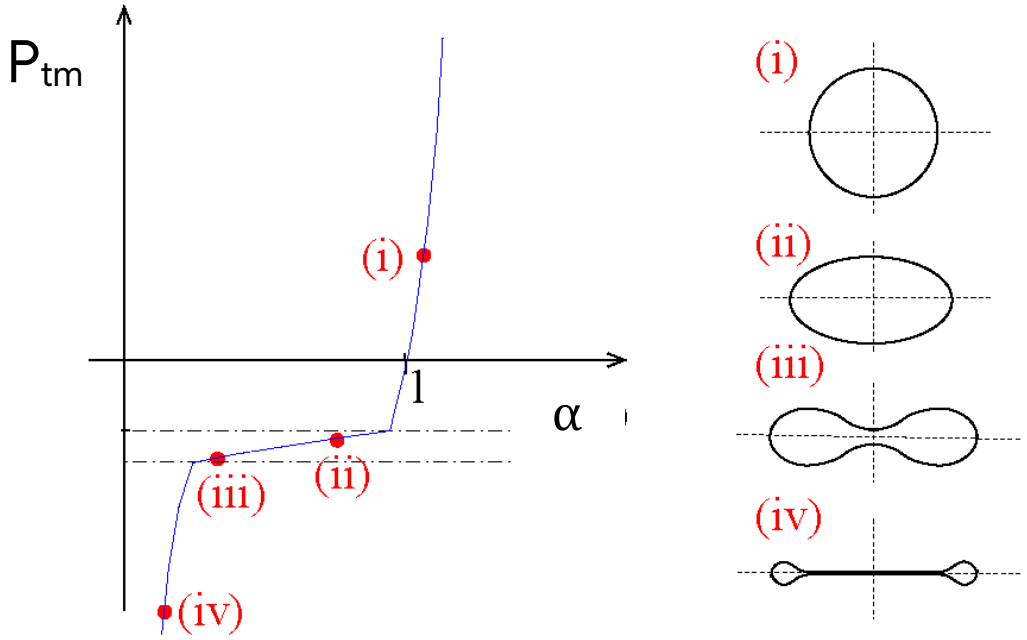

Figure 4.1: behavior of the section of an elastic tube when varying the transmural pressure (Carpenter & Pedley, 2003)

The transmural pressure P_{tm} is then defined as $P_{tm}=P-P_{ext}$. Since the Tube walls are not able to self-support, when P_{tm} is approaching zero or becomes negative the cross-section does not remain cylindrical as in rigid tubes but it collapse to an approximately elliptical configurations as shown in Figure 4.1. On the other hand, when P_{tm} is positive, the Tube tends to assume a cylindrical section and behaves as an elastic tube.

In equation 4.5 K [N/m] is the effective stiffness of the Tube (Shapiro, 1977), a quantity that represents both the elastic properties of the material and the wall thickness; in a thin walled tube (i.e. when $s_u << R_u$), it can be assumed equal to (Brook et al, 1999, Müller & Toro, 2013):

$$K = \frac{E}{12(1-\nu_P{}^2)}\left(\frac{s_u}{R_u}\right)^3 \qquad 4.6$$

where E [Pa] is the elasticity of the Tube, ν_P [-] is the Poisson coefficient, and s_u and R_u are the "undisturbed" thickness and radius of the Tube, respectively.

However, this TL works correctly only if the Tube is subjected to an isotropic external pressure (Figure 4.2a); in our case study, the external pressure is practically oriented only in the vertical direction (Figure 4.2b).

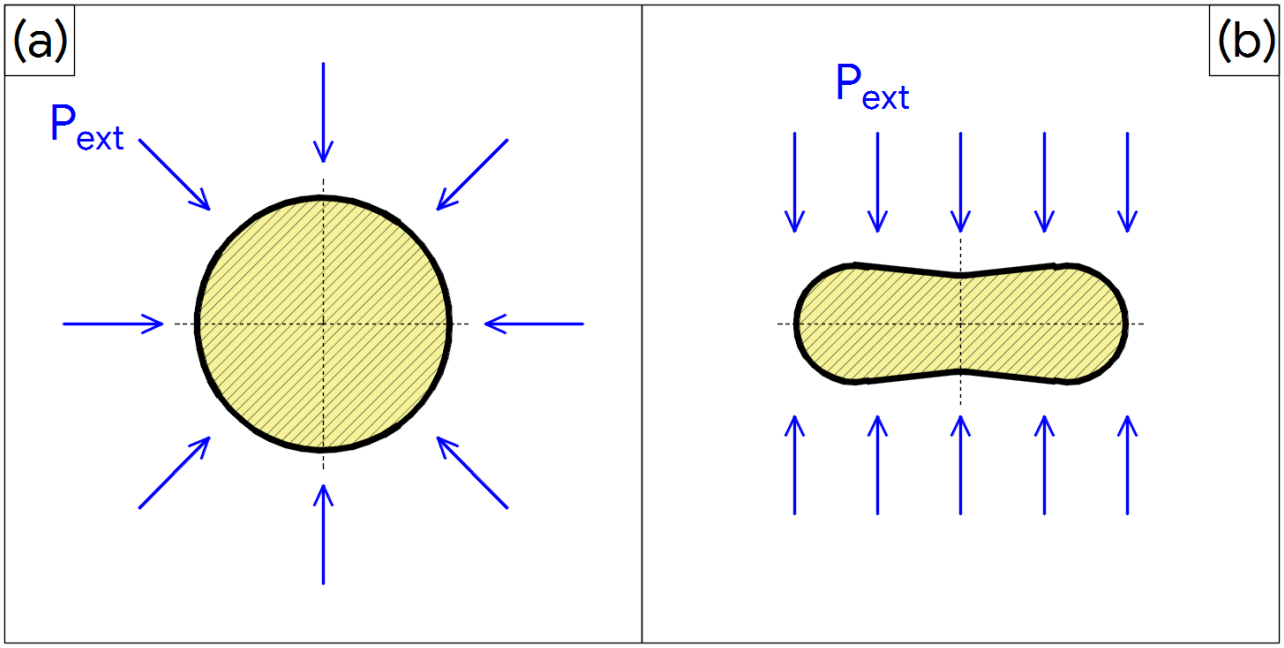

Figure 4.2: (a) isotropic external pressure; (b) our case study: the pressure is oriented only in the vertical direction

That is why our experimental data cannot fit the TL 4.5 proposed by literature (Figure 4.3), for any values of β_1 and β_2. Therefore, it is proposed here a specific TL, chosen to fit our experimental data as follows:

$$P_{tm} = \tan[(\alpha + m_1)\cdot\pi]\cdot m_2 + m_3 \qquad 4.7$$

$$m_1 = 0.5 \qquad 4.8$$

$$m_2 = 6000 \qquad 4.9$$

$$m_3 = -725.8\cdot H_c - 607.5 \qquad 4.10$$

Since the coefficient m_3 is a function of the total head at the beginning of the Tube H_c, the results is a bundle of curves as shown in Figure 4.4.

The TL also determines the wave speed c_w of small area perturbations, which according to Toro & Siviglia, 2003 is given by:

$$c_w = \sqrt{\frac{\Omega}{\rho}\frac{\partial(P - P_{ext})}{\partial\Omega}} = \sqrt{\frac{\alpha \cdot m_2 \cdot \pi}{\cos^2(\alpha \cdot \pi + m_1 \cdot \pi) \cdot \rho}} \qquad 4.11$$

Following Shapiro, 1977, it's possible to introduce the speed index $S=u/c_w$, a dimensionless controlling parameter that is the analogous to the Froude number for open channel flows: in steady flow in collapsible tubes, we can have subcritical flow if $S<1$ or supercritical flow if $S>1$.

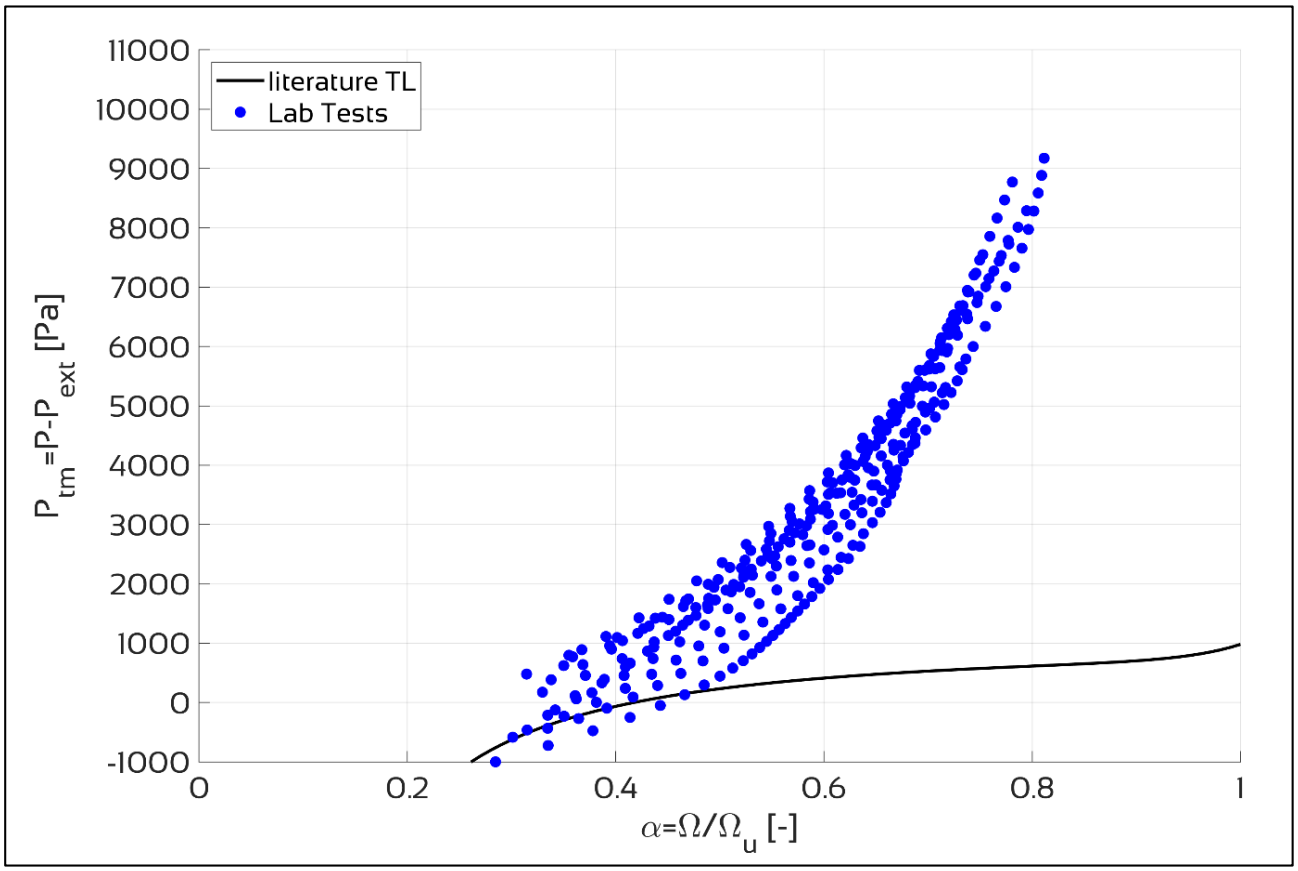

Figure 4.3: experimental measures of area ratio α (blue dots) and an example of the literature TL 4.5 (black line)

Subcritical flow implies that elastic perturbations can propagate both in downstream and upstream direction, while in supercritical flow elastic perturbations can propagate only in the downstream direction. Physically, it means that if, at some point along the Tube, $S>1$, then variation in downstream condition cannot propagate upstream (since small-amplitude waves travels at speed $c_w<u$).

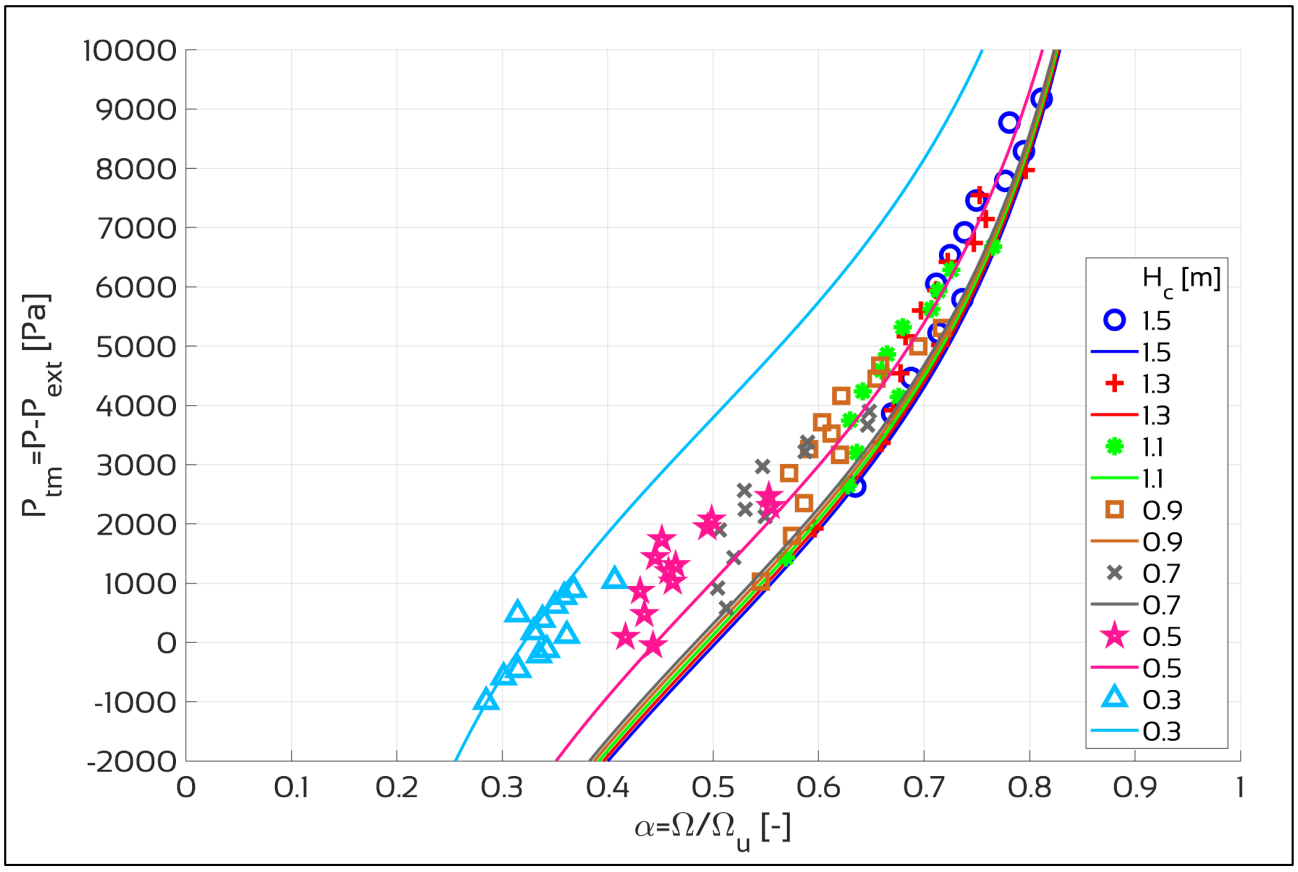

Figure 4.4: experimental data classified by H_c values (see legend); the lines, colored same as the markers, represent the interpolation of the data with the TL (equation 4.7)

4.2 Model implementation

The mathematical model represented by equations 4.1-4.5 is here adopted to describe the tests carried out on the physical model (section 3.5). The mathematical model has been implemented to simulate the experimental results under the following hypotheses:

- the fluid is water at ambient temperature (T=20÷25 °C, ρ=1000 kg/m^3), incompressible fluid, with dynamic viscosity μ=10^{-3} Pa·s and kinematic viscosity v=10^{-6} m^2/s;
- the emptying rate is defined according to the observed range of micturition: the level of a supply tank, H_0, measured with respect to the horizontal axis of the Tube, is decreasing in time as shown in Figure 4.5, starting from a maximum value $H_{0,max}$=1.6 m and ending when the level is $H_{0,min}$=0.2 m. The observed minimum emptying time is about 180 s;
- the falling level is the upstream boundary condition for the system, while the downstream boundary condition is represented by the constant atmospheric pressure at the Tube's exit;
- the Tube length between the upstream metal connector and the exit section is 20 cm (section 2.2);
- the spatial resolution of the experimental results is Δx=1 cm;

- time resolution is related to the acquisition frequency of the instrumentation which has been 12.5 Hz, corresponding to a sampling period of Δt=0.08 s.

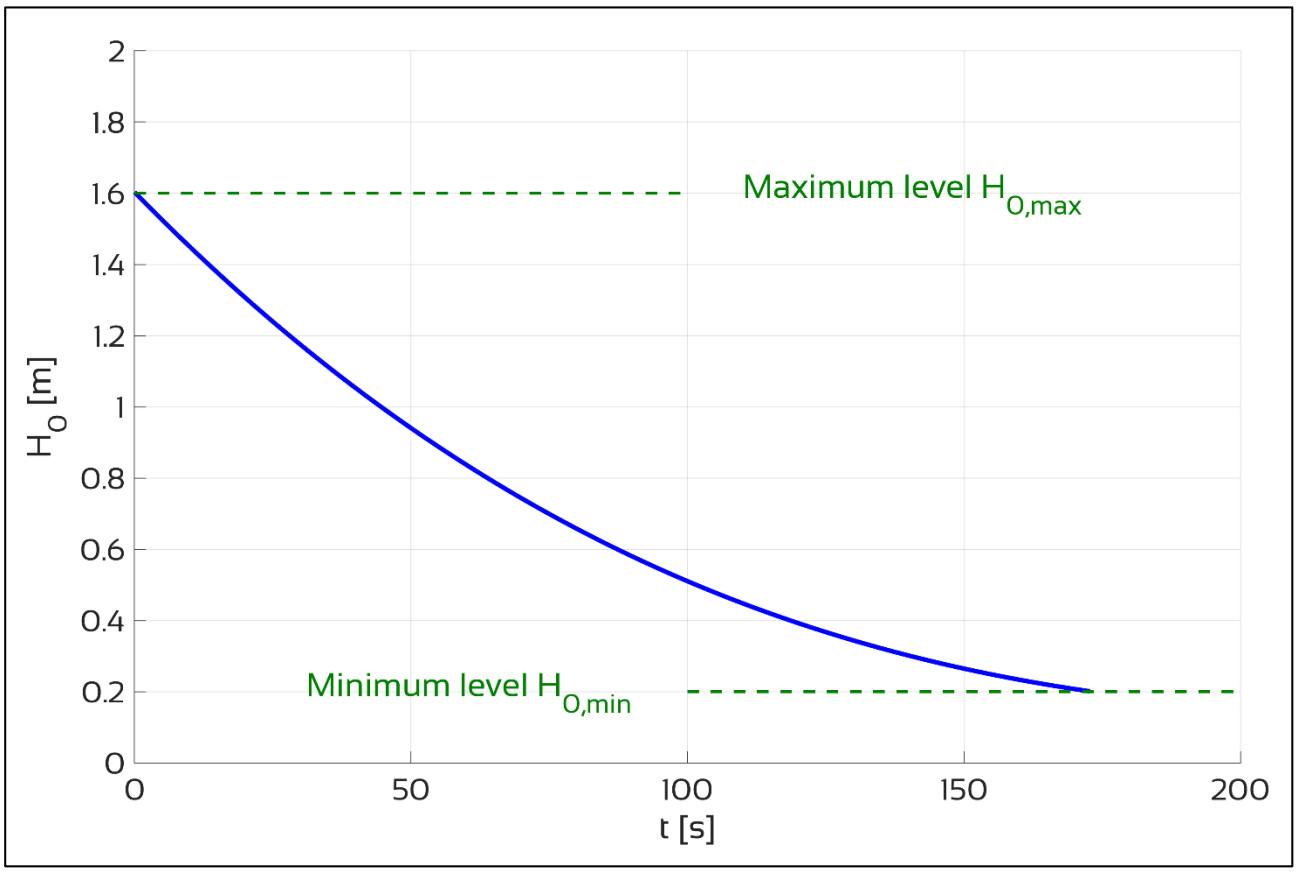

Figure 4.5: level in the supply tank, referred to the horizontal axis of the Tube, during the emptying phase

4.2.1 QUASI-STEADY FLOW HYPOTHESIS

The processes under study are governed by the imposed level H_0 decreasing in the supply tank, as shown in Figure 4.5. It can be assumed that the time rate of change of any variable is of the same order of magnitude as the time gradient of the emptying process. If the variables are changing slowly with time the fundamental fluid dynamics are essentially the same as for steady flow considering a time step, even if it has to be taken into account of the overall changes taking place over the total period of the emptying process. In this condition the flow can be assumed to be steady over a time step, i.e. quasi-steady flow, if the time variations at a spatial location are much smaller compared to spatial variations for any quantity. To verify this condition, let us reformulate eq. 4.2 in the following way:

$$\frac{1}{g}\frac{\partial u}{\partial t}+\frac{u}{g}\frac{\partial u}{\partial x}+\frac{1}{\gamma}\frac{\partial P}{\partial x}=\frac{1}{g}\frac{\partial u}{\partial t}+\frac{\partial}{\partial x}\left(\frac{u^2}{2g}+z+\frac{P}{\gamma}\right)+J=\frac{1}{g}\frac{\partial u}{\partial t}+\frac{\partial H}{\partial x}+J=0 \qquad 4.12$$

Quasi-steady flow can be assumed if:

$$\frac{1}{g}\frac{\partial u}{\partial t} \ll \frac{\partial H}{\partial x} \qquad 4.13$$

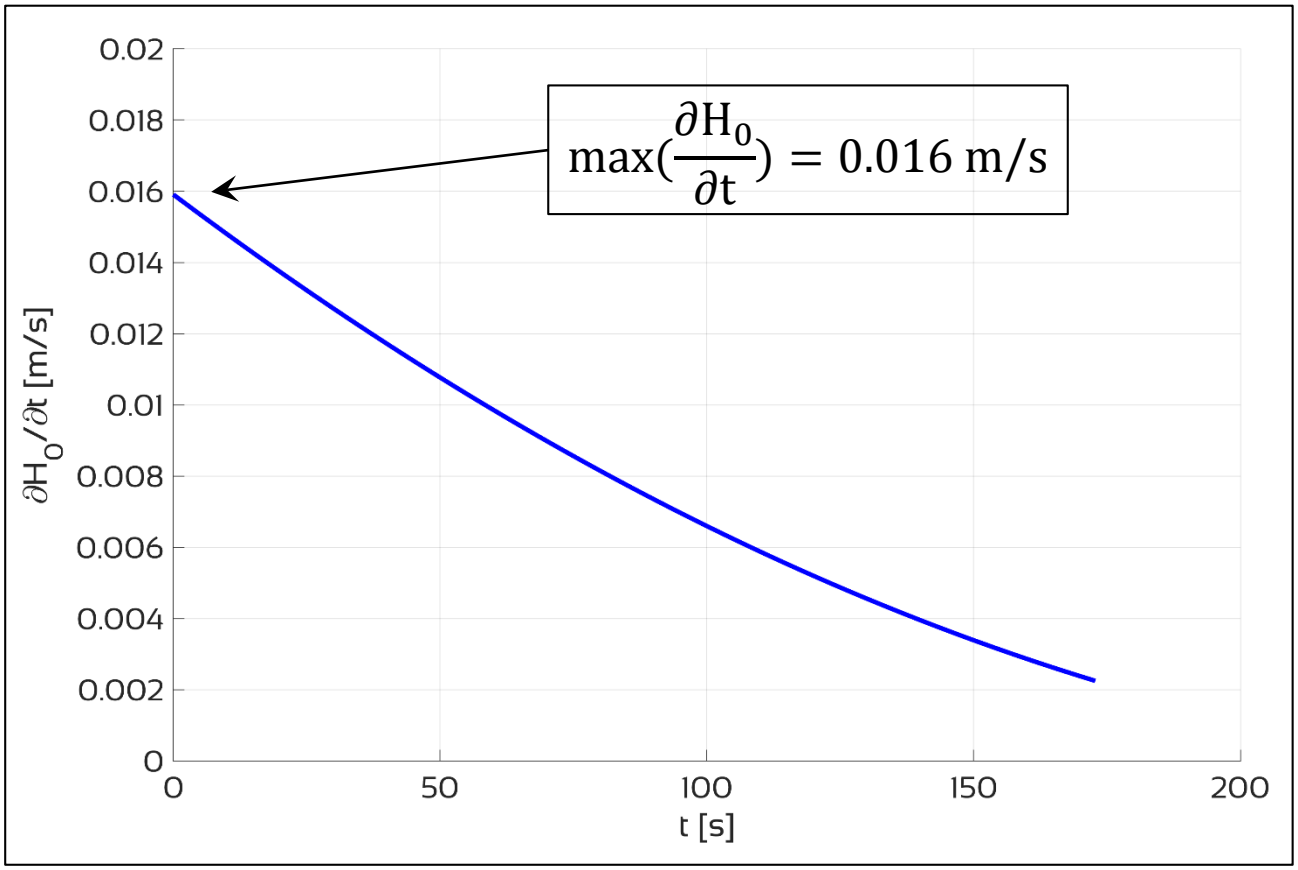

Figure 4.6: time variation of first derivative of H_0

With reference to Figure 4.6, it can be seen that the maximum value of the time variation of H (that is equal to H_0) is in the order of 1.6 cm/s at the beginning of the emptying process. The time step of the frequency acquisition is Δt=0.08 s; hence, during this time step the head H is varied of 0.13 cm. Assuming that this head variation leads to an analogous kinetic energy variation during the time step $\Delta t=t_{i+1}-t_i$ (where t_{i+1} and t_i are two successive time instants) as follows:

$$[\Delta H]_{\Delta t} = \left[\Delta\left(\frac{u^2}{2g}\right)\right]_{\Delta t} \qquad 4.14$$

then, the corresponding velocity variation Δu can be derived from 4.14 as follows:

$$2g[\Delta H]_{\Delta t} = [\Delta(u^2)]_{\Delta t} = [{u_{i+1}}^2 - {u_i}^2]_{\Delta t} = [(u_{i+1} - u_i)(u_{i+1} + u_i)]_{\Delta t} \qquad 4.15$$

By posing $u_{i+1} + u_i = 2u_m$, we obtain:

$$2g[\Delta H]_{\Delta t} = [(u_{i+1} - u_i)2u_m]_{\Delta t} \quad 4.16$$

that is:

$$\frac{g}{u_m}[\Delta H]_{\Delta t} = [\Delta u]_{\Delta t} \quad 4.17$$

and finally:

$$\frac{1}{\Delta t}\frac{[\Delta H]_{\Delta t}}{u_m} = \frac{1}{\Delta t}\frac{[\Delta u]_{\Delta t}}{g} \quad 4.18$$

By substituting $[\Delta H]_{\Delta t}/\Delta t$=0.016 m/s and u_m=2 m/s (average value from experiments, see Figure 3.23), the dimensionless term can be calculated as:

$$\frac{1}{\Delta t}\frac{[\Delta u]_{\Delta t}}{g} = 0.008 \quad 4.19$$

This term has to be compared to ∂H/∂x (4.13): in Table 4.1 it is reported the average values of ∂H/∂x and the correspondent total head at the Tube's entrance H_c, that also can be deducted from Figure 3.21. It can be seen that ∂H/∂x is in the order of 1÷4, much greater than 4.19.

∂H/∂x [-]	H_c [m]
3.57	1.5
3.14	1.3
2.71	1.1
2.28	0.9
1.82	0.7
1.30	0.5
0.93	0.3

Table 4.1: the average values of ∂H/∂x and the correspondent H_c

The unsteady feature of the process over the emptying time is taken into account only through the tank continuity equation 2.1, while the time dependent terms in equations 4.1 and 4.2 can be neglected. Finally, we obtain the simplified equations as follow:

$$u\frac{\partial \Omega}{\partial x} + \Omega\frac{\partial u}{\partial x} = 0 \quad 4.20$$

$$\frac{u}{g}\frac{\partial u}{\partial x} + \frac{1}{\gamma}\frac{\partial P}{\partial x} = -J \quad 4.21$$

4.2.2 THE SIMULATED PHYSICAL SYSTEM

As shown in Figure 4.7, the study domain is discretized with sections every Δx=1 cm, excluding the upstream and downstream subtracts (from section 1 to 6 and from section 20 to 21) in order to better define boundary conditions.

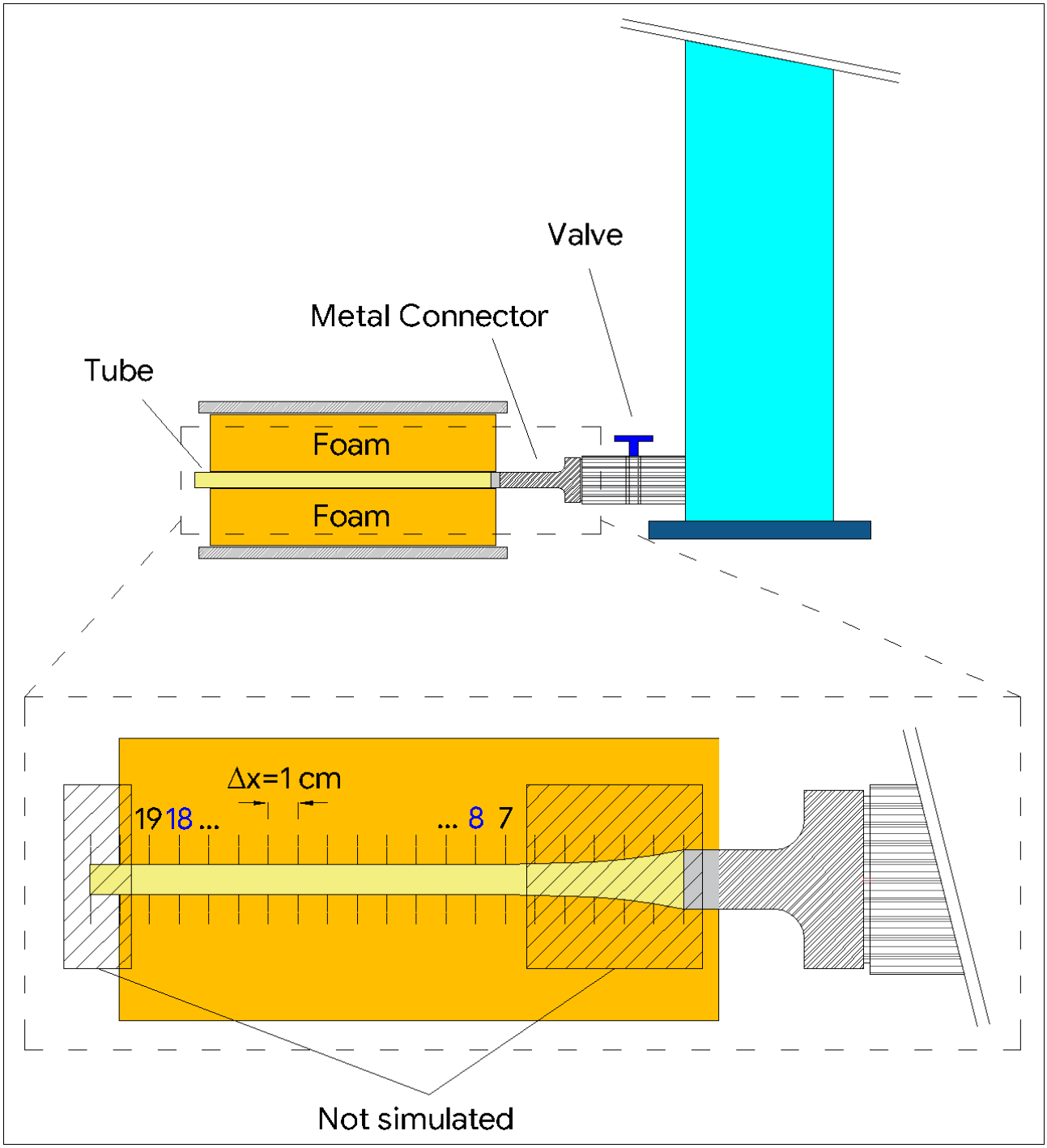

Figure 4.7: study domain: the regions from section 1 to 6 and from section 20 to 21 are excluded from the numerical simulation

In fact, these sub-tracts cannot be simulated by the numerical model since:

- from 1 to 6 the Tube is attached to a metal connector that has a much larger section, as explained in section 3.5.2;
- section 20 and section 21 are placed outside the foam compression in order to reproduce the navicular fossa, an enlargement of the urethra immediately proximal to the external urethral meatus (D2 in Figure 1.4), as seen in section 2.2.

Regarding the hydraulic radius, defined by $R_h=\Omega/p$, where Ω is the cross-sectional area and p the wetted perimeter, and considering that inside the Tube with the catheter a flow in an annulus is developed, it has been considered the following:

$$R_h = \frac{\Omega}{p_u + p_{cat}} = \frac{\alpha \cdot \Omega_u}{p_u + p_{cat}} \qquad 4.22$$

where p_{cat} is the perimeter of the catheter and Ω_u and p_u the "undisturbed" cross-sectional area and perimeter of the Tube, respectively.

From the analysis of experimental data of the speed index S (Figure 4.8), it is possible to see that the flow inside the Tube is always subcritical, since S<1. Because of subcritical flow, it is recognized that numerical solution has to be obtained by solving the equation starting from section 19 and moving along the upstream direction (Siviglia & Toffolon, 2013).

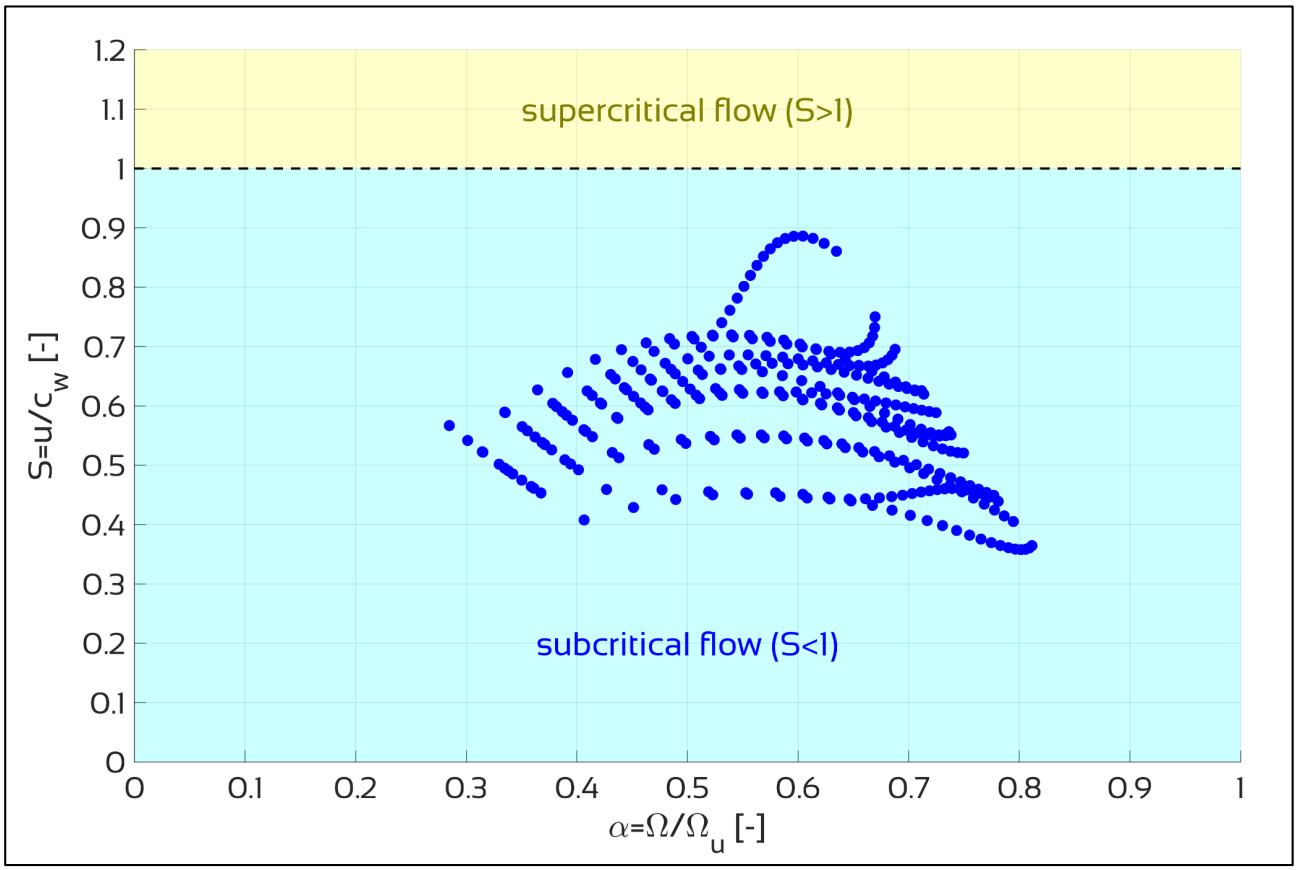

Figure 4.8: speed index S from experimental data as a function of the area ratio α

The system is consisting of equations 4.3, 4.4, 4.7, 4.20, 4.21 and 4.22. Considering that $\Omega = \alpha \cdot \Omega_u$ (from eq. 3.7) and that $p_u = \pi \cdot D_u$ ("undisturbed" perimeter of the Tube, Table 4.2), the system of partial derivative equations can be written as follows:

- ***Basic equations:***

$$u\frac{\partial \alpha}{\partial x}\Omega_u + \alpha\Omega_u\frac{\partial u}{\partial x} = 0 \quad (4.23)$$

$$\frac{u}{g}\frac{\partial u}{\partial x} + \frac{1}{\gamma}\frac{\partial P}{\partial x} = -J \quad (4.24)$$

$$P_{tm} = \tan[(\alpha + m_1)\cdot\pi]\cdot m_2 + m_3 \quad (4.25)$$

- ***Complementary equations:***

$$J = \frac{\lambda}{4R_h}\frac{u^2}{2g} \quad (4.26)$$

$$\frac{1}{\sqrt{\lambda}} = -2\log\left(\frac{2.51}{Re\sqrt{\lambda}} + \frac{\varepsilon}{4R_h}\right) \quad (4.27)$$

$$R_h = \frac{\alpha\Omega_u}{p_u + p_{cat}} \quad (4.28)$$

Then, the PDE system can be numerically discretized as follows:

$$\frac{u_i^{(k)} + u_{i+1}}{2}\cdot\frac{\alpha_i^{(k)}\cdot\Omega_u - \alpha_{i+1}\cdot\Omega_u}{\Delta x} + \frac{\alpha_i^{(k)}\cdot\Omega_u + \alpha_{i+1}\cdot\Omega_u}{2}\cdot\frac{u_i^{(k)} - u_{i+1}}{\Delta x} = 0 \quad (4.29)$$

$$\frac{u_i^{(k)} + u_{i+1}}{2\cdot g}\cdot\frac{u_i^{(k)} - u_{i+1}}{\Delta x} + \frac{1}{\gamma}\cdot\frac{P_i^{(k)} - P_{i+1}}{\Delta x} = J^{(k)} \quad (4.30)$$

$$P_i^{(k)} - P_{ext} = \tan\left[\left(\alpha_i^{(k)} + m_1\right)\cdot\pi\right]\cdot m_2 + m_3 \quad (4.31)$$

$$J^{(k)} = \frac{\lambda_i^{(k)}\cdot(p_u + p_{cat})\cdot\left(\frac{u_{i+1} + u_i^{(k)}}{2}\right)^2}{8\cdot\frac{\alpha_{i+1} + \alpha_i^{(k-1)}}{2}\cdot\Omega_u\cdot g} \quad (4.32)$$

$$\frac{1}{\sqrt{\lambda_i^{(j,k)}}} = -2\log\left(\frac{2.51}{\frac{Re_{i+1} + Re_i^{(k)}}{2}\cdot\sqrt{\lambda_i^{(j-1,k)}}} + \frac{\varepsilon\cdot(p_u + p_{cat})}{4\cdot\frac{\alpha_{i+1} + \alpha_i^{(k)}}{2}\cdot\Omega_u}\right) \quad (4.33)$$

where the unknowns are P_i, u_i and α_i.

Starting from the known values of u_{19} and Q, and therefore α_{19} at section 19, we can estimate the unknown values at section 18 P_{18}, u_{18} and α_{18}; then, the system is solved by proceeding by iterations to the subsequent sections and using the following criterion for convergence:

$$\frac{\lambda_{i+1}^{(j,k)} - \lambda_{i+1}^{(j-1,k)}}{\lambda_{i+1}^{(j-1,k)}} < 10^{-7} \quad (4.34)$$

$$\frac{\alpha_i^{(k)} - \alpha_i^{(k-1)}}{\alpha_i^{(k-1)}} < 10^{-7} \quad (4.35)$$

In the following Table 4.2 the main parameters used in the equations of the input numerical model are shown.

parameter	explanation	value
Ω_u	Tube's "undisturbed" cross-sectional area	$2.734 \cdot 10^{-5}$ m^2
D_u	Tube's "undisturbed" diameter	$5.9 \cdot 10^{-3}$ m
p_u	Tube's "undisturbed" perimeter	0.0185 m
R_u	Tube's "undisturbed" radius	$2.95 \cdot 10^{-3}$ m
s_u	Tube's "undisturbed" thickness	$0.3 \cdot 10^{-3}$ m
D_{cat}	catheter external diameter	$2 \cdot 10^{-3}$ m
p_{cat}	catheter's perimeter	$6.3 \cdot 10^{-3}$ m
P_{ext}	external pressure on the tube	981 Pa

Table 4.2: parameters and constants used in the numerical model

4.3 RESULTS

The numerical model has been applied for simulating the Laboratory tests described in section 3; each of them is associated with a particular physical condition of the LUT as follows:

- ***"Diagnostic flow condition" tests (FV-tests)***, characterized by the presence of the catheter inside the Tube;
- ***"Physiological flow condition" tests (Physiological-tests)***, used to calibrate the Innovative Instrumentation, characterized by a free Tube;
- ***"Pathological flow condition" tests (Pathological-tests)***, used to simulate the behavior of the Tube with urethral obstructions.

Let's see the results for each of the three above conditions.

4.3.1 "DIAGNOSTIC FLOW CONDITION" SIMULATIONS

First, the numerical model has been applied to the FV-tests (section 3.5). Since in these tests the pressures and the total head inside the Tube has been measured, it is possible to calibrate the coefficients m_1, m_2 and m_3 of the TL (Tube Law, equation 4.7).

In the following figures the comparison between Laboratory tests and numerical simulation is shown, for a total head at the Tube's entrance of H_c=0.6 m (Figure 4.9) and of H_c=1.2 m (Figure 4.10). It's possible to see the very good agreements between the cross-sectional area ratio α (Figure 4.9a and Figure 4.10a), the total head H (Figure 4.9b and Figure 4.10b) and the piezometric head h (Figure 4.9c and Figure 4.10c). The simulated tract is shown in Figure 4.7.

Very satisfying results can also be seen in Figure 4.11 showing:

- (a), the comparison between cross-sectional area ratio α from Laboratory tests and cross-sectional area ratio α_{est} from numerical simulations;
- (b), the comparison between total head H from Laboratory tests and total head H_{est} from numerical simulations;
- (c), the comparison between piezometric head h from Laboratory tests and piezometric head h_{est} from numerical simulations.

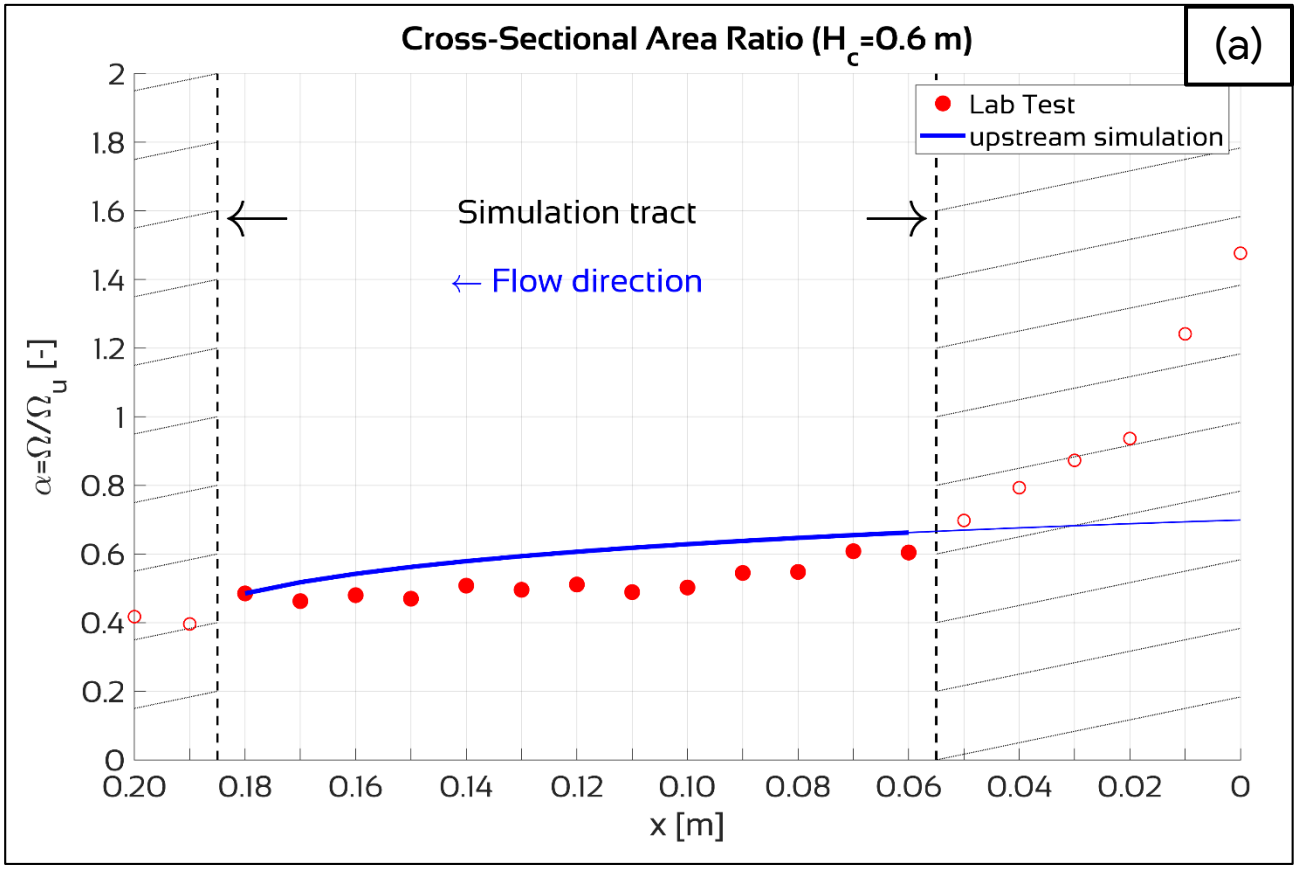

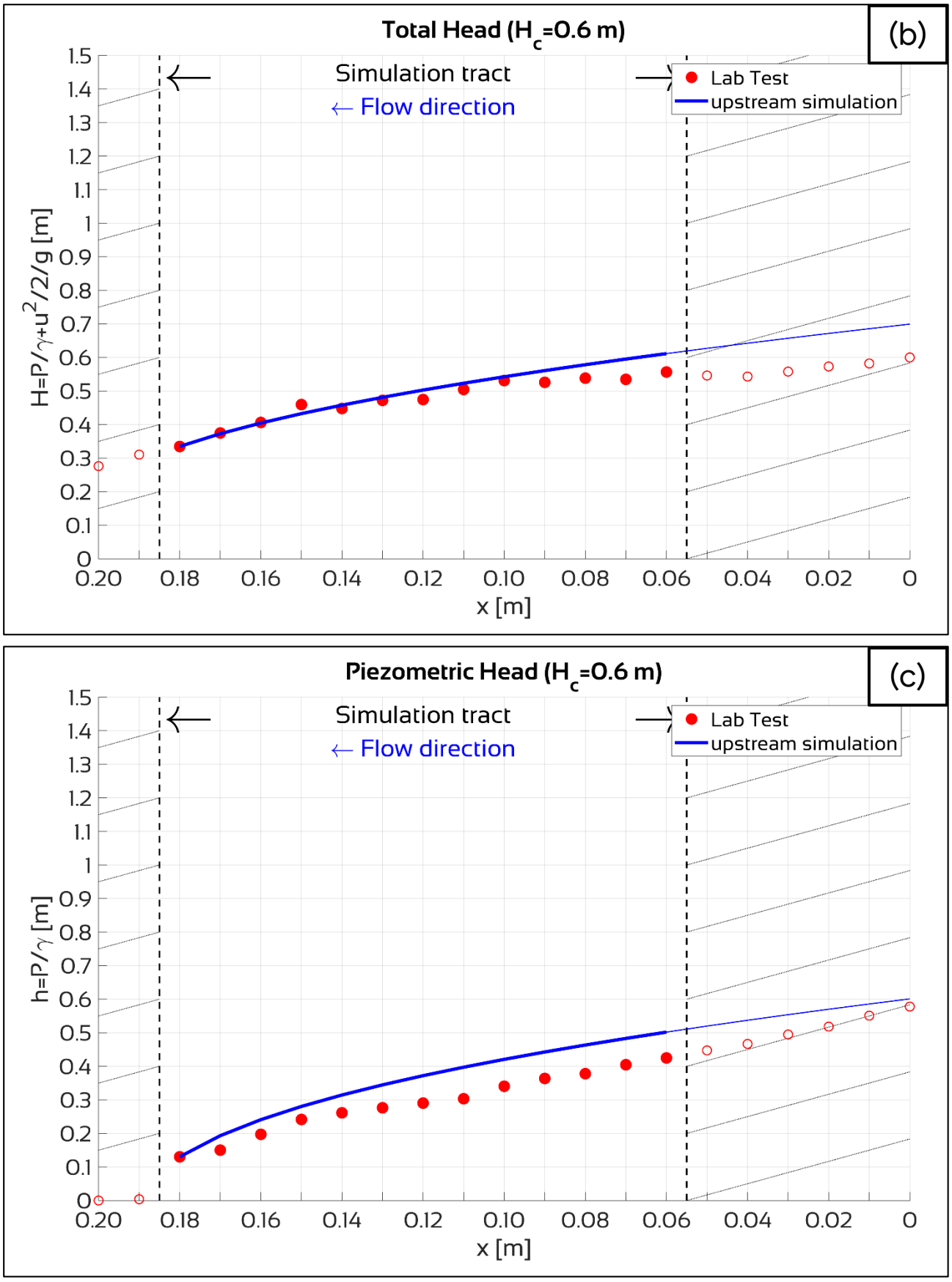

Figure 4.9: comparison between Laboratory test (red dots) and numerical upstream simulation (blue line) with a total head at the Tube's entrance H_c=0.6 m: (a) cross-sectional area ratio a, (b) total head H and (c) piezometric head h, along the Tube

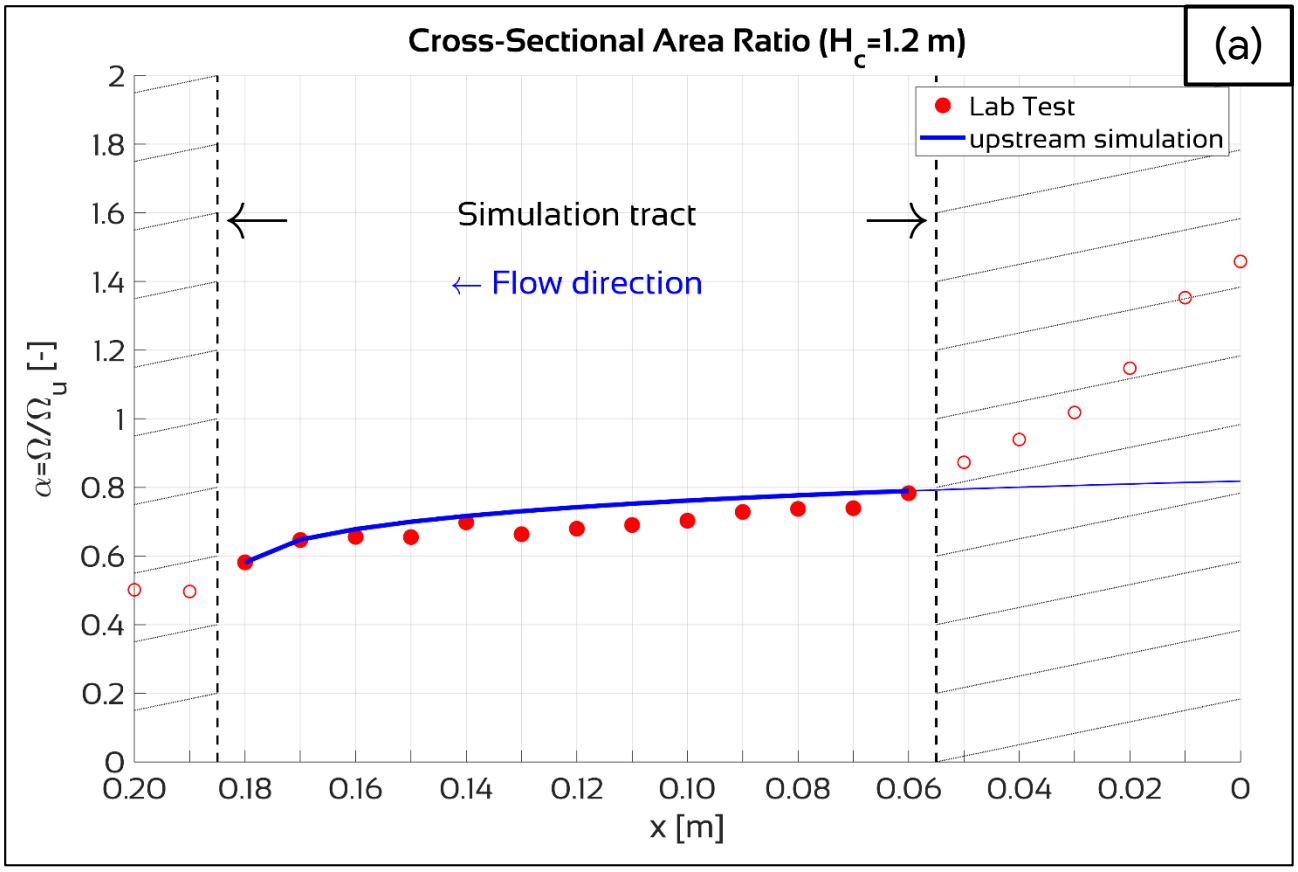
Cross-Sectional Area Ratio (H_c=1.2 m)
(a)
Lab Test
upstream simulation
Simulation tract
← Flow direction
α=Ω/Ω_u [-]
x [m]

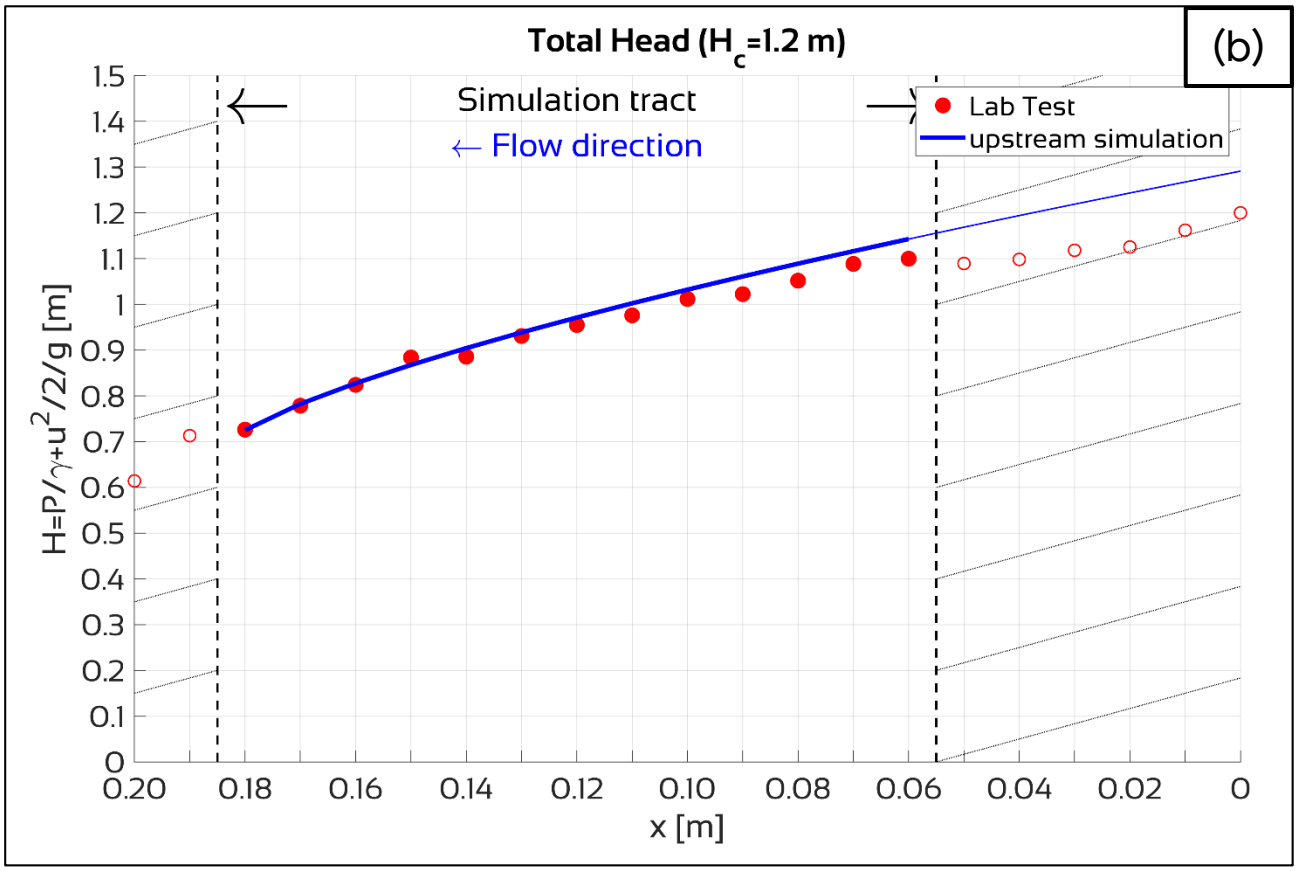
Total Head (H_c=1.2 m)
(b)
Lab Test
upstream simulation
Simulation tract
← Flow direction
H=P/γ+u^2/2/g [m]
x [m]

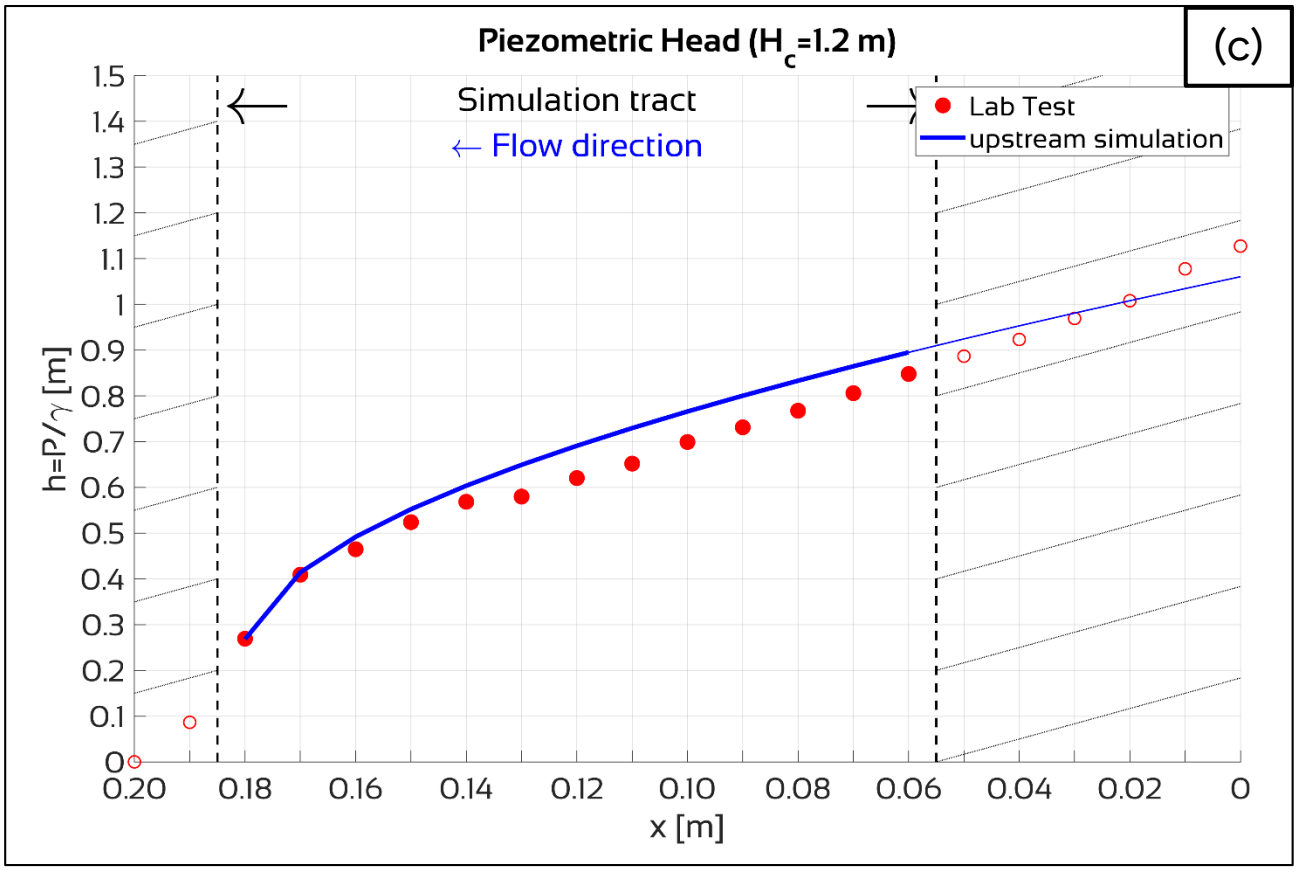

Figure 4.10: comparison between Laboratory test (red dots) and numerical upstream simulation (blue line) with a total head at the Tube's entrance H_c=1.2 m: (a) cross-sectional area ratio a, (b) total head H and (c) piezometric head h, along the Tube

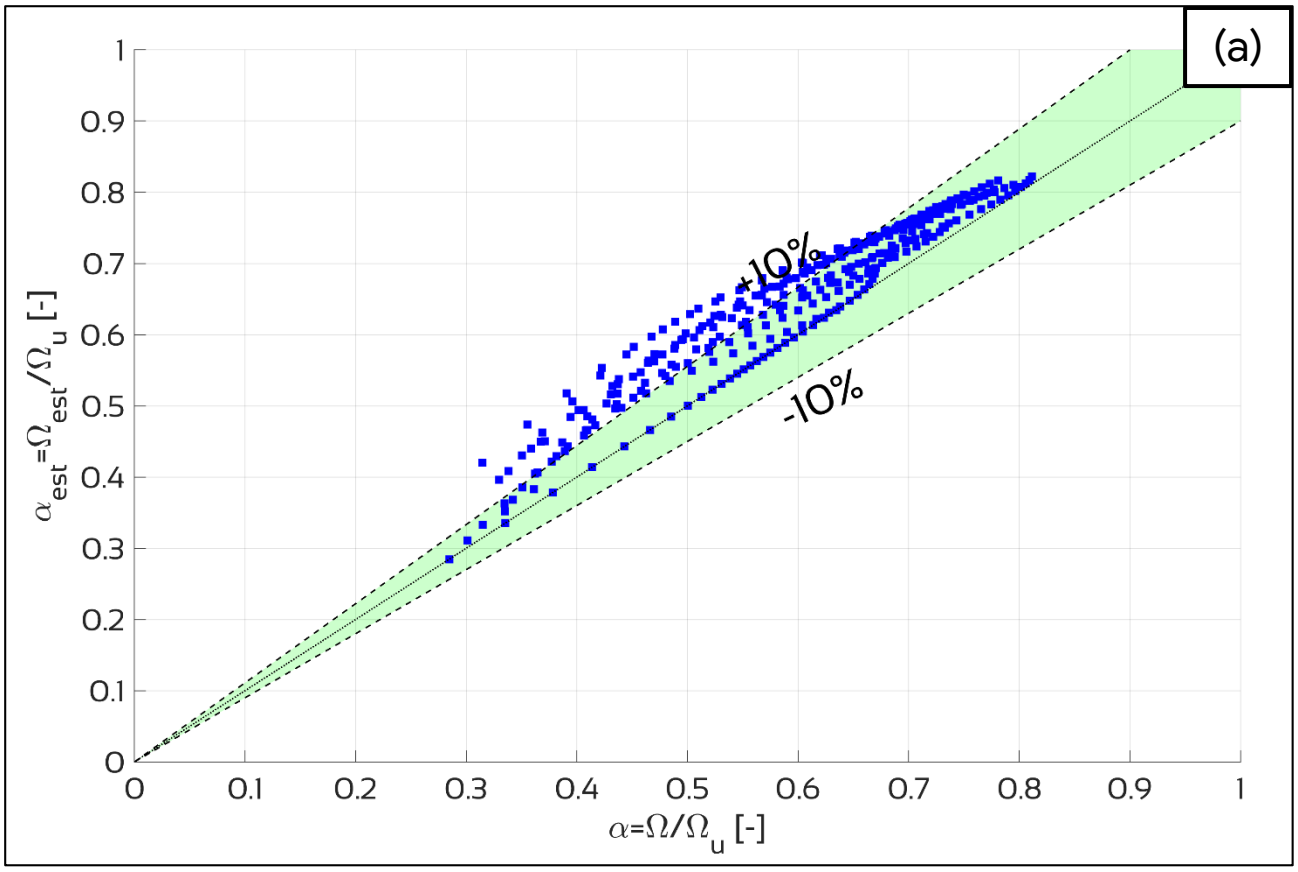
(a)
+10%
-10%
$\alpha_{est}=\Omega_{est}/\Omega_u$ [-]
$\alpha=\Omega/\Omega_u$ [-]

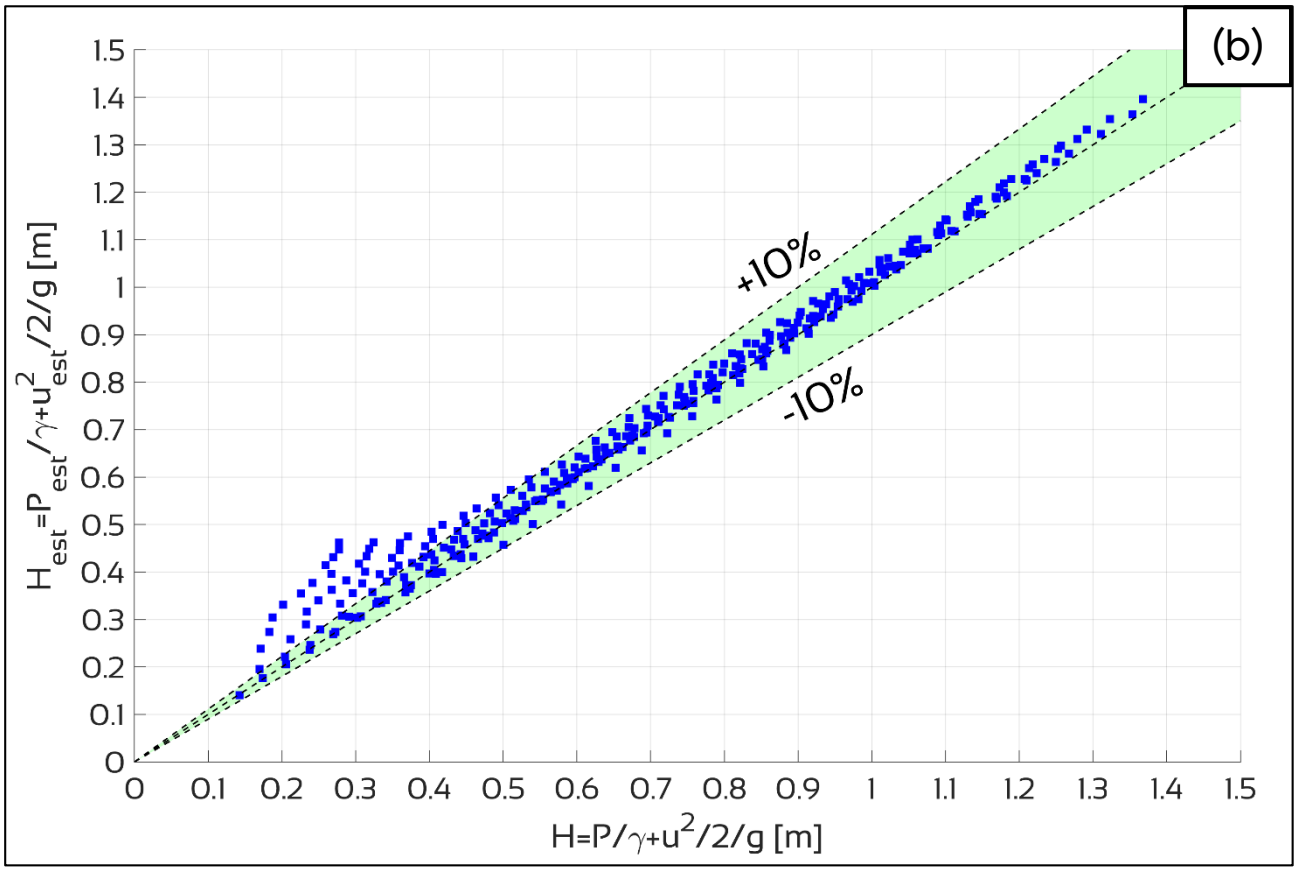
(b)
+10%
-10%
$H_{est}=P_{est}/\gamma+u^2_{est}/2/g$ [m]
$H=P/\gamma+u^2/2/g$ [m]

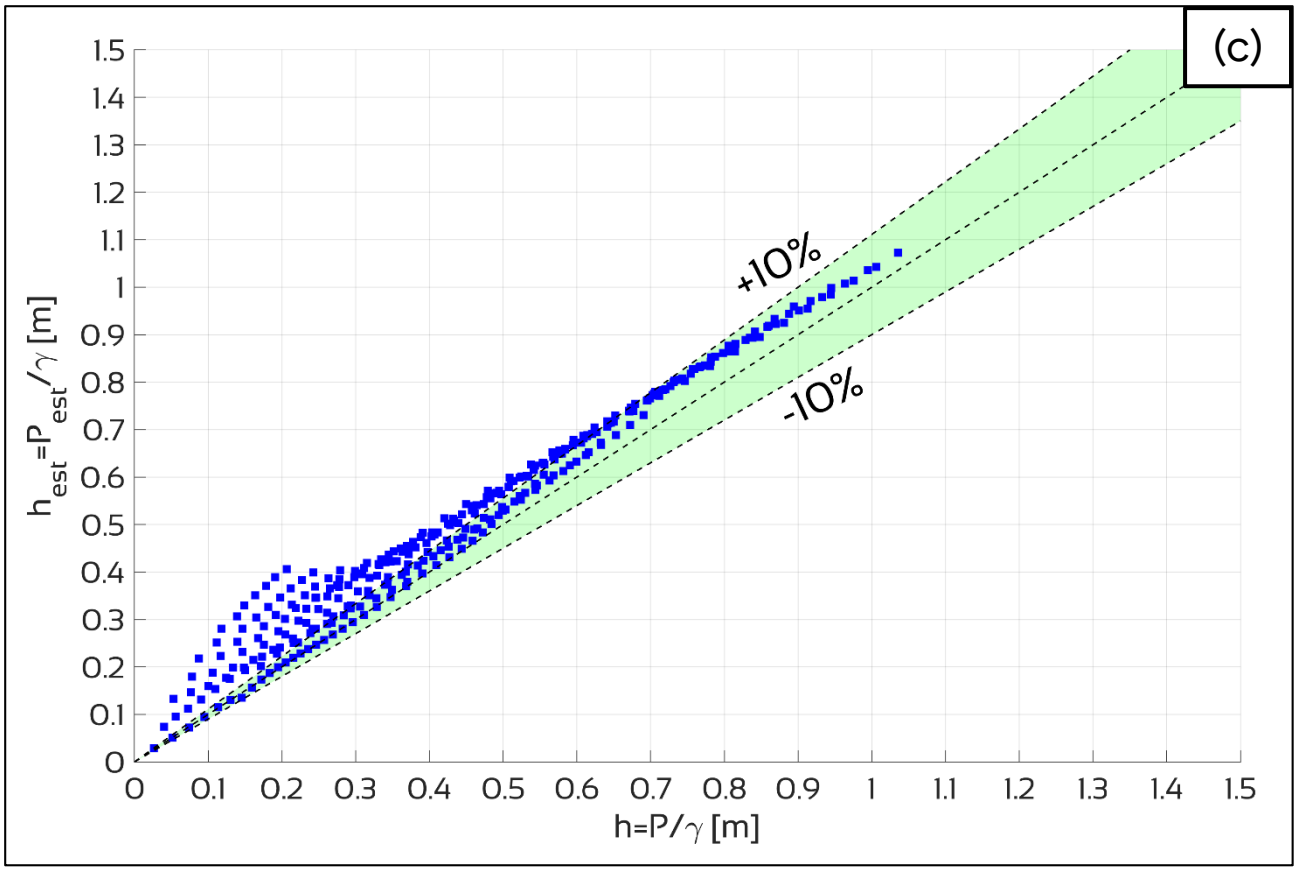

Figure 4.11: comparison between Laboratory tests and numerical simulation: (a) cross-sectional area ratio α; (b) total head H; (c) piezometric head h

4.3.2 "PHYSIOLOGICAL FLOW CONDITION" SIMULATIONS

Physiological-tests (see section 3.1) are based on the analysis of the various physical parameters of the jet at the Tube's exit while emptying the tank: they are denoted as "physiological" because the Tube is catheter free, so reproducing the behavior of the urethra of a healthy male.

In this type of tests, the Laboratory data are:

- the flow rate Q,
- the velocity u_e at the exit of the Tube (and, consequently, the cross-sectional area ratio α_e and the total head H_e),
- the total head at the Tube's entrance H_c.

The numerical model has been calibrated on the Diagnostic-tests, *characterized by the presence of the catheter inside the Tube*. It is therefore obvious that modifications have to be made to adapt it to the Physiological-tests case.

Another consideration to make is that in Physiological-tests no data is available inside the Tube. Consequently, to define the boundary conditions necessary for the resolution of the numerical system, some hypotheses have been made, using Diagnostic-tests data.

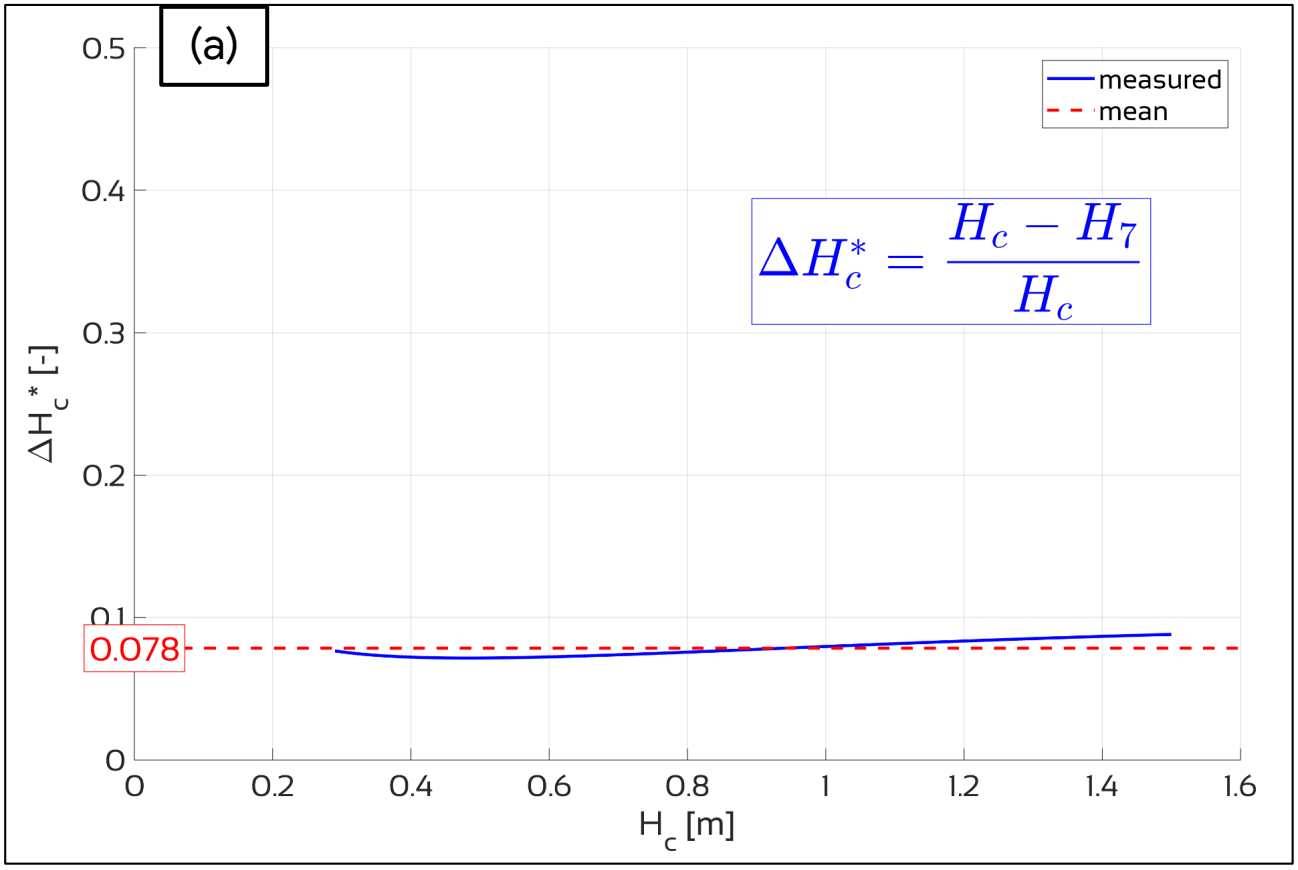
(a)
measured
mean
$\Delta H_c^* = \frac{H_c - H_7}{H_c}$
0.078
ΔH_c^* [-]
H_c [m]
0
0.1
0.2
0.3
0.4
0.5
0.2
0.4
0.6
0.8
1
1.2
1.4
1.6

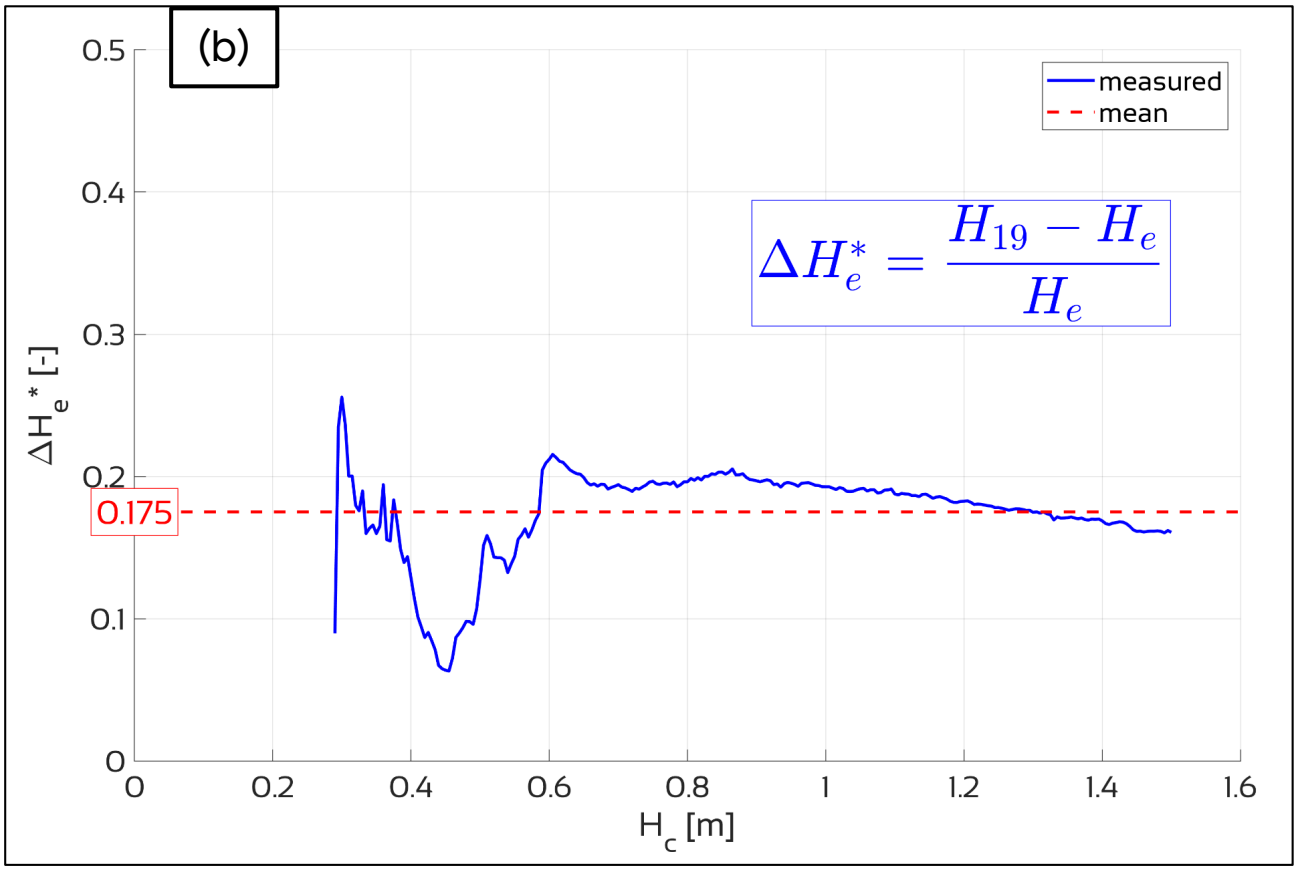
(b)
measured
mean
$\Delta H_e^* = \frac{H_{19} - H_e}{H_e}$
0.175
ΔH_e^* [-]
H_c [m]
0
0.1
0.2
0.3
0.4
0.5
0.2
0.4
0.6
0.8
1
1.2
1.4
1.6

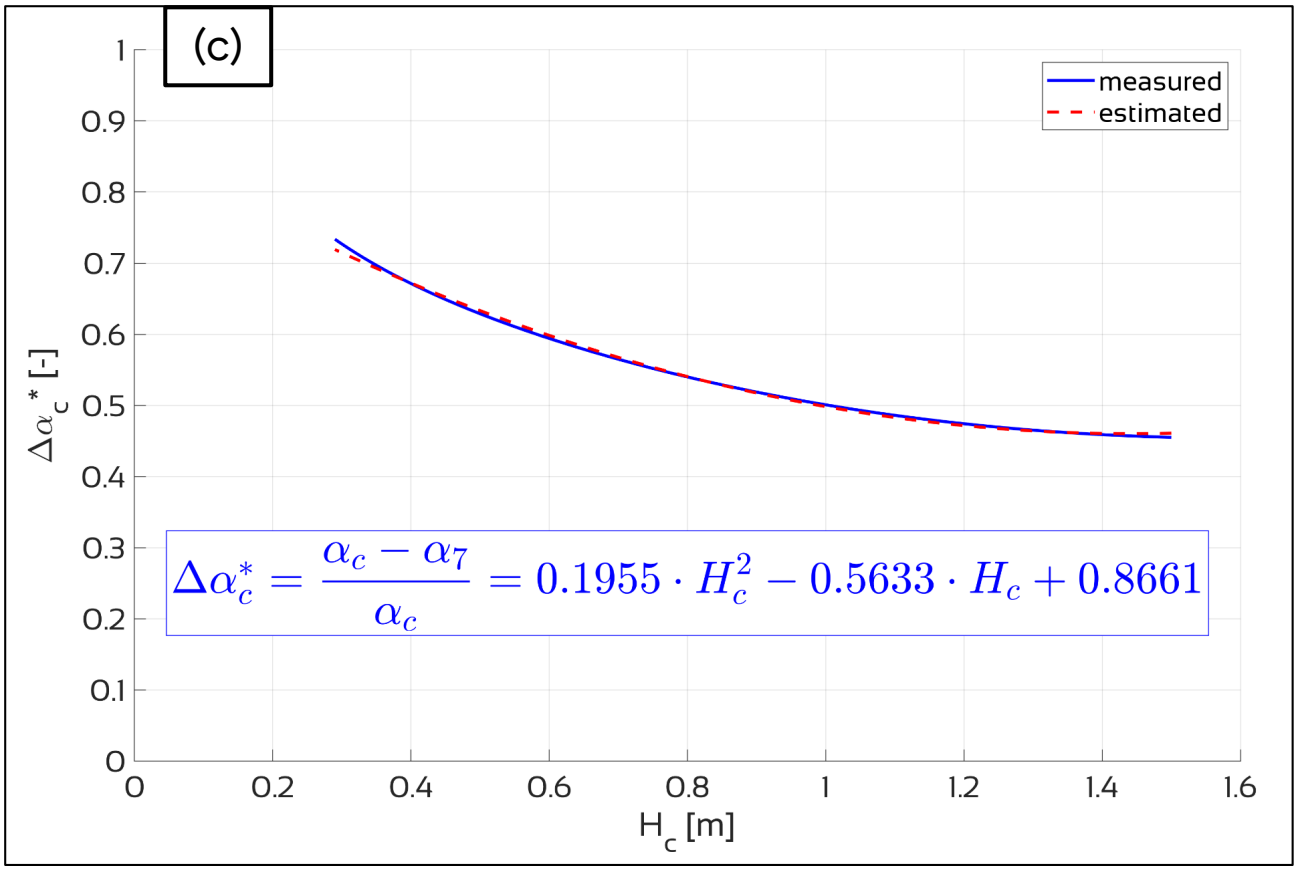

Figure 4.12: total head reduction ratio ΔH_c^* between section c (the Tube's entrance) and section 7 (a), total head increase ratio ΔH_e^* between section e (the Tube's exit) and section 19 (b), cross-sectional area ratio increase ratio $\Delta\alpha_c^*$ between section c and section 7 (c), as a function of H_c estimated using Diagnostic-tests data: the blue line is the Laboratory data while the red dashed line is the mean value (a,b) or the 2nd order polynomial fitting (c)

In particular, considering the Tube longitudinal section (Figure 3.18 and Figure 4.7):

- the total head reduction ratio ΔH_c^*=0.078 between section c (the Tube's entrance section) and section 7 has been estimated using the mean value shown in Figure 4.12a;
- the total head increase ratio ΔH_e^*=0.175 between section e (the Tube's exit section) and section 19 has been estimated using the mean value shown in Figure 4.12b;
- the cross-sectional area ratio increase $\Delta\alpha_c^*$ between section c (the Tube's entrance section) and section 7 has been estimated using a second order polynomial fitting as a function of H_c (Figure 4.12c);
- the cross-sectional area ratio reduction between section e (the Tube's exit section) and section 19 has been assumed constant $\Delta\alpha_e^* = (\alpha_e - \alpha_{19})/\alpha_e$=0.1.

Boundary conditions are:

- the flow rate Q;
- the cross-sectional area ratio α_{19}, estimated by applying the cross-sectional area ratio reduction $\Delta\alpha_e{}^*$ to α_e, as explained before.

As in Diagnostic-tests simulations, we started solving from section 19 going back to section 7 (and also section 1).

Figure 4.13 shows the results of the numerical simulations applied to Physiological-tests: (a) the cross-sectional area ratio α, (b) the total head H and (c) the piezometric head h, at different total head at the Tube's entrance H_c.

There is an excellent agreement between numerical simulation (solid lines) and Laboratory data (dots) regarding in particular total head and piezometric head. The correspondence with the cross-sectional area ratio can be considered of a good level: α is certainly the most sensitive parameter to changes in the TL.

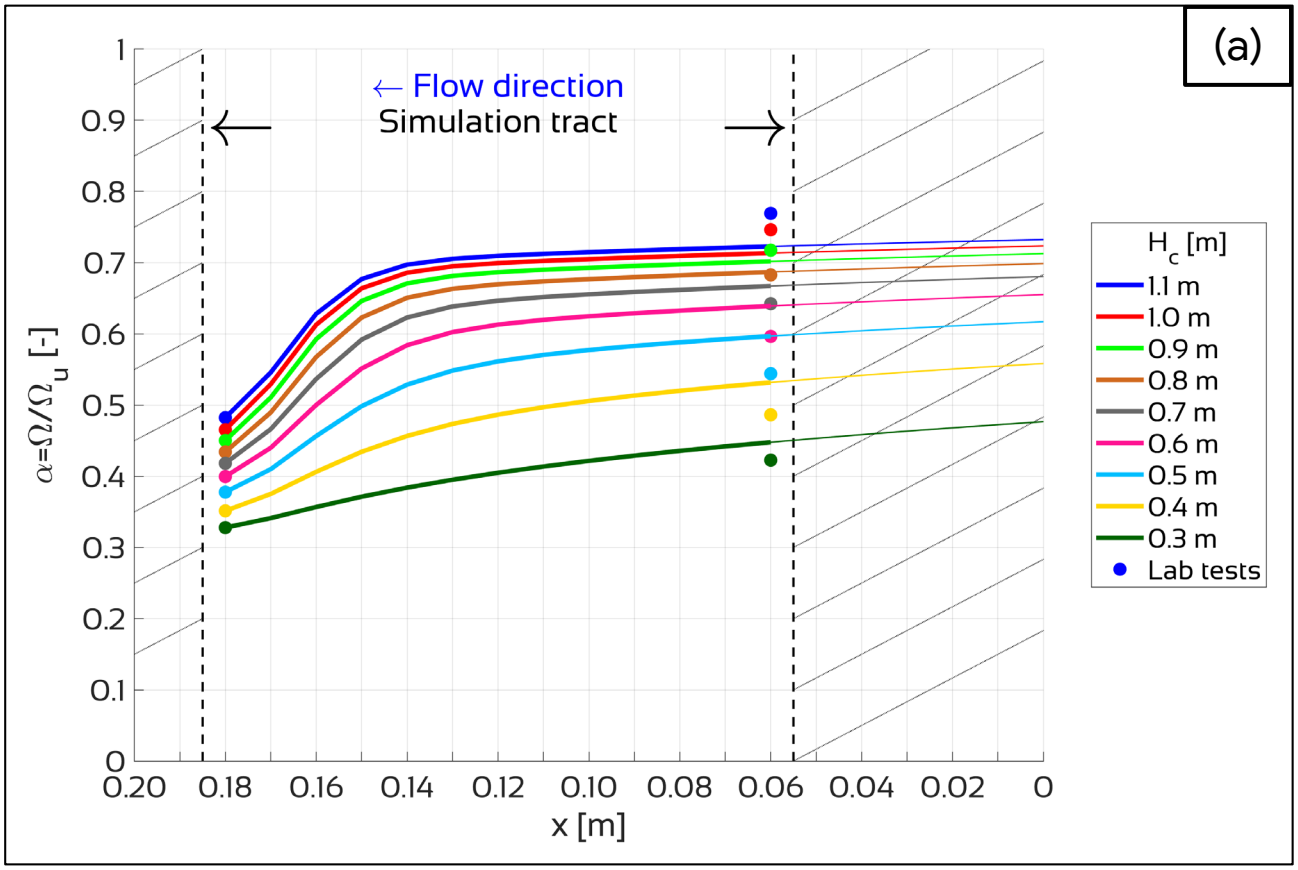

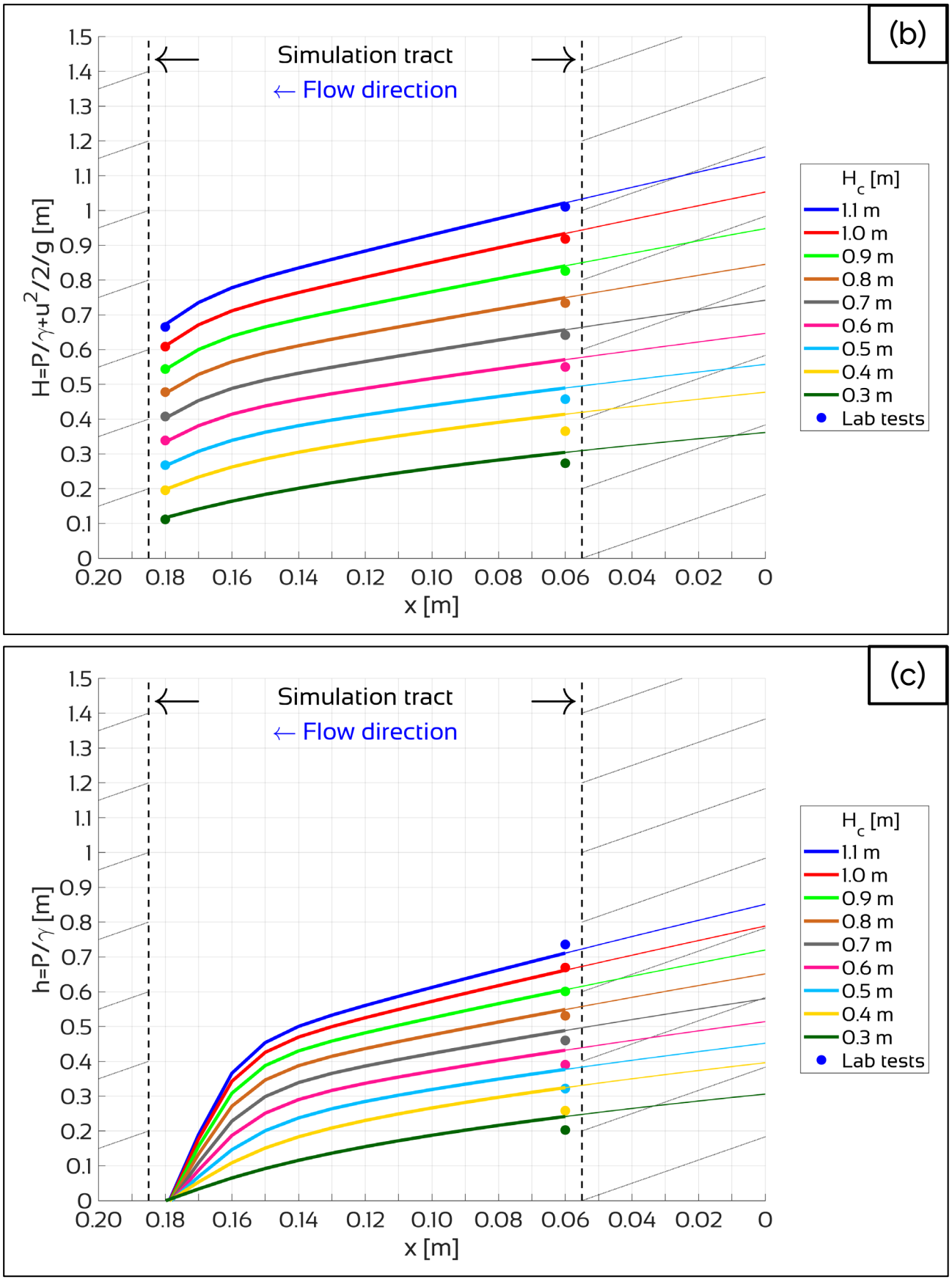

Figure 4.13: results of the numerical model applied to Physiological-tests: (a) cross-sectional area ratio α, (b) total head H, (c) piezometric head h. Solid lines represent the numerical simulation, while dots are the Laboratory tests data; each color represents the situation at a fixed total head at the Tube's entrance H_c, as shown in the legend.

4.3.3 "PATHOLOGICAL FLOW CONDITION" SIMULATIONS

Pathological-tests (section 3.2) are very similar to Physiological-tests, apart from the fact that an obstruction was inserted inside the Tube. The obstruction represents what is called urethral stricture (section 1.2.1), a stiffening of the urethra that reduces the flow area during voiding (i.e., the emptying of the tank in the Model).

As in Physiological-tests, the Laboratory data are:

- the flow rate Q,
- the velocity u_e at the exit of the Tube (and, consequently, the cross-sectional area ratio α_e and the total head H_e),
- the total head at the Tube's entrance H_c.

The obstructions are made by using metal cylinders with an external diameter equal to the external diameter of the "undisturbed" Tube D_{ext} and a variable internal diameter, in order to reproduce a rigid section reduction inside the Tube.

The numerical model developed for Physiological-tests has been applied by introducing the head losses due to the obstructions:

- local head loss at the exit of the obstruction, evaluated with Borda equation applied to a sudden expansion:

$$\Delta H_{conc2} = (\Omega_{ob} - \Omega_u)^2 \cdot \frac{{u_{ob}}^2}{2g} = (\alpha_{ob} - 1)^2 \cdot \frac{{u_{ob}}^2}{2g} \qquad 4.36$$

  where Ω_{ob} is the internal area and $\alpha_{ob}=\Omega_{ob}/\Omega_u$ the internal area ratio of the obstruction, and u_{ob} the average velocity inside the obstruction;
- friction head losses inside the obstruction, evaluated using the Darcy-Weisbach equation 4.3 with a roughness $\varepsilon_{ob}=0.01\cdot10^{-3}$ m;
- head loss at the entrance of the obstruction, estimated as:

$$\Delta H_{conc1} = 0.3 \cdot \frac{{u_{ob}}^2}{2g} \qquad 4.37$$

Boundary conditions are:

- the flow rate Q;
- the cross-sectional area ratio α_{19}, estimated by applying the cross-sectional area ratio reduction $\Delta{\alpha_e}^*$ to α_e, as explained before.

As in Diagnostic-tests and in Physiological-tests simulations, we started by solving from section 19 going back to section 7 (and also section 1).

Figure 4.14, Figure 4.15 and Figure 4.16 show the results of the numerical simulation applied to Pathological-tests with three different types of obstructions: (a) the cross-sectional area ratio α,

(b) the total head H and (c) the piezometric head h along the Tube, at different total head at the Tube's entrance H_c, as shown in the legend.

As in the Physiological-tests simulations, it is possible to see an excellent match between numerical simulation (solid lines) and Laboratory data (dots) regarding in particular total head and piezometric head.

Figure 4.17 shows the comparison between Physiological tests and Pathological tests with the numerical simulation in section 7 (see Figure 4.7): (a) cross-sectional area ratio α; (b) total head H; (c) piezometric head h. The colors represent the obstruction internal diameter D_{ob}, as shown in the legend. It is possible to see the good agreements regarding piezometric head and total head; the correspondence with the cross-sectional area ratio can be accounted as acceptable, considering the fact that in this case the most valuable parameter is the pressure (i.e., the piezometric head).

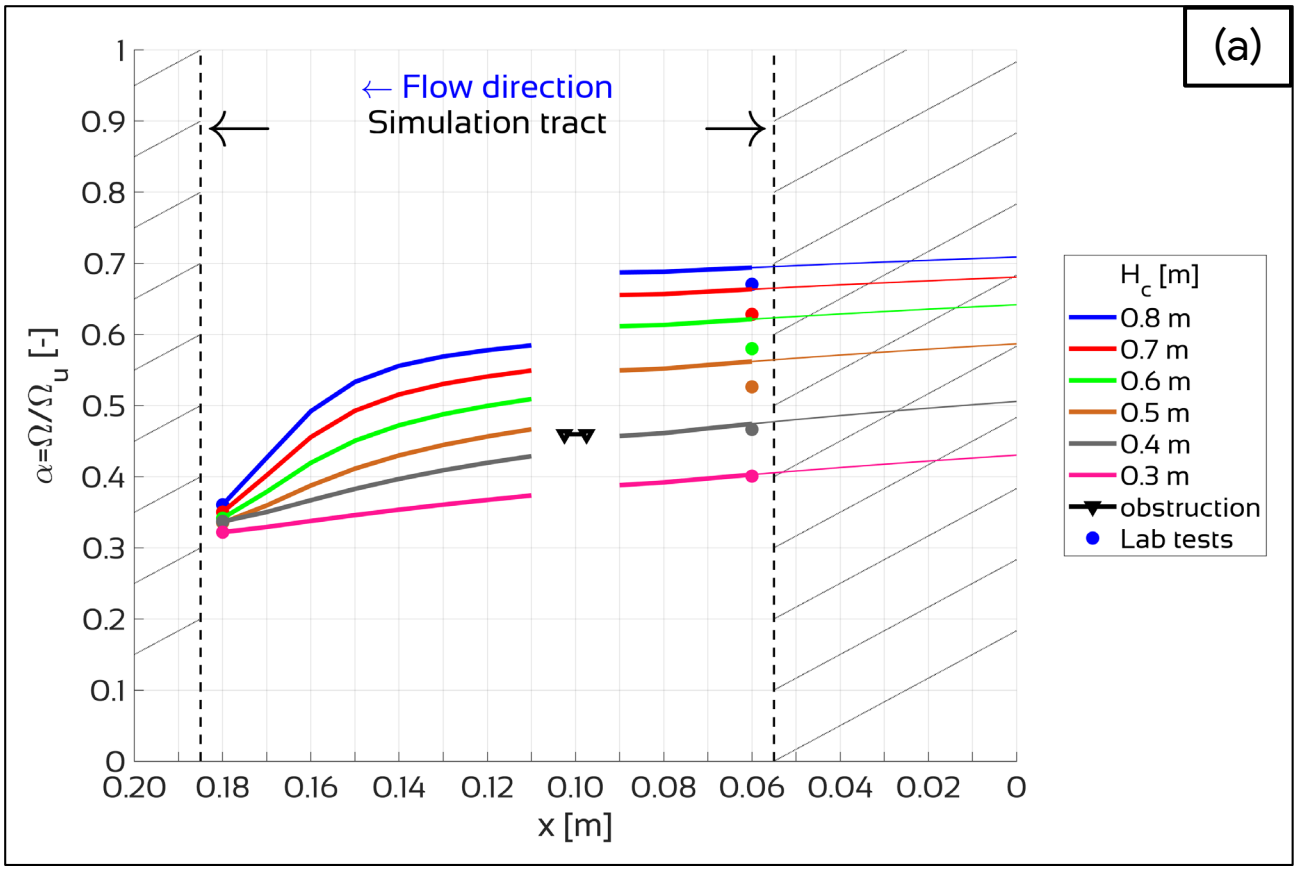
(a)
← Flow direction
Simulation tract
α=Ω/Ω_u [-]
x [m]
H_c [m]
0.8 m
0.7 m
0.6 m
0.5 m
0.4 m
0.3 m
obstruction
Lab tests

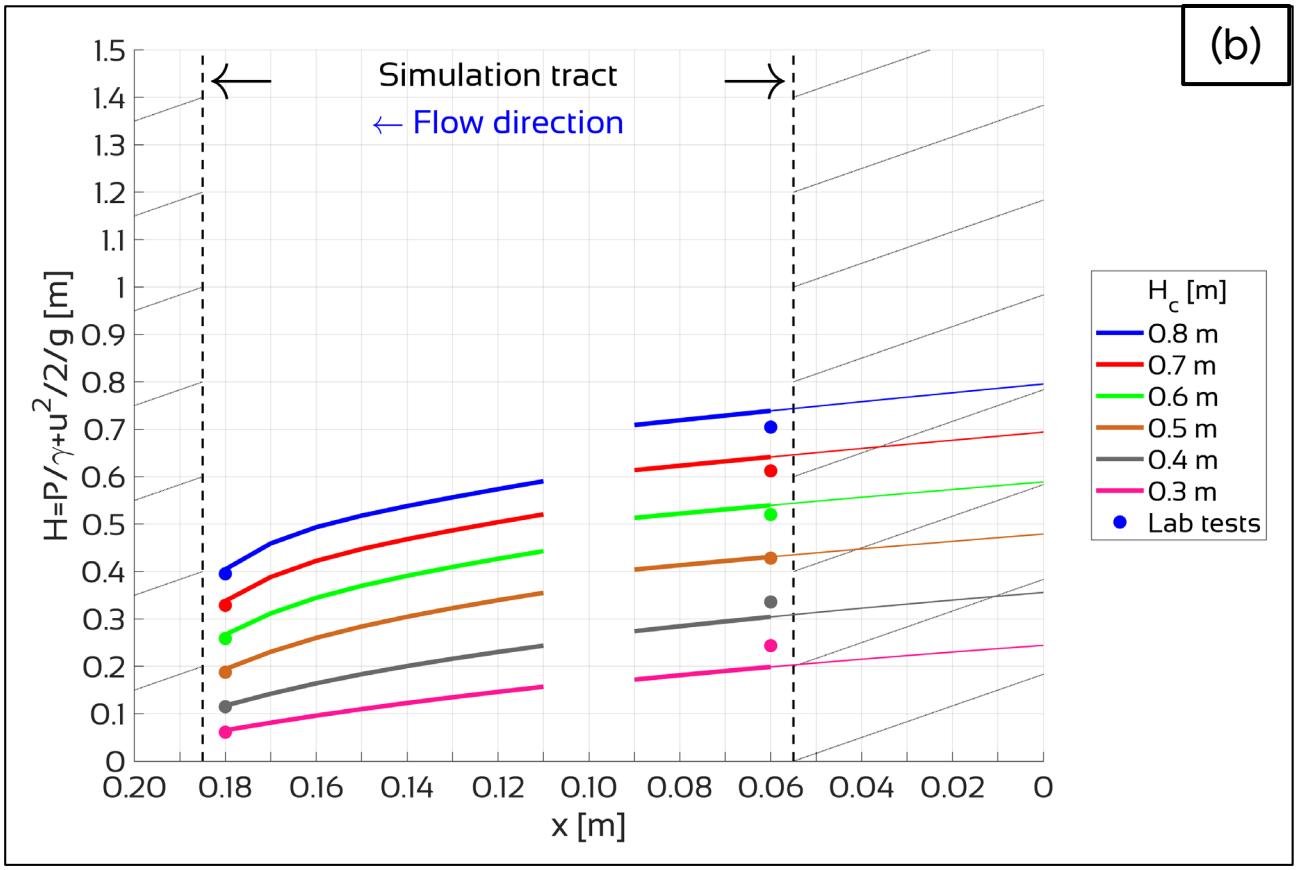
(b)
Simulation tract
← Flow direction
H=P/γ+u²/2/g [m]
x [m]
H_c [m]
0.8 m
0.7 m
0.6 m
0.5 m
0.4 m
0.3 m
Lab tests

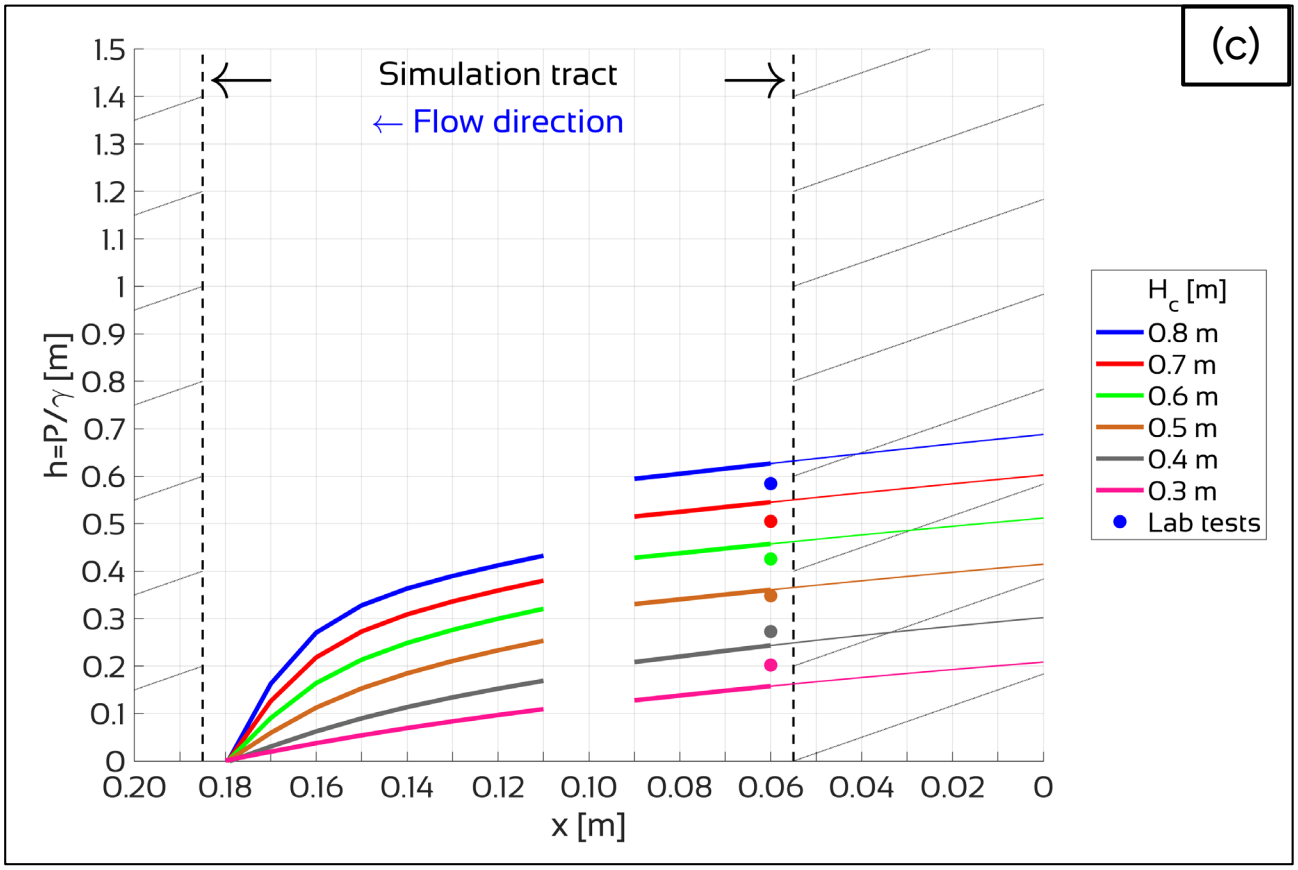

Figure 4.14: results of the numerical simulation applied to Pathological-tests with an obstruction 5 mm long, having 4 mm internal diameter and placed in the center: (a) cross-sectional area ratio α, (b) total head H, (c) piezometric head h. Solid lines represent the numerical simulation, while dots are the Laboratory tests data; each color represents the situation at a fixed total head at the Tube's entrance H_c, as shown in the legend. The black line with the triangles represents the obstruction

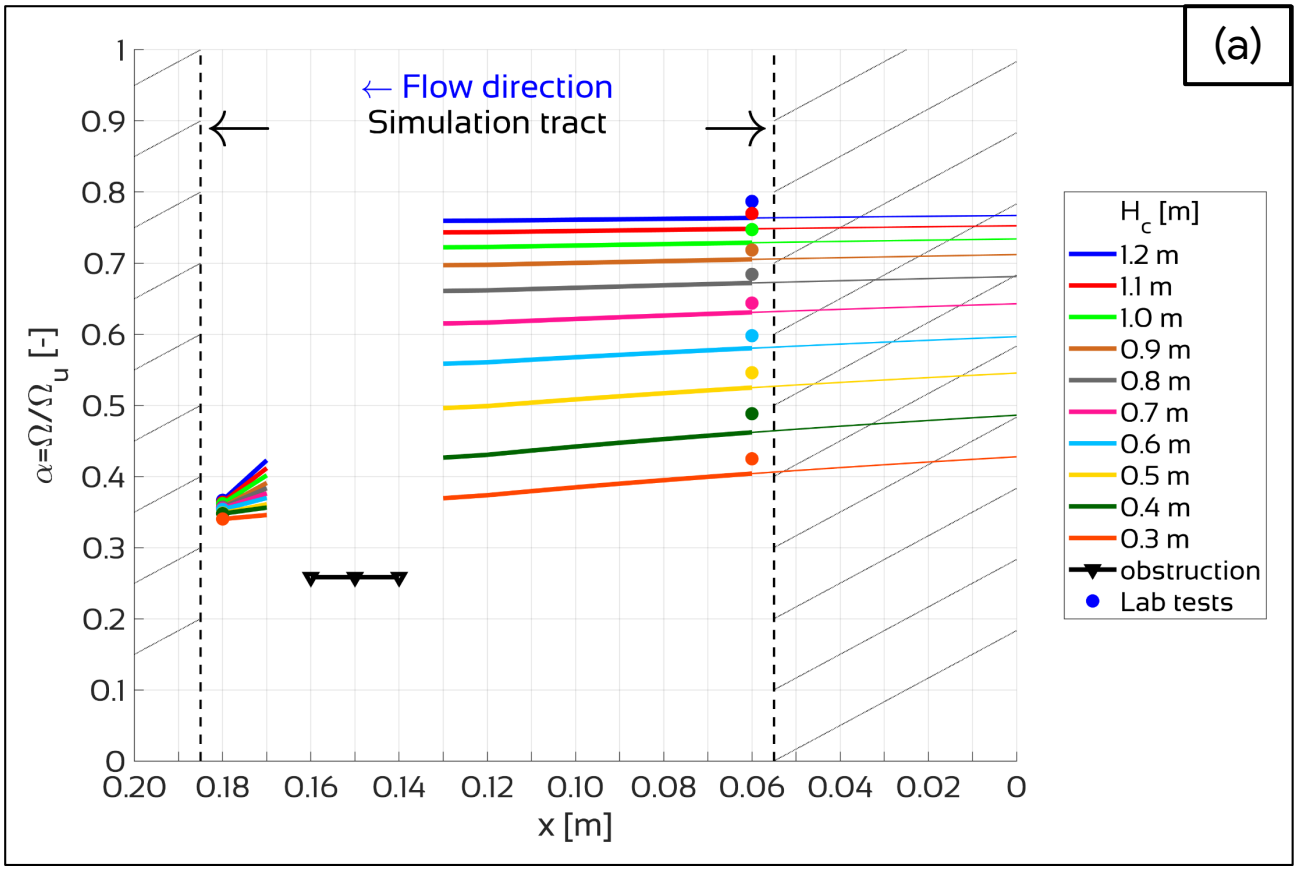
(a)
← Flow direction
Simulation tract
α=Ω/Ω_u [-]
x [m]
H_c [m]
1.2 m
1.1 m
1.0 m
0.9 m
0.8 m
0.7 m
0.6 m
0.5 m
0.4 m
0.3 m
obstruction
Lab tests

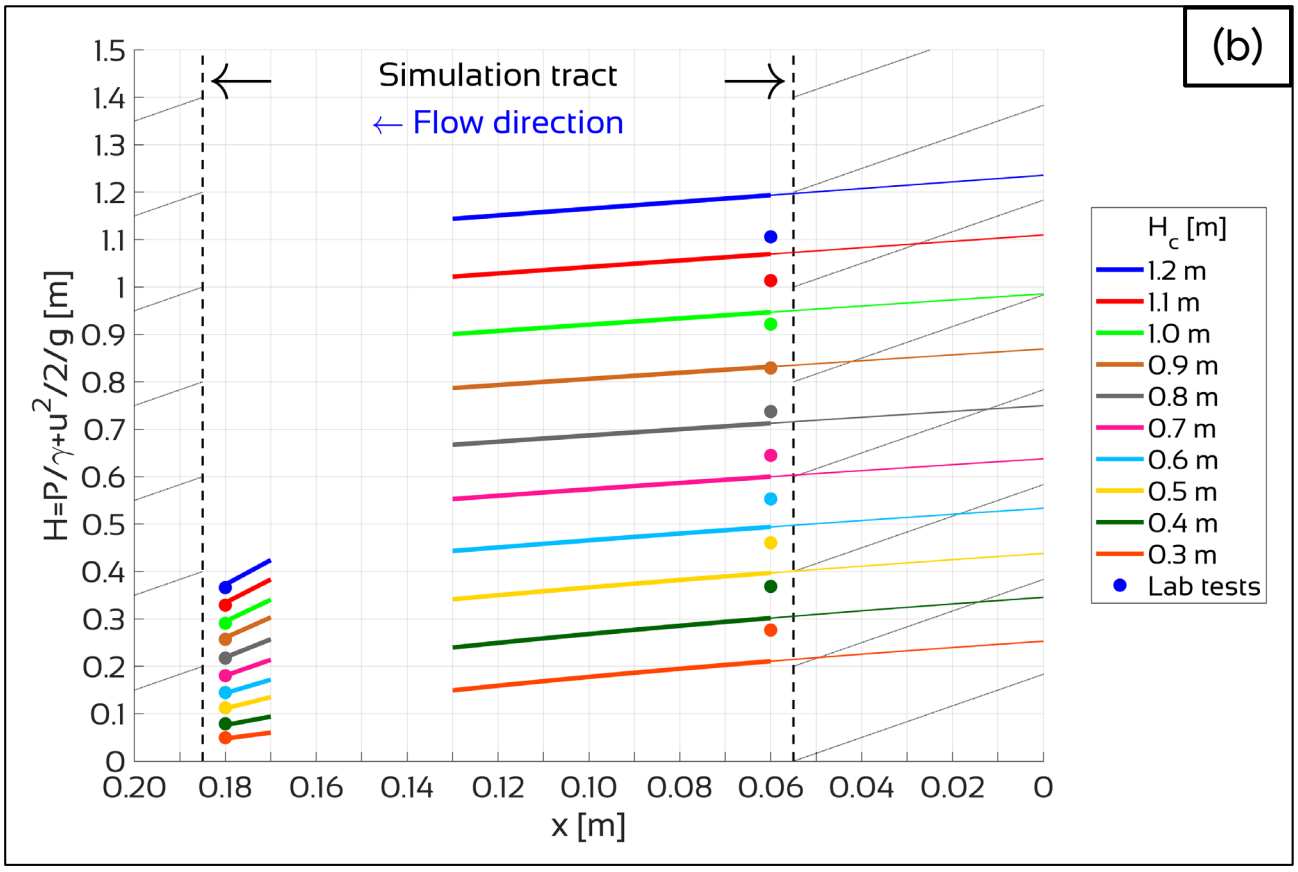
(b)
Simulation tract
← Flow direction
H=P/γ+u²/2/g [m]
x [m]
H_c [m]
1.2 m
1.1 m
1.0 m
0.9 m
0.8 m
0.7 m
0.6 m
0.5 m
0.4 m
0.3 m
Lab tests

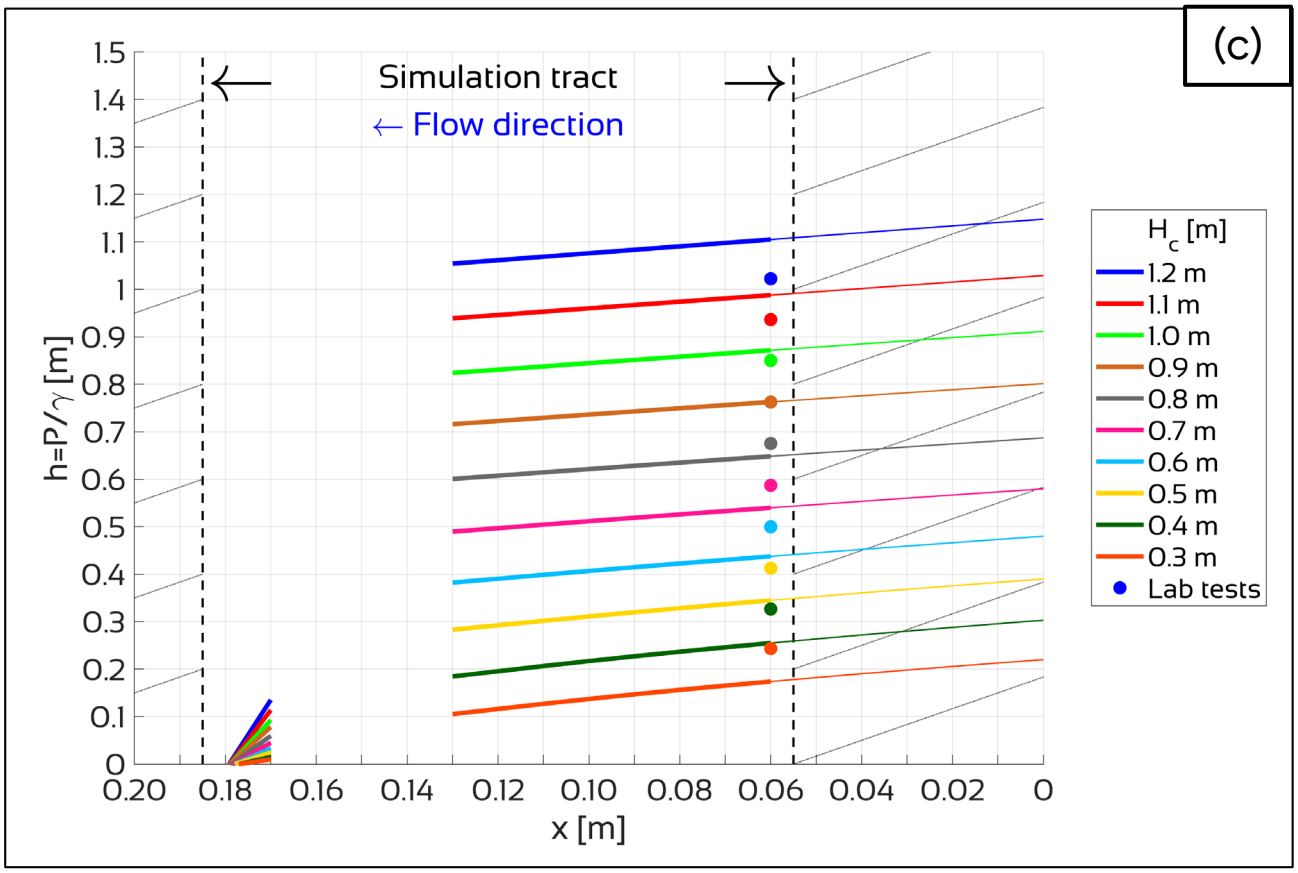

Figure 4.15: results of the numerical simulation applied to Pathological-tests with an obstruction 20 mm long, having 3 mm internal diameter and placed upstream: (a) cross-sectional area ratio α, (b) total head H, (c) piezometric head h. Solid lines represent the numerical simulation, while dots are the Laboratory tests data; each color represents the situation at a fixed total head at the beginning of the Tube H_c, as shown in the legend. The black line with the triangles represents the obstruction

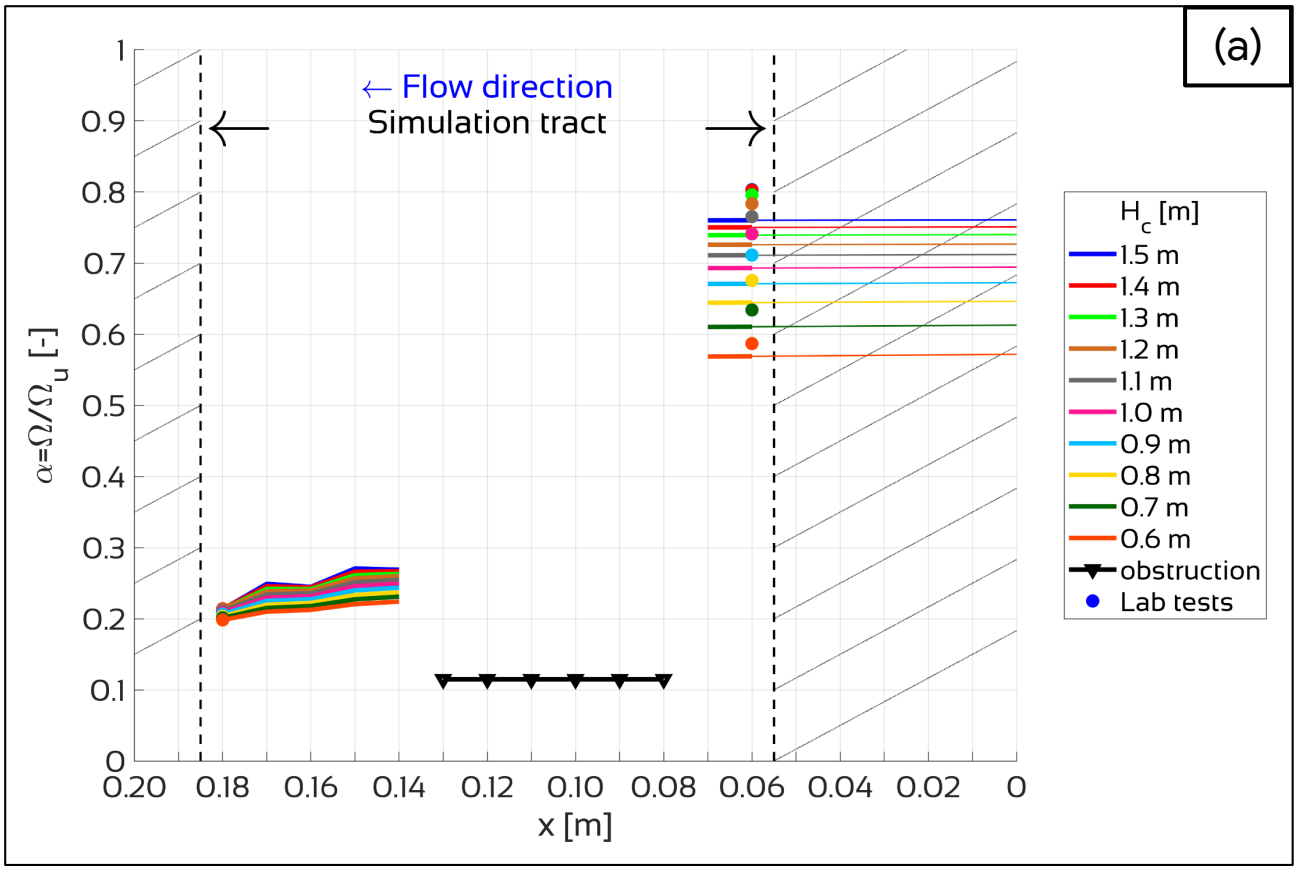
(a)
← Flow direction
Simulation tract
α=Ω/Ω_u [-]
x [m]
H_c [m]
1.5 m
1.4 m
1.3 m
1.2 m
1.1 m
1.0 m
0.9 m
0.8 m
0.7 m
0.6 m
obstruction
Lab tests

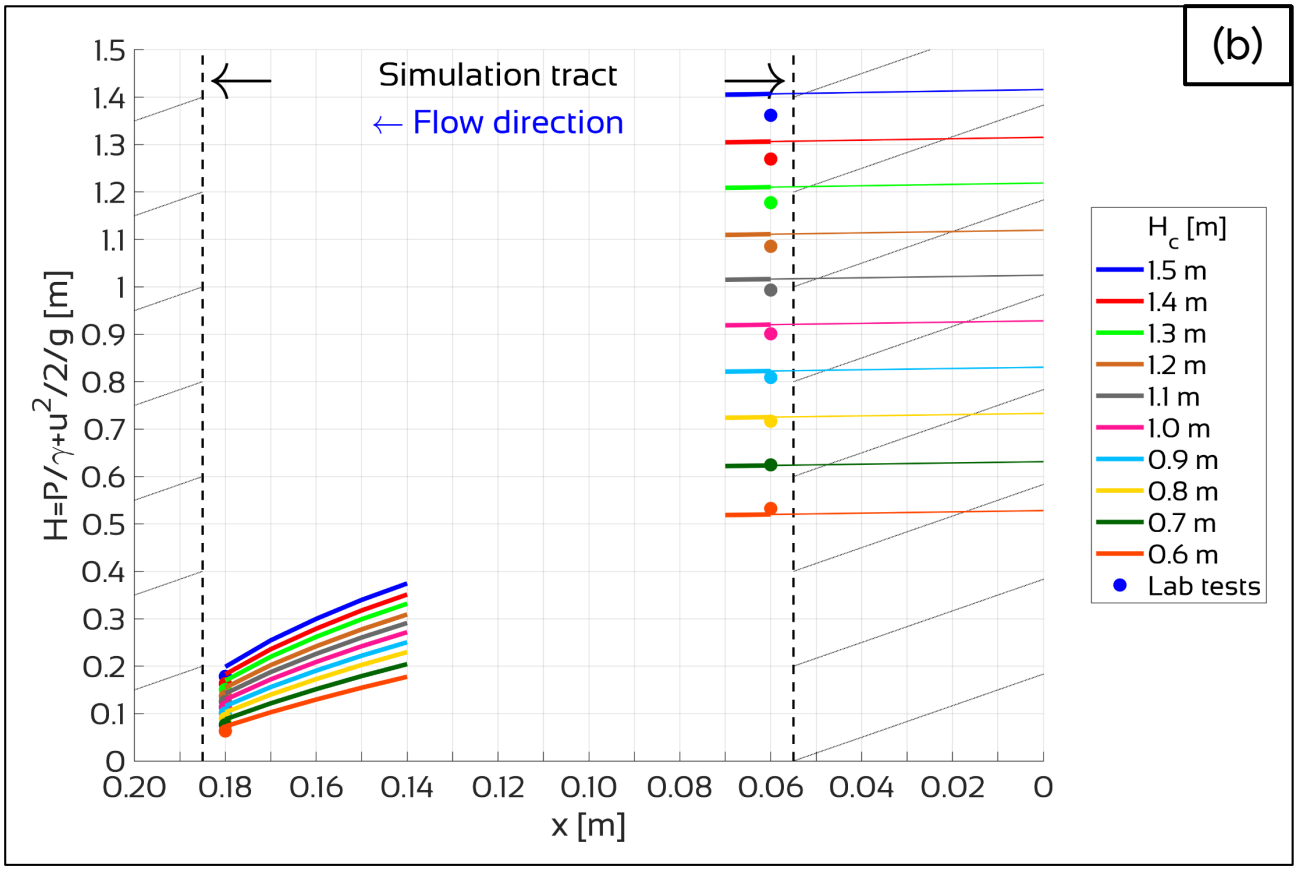
(b)
Simulation tract
← Flow direction
H=P/γ+u²/2/g [m]
x [m]
H_c [m]
1.5 m
1.4 m
1.3 m
1.2 m
1.1 m
1.0 m
0.9 m
0.8 m
0.7 m
0.6 m
Lab tests

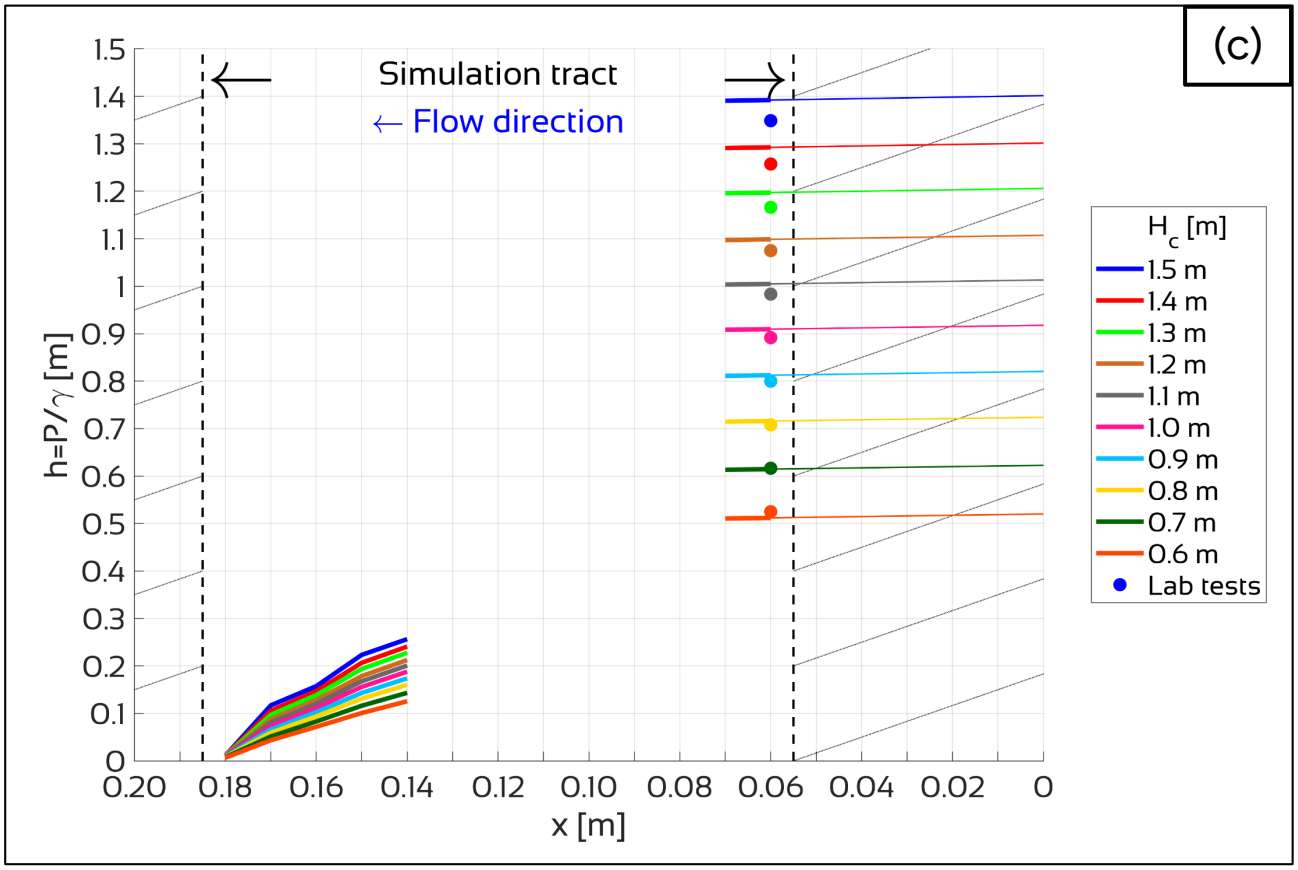

Figure 4.16: results of the numerical simulation applied to Pathological-tests with an obstruction 50 mm long, having 2 mm internal diameter and placed in the center: (a) cross-sectional area ratio α, (b) total head H, (c) piezometric head h. Solid lines represent the numerical simulation, while dots are the Laboratory tests data; each color represents the situation at a fixed total head at the beginning of the Tube H_c, as shown in the legend. The black line with the triangles represents the obstruction

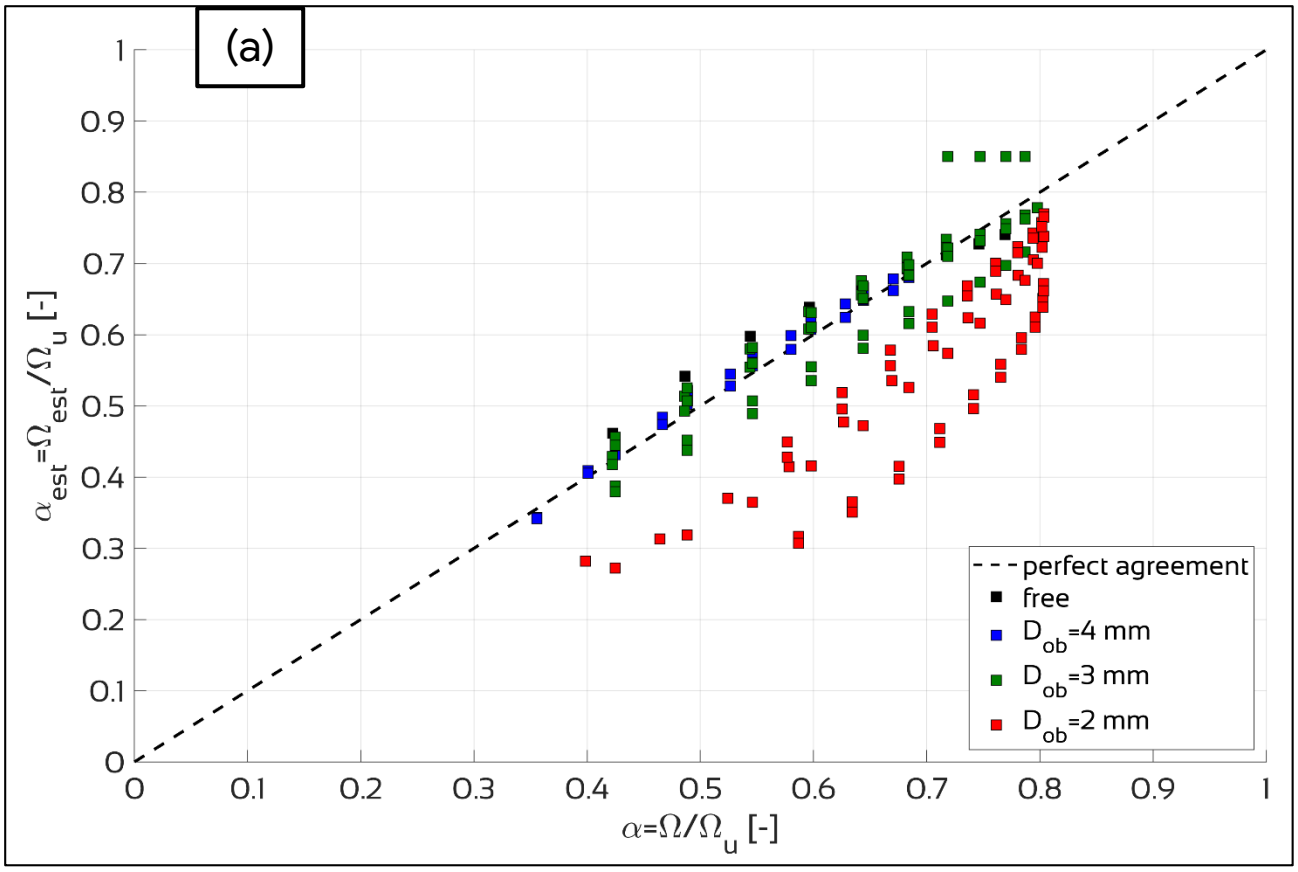
(a)
$\alpha_{est}=\Omega_{est}/\Omega_u$ [-]
$\alpha=\Omega/\Omega_u$ [-]
perfect agreement
free
D_{ob}=4 mm
D_{ob}=3 mm
D_{ob}=2 mm

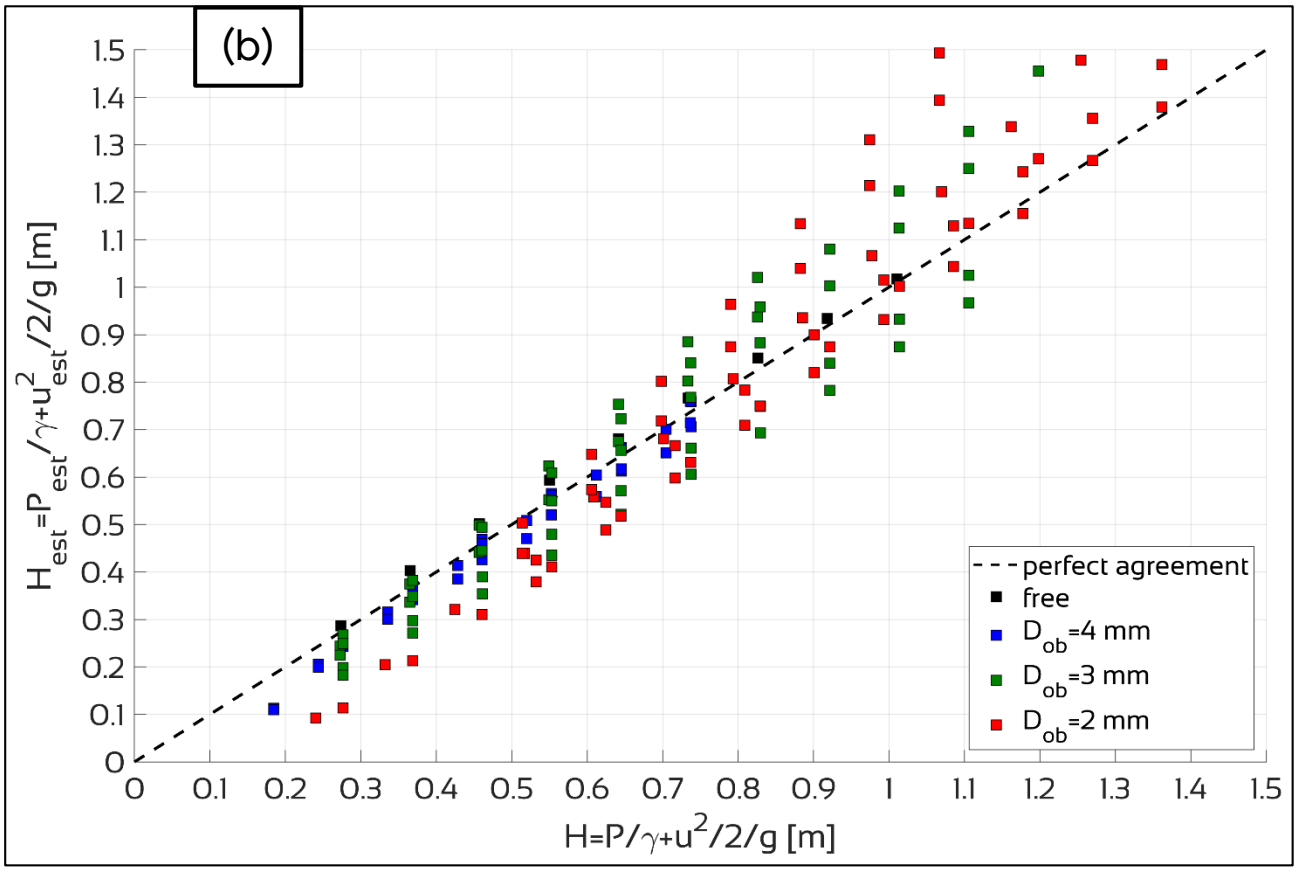
(b)
$H_{est}=P_{est}/\gamma+u^2_{est}/2/g$ [m]
$H=P/\gamma+u^2/2/g$ [m]
perfect agreement
free
D_{ob}=4 mm
D_{ob}=3 mm
D_{ob}=2 mm

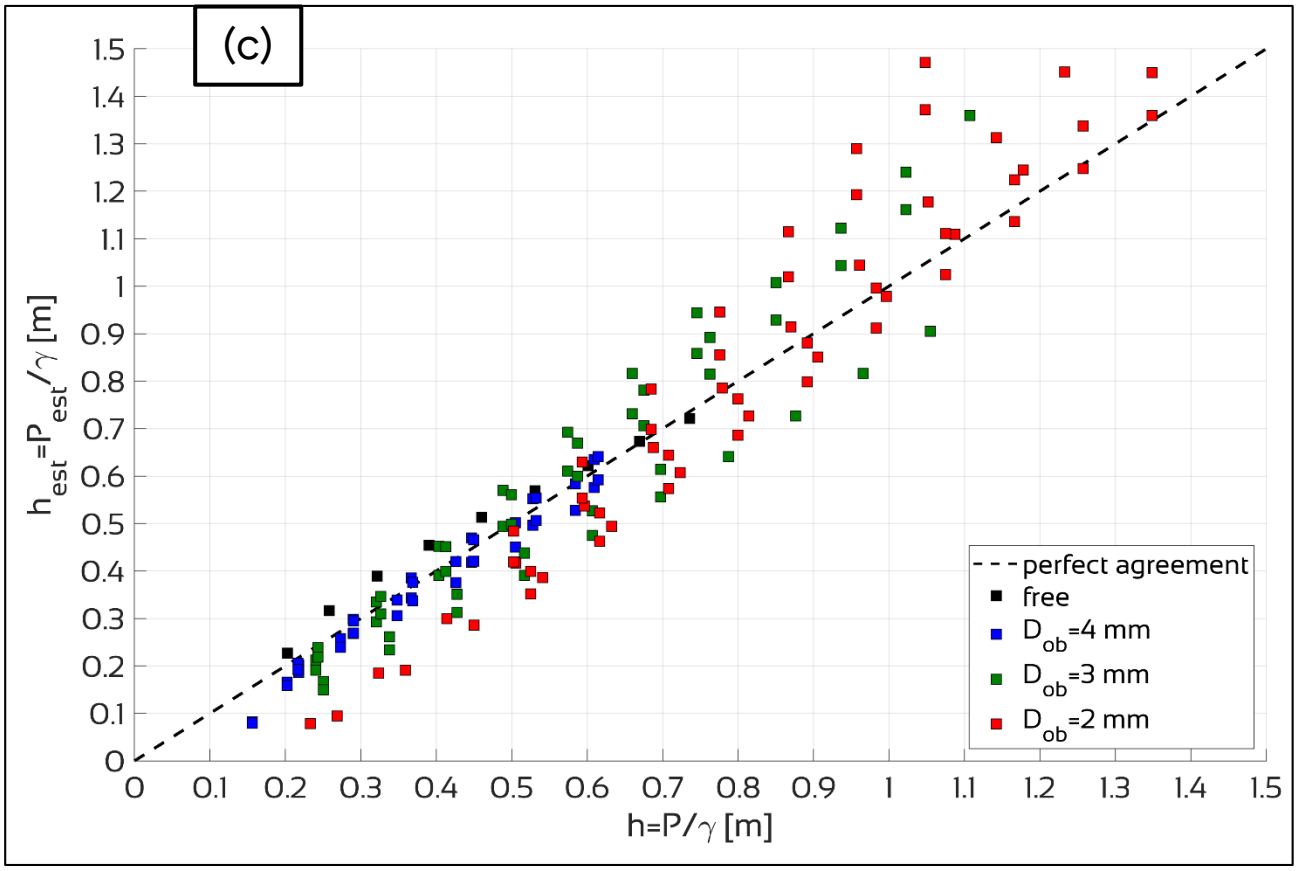

Figure 4.17: comparison between Physiological-tests and Pathological-tests with the numerical simulation in section 7 (see Figure 4.7): (a) cross-sectional area ratio α; (b) total head H; (c) piezometric head h; the colors represent the obstruction internal diameter D_{ob}, as shown in the legend

5 Innovative Instrumentation for non-invasive Urodynamics

5.1 Design and construction

The idea behind our project (section 2.4) is to measure the flow rate and the jet exit speed of the urine (and then estimate the intravesical pressure through a physical-mathematical model valid for healthy male subjects) in order to be able to perform a P/F Study in a non-invasive way (i.e. without using the catheter) and with a single measurement.

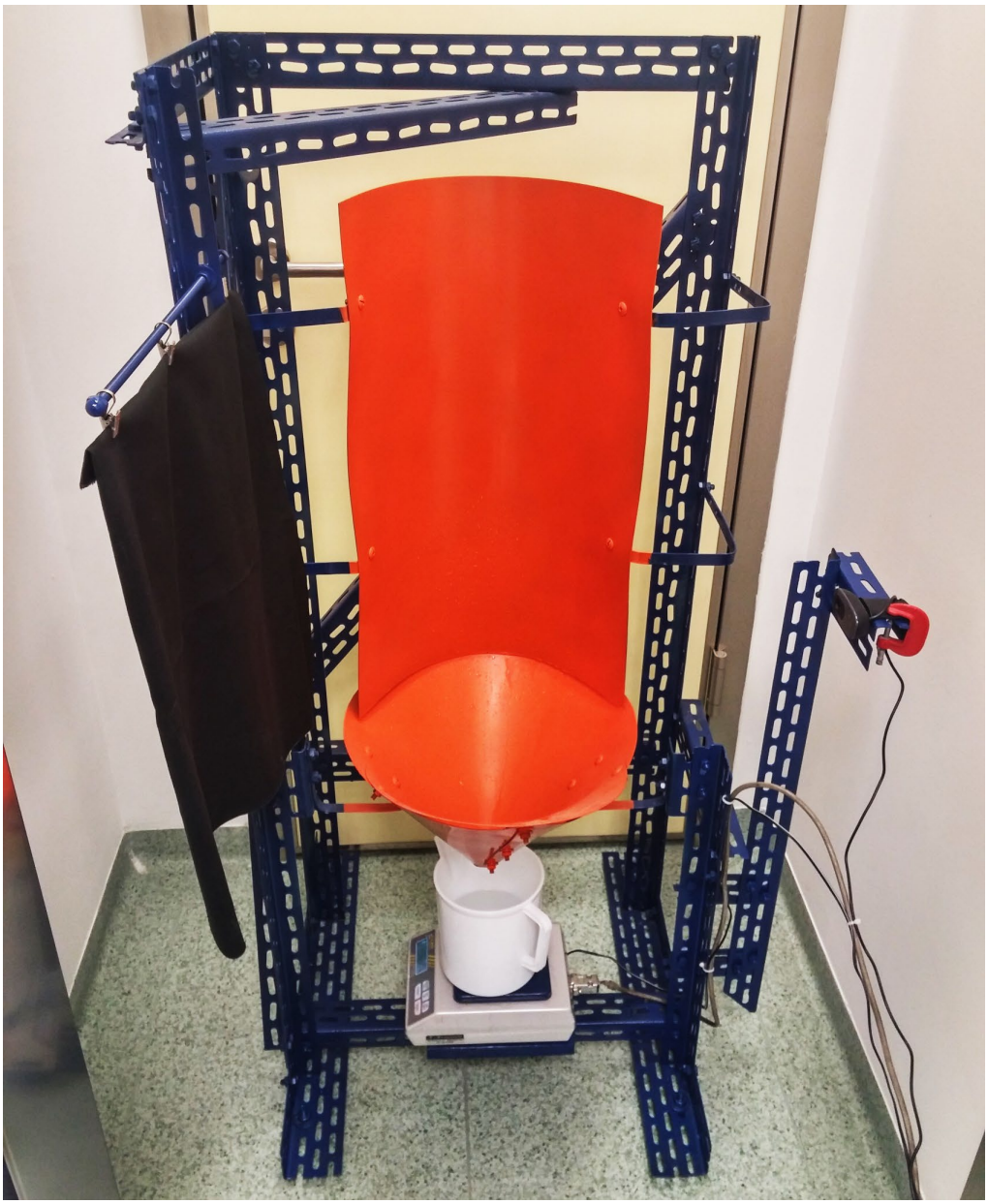

Figure 5.1: prototype of the Innovative Instrumentation

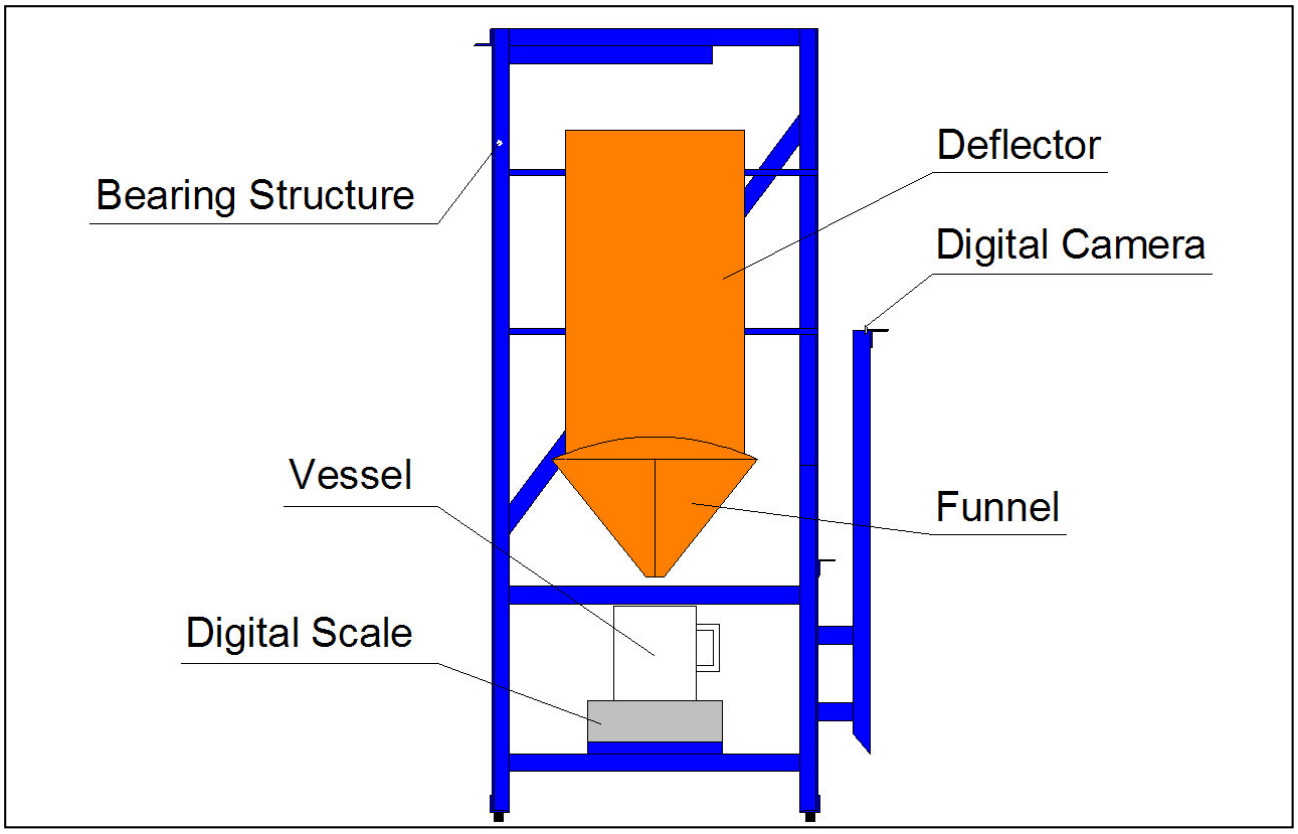

Figure 5.2: diagram of the components of the Innovative Instrumentation

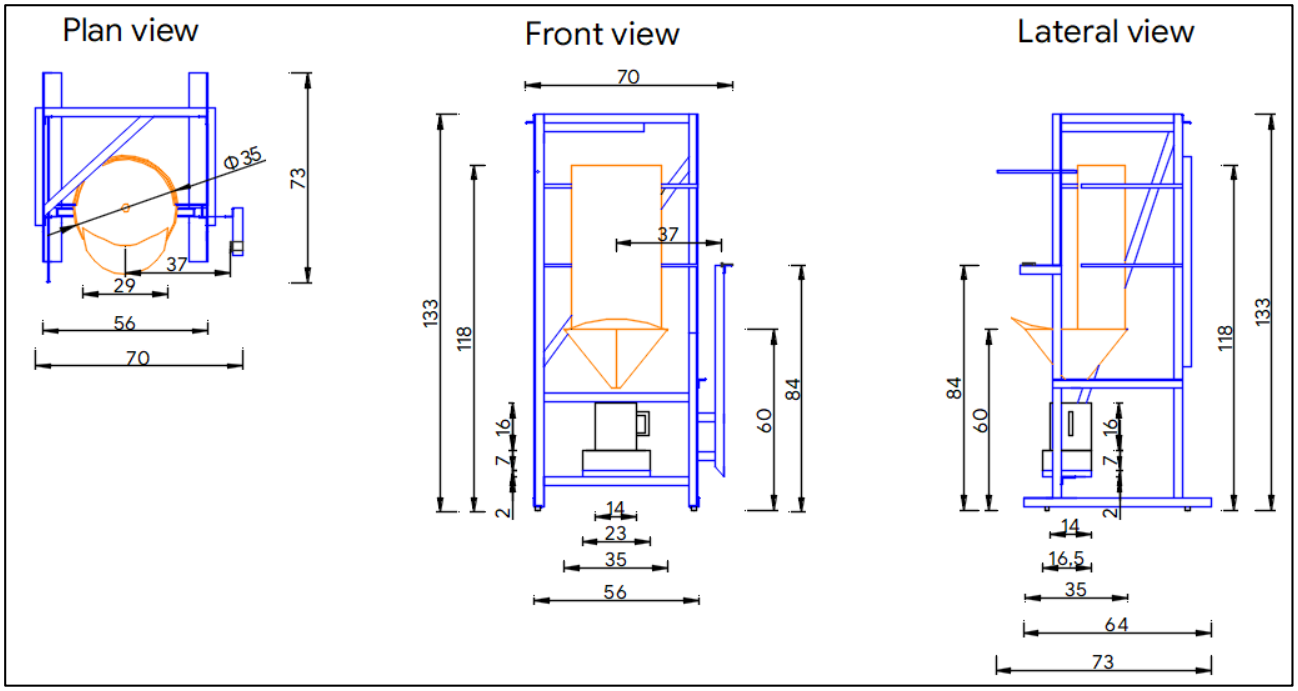

Figure 5.3: project of the Innovative Instrumentation, all measures in cm

The first phase of the construction of the Innovative Instrumentation consisted in designing the structure to be as compact as possible. The idea was in fact to create a structure that basically supports a camera (to record the jet) and a funnel (to convey the urine into a collector brick

positioned on a precision scale). Considering the simplicity of use, it has been taken the classic wall urinal, commonly used in private and public bathroom, as an initial idea for the construction of the Innovative Instrumentation; an overall view is visible in Figure 5.1.

According to the schemes project in Figure 5.2 and in Figure 5.3, it is possible to identify:

- *Bearing structure* 70x56x133 cm LxDxH which has the purpose of supporting funnel, deflector, digital scale, digital camera, using L-shaped iron profiles (3x5x0.1 cm) joined by bolts;
- *Funnel* and *deflector* that have the purpose of conveying the jet of urine inside a *vessel* that is placed under the funnel and above the scale. Funnel and deflector are connected to the supporting structure with aluminum strips and are made of 1 mm thick polycarbonate sheet;
- *Digital camera*, positioned at a height of 84 cm from the ground;
- *Digital scale* and *vessel*, which can contain about 2.5 l.

5.2 Hardware & Software

Image acquisition is performed using a Logitech c270 webcam (Figure 5.4a) that has a maximum resolution of 3 Mpixel. The webcam is fixed to the bearing structure at 37 cm from the center of the funnel and 84 cm high from the ground. The webcam frames a portion of space 15 cm wide and 22 cm high above the center of the funnel; this positioning allows shooting the jet of urine of men between about 160 cm and 190 cm high. The images are processed by a Matlab code and are not stored on the hard drive.

A KERN 440 digital scale (Figure 5.4b) records the weight over time of the urine that collects inside the vessel synchronously with image acquisition.

Figure 5.4: Innovative Instrumentation hardware: webcam Logitech c270 (a); digital scale Kern 440 (b)

Figure 5.5: overall view of the Innovative Instrumentation

The digital camera and the digital scale are connected to the computer and managed by LabVIEW software (Laboratory Virtual Instrumentation Engineering Workbench) developed by National Instruments. Data processing is done with a code written in Matlab software, developed by MathWorks.

All instruments record at 5.5 Hz frequency, that is an interval between acquisitions $\Delta t=0.18$ s.

The hardware (camera and scale) is connected to a computer (Figure 5.5); digital data acquisition is managed by LabView software, while data processing is managed by MATLAB software. After processing, a clinical report which contains the patient's data and the test results is automatically printed.

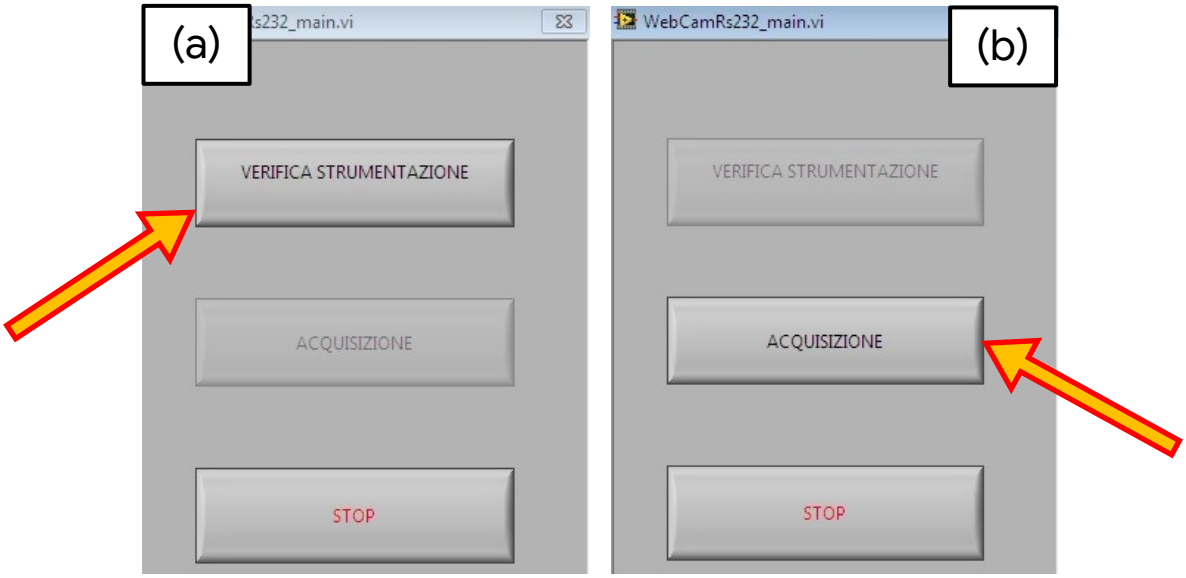

Figure 5.6: first screen of the Innovative Instrumentation software: check instrumentation (a), data acquisition (b)

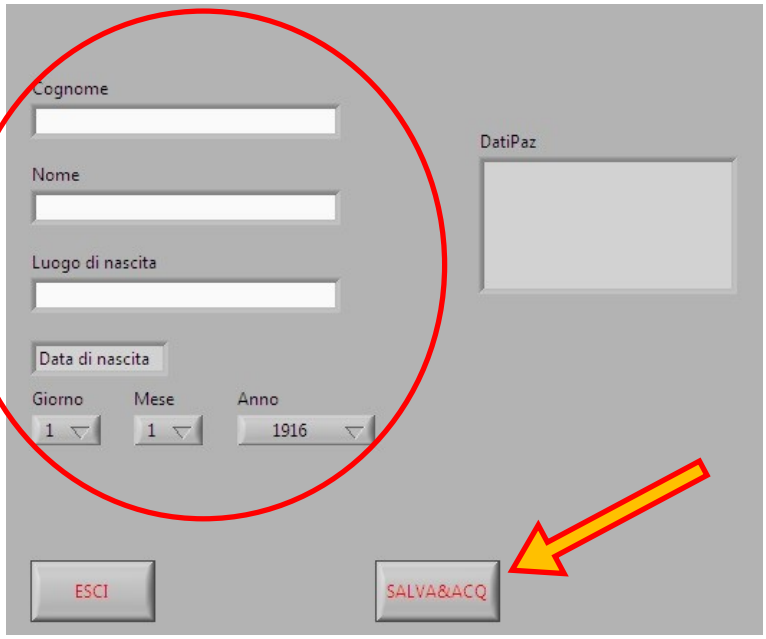

Figure 5.7: patient data entering window of the Innovative Instrumentation

The operating procedure of the Innovative Instrumentation is completely automatic. The first thing to do is a check of the hardware by clicking on “VERIFICA STRUMENTAZIONE” (i.e. “check instrumentation”, Figure 5.6a). If the instrumentation is not connected correctly, it won’t be possible to perform the acquisition and the message "ATTENTION: MISSING SCALE" or "ATTENTION: CONNECT WEBCAM" will appear. Otherwise, it’s possible to go to the next step by clicking on “ACQUISIZIONE” (i.e. “acquisition”, Figure 5.6b).

After clicking on "ACQUISIZIONE", before proceeding with the actual acquisition it is necessary to enter the patient data in the appropriate fields (Figure 5.7, red circle) and then click on "SALVA&ACQ" (i.e. “save & acquire”, yellow arrow on Figure 5.7) to proceed with the acquisition.

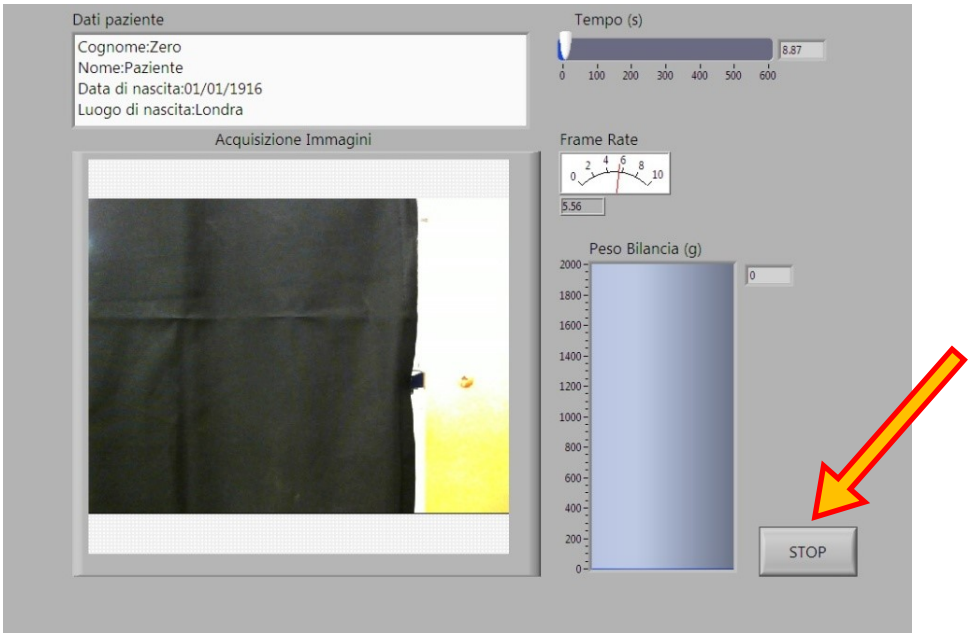

Figure 5.8: interface of the Innovative Instrumentation during micturition data acquisition

The patient has to position its body on the edge of the funnel and has to direct the jet more or less horizontally for a better jet velocity measurement. In addition to the patient's personal data, the interface (Figure 5.8) displays the live image taken by the webcam, the acquisition time in seconds and the total weight recorded by the digital scale in grams.

At the end of the measurement, the user clicks on “STOP” (Figure 5.8, yellow arrow). After that, processing of the recorded data begins, and the clinical report will be printed.

5.3 MATHEMATICAL SCHEMES

5.3.1 FLOW RATE Q

Digital scale records the weight W_{raw} [kg] of the vessel over time. For each value of the $W_{raw,i}$ weight, measured at the i^{th} instant, it is performed a moving average calculated on nine values:

$$W_i = \frac{\sum_{i-4}^{i+4} W_{raw,i}}{9} \qquad 5.1$$

Subsequently, the flow rate $Q_{raw,i}$ [m^3/s] is calculated at each i^{th} instant by:

$$Q_{raw,i} = \frac{W_i - W_{i-1}}{\rho_u \cdot \Delta t} \qquad 5.2$$

assuming steady flow between two consecutive recordings; Δt [s] is the interval between acquisitions and ρ_u=1020 kg/m^3 is the average density of the urine.

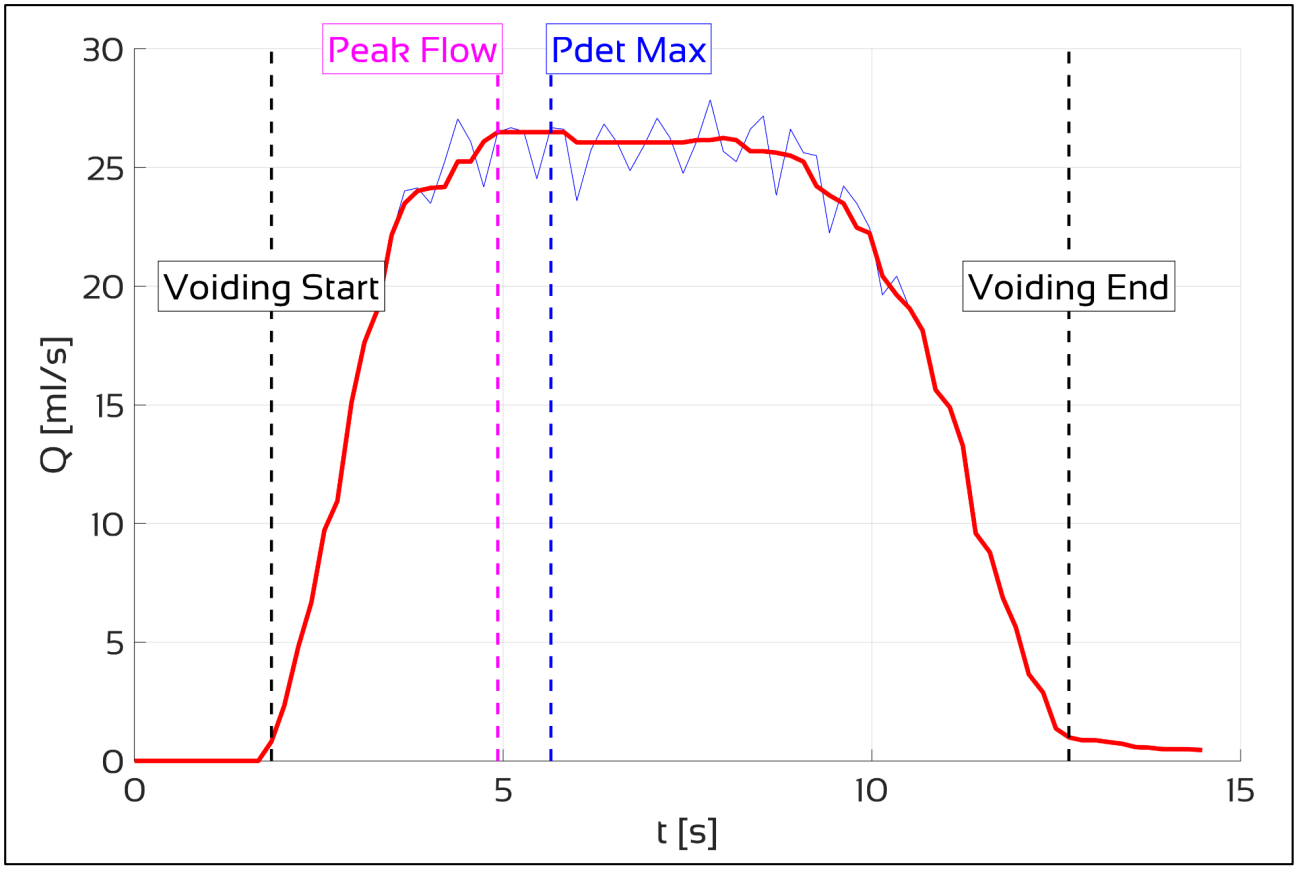

Figure 5.9: plot example of flow rate Q: the red line is Q, while the thin green line is Q_{raw}. From left to right, vertical dashed black, magenta, blue and black lines represent the time of the beginning of the micturition, the maximum flow Q_{peak}, the maximum detrusorial pressure P_{det} and the ending of the micturition, respectively

Finally, the signal is cleaned up by applying on every $Q_{raw,i}$ the median on eleven values and then the results is plotted on a Q-t graph (Figure 5.9).

5.3.2 JET EXIT VELOCITY u_E

The jet exit velocity u_e is measured with image acquisition and processing system, as already explained in section 2.3.4: in every frame, the part of the image where the jet appears it is cropped (red rectangle on Figure 5.10); then, thanks to the black background, only the pixels that are part of the jet are highlighted, converted in meters with a previously estimated pixel/m conversion factor, and interpolated as a parabola (Figure 5.11).

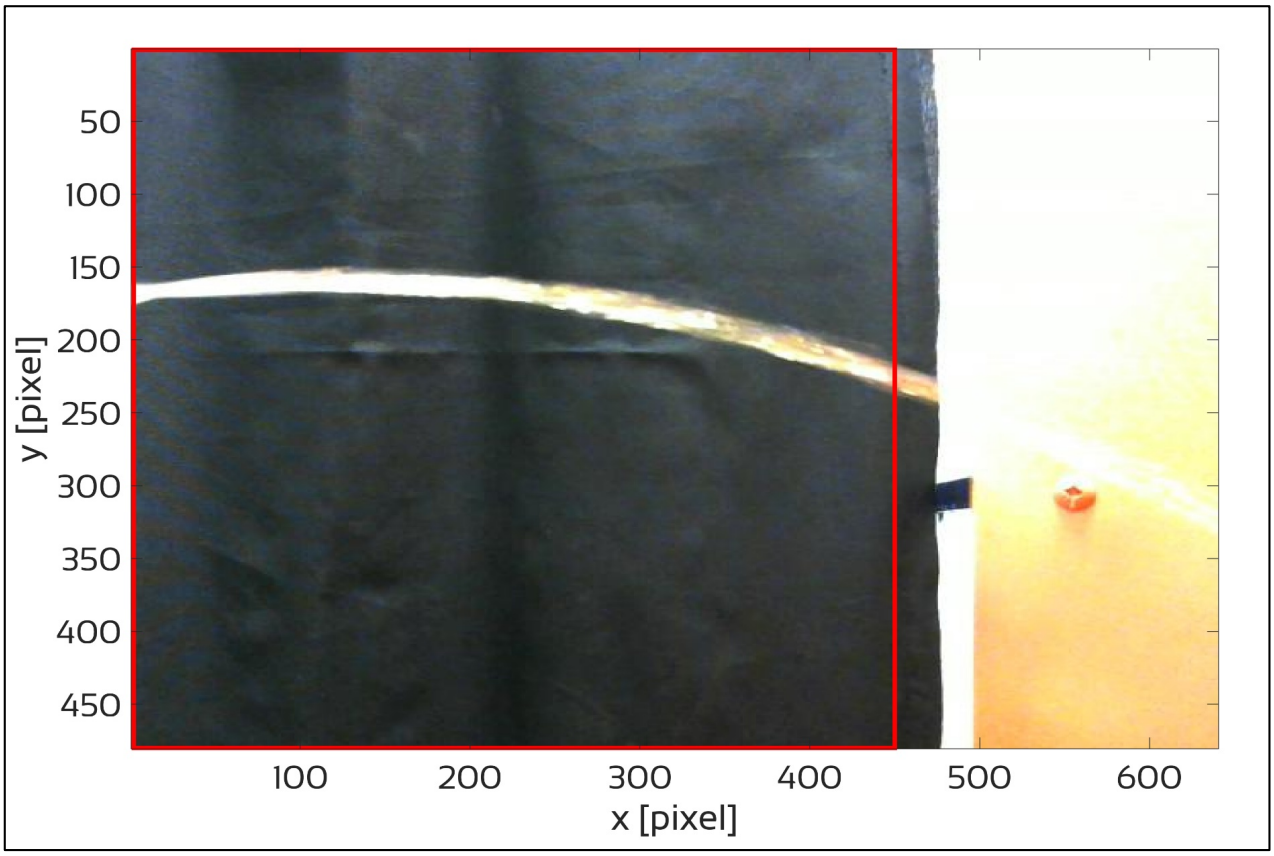

Figure 5.10: sample digital camera frame

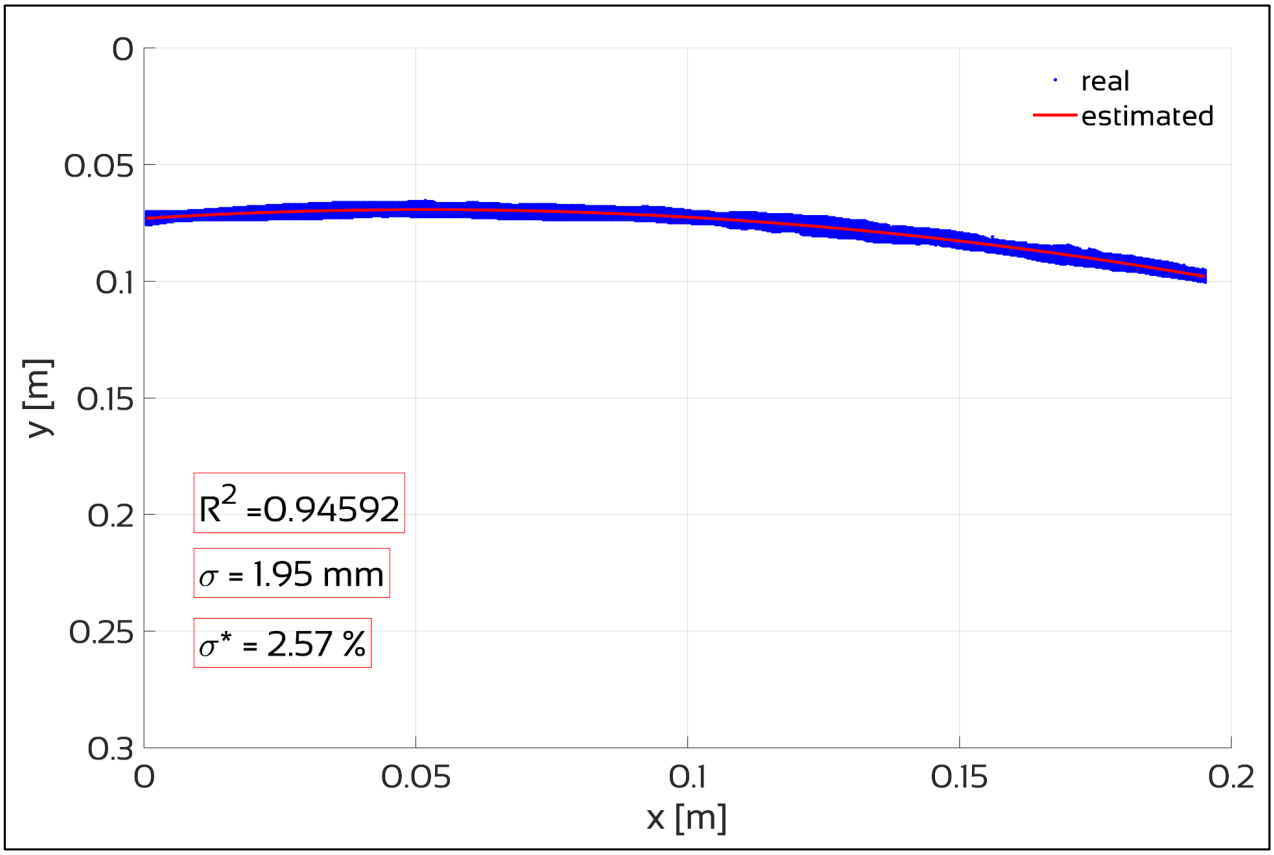

Figure 5.11: parabola trajectory of the frame in Figure 5.10: the blue dots are the real jet and the red line represents the estimated parabola; in the red boxes the relative & standard deviation values are reported

The parabola sequences are then elaborated to obtain jet exit velocity $u_{e,raw}$ [m/s]; finally the signal is cleaned up by applying, on every value, its median on eleven values and then the results is plotted on a u_e-t graph (Figure 5.12).

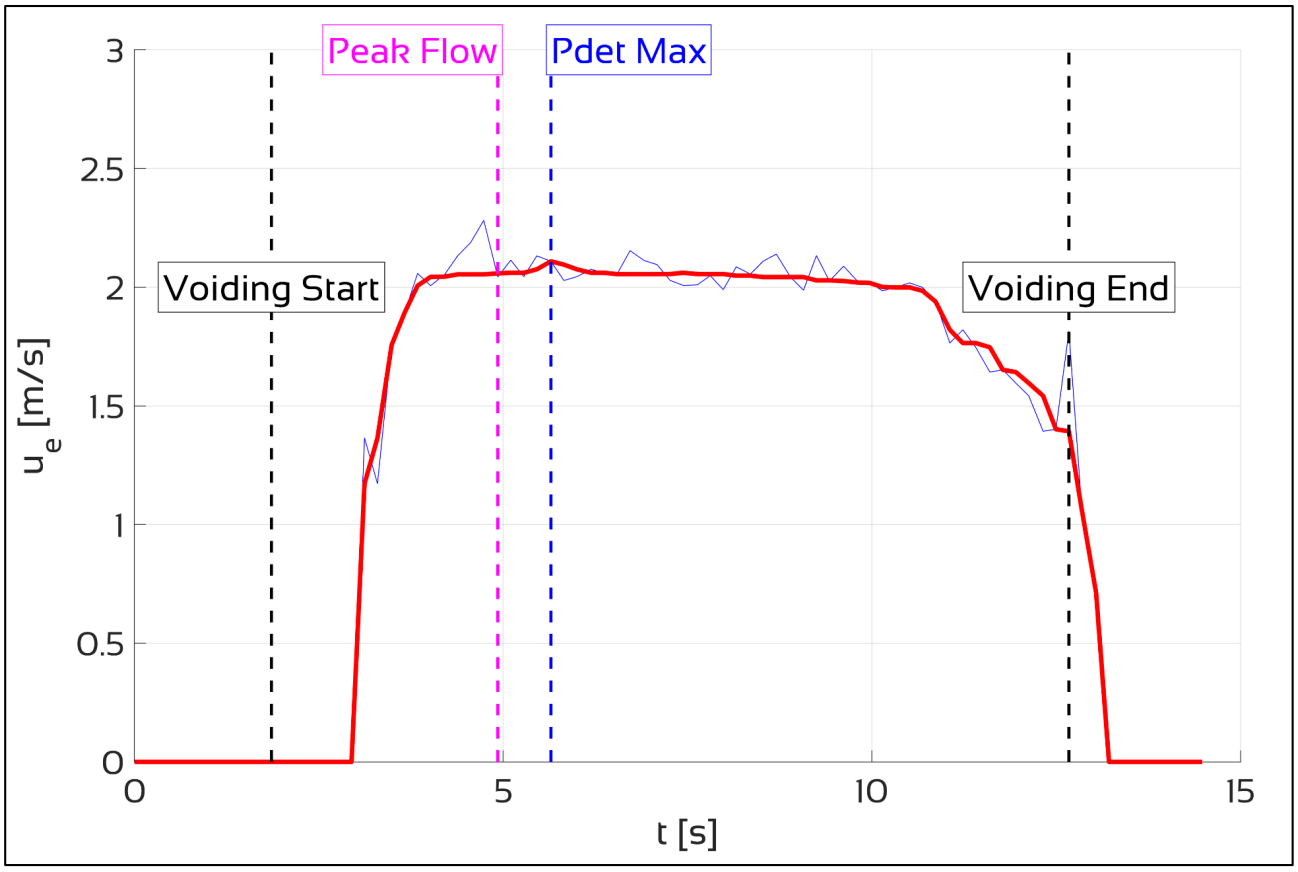

Figure 5.12: plot example of exit velocity u_e: the red line is u_e, while the thin blue line represents $u_{e,raw}$. From left to right, vertical dashed black, magenta, blue and black lines represent the time of the beginning of the micturition, the maximum flow Q_{peak}, the maximum detrusorial pressure P_{det} and the ending of the micturition, respectively

5.3.3 DETRUSORIAL PRESSURE P_{DET}

Using exit velocity u_e, the intravesical pressure P_{det} [cm H_2O] is estimated using relation 3.1, estimated as seen in section 3.1.2; in Figure 5.13 the plot of P_{det} starting from the u_e values of Figure 5.12 is shown.

To be noted that, as we have no information about abdominal pressure P_{abd}, and as $P_{det}=P_{ves}-P_{abd}$, despite the Schäfer's diagram represents the detrusorial pressure P_{det}, ***in the present paper it was considered $P_{det} \equiv P_{ves}$.***

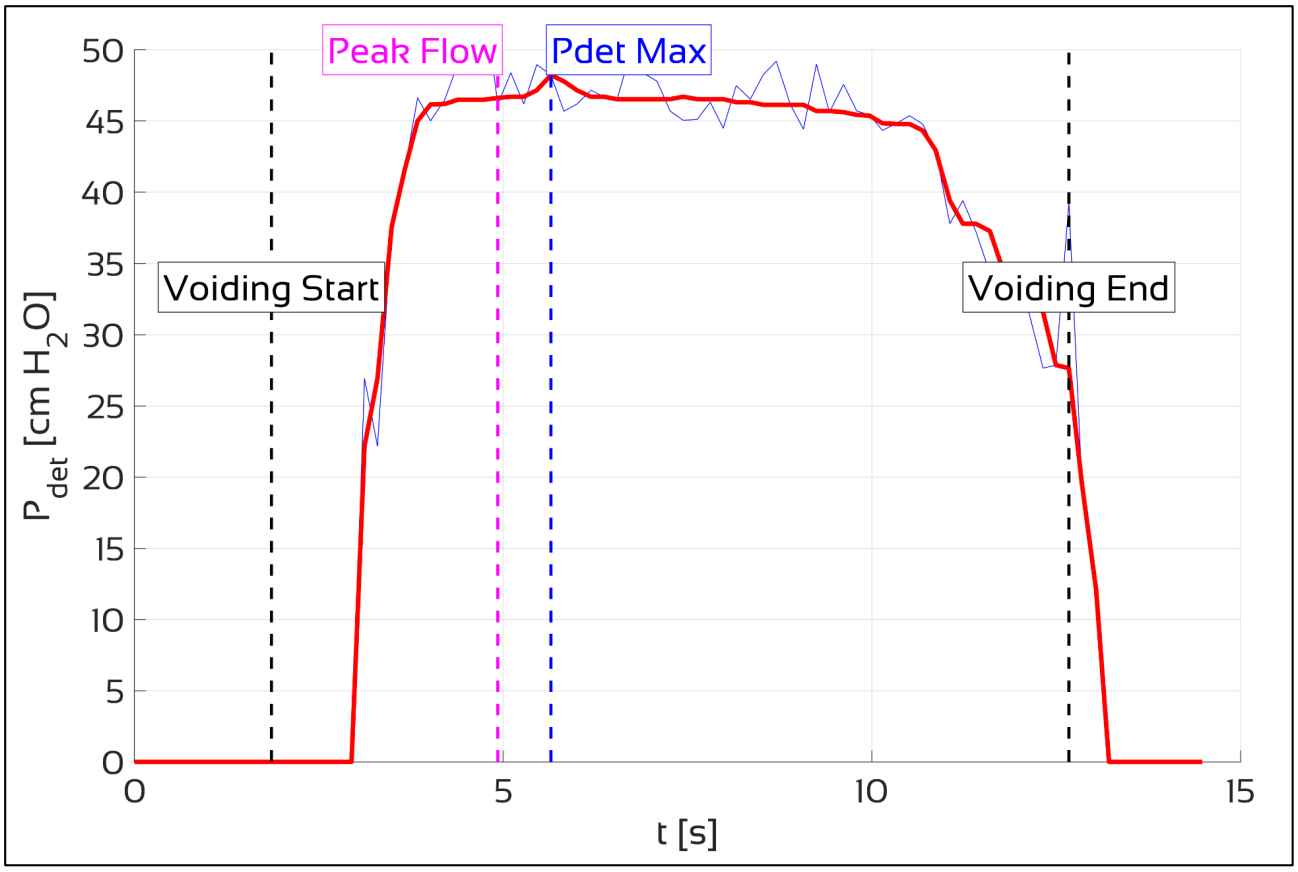

Figure 5.13: plot of intravesical pressure P_{det} (red line) estimated from jet exit velocity u_e values shown in Figure 5.12. From left to right, vertical dashed black, magenta, blue and black lines represent the time of the beginning of the micturition, the maximum flow Q_{peak}, the maximum detrusorial pressure P_{det} and the ending of the micturition, respectively

5.3.4 "Lag time" evaluation

During the measurements it has been observed a time interval (called lag time, T_L) between the acquisition of the jet velocity and the acquisition of the flow rate since the liquid takes some time to flow into the brick-collector located on the scale. We performed some tests on the Innovative Instrumentation using a cylinder full of water that has a horizontal metal tube on the bottom as an exit hole, recording its emptying. Given that we should have the maximum velocity $u_{e,max}$ in correspondence with maximum flow Q_{peak}, we estimate T_L by measuring the time elapsed between $u_{e,max}$ and Q_{peak}. The result is T_L=1.8 s, as shown in Figure 5.14: flow rate and jet exit velocity over time in one of the tests are presented. The blue line is the flow rate Q, the grey line is the jet exit velocity u_e, and the green line is again u_e but shifted by +1.8 s: the maximum flow and the maximum jet exit velocity are aligned.

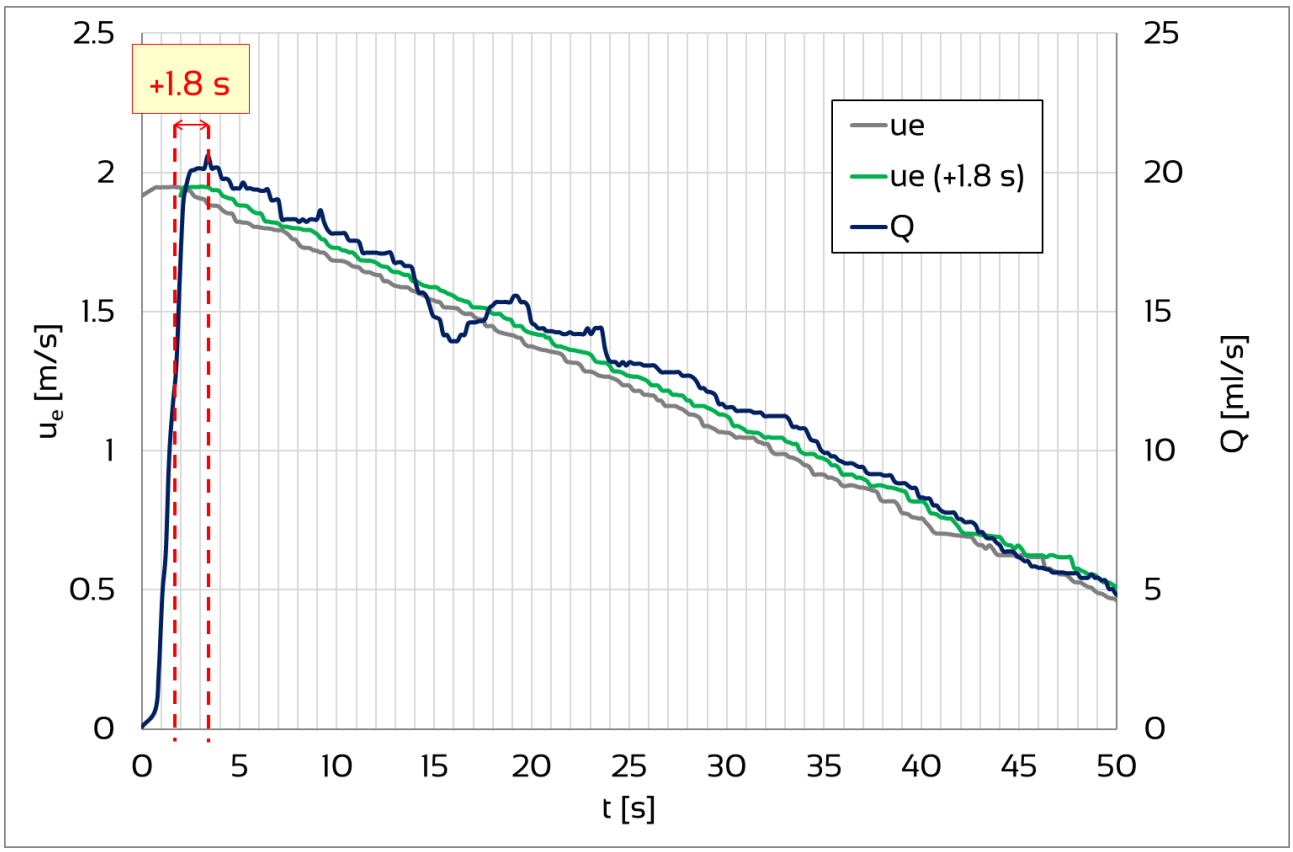

Figure 5.14: evaluation of lag time TL between acquisition of jet velocity and flow rate: the blue line is the flow rate Q, the grey line is the jet exit velocity u_e, and the green line is again u_e shifted by +1.8 s

5.4 CLINICAL REPORT

At the end of the data elaboration, a clinical report which contains the patient's data and the test results is automatically printed (Figure 5.15).

In the first part, top, there are 4 diagrams, synchronized over time, that show from top to bottom:

- Q-t diagram: Q is shown in ml/s, with the indication of the maximum flow (Peak Flow, vertical red line);
- V-t diagram: total volume voided V in ml, with the indications of voiding's beginning (Voiding Start, black vertical line) and of voiding's end (Voiding End, black vertical line);
- u_e-t diagram: jet exit velocity;
- P-t: detrusorial pressure in cm H_2O, with the indication of maximum pressure (P_{det} max, vertical blue line).

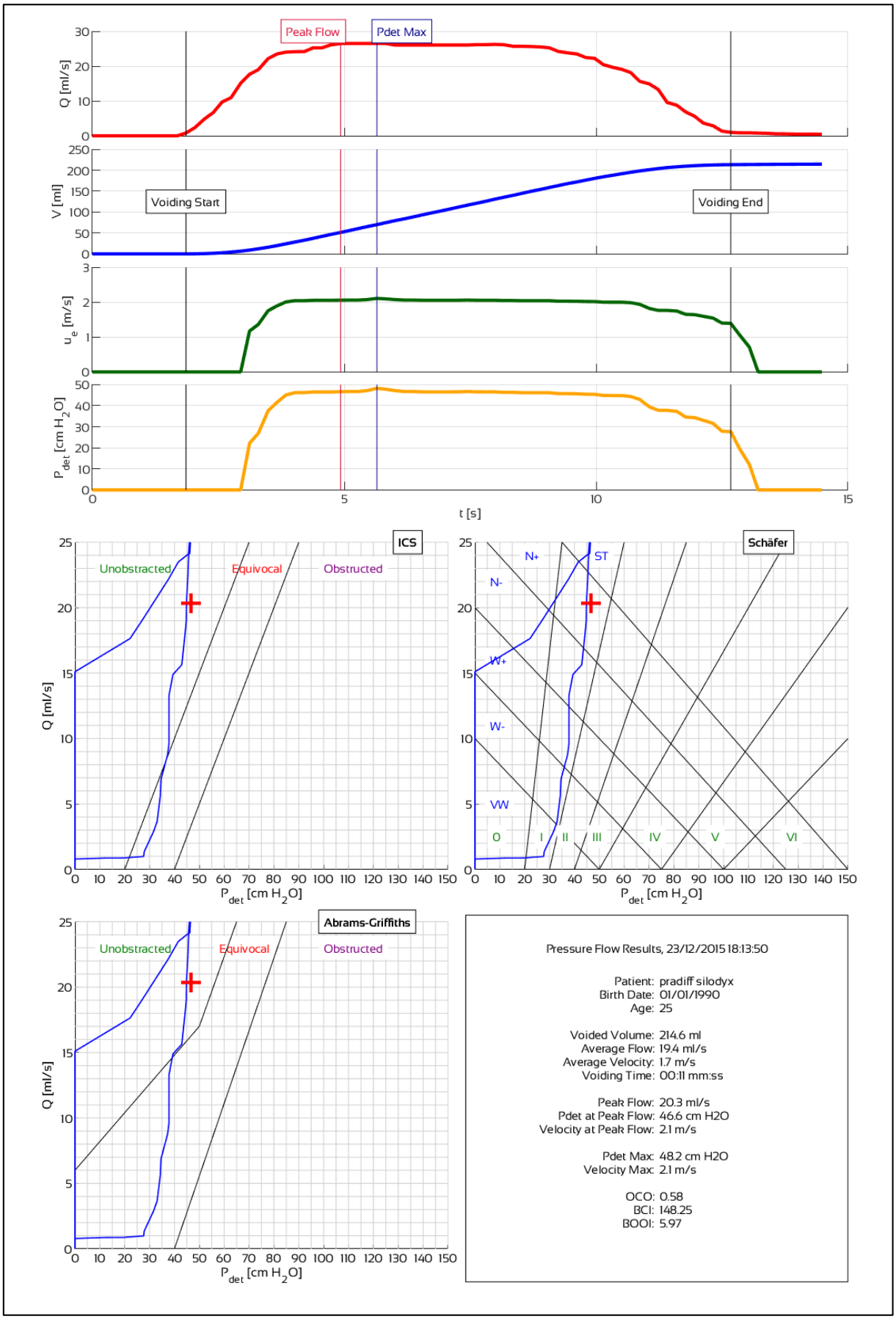

Figure 5.15: clinical report example

In the second part, bottom, there are 3 diagrams currently used in clinical report to quantify the urodynamic functionality, that is:

- ICS previsional method (section 1.4.4);
- Abrams-Griffiths diagram (section 1.4.1);
- Schäfer's diagram (section 1.4.3).

Finally, in the bottom right box, the information about the patient are shown, as well as the main physical parameters and the parameters showing the urodynamic functionality (section 1.5).

5.5 CLINICAL TRIALS: PRELIMINARY RESULTS

Clinical trials ran from January 2019 to February 2020, when they had to stop due to restriction prevention measures for Covid19 pandemic. 123 tests were performed on healthy male volunteers and 4 on obstructed male volunteers, for a total of 127 tests; 5 of them had to be excluded because it was not possible to estimate intravesical pressure from the analysis of the images, thus obtaining a total of 122 tests. Among those, 118 tests show agreement between the results of the Innovative Instrumentation and the Schäfer's diagram.

Table 5.1a-f shows a summary of all the tests performed; the columns represent:

- #, test progressive number;
- # OK: progressive number of test outcomes according to health status;
- Test Name, self-explained, same name represents the same male;
- T_{tot} [s], total voiding time;
- V_{tot} [ml], total volume voided;
- Q_{mean} [ml/s], average flow rate;
- Q_{peak} [ml/s], maximum flow rate;
- Q_{peak_mod} [ml/s], maximum flow rate reduced by 23.3% to take into account flow rate's reduction due to the urethral catheter (as seen in section 3.4.2);
- $u_{e[Qpeak]}$ [m/s], velocity of the urine stream recorded at the same time of the maximum flow rate Q_{peak};
- $P_{det[Qpeak]}$ [cm H_2O], estimated intravesical pressure recorded at the same time of the maximum flow rate Q_{peak};
- OCO, BCI and BOOI [-], urodynamic functionality parameters, as seen in section 1.5;
- Schäfer Obstruction Grade (SOB), where 0 and 1 are considered not obstructed, as explained in section 1.4.3;
- Schäfer Strength Grade (SSG), where from 6 to 2 are considered adequate, as explained in section 1.4.3, with the following conversion table: 6 corresponds to Strong, 5 to Normal+, 4 to Normal-, 3 to Weak+, 2 to Weak- and 1 to Very Weak.

The colors in Table 5.1 (a-f) represents:

- green, the Innovative Instrumentation result agrees with the healthy status of the volunteer, according to the Schäfer's diagram;
- blue, the Innovative Instrumentation result agrees with the obstructed status of the volunteer, according to the Schäfer's diagram;
- white, although the patient is healthy, the outcome of the Innovative Instrumentation is uncertain, according to the Schäfer's diagram;
- red, although the patient is obstructed, the outcome of the Innovative Instrumentation is uncertain, according to the Schäfer's diagram;
- yellow, it was not possible to determine the health status of the volunteer;
- yellow-ochre, the parameters that are not aligned with the correspondent status of the patient.

In Figure 5.16 the results of the clinical trials are presented on a Schäfer's diagram. Each star represents one test, with cyan stars for healthy males and magenta dots for obstructed males: it can be seen that the majority of them are in the proper area of the chart. To be noted that every star is represented by the pair of values (Q_{peak_mod}, $P_{det[Qpeak]}$) to take into account the flow rate's reduction due to the urethral catheter (section 3.4.2).

Figure 5.17 shows the results of the reproducibility test on the Innovative Instrumentation plotted on a Schäfer's diagram, where each color represents a test of the same healthy male. It can be seen that same colors are very close.

#	# OK	Test Name	T_{tot} [s]	V_{tot} [ml]	Q_{mean} [ml/s]	Q_{peak} [ml/s]	$Q_{peak,mod}$ [ml/s]	$u_{e[Qpeak]}$ [m/s]	$P_{det[Qpeak]}$ [cm H_2O]	OCO	BCI	BOOI	SOG	SSG
		MIN REFERENCE VALUE:								0	100	-∞	0	2
		MAX REFERENCE VALUE:								1	∞	20	2	6
1	1	lok_l	15.4	79.4	5	7.7	5.9	1.3	26.4	0.51	55.81	14.57	1	2
2	2	lok_l	26	264	10	14.5	11.2	1.7	36	0.58	91.84	13.73	1	3
3	3	lok_l	12.8	115	8.7	13	9.9	1.6	33	0.55	82.75	13.12	1	3
4	4	lok_l	12.8	73.7	5.5	9.7	7.5	1.5	29.9	0.54	67.32	14.96	1	2
5	5	lok_l	17.8	186	10.3	14.1	10.8	1.8	38.2	0.62	92.09	16.62	1	3
6	6	lok_l	15.6	113	7.1	11.7	9	1.5	31.2	0.54	76.14	13.25	1	3
7	7	l_l	14.8	82.8	5.4	8.6	6.6	1.3	25.7	0.48	58.7	12.48	1	2
8	8	a_b	8.1	88.6	10.5	19.1	14.7	2.1	46.5	0.67	119.8	17.13	1	4
9	9	1_a	15.3	270	17.3	22.6	17.3	2.2	50	0.67	136.7	15.34	1	5
10	10	2_a	15.5	231	14.6	26.6	20.4	1.6	32.9	0.41	135.1	-8.04	1	5
11	11	hh_n	20.4	355	17.2	26.2	20.1	2.1	49.4	0.62	150.1	9.15	1	5
12	12	a_3	13.3	134	9.8	14.1	10.8	0.9	16.4	0.27	70.57	-5.22	0	2
13	13	spatafora_p	22.9	278	12	18.3	14.1	1.9	41.9	0.61	112.3	13.76	1	4
14	14	a_6	27	474	17.4	32.7	25.1	2.6	63.2	0.7	188.6	13.07	2	6
15	-	a_a	25.3	332	13	19	14.6	2.7	69.4	1	142.5	40.19	3	5
16	15	a_3	28.1	428	15.1	20.8	16	2.1	49	0.68	128.8	17.12	1	5
17	16	a_t	20.9	253	12	18.8	14.5	0.5	7.6	0.11	79.82	-21.3	0	3
18	17	dur_y	24.2	329	13.5	20.7	15.9	1.9	42.8	0.6	122.1	11.06	1	4
19	18	gds_t	21.8	425	19.3	33.3	25.6	2.8	72.6	0.8	200.3	21.45	2	6
20	19	jhfbtf_j	23.8	226	9.4	15.9	12.2	1.6	34.1	0.53	95.02	9.77	1	3
21	20	lnkuk_l	31.7	290	9.1	14.5	11.1	2	44.8	0.72	100.3	22.53	2	4

Table 5.1: summary of clinical tests on healthy males (a)

#	# OK	Test Name	T_{tot} [s]	V_{tot} [ml]	Q_{mean} [ml/s]	Q_{peak} [ml/s]	$Q_{peak,mod}$ [ml/s]	$u_{e[Qpeak]}$ [m/s]	$P_{det[Qpeak]}$ [cm H_2O]	OCO	BCI	BOOI	SOG	SSG
22	21	q_q	34.6	435	12.5	19.2	14.8	2.3	55.3	0.8	129.1	25.81	2	5
23	-	as_u	27	427	15.7	20.6	15.8	3.1	82.3	1.15	161.4	50.72	3	6
24	22	tet_t	19.3	363	18.6	30.2	23.2	2.4	57.9	0.67	173.8	11.54	2	6
25	23	antonino_c	12.6	71.4	5.5	8.3	6.4	1.2	23.7	0.45	55.55	10.92	0	2
26	24	lento_f	16.5	144	8.6	13.7	10.5	1.8	39.8	0.65	92.43	18.72	1	3
27	+	rosati_e	45.1	229	5	11.3	8.7	0.7	12.3	0.21	55.72	-5.12	0	2
28	25	aaa_a	16.8	240	14.1	19.6	15	2	44.1	0.63	119.1	14.05	1	4
29	26	kk_p	27.6	391	14	23.2	17.8	2	46	0.61	135.1	10.43	1	5
30	27	1_1	15.7	304	19.1	26.2	20.1	2.2	50.6	0.63	151.3	10.37	1	5
31	28	a_m	30.9	393	12.7	20.9	16	2.2	50.1	0.7	130.1	18.1	2	5
32	29	io_i	25.6	193	7.4	15.8	12.1	0.9	14.9	0.23	75.56	-9.32	0	3
33	30	asd_a	9.9	123	12.1	18.2	14	2	45	0.66	114.8	17.06	1	4
34	31	xx_x	16.1	269	16.5	24.4	18.7	1	17.6	0.23	111.1	-19.8	0	4
35	32	c_a	17.5	232	13	20	15.3	1.1	19.6	0.28	96.32	-11.1	0	3
36	33	micheli_p	23.4	234	9.8	15.2	11.6	2.3	55.2	0.87	113.4	31.96	2	4
37	34	asd_a	15.2	250	16.2	26.3	20.2	2.3	53.8	0.67	154.7	13.52	1	5
38	35	gfdds_s	18.4	329	17.7	26.2	20.1	1.7	36	0.45	136.4	-4.09	1	5
39	36	324519_u	12.6	233	18.1	29.8	22.9	2.4	58	0.68	172.4	12.18	2	6
40	37	mi-spiego----va-bene-_c_c	26.5	215	8.1	13.2	10.1	1.7	36.1	0.6	86.56	15.89	1	3
41	38	LaCetra_B	7.9	106	12.8	19.8	15.2	1.8	39.6	0.56	115.4	9.32	1	4
42	39	AAA_B	10.6	194	17.7	29.6	22.7	2.1	48.6	0.57	162.1	3.12	1	6
43	40	1_1	22.5	383	16.8	22.5	17.2	2.1	46.5	0.62	132.7	12.03	1	5
44	41	bra-1_b	51	316	6.1	11.6	8.9	1.2	23	0.4	67.59	5.11	0	2
45	42	syggdf_s	23.5	317	13.3	24.6	18.9	2.1	48.4	0.62	142.7	10.74	1	5
46	43	rtrd_y	17.3	257	14.6	27.3	20.9	2.8	70.3	0.86	175	28.51	2	6

Table 5.1: summary of clinical tests on healthy males (b)

#	# OK	Test Name	T_{tot} [s]	V_{tot} [ml]	Q_{mean} [ml/s]	Q_{peak} [ml/s]	$Q_{peak,mod}$ [ml/s]	$u_{e[Qpeak]}$ [m/s]	$P_{det[Qpeak]}$ [cm H_2O]	OCO	BCI	BOOI	SOG	SSG
47	44	turur_h	13.5	230	16.7	24.5	18.8	1.5	30.5	0.39	124.5	-7.16	0	4
48	45	aaaa_a	11.2	158	13.8	20.5	15.8	2.7	66.7	0.93	145.5	35.14	2	5
49	46	a_c	19.7	313	15.7	22.5	17.3	0.9	15.3	0.21	101.8	-19.2	0	4
50	47	ad_a	17.7	190	10.7	14.1	10.8	2.1	48.5	0.79	102.7	26.88	2	4
51	48	tger_e	15.7	252	15.7	27.5	21.1	2.1	48.5	0.59	153.9	6.31	1	5
52	49	Rocky_B	13.5	298	21.3	34	26.1	2.3	53.2	0.58	183.5	1.04	1	6
53	50	x_x	28.5	384	13.4	22.6	17.3	0.8	13.9	0.19	100.5	-20.8	0	4
54	51	jhgk_k	15.7	251	15.8	30.6	23.5	2	44.2	0.51	161.7	-2.81	1	6
55	52	si--pronto_c	20.7	174	8.3	12.1	9.3	1.6	32.8	0.56	79.41	14.22	1	3
56	53	silodyx_p	10.8	215	19.4	26.5	20.3	2.1	46.6	0.58	148.3	5.97	1	5
57	54	a_m	13.5	142	10.3	17.8	13.7	1.7	36.7	0.54	105.1	9.34	1	4
58	55	ventrice_g	34.6	34.7	1	3.2	2.4	1	17.8	0.4	29.92	12.97	0	1
59	56	kjhsfd_n	27.4	236	8.5	13.9	10.7	1.8	37.5	0.61	90.84	16.13	1	3
60	57	M_A	22.2	253	11.2	18.7	14.4	2	43.8	0.64	115.6	15.14	1	4
61	58	fabiani_l	19.8	288	14.3	21	16.1	2.3	53.4	0.74	134.2	21.14	2	5
62	59	aa_a	26.1	327	12.5	17.5	13.4	2.1	47.1	0.7	114.3	20.18	2	4
63	60	aaa_a	10.8	186	16.8	27.3	20.9	1.9	40.6	0.5	145.3	-1.27	1	5
64	61	nistri_a	15.1	351	22.7	41	31.5	1.8	39.2	0.38	196.6	-23.8	1	6
65	62	dal-vago_a	58.4	326	5.5	15.7	12	1.7	35.9	0.56	95.93	11.83	1	3
66	63	bernini_r	20.4	71	3.4	5.6	4.3	1.8	37.9	0.78	59.53	29.27	2	2
67	64	gjonaj_a	16.2	139	8.4	13.9	10.7	1.5	30.9	0.5	84.28	9.48	1	3
-	-	david_l	32.5	466	14.3	22.4	-	-	-	-	-	-	-	-
68	65	francia_p	18.2	279	15.1	26.4	20.2	1.7	36.1	0.45	137.3	-4.31	1	5
69	66	costa_s	33	228	6.8	15	11.5	1.6	32.3	0.51	89.89	9.23	1	3
70	67	a_a	22.5	284	12.5	21	16.1	1	17.4	0.24	97.91	-14.8	0	3

Table 5.1: summary of clinical tests on healthy males (c)

#	# OK	Test Name	T_{tot} [s]	V_{tot} [ml]	Q_{mean} [ml/s]	Q_{peak} [ml/s]	$Q_{peak,mod}$ [ml/s]	$u_{e[Qpeak]}$ [m/s]	$P_{det[Qpeak]}$ [cm H_2O]	OCO	BCI	BOOI	SOG	SSG
-	-	saccomando_c	51.2	19.5	0.4	2.2	-	-	-	-	-	-	-	-
71	68	alterini_l	61.5	197	3.2	8.9	6.8	1.2	22.8	0.43	56.74	9.2	0	2
72	69	d'amore_v	66.5	122	1.8	4.2	3.2	1.8	37.6	0.81	53.8	31.12	2	2
73	70	12_1	19.3	168	8.6	13.5	10.4	1.9	42.5	0.7	94.25	21.78	2	3
74	71	10_1	10.1	146	14	24.2	18.6	2.6	64	0.83	156.8	26.83	2	5
75	72	14_1	38.6	522	13.5	22.3	17.1	0.9	15.2	0.2	100.9	-19.1	0	4
76	73	14_1	30.5	465	15.1	24.9	19.1	0.9	15.3	0.2	110.7	-22.8	0	4
77	74	a_c	12.4	138	10.8	15.6	12	1.4	27.4	0.43	87.41	3.45	1	3
78	75	w_e	18.2	249	13.4	20.4	15.7	0.9	16.8	0.24	95.22	-14.5	0	3
79	76	18_1	16.8	251	14.8	21.1	16.2	2.2	49.8	0.69	130.8	17.37	2	5
80	77	23_2	20.7	324	15.4	22.2	17	2.1	48.5	0.66	133.5	14.52	1	5
81	78	14_1	29.4	441	14.8	22.9	17.6	0.8	13.4	0.18	101.3	-21.8	0	4
82	79	1_1	14.6	319	21.4	34	26.1	2.2	51.9	0.56	182.3	-0.25	1	6
83	80	4_4	7.9	72.8	8.8	15.3	11.8	2	44.5	0.7	103.4	20.95	2	4
84	81	1_1	12.6	204	15.8	28	21.5	2.1	48.1	0.58	155.5	5.21	1	5
85	82	cocci_a	24.3	255	10.4	13.9	10.7	1.9	40.3	0.66	93.58	18.97	1	3
86	83	antani_a	10.3	57.6	5.4	9.2	7	1.1	20.1	0.37	55.3	6.05	0	2
87	-	antani-2_a	44.7	134	3	6	4.6	0.8	14.9	0.3	37.98	5.69	0	1
88	84	cocci_a	26.1	226	8.6	12.7	9.7	1.9	41.8	0.7	90.47	22.38	2	3
89	85	cocci_a	28.9	229	7.9	11.2	8.6	1.6	33.5	0.58	76.62	16.2	1	3
90	86	12_1	23.6	142	5.9	8.9	6.8	1.4	28.2	0.52	62.31	14.5	1	2
91	87	cocci_a	23.6	187	7.8	11.6	8.9	1.8	37.5	0.65	81.95	19.78	1	3
92	88	3_3	22.5	292	12.8	23	17.6	2.1	47.8	0.64	135.9	12.58	1	5
93	89	7_7	13.5	153	11.1	16.4	12.6	0.4	5.5	0.08	68.53	-19.7	0	2
94	90	cocci_a	25.2	225	8.9	12.5	9.6	1.7	36.2	0.61	84.3	16.98	1	3

Table 5.1: summary of clinical tests on healthy males (d)

#	# OK	Test Name	T_{tot} [s]	V_{tot} [ml]	Q_{mean} [ml/s]	Q_{peak} [ml/s]	$Q_{peak,mod}$ [ml/s]	$u_{e[Qpeak]}$ [m/s]	$P_{det[Qpeak]}$ [cm H_2O]	OCO	BCI	BOOI	SOG	SSG
95	91	cocci_a	18.2	191	10.4	16.8	12.9	1.8	39.1	0.59	103.5	13.35	1	4
96	92	cocci_a	17.8	170	9.4	14.6	11.2	1.7	36.6	0.59	92.66	14.2	1	3
97	93	cocci_a	18.6	175	9.3	14.7	11.3	1.9	41.6	0.66	98.03	19.03	1	3
-	-	000001_0	27.6	247	8.8	13.7	-	-	-	-	-	-	-	-
98	94	testosterone_t	23.6	126	5.3	10.5	8.1	1.3	25.2	0.45	65.56	9.03	1	2
-	-	king_k	17.5	406	22.9	37.1	-	-	-	-	-	-	-	-
-	-	white_b	17.7	215	12	17.8	-	-	-	-	-	-	-	-
99	95	vlam_v	13.7	197	14.2	21.1	16.2	1.8	38.3	0.53	119.4	5.93	1	4
100	96	testosterone_t	16.6	171	10.1	19.1	14.7	1.7	36.7	0.53	110.1	7.38	1	4
101	97	berry_w	18.8	237	12.4	19.6	15	2.2	51.5	0.74	126.6	21.49	2	4
102	98	Pippo_F	26.5	535	20	33.6	25.8	2.6	64.8	0.71	193.7	13.2	2	6
103	99	LUTS_L	14	190	13.2	21.5	16.5	1.9	41.7	0.57	124.3	8.63	1	4
104	100	LUTS_L	16.4	205	12.3	21.4	16.4	1.8	38.2	0.52	120.4	5.37	1	4
105	101	John_H	14.4	244	16.7	30.1	23.1	2.1	47.1	0.55	162.5	1	1	6
106	102	er-piscione_e	16	292	17.9	31.9	24.4	2.5	60.8	0.68	183.1	11.96	2	6
107	103	ossa-_r	33.7	403	11.9	18.2	14	2.1	47	0.69	116.8	19	2	4
108	104	LUTS_L	21.3	146	6.8	10.5	8.1	1.4	27	0.48	67.37	10.86	1	2
109	105	TESTOSTERONE_T	19.5	262	13.2	20.7	15.9	1.8	38.1	0.53	117.5	6.39	1	4
110	106	VLAM_V	39.7	650	16.3	23.2	17.8	1.9	40.5	0.54	129.5	4.87	1	5
111	107	VLAM_V	27.4	441	16	23.8	18.3	1.9	42	0.55	133.3	5.4	1	5
112	108	testosterone_t	18.6	167	8.9	14.1	10.8	1.5	29.7	0.48	83.87	8.08	1	3
113	109	prova_p	6.1	57.1	8.8	16.9	12.9	1.3	26.1	0.4	90.73	0.22	0	3
114	110	cerbero_c	16.6	293	17.4	32.6	25	2.3	52.9	0.59	178.1	2.85	1	6
115	111	el_m	24.2	403	16.6	28.3	21.8	1.7	36.4	0.44	145.1	-7.12	1	5
116	112	prova_p	5.4	53.1	9.2	16.6	12.7	1.1	19.5	0.3	83.28	-5.95	0	3

Table 5.1: summary of clinical tests on healthy males (e)

#	# OK	Test Name	T_{tot} [s]	V_{tot} [ml]	Q_{mean} [ml/s]	Q_{peak} [ml/s]	$Q_{peak,mod}$ [ml/s]	$u_{e[Qpeak]}$ [m/s]	$P_{det[Qpeak]}$ [cm H_2O]	OCO	BCI	BOOI	SOG	SSG
117	113	nostress_n	14.4	167	11.4	18.2	13.9	1.7	36	0.53	105.7	8.14	1	4
118	114	cerbero_c	10.3	171	16.2	26.1	20	2.2	50.5	0.63	150.5	10.54	1	5
119	115	john_c	19	442	23	36.3	27.9	1.9	40.9	0.43	180.2	-14.8	1	6
120	116	supertramp_a	16.9	444	25.9	36.5	28	2	44.7	0.47	184.8	-11.3	1	6
121	117	baudo_p	14.1	272	18.9	30.5	23.4	1.4	27.3	0.31	144.4	-19.5	0	5
122	118	Pioggia_D	19.1	306	15.8	27.4	21	2	43.8	0.53	148.8	1.85	1	5

Table 5.1: summary of clinical tests on healthy males (f)

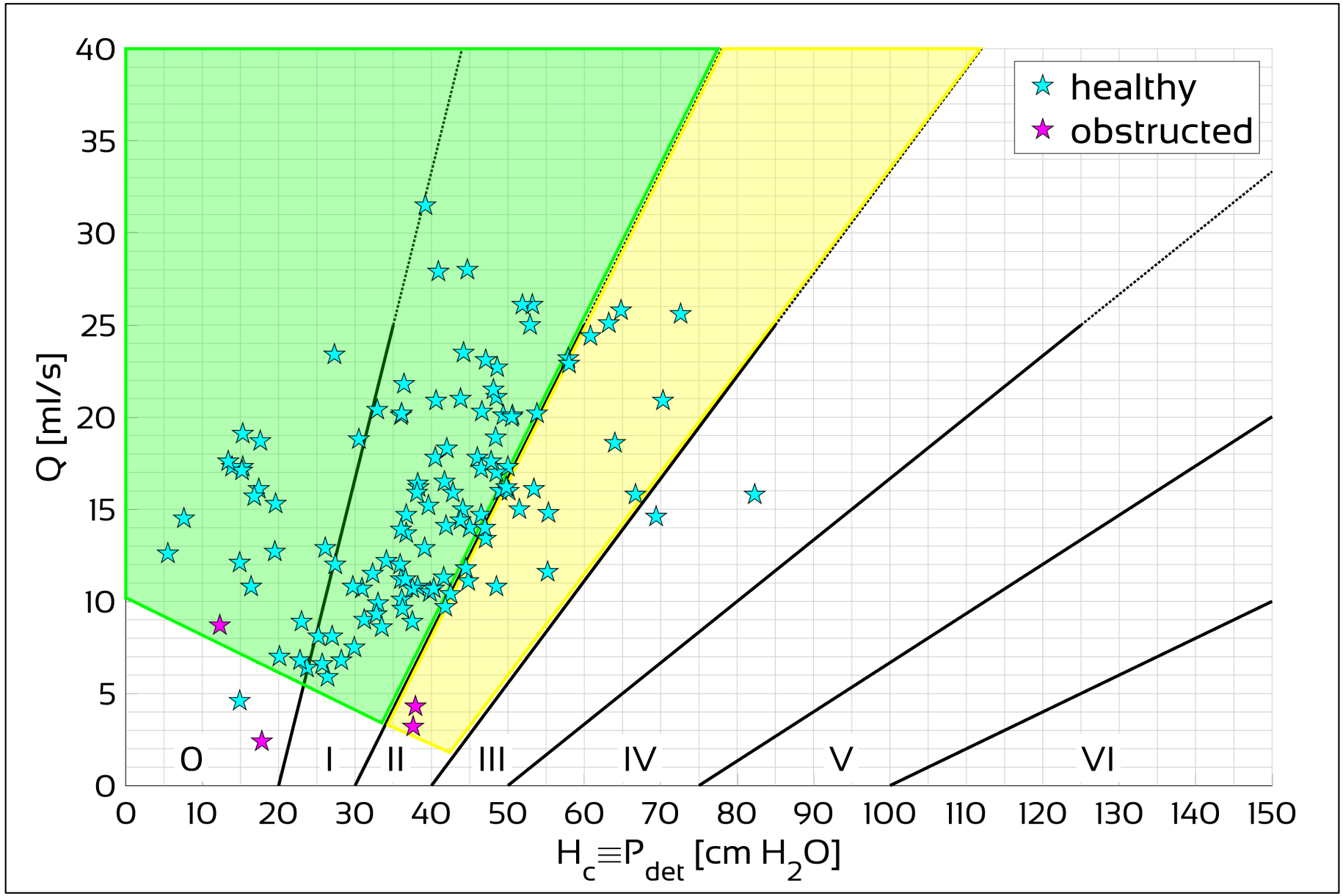

Figure 5.16: clinical trials on the Innovative Instrumentation; each star represents a different test

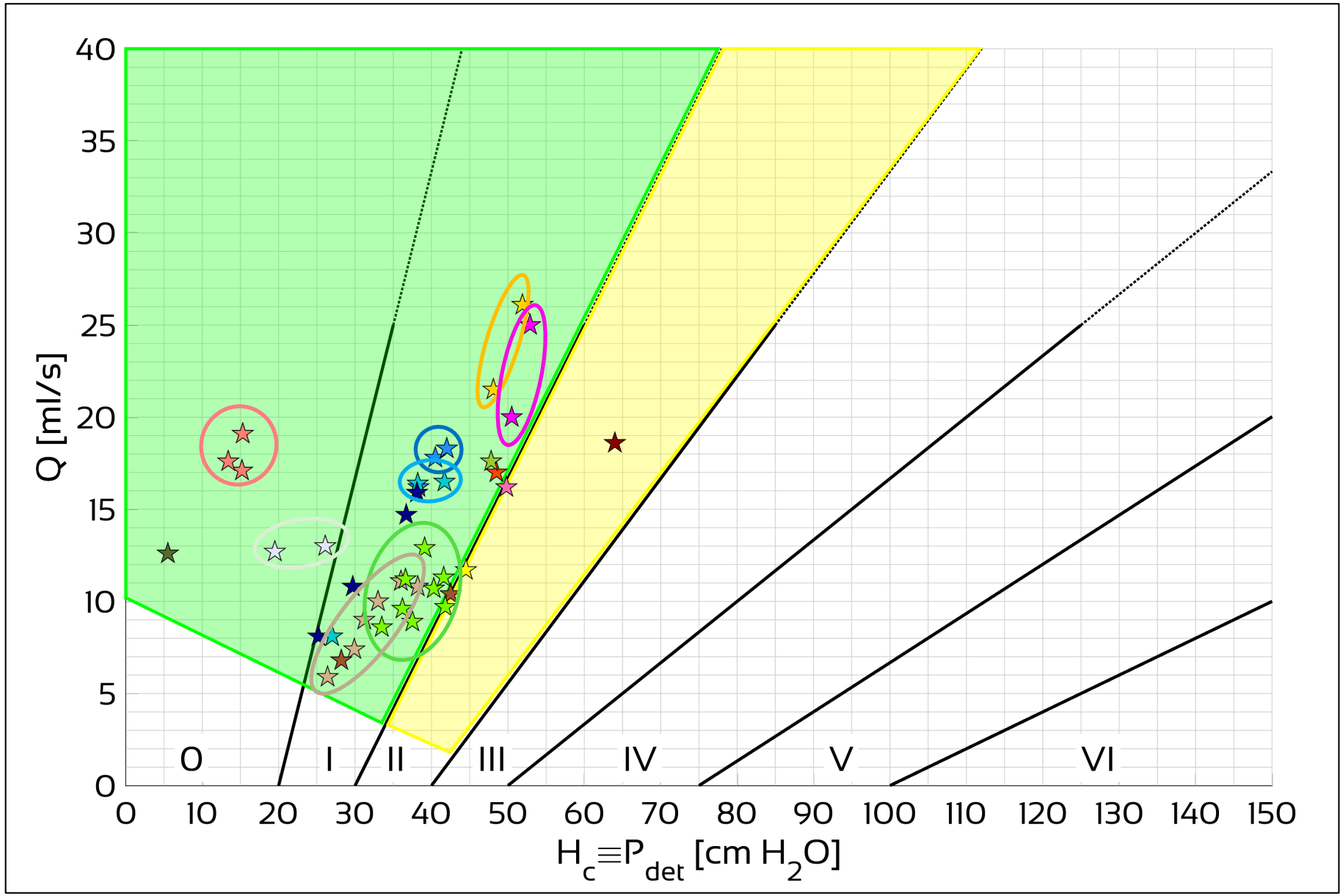

Figure 5.17: reproducibility test on the Innovative Instrumentation; each color represents a test of the same healthy male

6 Results and Discussion

An Innovative Instrumentation aimed to assess the functionality of the LUT in a very non-invasive way has been developed. A Prototype of this Innovative Instrumentation, built in the Fluvial and Lagoon Hydraulics and Biofluidodynamics Laboratory of the Department of Civil and Environmental Engineering (DICEA), has been taken to the Urology Clinic at the Department of Experimental and Clinical Medicine (DMSC) of Careggi Hospital, Florence, to perform a clinical testing campaign. Clinical trials ran from January 2019 to February 2020, when they had to stop due to restriction measures for Covid19 pandemic. The details of the design and the instrumentation have been shown in section 5, as well as the results.

Moreover, it has been performed an extensive laboratory activity on a Model of the LUT, built in the Hydraulics Laboratory of the DICEA of the University of Florence. The main experimental activities can be summarized as follows:

- estimation of the jet velocity by detecting the jet parabola through image acquisition and processing system (section 2.3.4).
- estimation of the physical properties of the Tube (section 2.3.5);
- "Physiological flow condition" tests, performed with a free Tube, to link the intravesical pressure to the external characteristics of the jet (section 3.1);
- "Pathological flow condition" tests, performed by inserting an obstruction inside the Tube (section 3.2);
- "Diagnostic flow condition" tests, performed by introducing a catheter inside the Tube (section 3.4).

The laboratory activities were carried out in parallel with the development of a numerical model of the LUT, aimed to simulate its functionality by using the basic equations of fluid mechanics. The mechanical behavior of the Tube is numerically described by the Tube Law. Through the "Diagnostic flow condition" tests it was possible to collect experimental data (velocity, cross-sectional area) to calibrate a Tube Law able to provide an adequate relationship between pressure and cross-sectional area deformation (section 4.1.2).

With "Physiological flow condition" tests it was possible to recalibrate the Tube Law for micturition without catheter in healthy people (section 4.3.2), while "Pathological flow condition" tests were used to verify the Tube Law in obstructed subjects (section 4.3.3).

Once the numerical model has been calibrated, the detrusor pressure can be estimated from the values of flow rate and exit velocity obtained by non-invasive measurements, that is measurements taken with no contact with the human body.

Figure 6.1 shows a new version of the Schäfer's diagram: on the abscissas we have the kinetic head at the Tube's exit K_e, defined by:

$$K_e = \frac{{u_e}^2}{2g} \qquad 6.1$$

while on the ordinates the flow rate Q. The diagram shows the data of the "Physiological flow condition" tests (black dots) and the "Pathological" (colored dots), and data from clinical trials (cyan stars for healthy males and magenta stars for obstructed males). Each point or star represents the peak value of the flow rate Q_{peak} and the corresponding kinetic head value $K_{e[Qpeak]}$. The diagram can be divided into three areas:

- the area above the black line, which represents healthy subjects;
- the area between the black line and the red line, which represents subjects who are uncertain, or with light obstructions;
- the area under the red line, which represents the obstructed subjects.

Note that the area below the red line and to the right of the red dashed line was marked as uncertain as we do not have enough data to identify it.

It is possible to see that the stars (clinical trials data) are the most in the proper area of the diagram.

According to Figure 6.2, this diagram can be coupled to another diagram having on the abscissa K_e again, while in the ordinate H_c (or the detrusorial pressure P_{det}): on this second diagram the results from the "Pathological flow condition" tests were reported (colored dots) with trend dashed lines (blue for healthy, green for lightly obstructed and red for obstructed). These coupled diagrams are called "Coupled Urodynamic Diagram".

The Coupled Urodynamic Diagram can be used to estimate the detrusorial pressure, as shown in Figure 6.3: the cyan star represents one of the healthy clinical trials, the detrusorial pressure (cyan cross) can be estimated following the relation in the second diagram according to the state of the patient (healthy, lightly obstructed or obstructed).

The proposed Coupled Urodynamic Diagram appears to be quite interesting since it allows to trace the functional status of the patient, but unlike Schäfer it uses only non-invasive data.

Moreover, in order to have an estimation of the detrusorial pressure P_{det}, a relationship between K_e and P_{det} can be obtained by using the results of the numerical model. For example, Figure 6.4 shows the computed total head in section 7 (H_7, which corresponds to the pressure in the bladder P_{det}) as a function of K_e. It is possible to see well-defined correlations for the various obstruction types providing additional tools for improving the diagnosis reliability of the LUT functionality.

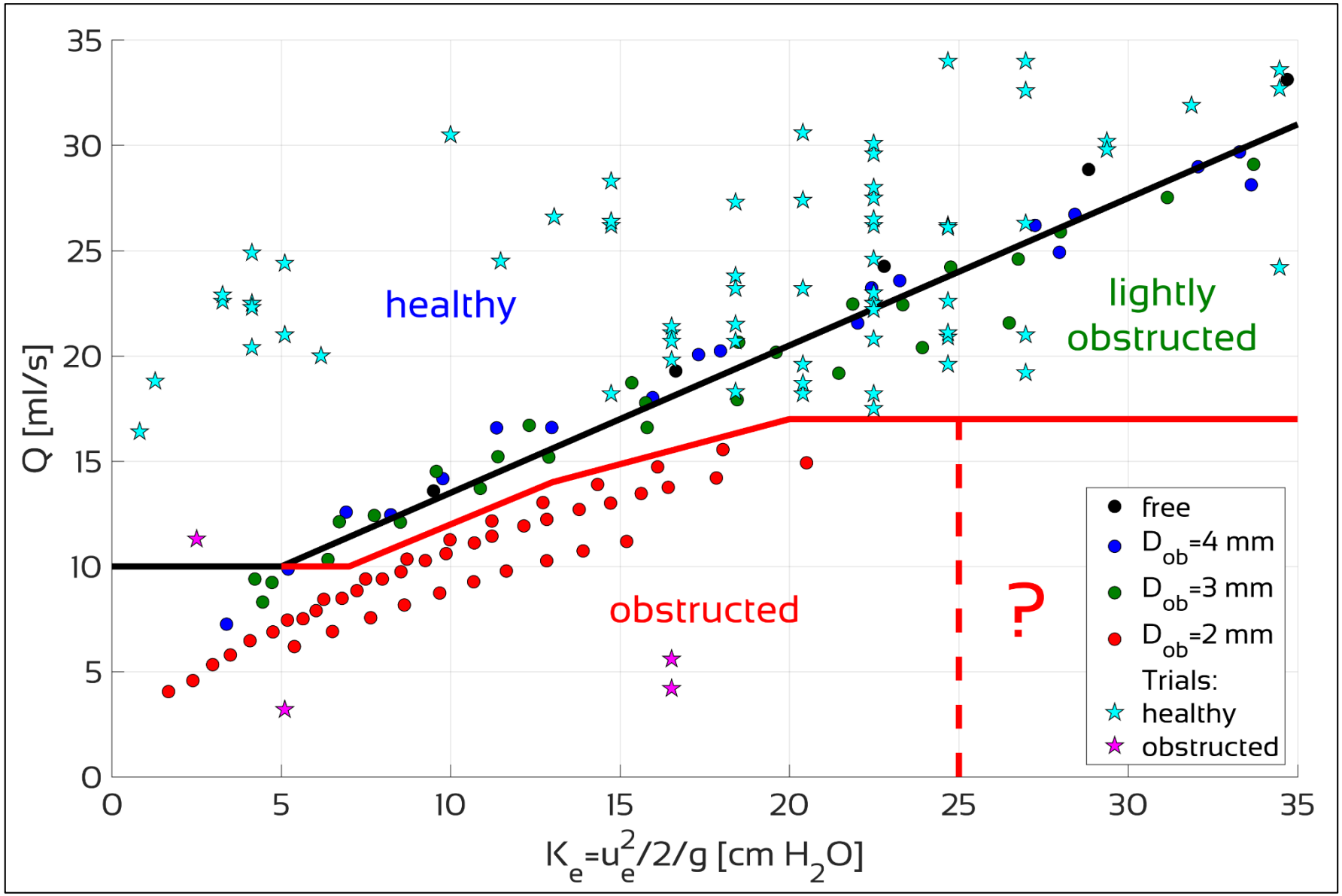

Figure 6.1: new version of Schäfer's diagram: lab data (dots) and clinical data (stars); the black and red lines divide the chart in three areas (healthy subjects, uncertain or lightly obstructed, and obstructed)

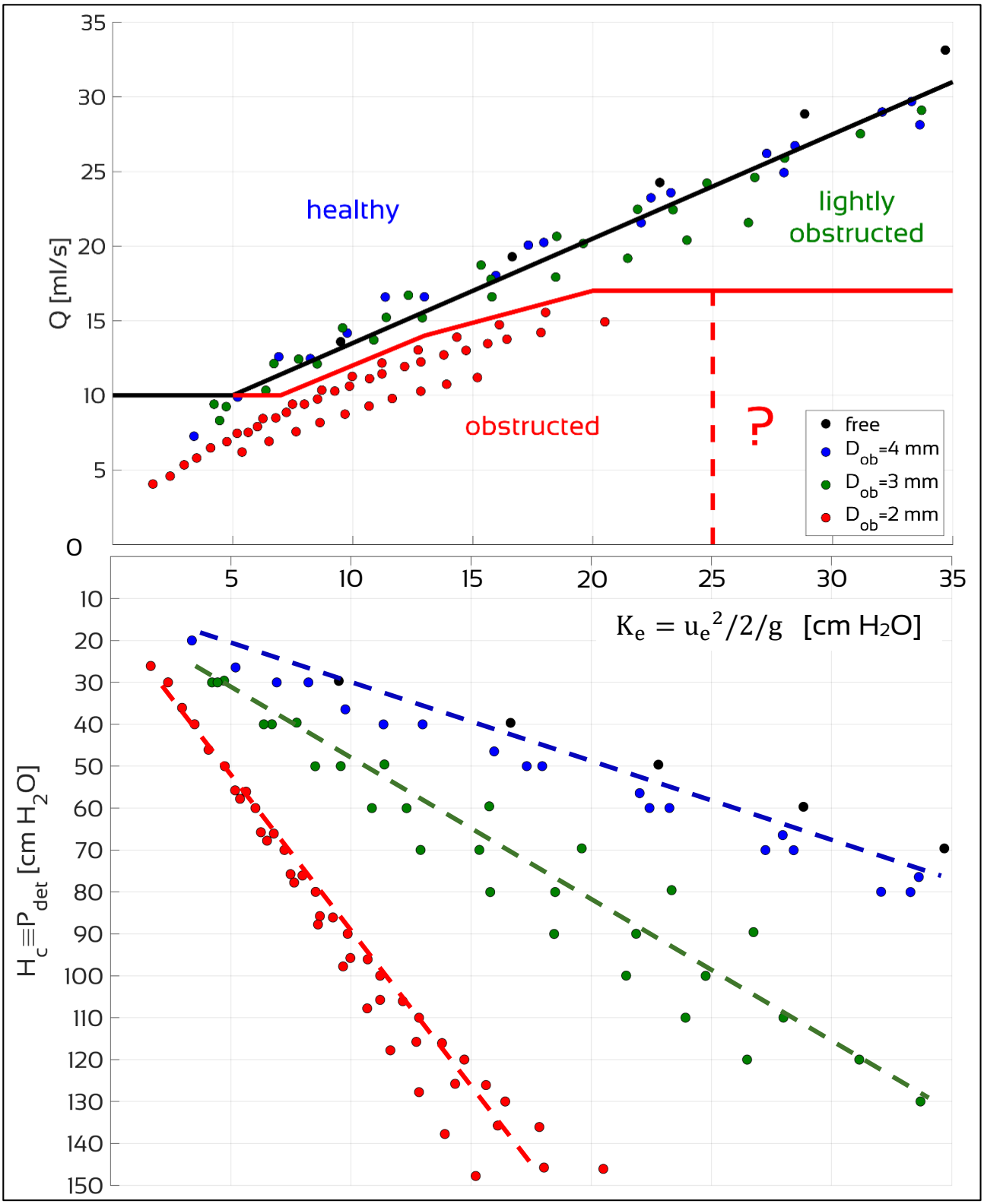

Figure 6.2: Coupled Urodynamic Diagram: above, the new version of Schäfer's diagram; below, "Pathological flow condition" tests (colored dots) with trend dashed lines (blue for healthy, green for lightly obstructed and red for obstructed)

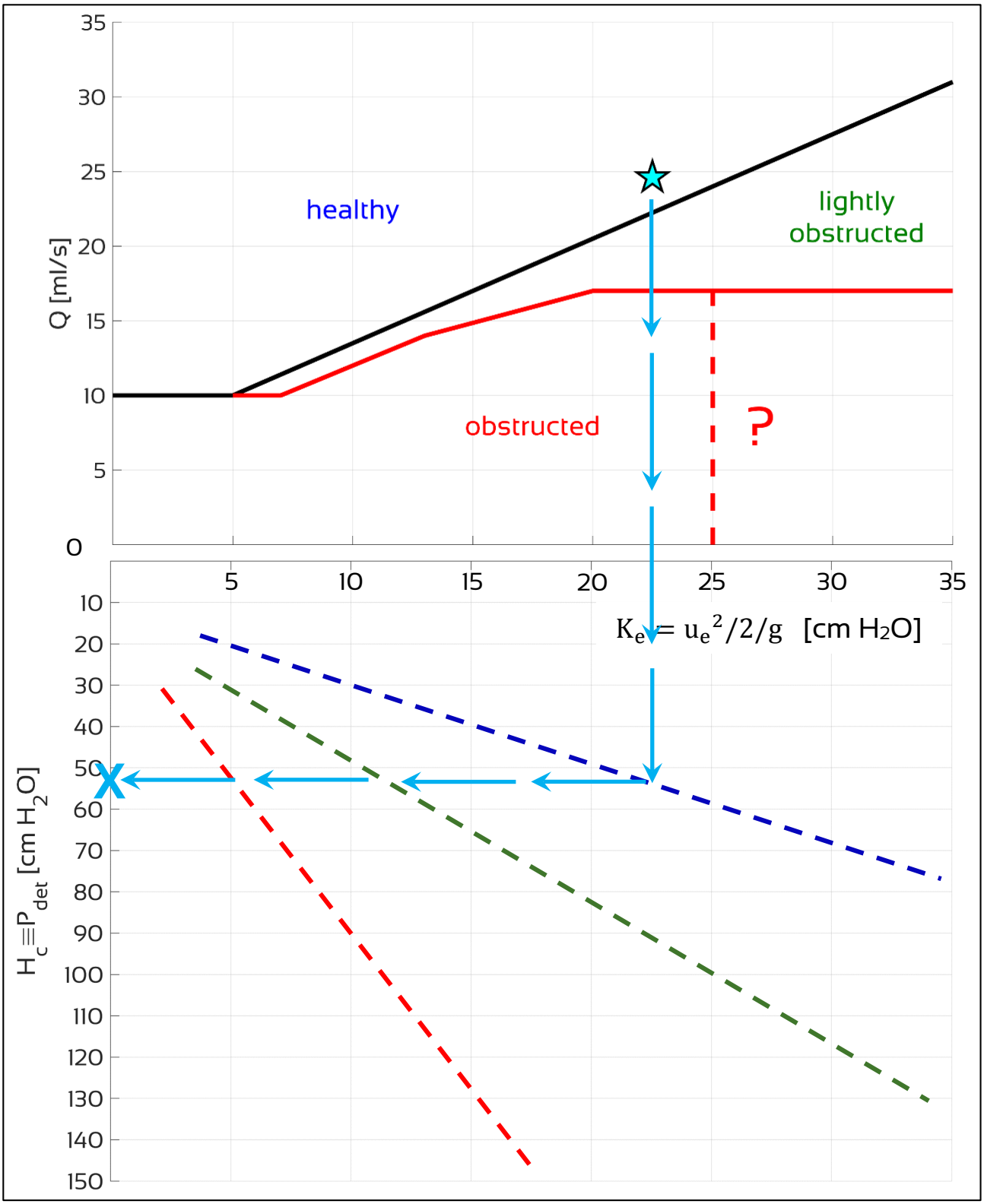

Figure 6.3: Coupled Urodynamic Diagram: the cyan star represents one of the healthy clinical trials: the detrusorial pressure (cyan cross) can be estimated following the relation in the second diagram according to the state of the patient (healthy, lightly obstructed or obstructed)

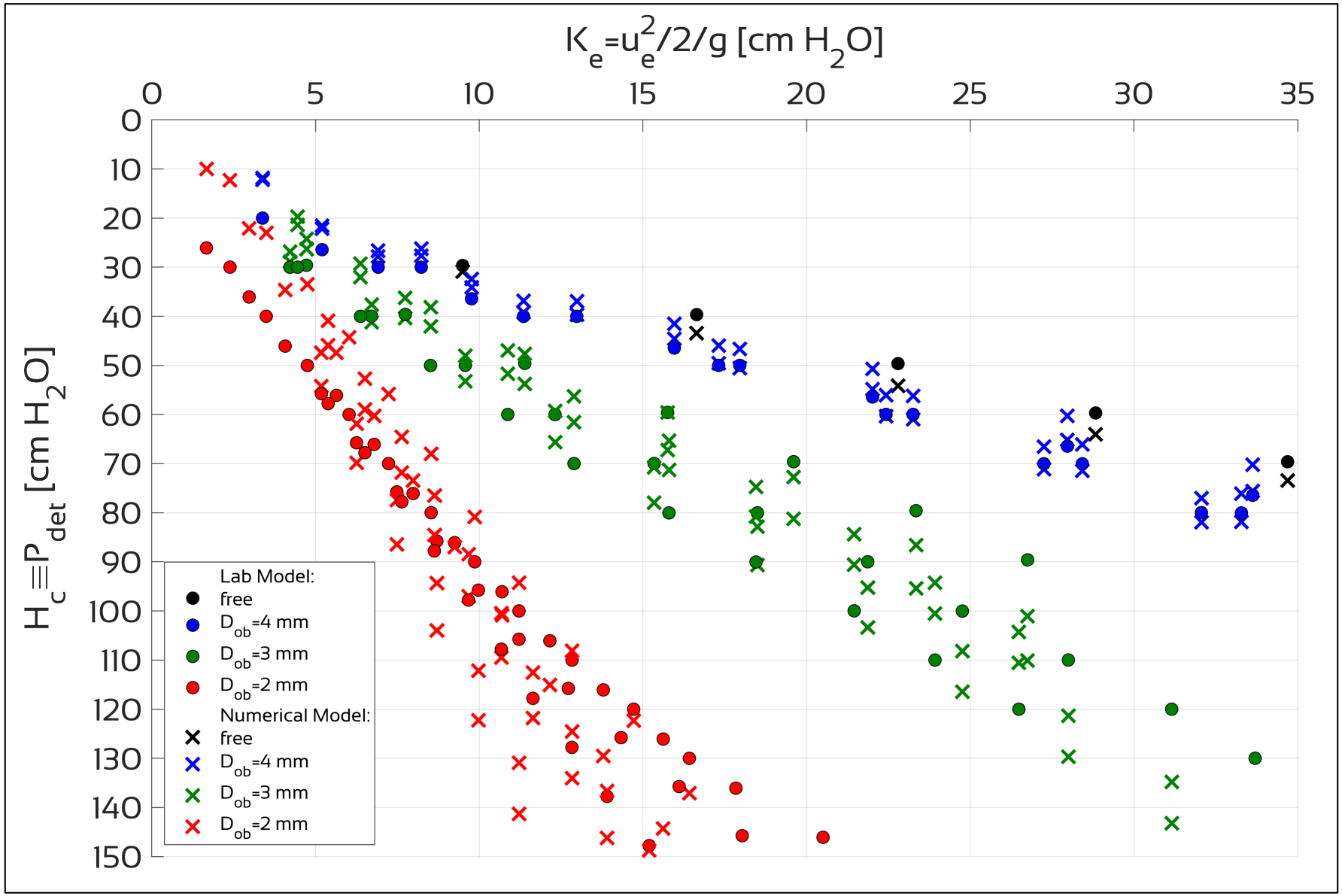

Figure 6.4: total head at the Tube entrance H_c (corresponding to detrusorial pressure P_{det}) as a function of kinetic head at the Tube exit K_e: comparison between Lab tests (dots) and numerical model (crosses)

CONCLUSIONS

An Innovative Instrumentation aimed to assess the functionality of the lower urinary tract (LUT) in a ***very non-invasive way*** has been developed, by which it is possible to take measurements of the main physical parameters, such as flow rate and exit jet velocity, without any contact with the human body.

Currently, the LUT functionality is investigated on the basis of the Pressure/Flow Study, ***which is highly invasive***: it is performed with a catheter positioned in the bladder through the urethra that allows the recording of the pressures inside the bladder during the micturition.

In order to relate the non-invasive measurements to the LUT functionality, extensive analysis have been carried out using both physical and numerical modelling based on the mechanical analogies between the LUT and a hydraulic system.

More specifically, the basic concept arises from considering the LUT similar to a hydraulic system consisting of a pressure feed tank (bladder) and an outlet elastic duct (urethra) whose physical behavior is governed by the laws of fluid mechanics. Starting from the knowledge of the physical quantities of the urinary jet measurable outside of the urethra it is possible to model the LUT internal urodynamic characteristics.

A physical model of the LUT has been designed and assembled in the Fluvial and Lagoon Hydraulics and Biofluidodynamics Laboratory of the Department of Civil and Environmental Engineering (DICEA) of the University of Florence: it consists of a pressure feed tank connected to a latex elastic collapsible output tube (Tube) that it is assumed to have a similar behavior to the urethra.

Extensive laboratory activities on the model of the LUT been carried out to collect experimental data. The tests have been divided into three main categories; each of them is associated with a particular physical condition of the LUT:

- ***"Physiological flow condition" tests (Physiological-tests)***, used to calibrate the Innovative Instrumentation and to correlate the jet exit velocity u_e with the detrusorial pressure P_{det} on healthy people;
- ***"Pathological flow condition" tests (Pathological-tests)***, to correlate the flow output characteristics in people with urethral obstructions;
- ***"Diagnostic flow condition" tests***, characterized by the presence of a catheter inside the Tube. These tests are subdivided in: ***Diagnostic-tests***, to evaluate the effects of the catheter on urethral flow; ***FV-tests***, to measure flow variables inside the Tube.

Regarding the FVtests, a specific device has been developed to measure piezometric and total head inside the collapsible tube, modifying the catheter that is currently used in urodynamic investigations.

In parallel with the Laboratory activities, two other aspects of this project have been carried out:

- developing a Prototype of the Innovative Instrumentation;
- developing a numerical model.

The Prototype of the Innovative Instrumentation, built in the Hydraulic Laboratory of the DICEA, has been designed to be as compact as possible. It has been created a structure that supports a camera, to record the jet, and a funnel, to convey the urine into a collector brick positioned on a precision scale. The classic wall urinal for men has been taken as the initial idea for the construction of the Innovative Instrumentation.

After the calibration, the Prototype has been taken to the Urology Clinic at the Department of Experimental and Clinical Medicine (DMSC) of Careggi Hospital, Florence, to perform a clinical testing campaign. Clinical trials ran from January 2019 to February 2020, when they had to stop due to restriction prevention measures for Covid19 pandemic. 123 tests were performed on healthy male volunteers and 4 on obstructed male volunteers, for a total of 127 tests: the results are very encouraging, showing good agreements with the standard clinical methods.

The numerical model has been developed to simulate the physical model, along with a new specific tube law that can relate the pressure inside the collapsible tube to its cross-sectional area ratio. It was particularly challenging to find a tube law for collapsible tubes that could fit this specific case; in fact, the results of the numerical model are strongly dependent on the reliability of the tube law.

Finally, a Coupled Urodynamic Diagram (that basically is a new version of the Schäfer's diagram) in terms of non-invasive measurements has been proposed. ***A preliminary analysis based on laboratory and clinical data seems to confirm the validity of the proposed approach***.

Some considerations on possible perspectives are the following:

- the proposed Innovative Instrumentation seems to be a promising improvement in the urology instrumentation. However, more clinical data, together with additional laboratory experiments will require in order to better define the preliminary results obtained in this work;
- the proposed instrumentation would allow the progressive replacement of current invasive technologies, thus reducing discomfort for patients, eliminating clinical complications and cutting down operating costs for the healthcare facilities;
- the engineering of the Innovative Instrumentation, and its possible patenting, could represent a significant step forward in the prevention and control of citizens' health, thanks to the reduced costs and its non-invasiveness. This process would allow the progressive replacement of the current invasive technologies, thus reducing the discomfort for patients and eliminating any complications due to the positioning of the

urethral catheter necessary for a correct execution of the investigations; furthermore, the operating costs (in terms of materials and human resources) for the health facilities would be considerably reduced, which annually exceed the cost of the instrument itself. The analysis would be simple and cheap, it could be installed in any public and private structure like a common toilet, and it could give a first indication of the functional conditions of the LUT through simple urination.

BIBLIOGRAPHY

Abrams P, *Urodynamics*, Springer Science, 2006

Abrams P, Cardozo L, Fall M, Griffiths DJ, Rosier P, Ulmsten U, Van Kerrebroeck P, Victor A, Wein A, *The Standardisation Of Terminology Of Lower Urinary Tract Function: Report From The Standardisation Sub-Committee Of The International Continence Society*, Neurourology And Urodynamics 21:167-178, 2002

Abrams P & Griffiths DJ, *The Assessment Of Prostatic Obstruction From Urodynamic Measurements And From Residual Urine*, British Journal Of Urology 51-2:129-134, 1979

Abrams P & Lim CS, *The Abrams-Griffiths Nomogram*, World Journal Of Urology 13:34-39, 1995

Arbuckle LD Jr & Paquin AJ Jr, *Urinary Outflow Tract Resistance In Normal Human Females*, Investigative Urology 1:216-28, 1963

Baseman AG, Baseman JG, Zimmern PE & Lemack GE, *Effect Of 6f Urethral Catheterization On Urinary Flow Rates During Repeated Pressure-Flow Studies In Healthy Female Volunteers*, Urology 59:843-846, 2002

Belal M & Abrams P, *Noninvasive Methods Of Diagnosing Bladder Outlet Obstruction In Men. Part 2: Noninvasive Urodynamics And Combination Of Measures*, The Journal Of Urology 176:29-35, 2006

Blake C & Abrams P, *Noninvasive Techniques For The Measurement Of Isovolumetric Bladder Pressure*, The Journal Of Urology 171:12-19, 2004

Brooks BS, Falle SAEG & Pedley TJ, *Numerical Solutions For Unsteady Gravity-Driven Flows In Collapsible Tubes: Evolution And Roll-Wave Instability Of A Steady State*, Journal Of Fluid Mechanics 396:223-256, 1999

Brown M & Wickham JEA, *The Urethal Pressure Profile,* British Journal Of Urology 41-2:211-217, 1969

Bryndorf J & Sandøe E, *The Hydrodynamics Of Micturition*, Danish Medical Bullettin 7:65-71, 1960

Carpenter PW & Pedley TJ, *Flow Past Highly Compliant Boundaries And In Collapsible Tubes*, Springer-Science+Business Media B.V., 2003

Chapple CR, Steers WD & Evans CP, *Urologic Principle And Practice*, Springer, 2020

Claridge M & Shuttleworth KE, *The Dynamics Of Obstructed Micturition*, Investigative Urology 25:188-199, 1964

Colebrook CF, *Turbulent Flow In Pipes, With Particular Reference To The Transition Region Between The Smooth And Rough Pipe Laws*, Journal Of The Institution Of Civil Engineers 11,4:133-156, 1939

Di Benedetto P, Pesce F, & Tubaro A, *Urodinamica Clinica-Tecniche*, McGraw-Hill, 2005

Elad D, Kamm RD & Shapito AH, *Choking Phenomena In A Lung-Like Model*, Journal Of Biomechanical Engineering 109:1-9, 1987

Elterman DS, Chughtal B, Lee R, Te AE & Kaplan SA, *Noninvasive Methods To Evaluate Bladder Obstruction In Men*, International Brazilian Journal Of Urology, 39:4-9, 2013.

Gleason DM & Lattimer JK, *The Pressure-Flow Study: A Method For Measuring Bladder Neck Resistance*, Urology 87:844-52, 1962

Griffiths CJ, Harding C, Blake C, McIntosh S, Drinnan MJ, Robson WA, Abrams P, Ramsden PD & Pickard RS, *A Nomogram To Classify Men With Lower Urinary Tract Symptoms Using Urine Flow And Noninvasive Measurement Of Bladder Pressure*, The Journal Of Urology 174:1323-1326, 2005

Griffiths DJ, *Urethral Elasticity And Micturition Hydrodynamics In Females*, Medical And Biological Engineering 7:201-215, 1969

Griffiths DJ, *Hydrodynamics Of Male Micturition*, Medical And Biological Engineering 9:581-588, 1971

Griffiths DJ, *Urodynamics*, Adam Hilger Ltd, 1980

Griffiths DJ, Höfner K, Van Mastrigt R, Rollema HJ, Spångberg A, Gleason D, *Standardization Of Terminology Of Lower Urinary Tract Function: Pressure-Flow Studies Of Voiding, Urethral Resistance, And Urethral Obstruction*, Neurourology And Urodynamics 16:1-18, 1997

Groutz A, Blaivas JG & Sassone AM, *Detrusor Pressure Uroflowmetry Studies In Women Effect Of A 7fr Transurethral Catheter*, The Journal Of Urology, 164:109-114, 2000

Holm HH, *The Hydrodynamics Of Micturition*, Acta Radiologica: Diagnosis, Scandinavian Supplement 231:1, 1964

Müller LO &Toro EF, *A Global Multiscale Mathematical Model For The Human Circulation With Emphasis On The Venous System*, International Journal For Numerical Methods In Biomedical Engineering 30:681-725, 2014

Nitti WD, *Pressure Flow Urodynamics Studies: The Gold Standard For Diagnosing Bladder Outlet Obstruction*, Reviews In Urology, 7(suppl 6):S14-S21, 2005.

Nose H, Tatt Foo K, Bin Lim K, Yokoyama T, Ozawa H & Kumon H, *Accuracy Of Two Noninvasive Methods Of Diagnosing Bladder Outlet Obstruction Using Ultrasonography: Intravesical Prostatic Protrusion And Velocity-Flow Video Urodynamics*, Urology 65:493-497, 2004

Palminteri E, Berdondini E, Verze P, De Nunzio C, Vitarelli A & Carmignani L, *Contemporary Urethral Stricture Characteristics In The Developed World*, Urology 81:191-197, 2013

Parsons BA, Bright E, Shaban AM, Whitehouse A & Drake MJ, *The Role Of Invasive And Non-Invasive Urodynamics In Male Voiding Lower Urinary Tract Symptoms*, World Journal Of Urology, 29:191-197, 2011

Pedley TJ, *The Fluid Mechanics Of Large Blood Vessels*, Cambridge University Press, 1980

Richard P, Ordonez NI & Tu LM, *The Effect Of A 6 Fr Catheter On Flow Rate In Men*, Urology Annals, vol. 5, pp. 264-267, 2003

Santucci AR, Joyce FJ & Wise M, *Male Urethral Stricture Disease*, The Journal Of Urology 177:1667-1674, 2007

Schäfer W, *The Contribution Of The Bladder Outlet To The Relation Between Pressure And Flow Rate During Micturition*, Benign Prostatic Hypertrophy:470-498, Springer, 1983

Schäfer W, *Principles And Clinical Application Of Advanced Urodynamic Analysis Of Voiding Function*, The Urologic Clinics of North America, 17(3):553-566, 1990

Schäfer W, Abrams P, Liao L, Mattiasson A, Pesce F, Spangberg A, Sterling AM, Zinner NR & Van Kerrebroeck P, *Good Urodynamic Practices: Uroflowmetry, Filling Cystometry, And Pressure-Flow Studies*, Neurourology And Urodynamics 21:261-274, 2002

Scott JES, Clayton CB, Dee PM & Simpson W, *A Study Of The Hydrodynamics Of The Female Urethra*, The Journal Of Urology 96-5:763-778, 1966

Sekido N, *Bladder Contractility And Urethral Resistance Relation: What Does A Pressure Flow Study Tell Us?*, International Journal Of Urology, 19:216-228, 2012

Siviglia A & Toffolon M, *Steady Analysis Of Transcritical Flows In Collapsible Tubes With Discontinuous Mechanical Properties: Implications For Arteries And Veins*, Journal Of Fluid Mechanics 736:195-215, 2013

Shapiro AH, *Steady Flow In Collapsible Tubes*, Journal Of Biomechanical Engineering 126-147, 1977

Smith JC, *Urethral Resistance To Micturition: British Association Of Urological Surgeons Prize Essay*, British Journal of Urology 40:2,125-156, 1968

Toro EF & Siviglia A, *Flow In Collapsible Tubes With Discontinuous Mechanical Properties: Mathematical Model And Exact Solutions*, Communications In Computational Physics 13:361-385, 2013

US4187722 Patent, "*Device for measuring the velocity of a urine discharge*", 1981

Van Mastrigt R & Pel JJM, *Towards A Noninvasive Urodynamic Diagnosis Of Infravesical Obstruction*, BJU International 84:195-203, 1999